# The single module for Cuoricino and CUORE detectors: tests, construction and modelling

Marisa Pedretti


A thesis submitted for the degree of
Doctor of Philosophy in Physics
Università degli Studi dell'Insubria
Department of Chemical, Physical and Mathematical Sciences
March 2004

Supervisor: Prof. Andrea Giuliani

To my parents

# Contents

# INTRODUCTION

The recent experimental results about neutrino flavor oscillations show that neutrinos have finite masses; however, these studies can give indications only on the difference of the squares of the neutrino masses. Many other neutrino features, e.g. the absolute mass values, remain unknown. For this reason, the interest of the scientific community in the neutrinoless Double Beta Decay ($0\nu$DBD ) – a rare nuclear transition which violates lepton number conservation – has been increasing more and more in the last years. In fact, the study of $0\nu$DBD can provide crucial information on both the absolute neutrino mass scale and the neutrino nature (Dirac or Majorana particle).

This doctoral thesis deals with a series of experiments searching for $0\nu$DBD of $^{130}$Te with bolometric detectors: MiDBD (Milano Double Beta Decay experiment), Cuoricino (small "CUORE") and CUORE (Cryogenic Underground Observatory for Rare Events). My research work concerns basic experimental aspects of these experiments, in particular about the design and the construction of the elementary detecting modules, and was performed at the Università degli Studi dell'Insubria (Como, Italy) and at the Laboratori Nazionali del Gran Sasso (L'Aquila, Italy). The fundamental principle on which this search is based is the use of bolometric devices acting both as source and detector of $0\nu$DBD of $^{130}$Te and cooled down to a few mK in a low radioactivity deep underground environment. High sensitivity to the $0\nu$DBD process requires high energy resolution of the detectors (of the order of 0.1 %), low spurious counts in the relevant $0\nu$DBD spectral region (of the order of 0.1–0.001 counts/kev/kg/y) and high sensitive masses (of the order of 100–1000 kg).

The MiDBD experiment, consisting of 20 $TeO_2$ bolometers for a total mass of 6.8 kg, can be divided in two phases, named MiDBD-I and MiDBD-II respectively: at the beginning of the year 2001 the MiDBD detector was modified in order to improve the detector performance and to achieve greater sensitivity to the $0\nu$DBD (MiDBD-II). In addition, the first prototypes of the Cuoricino single module were tested in this phase. The first part of this PhD work deals with the fabrication and the operation of the MiDBD-II detector.

The Cuoricino experiment, consisting of 62 large mass bolometric detectors for a total mass of 44 kg, is the natural expansion of MiDBD-II and represents the most massive cryogenic experiment in the world at the moment. It allowed to reach a very good limit on the Majorana neutrino mass, the second in the world at the moment after only a few months run, and it has the potential to become the most sensitive search in $0\nu$DBD in the near future.

Most of the part of this thesis work focused on the Cuoricino project, which

is not only a very powerful experimental tool to dip into the Majorana neutrino mass down to the fraction of eV region, but also a first test for the CUORE experiment, which was recently proposed by a large international collaboration. CUORE, with a total mass of about 1000 kg, is the long term goal of the research activity of these years. This experiment aims at probing the neutrino absolute mass down to about 50 meV, and it has a high discovery potential if the inverted hierarchy holds in the neutrino mass pattern.

In addition to the participation to the various phases of the experiments mentioned above, my research activity focused in particular on the design and optimization of the single module of the Cuoricino detector, and on the tests performed in order to define the final structure of the basic detecting element. This R&D work was required in order to improve the signal-to-noise ratio and the homogeneity in the detector response. Moreover, this work included the study and the selection of the materials and of the methods for treating the surface of the $TeO_2$ crystals, in order to reduce the radioactive background in the region of interest of the energy spectrum, e.g. around 2.5 MeV.

In the first chapter of this thesis, the theory of the neutrino flavor oscillation is briefly reviewed and the recent experimental results in this field are presented. The problem of the nature of neutrino is introduced in the second part of this chapter. Finally, Double Beta Decay is illustrated from a general point of view and the most relevant current experiments are described. The second chapter introduces the bolometric technique in general, with special concern about macro-bolometers for the search for rare events, while in the subsequent chapter the techniques used in MiDBD-I experiment are described in greater detail. In particular, chapter three illustrates the status of the MiDBD experiment previous to the modifications made during my PhD work.

The improvements of the MiDBD detector and of its experimental set-up are described in chapter four. The subsequent three chapters describe the R&D work on the Cuoricino single module, consisting of a set of four $TeO_2$ crystals with a mass of about 800 g each: the tests that lead to define the structure and the characteristics of the single detector module are summarized in chapter five; the results obtained up to now by the Cuoricino experiment are reported in chapter six; the development of a full thermal model of the fundamental detecting element is detailed in chapter seven. The work described in this last chapter aims at improving the comprehension of the detector behavior and then at simulating the performance of the detectors as a function of critical construction parameters, in order to optimize the single CUORE module.

The CUORE project as a whole is described in chapter eight, where I report and discuss as well possible radical innovations with respect to the presently envisaged structure, aiming at a substantial improvement of the sensitivity to the Majorana neutrino mass. In particular, a new original structure of the single detecting element is described and simulated, with the purpose to develop a $TeO_2$ bolometer capable to identify an event where energy is deposited close to the surface. This would allow the rejection of the background generated by external alpha interactions, which at the moment seems to be the most limiting factor to the CUORE sensitivity.

# Chapter 1

# Neutrinos and Double Beta Decay

## 1.1 Introduction

In 1931, Pauli hypothized the existence of a very light, or massless, neutral particle involved in beta decays, in order to explain the continuous energy spectra of the beta electrons. Today this particle is named the *electron antineutrino*. Since those years, many efforts have been spent to collect information on neutrinos. In 1934, E. Fermi published the first theory on beta decay; further progress was made in the '50s, thanks to Lee and Yang's hypothesis on the P–parity violation, experimentally proved in 1956 by Wu. In 1959 F. Reines and C. Cowan performed the first direct observation of the electron antineutrino at a nuclear reactor. In 1962 muon neutrinos were discovered by L. Lederman, M. Schwartz, J. Steinberger and colleagues at the Brookhaven National Laboratories and it was confirmed that they are different from electron neutrinos. In recent years, the most exciting development has been evidenced on neutrino oscillations, that, as it will be discussed in sec. 1.2, implies that neutrinos have finite masses. However, there are many open problems in the physics of massive and mixed neutrinos: for example the absolute neutrino masses and the neutrino nature (Dirac or Majorana particle) are still unknown.

The study of neutrino properties plays an important role in fundamental physics, as it can give indications for theoretical physics beyond the Standard Model (SM). Given that fermion masses are in general one of the major problems for the SM, the observation of neutrino masses can introduce a useful new perspective on the subject.

All known particle physics phenomena are extremely well described within the SM of the elementary particles and their fundamental interactions. The SM provides a very elegant theoretical framework and it has successfully passed very precise experimental tests. The SM is a gauge theory that assumes the local gauge invariance of the Lagrangian under the transformations of

$$SU(3)_c \times SU(2)_L \times U(1)_Y \tag{1.1}$$

Since in the SM all the fundamental particles are fermions, they are described by the Dirac Lagrangian as:

$$\mathcal{L}_i = \overline{\psi}_i(x) \left[ i\gamma^\mu \partial_\mu - m \right] \psi_i(x) \tag{1.2}$$

where $\psi_i$ is the field operator, that acts on the states, and $\overline{\psi}_i = \psi_i^\dagger \gamma_0$ .
The SM contains three left-handed neutrinos. The three neutrinos are represented by two–component Weyl spinors $\nu_i$ , $i = e, \mu, \tau$, each describing a left–handed fermion. In the SM neutrinos are strictly massless, although there is no theoretical reason for such a prejudice. Furthermore, neutrinos and antineutrinos are supposed to be different particles, but no experimental proof has been provided so far.
The weak interaction processes in which neutrinos take part are described by charged–current (CC) and neutral–current (NC) Lagrangians:

$$\mathcal{L}_I^{CC} = -\frac{g}{\sqrt{2}} \sum_{l=e,\mu,\tau} \overline{\nu_{lL}} \gamma_\alpha l_L W^\alpha + h.c. \tag{1.3}$$

$$\mathcal{L}_I^{NC} = -\frac{g}{2\cos\theta_W} \sum_{l=e,\mu,\tau} \overline{\nu_{lL}} \gamma_\alpha \nu_{lL} Z^\alpha + h.c. \tag{1.4}$$

The CC and NC interaction Lagrangians conserve the three lepton numbers $L_{e,\mu,\tau}$ while CC interactions determine the notion of flavor neutrinos $\nu_{e,\mu,\tau}$.

In the first part of this chapter, an introduction to neutrino oscillation theory and to the experimental evidence is given. Then the lacking information on neutrino will be underlined. The second part of this chapter is dedicated to introduce a rare nuclear process: Double Beta Decay (DBD). The research for this decay is a intriguing challenge for the experimenters, but above all it could permit one to obtain important indications on the absolute mass scale and on the nature of neutrino. The main techniques used in DBD experiments will be presented in sec.1.7.1.

## 1.2 Neutrino flavor oscillations

Let us imagine a $W^+$ decay in which a lepton and a neutrino of a defined flavor are produced:

$$W^+ \to l_\alpha^+ + \nu_\alpha \,, \quad \alpha = e, \mu, \tau \tag{1.5}$$

Now, let's imagine that this neutrino $\nu_\alpha$ travels for a length L and finally interacts with matter producing a lepton in the final state. For the SM the charged lepton involved in this interaction will be again $l_\alpha$ but it is possible to image, beyond the SM, that the final produced lepton is of a different flavor, let's say $l_\beta$. This change of properties of the neutrino interaction with matter is called "neutrino oscillation".

In the last few years many experiments have clearly observed the oscillation of the neutrino flavors. I would like to remark in this section the implications of these phenomena.

Let's call $\nu_e$, $\nu_\mu$ and $\nu_\tau$ the neutrinos flavor eigenstates, and let's call $\nu_1$, $\nu_2$ and $\nu_3$ the neutrinos mass eigenstates. In the general case these eigenstates are different. Thus an unitary mixing matrix $U$ exists to describe the relationship between the eigenstates in the following way:

$$\begin{pmatrix} \nu_e \\ \nu_\mu \\ \nu_\tau \end{pmatrix} = \begin{pmatrix} U_{e1} & U_{e2} & U_{e3} \\ U_{\mu 1} & U_{\mu 2} & U_{\mu 3} \\ U_{\tau 1} & U_{\tau 2} & U_{\tau 3} \end{pmatrix} \cdot \begin{pmatrix} \nu_1 \\ \nu_2 \\ \nu_3 \end{pmatrix} \tag{1.6}$$

It is clear that this matrix is, for leptons, definitely equivalent to the hadronic CKM matrix. Moreover, again like the CKM matrix, $U$ can be expressed with three angles and a phase. For a given mass eigenstate $\nu_i$, the corresponding mass eigenvalue is $M_i$, for $i = 1, 2, 3$.

If the neutrino oscillations involve also "sterile" neutrinos, i.e. particles that don't participate in the SM weak interactions, the relation 1.6 takes the general form:

$$\begin{pmatrix} \nu_e \\ \nu_\mu \\ \nu_\tau \\ \nu_{s1} \\ \vdots \\ \nu_{sN} \end{pmatrix} = \begin{pmatrix} U_{e1} & U_{e2} & U_{e3} & \cdots & U_{eN} \\ U_{\mu 1} & U_{\mu 2} & U_{\mu 3} & \cdots & U_{\mu N} \\ U_{\tau 1} & U_{\tau 2} & U_{\tau 3} & \cdots & U_{\tau N} \\ U_{s11} & U_{s12} & U_{s13} & \cdots & U_{s1N} \\ \vdots & \vdots & \vdots & \ddots & \vdots \\ U_{sN1} & U_{sN2} & U_{sN3} & \cdots & U_{sNN} \end{pmatrix} \cdot \begin{pmatrix} \nu_1 \\ \nu_2 \\ \nu_3 \\ \nu_4 \\ \vdots \\ \nu_N \end{pmatrix} \tag{1.7}$$

where N is the number of sterile neutrinos and $\nu_i$ is again a mass eigenstate with mass eigenvalue of $M_i$, with $i = 1, ...N$.

From eqs. 1.6 and 1.7 it is easy to understand that a flavor eigenstate is a linear combination of mass eigenstates:

$$\mid \nu_\alpha \rangle = \sum_i U^*_{\alpha i} \mid \nu_i \rangle \tag{1.8}$$

From these considerations it's possible to show that experiments on neutrino oscillations cannot give the absolute value of neutrino masses but only the square differences among neutrinos mass eigenvalues. In fact, suppose one produces a neutrino of a certain flavor, say $\nu_\alpha$, and that, after it has traveled for a length L, it interacts in a target. What is the probability that the charged lepton produced in the final states is $l^+_\beta$? In other words, what is the probability that $\nu_\alpha$ oscillates in $\nu_\beta$? Before trying to answer this question, let's write the probability amplitude A that a $\nu_\alpha$ could change into a $\nu_\beta$. This probability is given by the product of three independent probabilities:

$$\begin{aligned} A(\nu_\alpha \to \nu_\beta) = \sum_i \big[ & A\left(\text{neutrino born with } \ell^+_\alpha \text{ is } \nu_i\right) \times \\ & A\left(\nu_i \text{ propagates }\right) \times A(\text{when } \nu_i \text{ interacts it makes } \ell^-_\beta \text{ }) \big] \end{aligned} \tag{1.9}$$

The SM interactions are described by the following Lagrangian:

$$\mathcal{L}_{\ell\nu W} = -\frac{g}{\sqrt{2}} \sum_{\substack{\alpha=e,\mu,\tau \\ i=1,...,N}} \overline{\ell_{l\alpha}} \gamma^\lambda U_{\alpha i} \nu_{Li} W^-_\lambda - c.c. \tag{1.10}$$

ans so, neglecting irrelevant factors,

$$A\left(\text{neutrino born with } \ell_\alpha^+ \text{ is } \nu_i\right) = U_{\alpha i}^* \tag{1.11}$$

and

$$A\left(\text{when } \nu_i \text{ interact it makes } \ell_\beta^-\right) = U_{\beta i}. \tag{1.12}$$

From the Schrödinger equation that describes the temporal evolution of a neutrino mass eigenstate at the interaction time $\tau$:

$$i\frac{\partial}{\partial \tau_i} \mid \nu_i(\tau_i)\rangle = M_i \mid \nu_i(\tau_i)\rangle \tag{1.13}$$

follows that

$$\mid \nu_i(\tau_i)\rangle = e^{-iM_i\tau_i} \mid \nu_i(0)\rangle \tag{1.14}$$

and so

$$A\left(\nu_i \text{ propagates }\right) = \langle \nu_i(0) \mid \nu_i(\tau_i)\rangle = e^{-iM_i\tau_i} \tag{1.15}$$

The Lorentz–invariant phase factor $\exp(-iM_i\tau_i)$ could be rewritten in terms of the time $t$ and the position $L$ in the laboratory frame as

$$e^{-i(E_it-p_iL)} = e^{-i(E_i-p_i)L}, \tag{1.16}$$

where $E_i$ and $p_i$ are respectively the neutrino energy and momentum in the laboratory frame and the highly relativistic approximation has been used so that $t \simeq L$.

Let's suppose that the neutrino is created with a defined energy $E_i$, regardless of which $\nu_i$ it happens to be. Then its total energy is

$$E_i = \sqrt{p^2 + M_i^2} \simeq p + \frac{M_i^2}{2p} \tag{1.17}$$

So the second probability that appears in (1.9) is

$$A\left(\nu_i \text{ propagates }\right) \simeq e^{-i\dfrac{M_i^2}{2p}L}. \tag{1.18}$$

The same result could have been gained starting from a neutrino of defined momentum $p$, since highly relativistic neutrinos have $E \simeq p$.

Using equations 1.11, 1.18 and 1.12 the total oscillation amplitude becomes

$$A(\nu_\alpha \to \nu_\beta) = \sum_i U_{\alpha i}^* e^{-iM_i^2\frac{2p}{L}} U_{\beta i} \tag{1.19}$$

Therefore, writing $\delta M_{ij}^2$ for $\delta M_{ij}^2 = M_i^2 - M_j^2$, the oscillation probability from $\nu_\alpha$ to $\nu_\beta$ is

$$\begin{aligned} P(\nu_\alpha \to \nu_\beta) &= \mid A(\nu_\alpha \to \nu_\beta) \mid^2 \\ &= \delta_{\alpha\beta} - 4\sum_{i>j} \Re(U_{\alpha i}^* U_{\beta i} U_{\alpha j} U_{\beta j}^*) \sin^2\left(\delta M_{ij}^2 \frac{L}{4E}\right) \\ &+ 2\sum_{i>j} \Im(U_{\alpha i}^* U_{\beta i} U_{\alpha j} U_{\beta j}^*) \sin\left(\delta M_{ij}^2 \frac{L}{2E}\right). \end{aligned} \tag{1.20}$$

Using natural units ($\hbar = 1, c = 1$), the previous equation leads to the important result that

$$\delta M_{ij}^2 \frac{L}{4E} = 1.27 \delta M_{ij}^2 (\mathrm{eV}^2) \frac{L(\mathrm{km})}{E(\mathrm{GeV})}. \tag{1.21}$$

It's possible to note that the probability $P(\nu_\alpha \to \nu_\beta)$ oscillates as a function of $L/E$ (after which this phenomena is named). This oscillation behavior is due to the interference between two different mass eigenstates. The phase of this interference is proportional to $\Delta M_i^2$ and so, as already said, experiments on neutrino oscillations can provide information on $M_i^2 - M_j^2$ but not on the absolute neutrino masses. From eq. 1.21, it is possible to observe that the relative masse sensitivities are related to the $L/E$ ratio:

$$\delta M_{ij}^2 (eV^2) \gtrsim \left[ \frac{L[\mathrm{km}]}{E[\mathrm{GeV}]} \right]^{-1}. \tag{1.22}$$

Furthermore the eq. 1.20 shows that the neutrino flavor oscillation phenomenon doesn't occur if all the neutrino masses vanish, because in this case $P(\nu_\alpha \to \nu_\beta) = \delta_{\alpha\beta}$.

In the simpler case where only two neutrino flavors are involved in the oscillation process, the calculation can be easily carried on a bit further. Suppose $\nu_e$ and $\nu_\mu$ are two neutrinos with their relative mass eigenstates. The unitary mixing matrix could be rewritten as

$$A = \begin{bmatrix} U_{e1} & U_{e2} \\ U_{\mu 1} & U_{\mu 2}. \end{bmatrix} \tag{1.23}$$

Following the same steps of the previous calculation and naming $\delta M_{21}^2 \equiv \delta M^2$ it results

$$P(\nu_e \to \nu_\mu) = 4 |U_{e2}|^2 |U_{\mu 2}|^2 \sin^2 \left( 1.27 \delta M^2 (\mathrm{eV}^2) \frac{L[\mathrm{km}]}{E[\mathrm{GeV}]} \right). \tag{1.24}$$

Eq. 1.23 can be rewritten, using an angle, usually called the leptonic mixing angle $\theta$, and three phases $\varphi_{1,2,3}$:

$$A = \begin{bmatrix} e^{i\varphi_1} \cos\theta & e^{i\varphi_2} \sin\theta \\ -e^{i(\varphi_1+\varphi_3)} \sin\theta & e^{i(\varphi_2+\varphi_3)} \cos\theta \end{bmatrix} \tag{1.25}$$

Since $4|U_{e2}|^2 |U_{\mu 2}|^2 = \sin^2 2\theta$ the probability assumes the more common expression

$$P(\nu_e \to \nu_\mu) = \sin^2 2\theta \sin^2 \left( 1.27 \delta M^2 (\mathrm{eV}^2) \frac{L[\mathrm{km}]}{E[\mathrm{GeV}]} \right). \tag{1.26}$$

Another useful case happens when 3 neutrinos are involved in the oscillation processes. Let's suppose that the mass differences can be expressed as

$$\delta M_{21}^2 \equiv \delta M_{\mathrm{small}}^2 \ll \delta M_{31}^2 \simeq \delta M_{32}^2 \equiv \delta M_{\mathrm{big}}^2. \tag{1.27}$$

as described in fig. 1.1. Let's consider also an experiment for which $L/E$ is such that $M_{\mathrm{big}}^2 \frac{L}{E} \sim 1$, and so $M_{\mathrm{small}}^2 \frac{L}{E} \ll 1$. Making proper calculations (see for example [1]), it results that

$$P(\nu_\alpha \to \nu_{\beta \neq \alpha}) = 4 |U_{\alpha 2}|^2 |U_{\beta 2}|^2 \sin^2 \left( 1.27 \delta M_{\mathrm{big}}^2 (\mathrm{eV}^2) \frac{L(\mathrm{km})}{E(\mathrm{GeV})} \right). \tag{1.28}$$

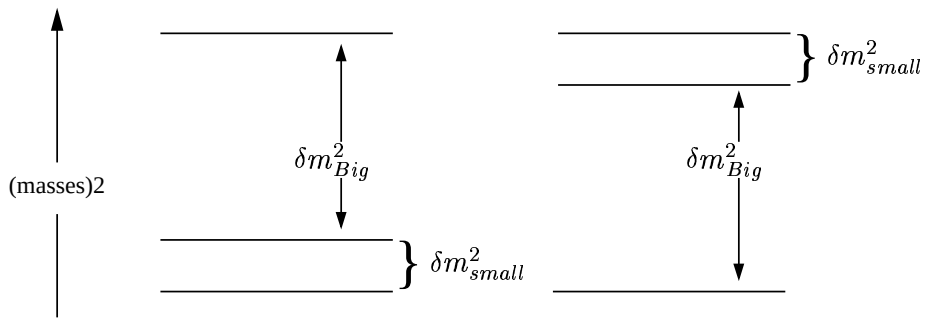


Figure 1.1 - Normal (left) and inverted (right) neutrino mass hierarchy.

This expression is very similar to that obtained with two neutrinos. This fact can be easily explained: for an experiment for which $M^2_{\rm small}\frac{L}{E} \ll 1$, the $\nu_1$ and $\nu_2$ neutrinos look like a single neutrino because it not possible to distinguish between them.

## 1.3 Experiments on the neutrino flavor oscillations

A very short introduction on neutrino flavor oscillation experiments follows here only to give an idea of the techniques and of the experimental steps that have lead to the present knowledge on oscillation parameters. For a complete review papers see [2, 3, 4, 5].

The experiments on neutrino flavor oscillations could be divided into two main classes:

- in the appearance experiments, a neutrino beam with a defined flavor is created, usually by means of accelerators, and, at a certain distance L, the appearance of neutrinos with different flavor is searched.
- in the disappearance case, experimenters have to show the lack of neutrinos from a beam produced with a certain flavor in an initial spatial point and detected at a distance L. This category includes the experiments that study solar neutrinos, atmospheric neutrinos, and the experiments performed with accelerators and nuclear reactors.

All these experiments are characterized by the neutrino source, the energy $E_\nu$ of the neutrino beam, the detector placed at a distance $L$ and by the $L/E_\nu$ parameter. Ideally, one would like to study all the neutrino beam transitions listed in table 1.3, with the transitions of the respective antiparticles. The neutrino discrimination is achieved by identification and charge measurements of the related charged leptons. In practice, muons are the easiest to identify, taus are the next easiest only because of their muon decay, and finally electrons are the most difficult. Although detector technologies exist that could achieve all these goals, the fact that neutrinos are weakly interacting particles makes their detection a tough task. Thus, typical experiment requirements are large detector volume, high detection sensitivity and low background environments.

| | $\nu_e$ beam | $\nu_\mu$ beam | $\nu_\tau$ beam |
|---|---|---|---|
| Appearance | $\nu_e \to \nu_\mu$ | $\nu_\mu \to \nu_e$ | $\nu_\tau \to \nu_e$ |
| Appearance | $\nu_e \to \nu_\tau$ | $\nu_\mu \to \nu_\tau$ | $\nu_\tau \to \nu_\mu$ |
| Disappearance | $\nu_e \to \nu_e$ | $\nu_\mu \to \nu_\mu$ | $\nu_\tau \to \nu_\tau$ |

Table 1.1 - List of all the possible neutrino beams that can present evidence of flavor oscillation.

It is common practice to deduce these results in the two–neutrino framework and translate the constraints on $P(\nu_\alpha \to \nu_\beta)$ into allowed or excluded regions in the plane $(\delta M^2, \sin^2\theta)$ or $(\delta M^2, \tan^2\theta)$.

### 1.3.1 Solar neutrino experiments

In the case of experiments studying solar neutrinos, the neutrino source is, of course, the nuclear activity of the Sun. In fact the Sun produces, in its core, electron neutrinos from the p–p reaction chain (in particular $p+p \to D+e^+ +\nu$) and from the $^8B$ and $^7Be$ reaction chains. The Standard Solar Model (SSM) [6] predicts the probability of neutrino production, with their rates and their energies. The fig. 1.2 shows the solar neutrino spectrum predicted by the SSM along with the thresholds of the principal experiments.

Presently, two types of solar neutrino detectors exist:

- radiochemical detectors,

- Cherenkov detectors.

The radiochemical experiments use the nuclear reaction

$$(A, Z) + \nu_e \rightleftharpoons (A, Z+1) + e^- \tag{1.29}$$

The target is exposed to the solar neutrino flux for a certain period of time after which the nucleo that have interacted are extracted using radiochemical techniques and counted by electron capture decays of the nucleo themselves. In a Cherenkov detector the charged leptons produced by neutrino interactions emit Cherenkov light while passing through the detector. This light is recorded by photomultiplier tubes which produce an electrical pulse. This technique has the advantage to make use of a real time detector, that gives directional information (Cherenkov light allows event reconstruction), and on the fact that the recoil electron distribution gives information about the incident neutrino energy spectrum.

Historically, the first experiment that gave evidence for a deficit in the solar neutrino flux was the Homestake experiment, proposed by R. Davis and started operating from 1968 in a gold mine in Lead, South Dakota. This experiment was followed by other experiments (Gallex, Sage and GNO). Their results suggested to B. Pontecorvo the idea of the solar neutrino oscillation phenomena. All the cited experiments are based on the radiochemical techniques.

The **Homestake** experiment measured the solar neutrino flux using the $\nu_e + ^{37}Cl \to e^- + ^{37}Ar$ reaction [7, 8, 9]. This reaction has a threshold of 0.814 MeV and is sensitive to the $^8$B and $^7$Be chains. The total predicted rate in the

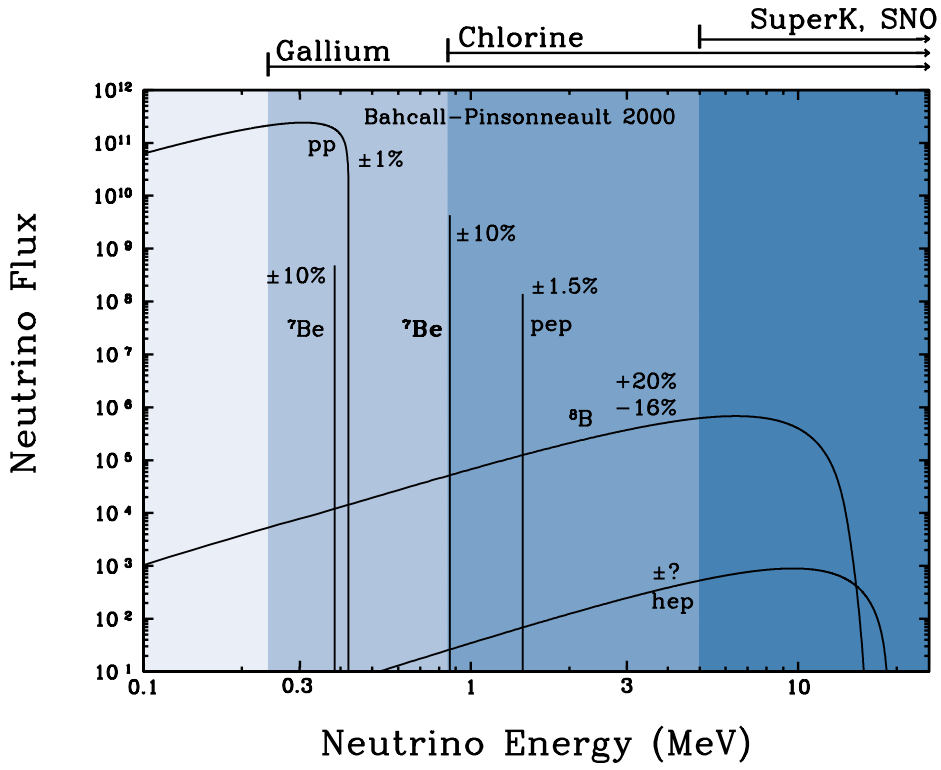


Figure 1.2 - In this figure it is possible to see the predictions of the Standard Solar Model concerning the neutrino flux from the Sun as function of the $\nu$ energy. On the top of the spectrum the bars show the range of the neutrino spectrum investigated by some experiments.

Cl experiment is $7.6^{-1.3}_{+1.1}$ Solar Neutrino Unit (SNU), where a SNU is defined as 1 SNU = $10^{-36}$ events/(target atom ×second). The observed rate of solar neutrinos in the experiment was 2.56± 0.16 (stat) ± 1.1 (syst) SNU. This gives a ratio of observed to expected SSM rate of 0.335 ± 0.029, implying a deficit in the solar neutrino flux.

Three experiments measure the solar neutrino flux using the reaction $\nu_e + {}^{71}Ga \rightarrow e^- + {}^{71}Ge$ that has a low energy threshold (0.233 MeV), and so they were sensitive to the basic *pp* solar neutrinos. The SSM prediction for this reaction is $130^{-9}_{+7}$ SNU.

The **Soviet American Gallium Experiment (SAGE)**, located in the deep underground Baksan Neutrino Observatory, gave a solar neutrino capture rate of $70.8^{-5.3}_{+5.2}(\text{stat})^{-5}_{+7}(\text{syst})$ SNU [10, 11].

The **GALLEX** experiment [12, 13], located in the Gran Sasso underground laboratory in Italy, gave $77.5^{+7.6}_{-7.8}$ SNU.

The **Gallium Neutrino Observatory (GNO)** is an upgraded version of the GALLEX experiment which has taken data until a few months ago [14]. Up to now it has observed a rate of 67.7±7.2 (stat) ± 3.2 (syst) SNU.

The **Kamiokande (Kamioka Nucleon Decay Experiment)** experiment was started in 1983 to look for proton decay. In 1985 it was renovated for the solar neutrino research to test the anomaly observed by the Homestake experiment [15, 16]. The Kamiokande detector, located in a deep mine at Kamioka, Japan, is a Cherenkov detector. It used 4500 ton of pure water. The inner 680 ton was employed as the fiducial volume. The observed process was the elastic scattering of electron neutrinos on the water electrons:

$$\nu_e + e \rightarrow \nu_e + e \tag{1.30}$$

that produce the Cherenkov light. This reaction has a threshold of 7.5 MeV and then Kamiokande is sensitive to the $^8$B solar neutrinos. Furthermore the elastic scattering can be produced by neutrinos and antineutrinos of all flavors, in fact also the $\nu_\mu$ and $\nu_\tau$ contribute to neutral current interactions. However as the $\nu_e$ interactions are produced by both neutral and charged currents, the $\nu_\mu$ and $\nu_\tau$ events are suppressed by a factor 1/6 respect to the $\nu_e$ ones. Using the timing information and the ring pattern on the photomultipliers that cover the detector walls it is possible to know which neutrinos arrive from the Sun direction. Kamiokande observed rate is 2.82 ± 0.19 (stat) ± 0.33 (syst) x $10^6$ $\text{cm}^{-2}\text{s}^{-1}$, while the SSM predicts 5.05 x $10^6$ $\text{cm}^{-2}\text{s}^{-1}$ neutrino events.

The **SuperKamiokande (SK)** experiment is an upgraded version of Kamiokande. It has 22.5 ktons of fiducial volume. The total observed rate in SK is 2.35 ± 0.02 (stat) ± 0.08 (syst) x $10^6$ $\text{cm}^{-2}\text{s}^{-1}$, almost half of the prediction of the SSM [17, 18, 19].

The results of these experiments provided evidences of a systematic solar electron neutrino deficit, as shown in fig. 1.3 where the comparison between the standard SSM predictions and the experimental results is shown.

The most recent solar neutrino experiment using a Cherenkov detector is the **Sudbury Neutrino Observatory (SNO)** [20, 21, 22, 23]. The detector was built 6800 feet underground, in a mine near Sudbury, Ontario. It uses 1000

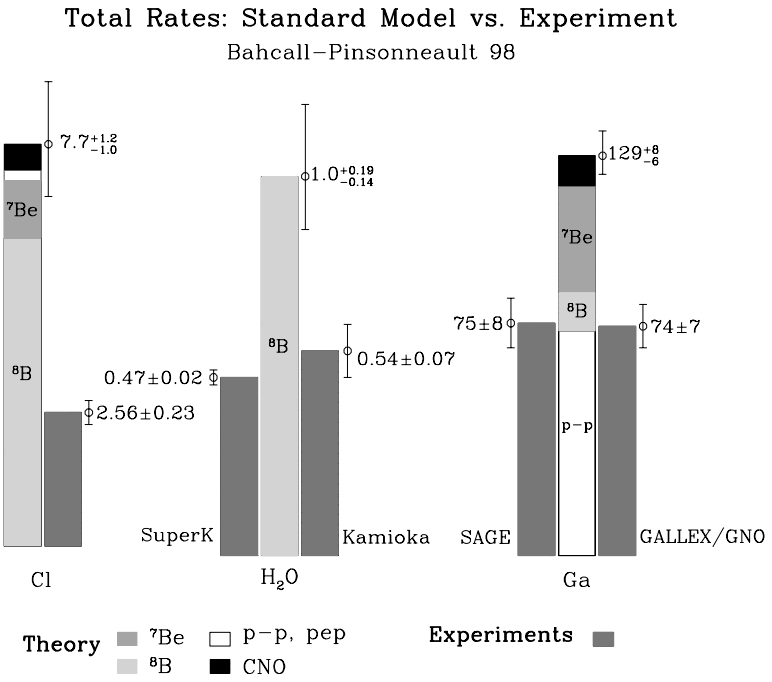


Figure 1.3 - Comparison between the experimental results of solar neutrino experiments and the SSM prediction.

tons of heavy water contained in a 12 meter diameter acrylic vessel. Neutrinos react with the heavy water ($D_2O$) to produce Cherenkov radiation detected by an array of 9600 photomultiplier tubes mounted on a geodesic support structure surrounding the heavy water vessel. SNO detects the following three reaction induced by $^8$B neutrinos above an electron threshold of 5 MeV:

$$\begin{aligned} &(CC) \qquad \nu_e + d \to e^- + p + p \qquad E_{\text{threshold}} = 1.44\text{MeV} \\ &(NC) \qquad \nu_x + d \to \nu_x + p + n \qquad E_{\text{threshold}} = 2.23\text{MeV} \\ &(ES) \qquad \nu_x + e^- \to \nu_x + e^- \end{aligned} \tag{1.31}$$

The charged current (CC) can be induced only by electron neutrinos, the neutral current (NC) can be induced by all the neutrino flavors and with the same cross section, while the elastic scattering (ES) is sensitive to all flavors but, as already pointed out, with a different cross section $\sigma$. In fact above 5 MeV:

$$\sigma_{ES}(\nu_\mu\ e) = \sigma_{ES}(\nu_\tau\ e) = 0.154 \cdot \sigma_{ES}(\nu_e\ e) \tag{1.32}$$

For each electron event collected, SNO measures the kinetic energy, the angle with respect to the Sun direction and the distance from the detector center. By combining these data, SNO obtained the following exciting results on the solar neutrino flux (all in $\times 10^6$ cm$^{-2}$s$^{-1}$):

$$\Phi_{\text{CC}}^{\text{SNO}} = 1.76 \pm 0.10, \qquad \Phi_{\text{NC}}^{\text{SNO}} = 5.09 \pm 0.62, \qquad \Phi_{\text{ES}}^{\text{SNO}} = 2.39 \pm 0.26 \tag{1.33}$$

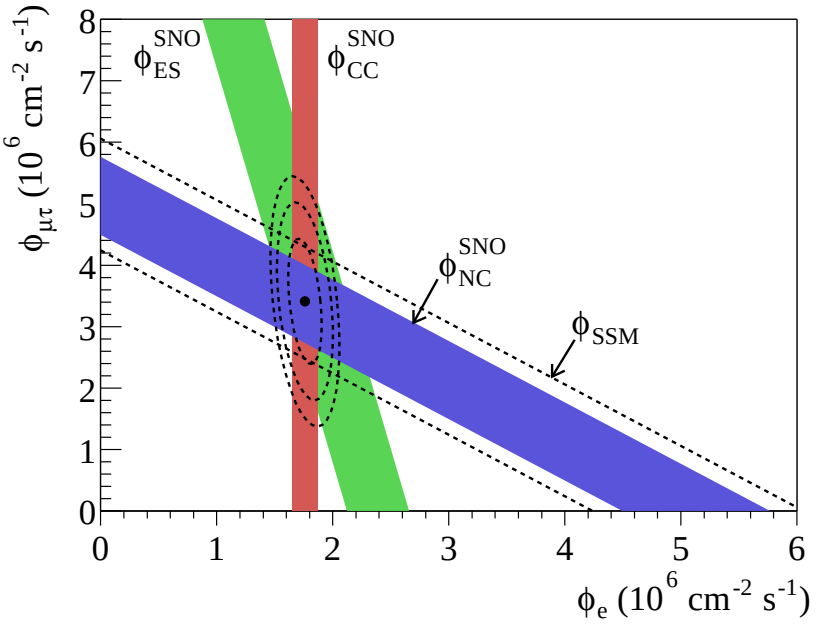


Figure 1.4 - Flux of solar $\nu_\mu$ and $\nu\tau$ neutrinos vs. flux of $\nu_e$ deduced from the three neutrino reactions in SNO. The diagonal bands show the total $^8$B flux as predicted by the SSM (dashed lines) and the one measured with the NC reaction (solid band).

The ES results are in agreement with the SK ones. The $\Phi_{CC}^{SNO}$ is a genuine measurement of the Sun $\nu_e$ flux. In case of no oscillations, it was expected that

$$\Phi_{\rm CC}^{\rm SNO} = \Phi_{\rm NC}^{\rm SNO} = \Phi_{\rm ES}^{\rm SNO} \tag{1.34}$$

The SNO results show that this is not what happens and so that a non–$\nu_e$ component is present in the solar neutrino flux, suggesting that $\nu_e$ oscillates into $\nu_\mu$ or $\nu_\tau$ . Therefore, using $\Phi(\nu_{\mu\tau}) = \Phi(\nu_\mu) + \Phi(\nu_\tau)$, the SNO results can be written as

$$\begin{aligned}
\Phi_{\rm CC}^{\rm SNO} &= \Phi(\nu_e) = 1.76 \pm 0.10 \\
\Phi_{\rm ES}^{\rm SNO} &= \Phi(\nu_e) + 0.154 \cdot \Phi(\nu_{\mu\tau}) = 2.39 \pm 0.26 \\
\Phi_{\rm NC}^{\rm SNO} &= \Phi(\nu_e) + \Phi(\nu_{\mu\tau}) = 5.09 \pm 0.62 \\
\Phi_{\rm tot}^{\rm SNO} &= \Phi(\nu_e) + \Phi(\nu_{\mu\tau}) = 5.09^{+1.01}_{-0.81}
\end{aligned} \tag{1.35}$$

and they are summarized in fig. 1.4. This plot shows that if the neutrino oscillation are taken into account than the previsions of SSM are substantially correct.

In September 2003 the SNO collaboration released the data obtained in the second phase [24], called salt phase, in which 2.5 ton of salt were added to the heavy water in the SNO detector, allowing the detection of the neutron produced in the neutral-current reaction by observing the photons produced in the reaction

$$n + {}^{35}Cl \rightarrow {}^{36}Cl + \text{several}\gamma' s (E_\gamma^{\rm tot} = 8.6\text{MeV}) \tag{1.36}$$

The better signature given by several photons and the higher cross–section of this reaction allowed the SNO collaboration to measure with good precision the total flux of active neutrinos coming from $^8$B decay in the core of the Sun. In this way SNO has achieved the ratio

$$\frac{\Phi_{\rm CC}^{\rm SNO}}{\Phi_{\rm NC}^{\rm SNO}} = 0.306 \pm 0.035 \tag{1.37}$$

that differs from the unity by about 19 standard deviations. This is a very convincing proof that solar neutrinos have transformed into muon and/or tau neutrinos on their way to the earth.

All these experimental results give as a best fit:

$$\delta M^2_{SUN} = 6.9 \times 10^{-5} \qquad tan^2\theta \sim 0.43 \tag{1.38}$$

### 1.3.2 Atmospheric neutrino experiments

When a high–energy cosmic–ray interacts with the Earth's atmosphere it produces an air shower. In particular these showers contain $\pi^{\pm}$ and $K^{\pm}$ mesons that decay in the following way:

$$\pi^+, K^+ \rightarrow \mu^+ + \nu_\mu$$

$$\pi^-, K^- \rightarrow \mu^- + \overline{\nu}_\mu$$

All muons obtained from these decays produce neutrinos in the following ways:

$$\mu^+ \rightarrow e^+ \nu_e \overline{\nu}_\mu$$

$$\mu^- \rightarrow e^- \overline{\nu}_e \nu_\mu.$$

These neutrinos are named "atmospheric neutrinos".

At low energy the ratio between the number of atmospheric muon and electron particles that reach the detectors is equal to 2 and so

$$\frac{\mu}{e} \equiv \frac{\nu_\mu + \overline{\nu}_\mu}{\nu_e + \overline{\nu}_e} = 2$$

but this ratio rises at higher energy. Using Monte Carlo calculations it is possible to predict the atmospheric neutrino flux composition.

The first "neutrino oscillation anomaly" was observed by the SuperKamiokande experiment. By means of shape analysis SK is able to distinguish between the lepton that generates the Cherenkov radiation (e or $\mu$): $\mu$–like events produce a sharp ring in the photomultiplier array that covers the walls of the detector while the e–like events produce a more diffuse and fuzzy boundary image. In addition SK is able to estimate the neutrino energy, and normally SK data are presented distinguishing between sub–GeV (E $<$ 1.33 GeV) and multi–GeV (E $>$ 1.33 GeV) neutrinos [25, 26, 27]. After these considerations it is clear that SK can compare the e–like event number to the $\mu$–like one observed ratio with the predicted one:

$$R = \frac{(\mu/e)_{\rm obs}}{(\mu/e)_{\rm MC}}. \tag{1.39}$$

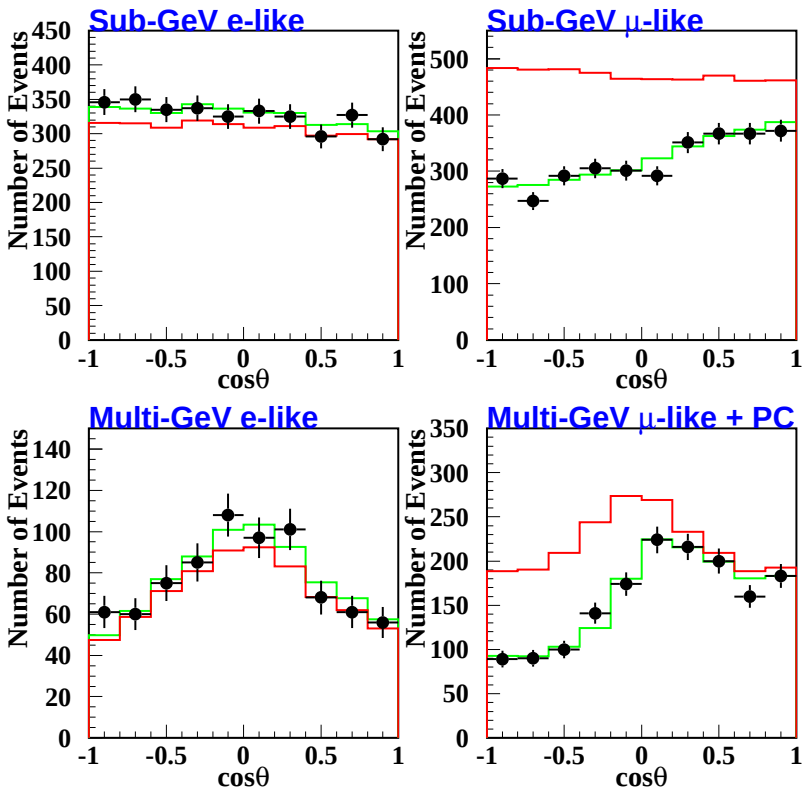


Figure 1.5 - In both figures the $\nu$ flux is shown as function of the zenith angles. The dots represent the experimental data, the symmetric black line represents the no–oscillation expected flux while the gray line is the expected flux in presence of oscillation.

The SK result obtained using this analysis is R=0.652±0.019±0.051 for sub–GeV events and R=0.661±0.034±0.079 using the collected multi-GeV events. This could indicate an increase of electron neutrinos or a decrease of muon neutrinos.

Furthermore, as pointed out in the previous section, SK is able to measure neutrino energy and direction. This event reconstruction is more efficient for high energy neutrinos. For this reason SK is able to study the $\nu$ flux as a function of the zenith angle $\Theta$ between the vertical (zenith) and the $\nu$ direction. A $\nu$ with $\Theta = 0°$ comes from above (down–going $\nu$) after travelling a distance of L $<$ 20 km (the atmosphere thickness); a $\nu$ with $\Theta = 180°$ reaches the detector from below (up–going $\nu$) after travelling the whole earth with L $<$ 13000 km. Assuming that the cosmic rays are isotropic, from Gauss's theorem a top–bottom symmetry is expected. This comparison is a powerful test because it is model independent. The results of this study are shown in fig. 1.5 where the expected symmetry for the $\nu_e$ flux (right) and a deficit of $\nu_\mu$ flux from the top detector direction (left) are highlighted. In other words only the farthest produced $\nu_\mu$ change their flavor. This result is less evident if sub–GeV events are used because the direction information is more difficult to achieve for them. These zenith analysis results indicate that the electron neutrino does not oscillate for

these energies and distances, whereas in the same conditions muon neutrinos oscillate into tau or sterile neutrinos. These results are confirmed by the MACRO experiment at the Gran Sasso National Laboratory (Italy). The ratio of the numbers of observed to expected events being $\mu_{\rm obs}/\mu_{\rm exp} = 0.72 \pm 0.13$ for upward through–going muons and $E_\nu \sim 100$ GeV [28]. Using accelerator neutrino experiments it is possible to infer that the oscillation $\nu_\mu \to \nu_{\rm sterile}$ happens with a very low probability. At 90% C.L. the oscillation parameters are in the ranges

$$1.6 \times 10^{-3} \leq \delta m^2 \leq 3.9 \times 10^{-3} eV^2 \qquad \sin^2 2\theta \geq 0.92 \tag{1.40}$$

### 1.3.3 Accelerator and reactor neutrino experiments

In the **accelerator experiments**, a neutrino beam with a defined flavor is created and, at a certain distance $L$, the appearance of neutrinos with different flavor or a lack of a neutrino beam fraction is searched for. Typically the accelerators produce a muon neutrino beams that are directed on the detector which is devoted to electron or tau neutrinos identification. Two relevant accelerator experiments will be described as examples of this approach.

A tau neutrino appearance experiment, named ICARUS, has been proposed [29]. In this experiment, proton accelerators provide essentially muon neutrino beams from the decay of p's and K's, produced when the extracted proton beam hits a target. The appearance of tau or electron neutrinos will be searched for in the underground National Laboratory of Gran Sasso where a new–generation 600–ton bubble chamber detector module (large liquid Argon TPC) will be soon installed as a first step towards the final set-up. The detector allows the three–dimensional reconstruction of the neutrino interactions with good imaging and energy resolution. The aim of the project is to detect $\tau$ particles, in particular in the golden $\tau \to e$ channel, and distinguish them from background. This kind of experiment is named "long baseline experiment" (LBL) because of the long distance (732 km) between the production and the detection points of the neutrino beam.

The LSND experiment at the Los Alamos Meson Physics Facility (LAMPF), New Mexico, USA, was originally designed to search for $\nu_\mu \to \nu_e$ oscillations using $\overline{\nu}_\mu$ from $\mu^+$ decay at rest (DAR). This is a short base–line experiment. In 1995 LSND reported an excess of electron–like events above background and gave an interpretation of that result in terms of neutrino oscillations [30, 31, 32]. The LSND detector was an approximately cylindrical tank (8.3 m long, 5.7 m diameter), located 30 m downstream from the neutrino source and filled with 167 tons of mineral oil doped with scintillator. Because of the low scintillator concentration, both scintillation and Cherenkov light could be detected by the 1220 photo–multiplier installed on the inside surface of the tank. The identification of $\nu_e$ events in LSND is based on the detection of quasi–elastic scattering:

$$\overline{\nu}_e + p \to e^+ + n \tag{1.41}$$

followed by the neutron capture process:

$$n + p \to d + \gamma(2.2 \text{ MeV}) \tag{1.42}$$

From a two neutrino analysis of the data, the best–fit values of the oscillation parameters are

$$\delta M^2_{LSND} \simeq 1.2eV^2, \qquad \sin^2 2\theta_{LSND} \simeq 3 \times 10^{-3} \tag{1.43}$$

In order to describe atmospheric, solar and LSND experiment results, it is necessary to assume that at least one sterile neutrino exists in addition to the three active neutrinos. However, in spite of the additional degree of freedom, schemes with four neutrinos do not fit well the data. The results of the LSND experiment require, however, confirmation. The MiniBooNE experiment at Fermilab, that started recently, aims at checking the LSND results.

In **nuclear reactor experiments** an electron antineutrino beam with less than 10 MeV is produced. The $\overline{\nu}_e$ is detected via the capture reaction $\overline{\nu}_e + p \rightarrow e^+ + n$. Two recent long-baseline experiments, named CHOOZ and PALO VERDE, based on this idea have given no evidence for neutrino oscillations [33, 34, 35]. Their $L$ parameter is $\sim$ 1 km and their neutrino flux energy $\sim$ 3 MeV. The CHOOZ excluded region can be expressed as:

$$\delta M^2 > 7 \times 10^{-4}\text{eV}^2 \text{ and } \sin^2 2\theta > 0.10 \tag{1.44}$$

Another important reactor experiment in the neutrino oscillation puzzle is KamLAND (Kamioka Liquid scintillator Anti–Neutrino Detector) [36, 37]. It is a disappearance experiment made in an underground laboratory in Japan, presently in operation. KamLAND measures the flux of electron antineutrinos at a certain distance ($\sim$ 180 km) from the nuclear reactors. The detector/target is 1 kton of ultra–pure liquid scintillator contained in a 13–m–diameter spherical balloon surrounded by photomultipliers. The ratio of the measured flux and the one without disappearance is $0.611 \pm 0.085$ (stat) $\pm 0.041$ (syst) for $\overline{\nu}_e$ energies $> 3.4$ MeV. The best fit of KamLAND results can be expressed in the two neutrino oscillation model as:

$$\delta M^2 > 6.9 \times 10^{-5}\text{eV}^2 \text{ and } \sin^2 2\theta = 1.0 \tag{1.45}$$

The oscillation explanation of the disappearance of atmospheric muon neutrinos has been confirmed in the long–baseline accelerator K2K experiment [38, 39]. In this case muon neutrinos are produced by pion decay. The K2K experiment measured 56 events instead of the expected $80.1^{+6.2}_{-5.4}$ in absence of oscillations, with a probability smaller than 1% that the suppression is due to statistical fluctuations. The best fit point in the physical region of the oscillation parameter space is found to be

$$\delta M^2 = 2.8 \times 10^{-3}\text{eV}^2 \text{ and } \sin^2 2\theta = 1.0 \tag{1.46}$$

Fig. 1.6 shows the allowed region resulting from a combined fit of the SK atmospheric data and K2K data.

### 1.3.4 The neutrino oscillation results: summary

The neutrino oscillation experiments provide evidence for flavor oscillations both in solar and in atmospheric neutrinos. The KamLAND experiment confirms the

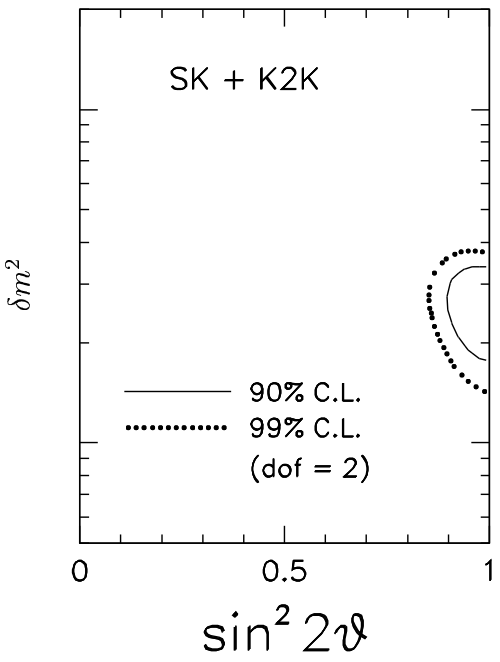


Figure 1.6 - Region allowed by a combined fit of the SK atmospheric data and K2K data.

solar neutrino oscillations and K2K and MACRO the atmospheric ones. The solar results show a $\Delta m^2_{SUN} \sim 7\times10^{-5}$ eV$^2$ and large but non–maximal mixing as summarized in fig. 1.8; the atmosperic results show a $\Delta m^2_{ATM} \sim 2\times10^{-3}$ eV$^2$ and maximal mixing. The parameter region allowed by atmospheric experiments is shown in fig. 1.7

The LSND results are not included in this summary (they will be tested at MiniBooNE).

Fitting all neutrino oscillation results it is possible to obtain the neutrino mixing matrix values [40]:

$$\|U\| \simeq \begin{pmatrix} 0.76-0.88 & 0.47-0.62 & 0.00-0.22 \\ 0.09-0.62 & 0.29-0.79 & 0.55-0.85 \\ 0.11-0.62 & 0.32-0.80 & 0.51-0.83 \end{pmatrix} \tag{1.47}$$

Three possible mass scales are possible:

- quasi degenerate (QD) : $m_1 \sim m_2 \sim m_3$, $m^2_{1,2,3} \gg |\delta m^2_{\rm atm}|$
- normal hierarchy (NH) : $m_1 \lesssim m_2 < m_3$
- inverted hierarchy (IH) : $m_3 < m_2 \lesssim m_1$

## 1.4 Open questions

As pointed out in the previous sections, in the last years much information on neutrinos has been collected. However there are still many open questions in the physics of massive and mixed neutrinos:

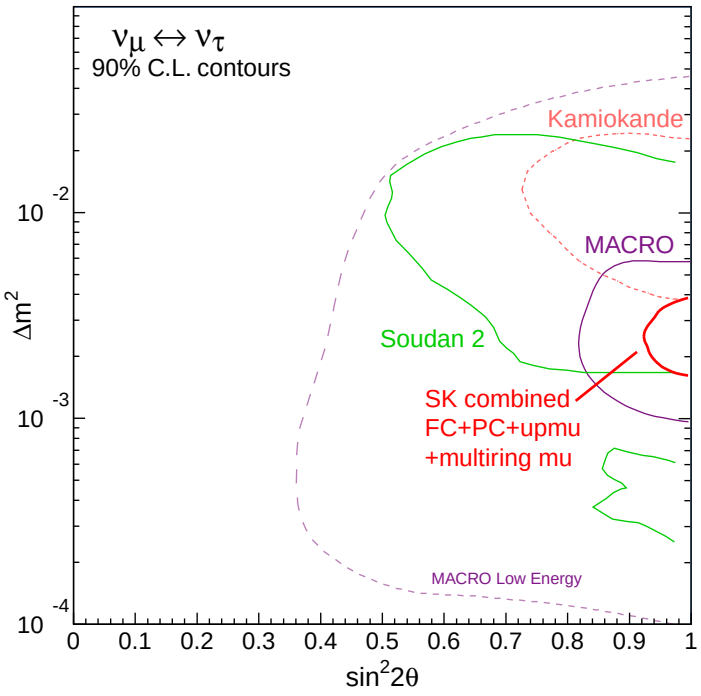


Figure 1.7 - 90% C.L. allowed regions of oscillation parameters from Super–Kamiokande (thick line), Kamiokande (thick broken line), Soudan–2 (thin line) and MACRO (thin broken line). Two flavor oscillations are assumed.

- How many neutrino flavors, active and sterile, are there? Equivalently, how many neutrino mass eigenstates are there?
- What are the masses, $M_i$, of the mass eigenstates $\nu_i$?
- Is each massive neutrino a Majorana particle ($\nu_i = \overline{\nu_i}$), or a Dirac particle ($\nu_i \neq \overline{\nu_i}$)?
- Does the behavior of neutrinos, in oscillation and other contexts, violate CP invariance?
- What are the lifetimes of the neutrinos?

To provide a more complete panorama on neutrino physics, the neutrino information obtained using direct $\nu$–mass experiments and the strongest cosmological constraints will be reported in the next sections. In the last part of the chapter, the role played by Double Beta Decay (DBD) experiments will be explained. In particular DBD experiments can give information on the neutrino nature and the neutrino mass scale, i.e. on the absolute value of neutrino mass eigenvalues.

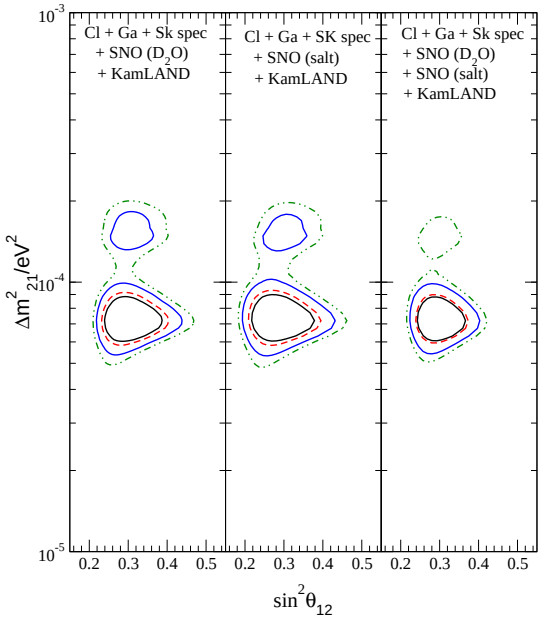


Figure 1.8 - The 90%, 95%, 99% and 99.73% C.L. regions allowed by solar and KamLAND data.

## 1.5 Direct measurements of the neutrino mass and cosmological implications

The measurement method of the neutrino mass through the detailed investigation of the high–energy part of the $\beta$–spectrum was proposed in 1934 by Fermi in his classical paper on the theory of $\beta$–decay [41] and by Perrin [42]. The first experiments on the measurement of the neutrino mass with this method were done in 1948-49 [43, 44]. Usually, the neutrino mass is measured through the measurement of the high energy part of the $\beta$–spectrum of tritium

$$^3H \rightarrow {}^3He + e^- + \overline{\nu}_e \tag{1.48}$$

but other beta sources have been used as well. The method looks for a deformation in the beta emission spectrum. This deformation will occur if the antineutrino mass is different from zero and it will be observable only very near the end–point of the spectrum, so it is very difficult to observe. Measurements of the beta–decay spectrum were carried out by the Mainz [45] group using tritium decay. They achieved a neutrino mass limit of $m_\nu < 2.2$ eV. In the Troitsk neutrino experiment [46], as in the Mainz experiment, an integral electrostatic

spectrometer with a strong inhomogeneous magnetic field, focusing the electrons, is used. They obtain about the same neutrino mass limit of the Mainz experiment ($m_\nu$ <2.2 eV).

The groups in Genova [47] and Milano/Como [48] are developing low temperature cryogenic detectors for the measurement of the beta–decay spectrum of $^{187}$Re. This element has the lowest known energy release ($Q = 2.5$ keV). The Milano/Como group has achieved a neutrino mass limit equal to $m_\nu < 15$ eV.

Cosmology can provide much information on neutrino physics as the neutrino mass has an impact on cosmological and astrophysical observables. Detailed work on the role of neutrinos in astrophysics and cosmology has been under the scrutiny of physicists with ever increasing intensity over the last few decades (see [49, 50, 51, 52, 53]).

Here only the recent WMAP implications are briefly reported. The Wilkinson Microwave Anisotropy Probe (WMAP) undertook a study of Cosmic Microwave Background radiation (CMB). The WMAP science team issued an impressive set of data on the cosmic temperature angular power spectrum and the temperature–polarization angular power spectrum [54]. Their data, combined with other CMB data that explore smaller angular scales show that:

$$\sum_i m_i < 0.71\text{eV} \tag{1.49}$$

at the 95%C.L., which implies, for 3 degenerate neutrino species, $m_i < 0.23$ eV. However, this result is strongly model–dependent and cannot be considered on equal footing as a direct measurement.

## 1.6 The neutrino nature problem: Dirac and Majorana neutrinos

Let's consider the following question: are the neutrino and the antineutrino the same particle?

In a phenomenological approach, neutrinos and antineutrinos produce leptons and antileptons via weak interaction with matter.

$$\nu_e + X \to e^- + Y \qquad \bar{\nu}_e + X \to e^+ + Z \tag{1.50}$$

There are two possible explanations of this phenomenology:

- as seen while introducing the Standard Model, leptons differ from their antiparticles for the sign of the lepton number, as

$$\mathbf{L}(\nu_e, e^-) = -1 \qquad \mathbf{L}(\bar{\nu}_e, e^+) = +1 \tag{1.51}$$

  It is thus possible to explain the relationship 1.50 stating that, like electric charge, lepton number is conserved in weak interactions. In this case, the neutrino is called a **Dirac neutrino** because the mass term that appears in the field theory lagrangian derives from the description of the neutrino as a Dirac particle with one left–side component and one right–side one.

As a consequence, it follows that neutrinos could be described as a 4–component spinor (particle and antiparticle state with opposite helicity). Furthermore,

$$\nu_e \neq \bar{\nu}_e \tag{1.52}$$

- the second possibility is to look at neutrinos and antineutrinos as particles characterized by different helicity:

$$\mathbf{H}(\nu_e) = -1\ (L) \qquad \mathbf{H}(\bar{\nu}_e) = +1\ (R) \tag{1.53}$$

When the different neutrino and antineutrino behaviors is described by their different helicity, neutrino is said to be a **Majorana neutrino**. In this case, neutrinos are represented with a 2–component spinor but, since helicity depends on the space–time reference system, then

$$\nu_e = \bar{\nu}_e \tag{1.54}$$

If neutrinos are massless particles the question about their nature is merely academic. In fact, in this case, neutrinos helicity is a well defined quantum number and so the relationship

$$\nu_e \neq \bar{\nu}_e \tag{1.55}$$

is true for both Majorana and Dirac neutrinos. On the other hand, if neutrinos have mass, then helicity depends on the reference frame.

It is in fact possible to conceive a *gedanken experiment* that makes use of this dependence of the helicity from the reference system. Let's consider an antineutrino with a mass of 1 eV, a kinetic energy of 1 GeV and helicity $R$ that strikes a proton at rest. It's known that, in this case, a positron is produced by charged current interaction. If the same antineutrino could be followed and striked by a proton of $10^{19}$ GeV, it will be seen, from the proton point of view, as a 1 GeV particle with helicity $L$. Thus, if a positron is produced from this reaction, it is clearly evident that neutrinos are Dirac particles. On the contrary, the detection of an electron will lead to the conclusion that neutrinos are Majorana particles.

In the next section it will be shown that neutrinoless double beta decay is a process able to give clear indication on the neutrino nature.

## 1.7 Double Beta Decay

The Double Beta Decay (DBD) is a rare spontaneous nuclear transition [55, 56, 57]. The existence of this decay was proposed for the first time by Maria Goeppert–Mayer [58] in 1935. In this transition a nucleus $(A,Z)$ changes the nuclear charge of two units maintaining the same mass number, so it becomes $(A,Z\pm2)$ nucleus. Let's focus the attention on the case in which a $(A,Z+2)$ nucleus appears in the final state. Normally DBD is not favored with respect to the single beta decay, and it is possible to observe this transition only for those nuclei for which the single $\beta$ decay is either energetically forbidden (this occurs when the intermediate $(A,Z+1)$ nucleus has a binding energy greater

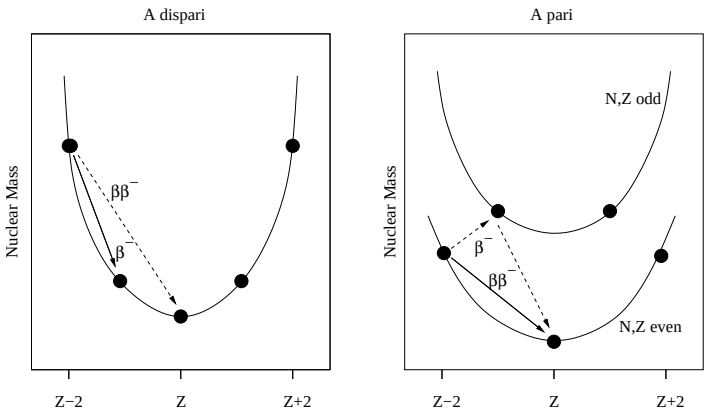


Figure 1.9 - Nuclear mass as function of the proton number.

than the $(A,Z)$ and $(A,Z+2)$ nuclei) or suppressed by a large change of the nuclear spin–parity state.

This situation can be understood by looking at the Weizsäker expression for the atomic mass as a function of the mass number $A$ and the number of neutrons $N$ and protons $Z$. In particular the Weizsäker formula contains the "pairing" term that takes into account that the binding energy of the nucleus increases if protons or neutrons are coupled to give an angular momentum equal to zero:

$$\delta = \begin{cases} +12/A^{1/2} & \text{for even A and odd Z,N} \\ -12/A^{1/2} & \text{for even A and even Z,N} \\ 0 & \text{for odd A} \end{cases} \tag{1.56}$$

If isobaric nuclei are considered and their atomic masses are plotted as function of $Z$ it is easy to find that, for odd $A$, the nuclei are positioned as described in fig. 1.9(a). If even $A$ nuclei are considered, it is found that the nuclear masses are disposed as shown in fig. 1.9(b).

Two different DBD modes are usually considered: first, the decay with two neutrinos, where lepton number is conserved and so it is allowed by the SM, that is described by the reaction

$$2\nu\text{DBD}: \quad (A,Z) \rightarrow (A,Z+2) + 2e^- + 2\bar{\nu}_e \tag{1.57}$$

and, second, the neutrinoless decay given by

$$0\nu\text{DBD}: \quad (A,Z) \rightarrow (A,Z+2) + 2e^- \tag{1.58}$$

where it is evident that lepton number is violated. An experimental confirmation of this decay mode will thus constitute an important step in the study of elementary particle physics beyond the SM.

The Feynman diagrams for both decay modes are shown in fig. 1.10.

The discrimination between these decay modes is, in principle, very simple and is based on the shape of the spectrum of the sum of the energy of the two emitted electrons. In fact, this spectrum is determined by the phase space of

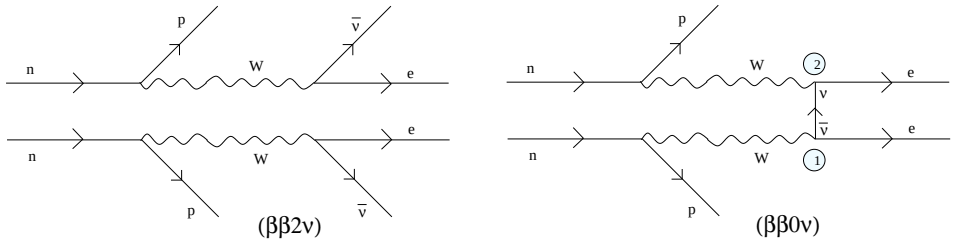


Figure 1.10 - Feynman diagrams for double beta decay with two neutrinos (left) and with no neutrino emission (right). In this second case, an antineutrino is produced at vertex 1 and a neutrino is absorbed at vertex 2. This process is allowed only for Majorana neutrinos.

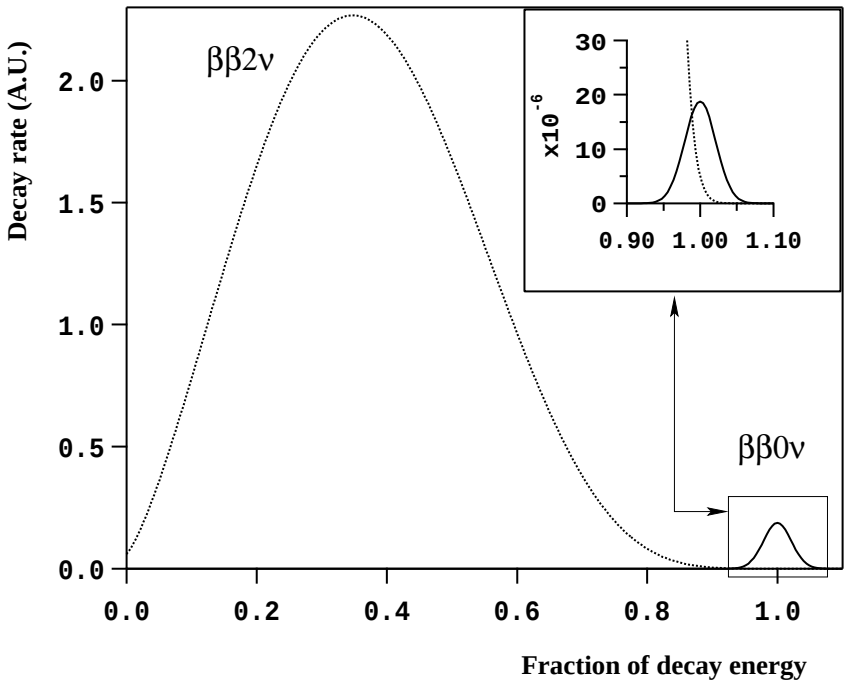


Figure 1.11 - Schematic representation of the spectrum of the sum of the energy of the electrons for DDB2$\nu$ (dashed line) and DDB0$\nu$ (solid line). In the inset the relative intensity of the two neutrinos decay is overestimated in order to underline its contribution to the DDB0$\nu$ background. All spectra are obtained with the convolution of a 5% energy resolution that is common to many experiments.

the other emitted particles. As shown in fig. 1.11, the $2\nu$DBD is a four body decay and so the spectrum is a continuum with a maximum value around one third of the $Q$ value. On the contrary, in $0\nu$DBD , the two electrons retain all the available kinetic energy (neglecting the nuclear recoil). For this reason, the spectrum is just a spike at the transition energy.

In both cases, the DBD is a semileptonic second–order weak interaction and thus is characterized by a very long lifetime: $\tau_{\beta\beta} \sim 10^{18} - 10^{22}$ years for the 2 neutrino channel. Thus, the experimental observation of this decay turns out to be a great challenge because very rare events have to be detected in the

presence of unavoidable traces from other radioisotopes with similar transition energies but with decay times that are even 10 orders of magnitude shorter. Presently, $2\nu$DBD has been observed for $\sim 10$ nuclei [59].

Neutrinoless DBD probability is usually expressed using the general relation derived from Fermi's golden rule:

$$\left[T_{1/2}^{0\nu}\right]^{-1} = G^{0\nu} \left|M^{0\nu}\right|^2 \langle m_\nu \rangle^2 \tag{1.59}$$

where $G^{0\nu}$ is the phase space integral and can be estimated exactly, $\left|M^{0\nu}\right|^2$ is the decay matrix element and $\langle m_\nu \rangle$ the effective neutrino mass:

$$\langle m_\nu \rangle = \sum_k \phi_k m_k |U_{ek}|^2 \qquad (k = 1, 2, 3) \tag{1.60}$$

Stressing again the fact that $0\nu$DBD is possible only for Majorana's neutrinos, let's observe that the $\phi_k$ phases that appear in the last equation are the CP intrinsic neutrino parities. Their presence implies that cancellations are possible. When neutrino is a Dirac particle then cancellation is total (it is equivalent to a couple of degenerate Majorana neutrinos with opposite phases). Therefore, $0\nu$DBD could take place only through the exchange of Majorana neutrinos. Since DBD is sensitive to neutrinos of a given nature, it can solve the puzzle about it.

The eq (1.60) points out also the importance of $0\nu$DBD in mass hierarchy discovery. In fact, even if $\langle m_\nu \rangle$ depends on $\phi_k$, their upper and lower limits depend on the absolute values of the mixing matrix elements. Thus, if it could be possible to measure $\langle m_\nu \rangle$ from oscillation experiments, it would mean that a range for the absolute neutrino mass can be gained, as shown in fig. 1.12 and 1.13. For this reason the $0\nu$DBD could help to solve the questions on the absolute value of neutrino masses and to disentangle the hierarchy scheme of the neutrino mass eigenvalues.

In particular a sensitivity of $\sim 10 - 50$ meV on $\langle m_\nu \rangle$ could definitely exclude the inverse and quasi–degenerate hierarchy [62].

From eq. (1.59), it is also clear that the evaluation of $\langle m_\nu \rangle$ from an experimental measure of $T_{1/2}^{0\nu}$ will require the exact knowledge of the nuclear matrix elements. From a theoretical point of view, this is the main limit when describing $0\nu$DBD . Several models have been proposed and is not simple to evaluate their correctness and accuracy, especially because they are not connected with other nuclear processes that allow a simple verification. Even the comparison with the two neutrino decay presents unclear points, mostly because of the different neutrino role in the two processes. In this situation, one possibility is to consider the spread of the theoretical values of the nuclear matrix elements as a measure of their uncertainty. In tab. 1.7 a list of values of $F_N = G^{0\nu} \left|M^{0\nu}\right|^2$ calculated in the framework of different nuclear models are summarized. More references and the results of the matrix elements calculation can be found in [63].

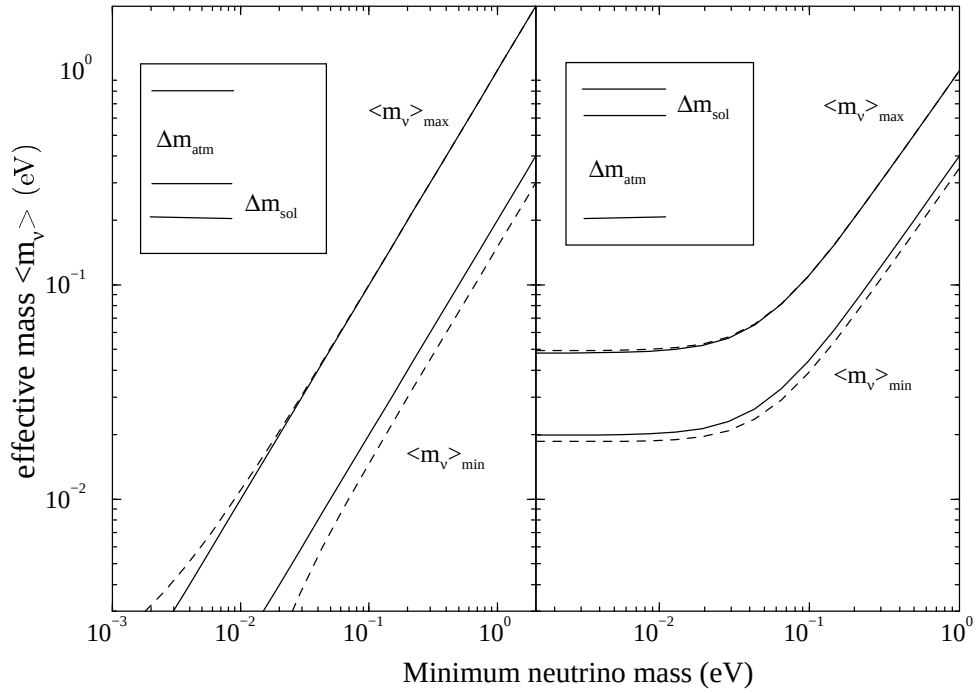


Figure 1.12 - Plot of the effective mass $\langle m_\nu \rangle$ as a function of the lightest neutrino mass (on a log-log scale) [56]. In the left side direct mass hierarchy has been supposed while on the right the inverse one. Both curves have been evaluated for the LMA solution with $\delta m^2_{\text{atm}} = 2.4 \times 10^{-3}$ eV$^2$, $\delta m^2_{\text{sol}} = 4.5 \times 10^{-5}$ eV$^2$ e $|U_{e,2}|^2 = 0.3$. Solid lines have been calculated for $U_{e,3} = 0$ while dashed line uses the latest limit obtained from the CHOOZ and Palo Verde experiments: $|U_{e,3}|^2 = 0.025$ [34, 60].

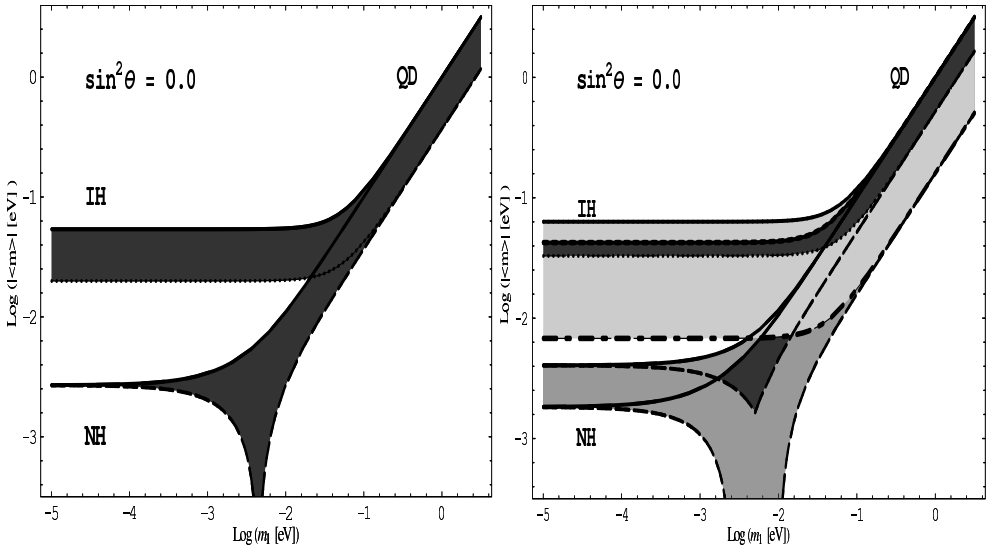


Figure 1.13 - The possibility to distinguish between the three neutrino mass hierarchies depends on the allowed values of $|\langle m_\nu \rangle|$ in each case. The acronyms NH, IH and QD stands for normal hierarchy, inverse hierarchy and quasi–degenerate. The left hand plot uses the best fit values while the right hand one uses 90% of confidence level [61].

| | Authors/Ref. | Method | $T_{1/2}(^{130}Te)$ ($10^{23}$ y) | $F_N(^{130}Te)$ ($10^{-13}$ $y^{-1}$) |
|---|---|---|---|---|
| QRPA | Staudt et al., 1992 [64] | pairing (Paris) | 0.77-0.88 | 29-34 |
| | | pairing (Bonn) | 0.9-1.1 | 24-29 |
| | Pantis et al., 1996 [65] | no p-n pairing | 8.64 | 3.0 |
| | | p-n pairing | 21.1 | 1.24 |
| | Vogel, 1986 [66] | | 6.6 | 3.96 |
| | Civitarese, 1987 [67] | | 5.2 | 5.0 |
| | Tomoda, 1991 [68] | | 5.2 | 5.03 |
| | Barbero et al., 1999 [69] | | 3.36 | 7.77 |
| | Simkovic, 1999 [70] | pn-RQRPA | 14.5 | 1.79 |
| | Suhonen et al., 1992 [71] | | 8.34 | 3.13 |
| | Muto et al., 1989 [72] | | 4.89 | 5.34 |
| | Stoica et al., 2001 [73] | large basis | 10.7 | 2.44 |
| | | short basis | 9.83 | 2.66 |
| | Faessler et al., 1998 [74] | | 9.4 | 2.78 |
| | Engel et al., 1989 [75] | generalized seniority | 2.4 | 10.9 |
| | Aunola et al., 1998 [76] | WS | 4.56 | 5.72 |
| | | AWS | 5.16 | 5.06 |
| | Rodin et al., 2003 [77] | | 27.5 | 0.95 |
| SM | Haxton et al., 1984 [78] | weak coupling | 1.6 | 16.3 |
| | Caurier et al., 1996 [79] | large basis | 58 | 0.45 |
| OEM | Hirsh et al., 1995 [80] | | 7.3 | 3.6 |

Table 1.2 - $0\nu$DBD nuclear factors of merit $F_N$ for $^{130}$Te according to different evaluation methods (QRPA: Quasi Random Phase Approximation, SM: Shell Model and OEM: Operator Expansion Method) and authors. The foreseen $0\nu$DBD half-lifetime for $^{130}$Te ($\mid m_\nu \mid$=1 eV) is also reported.

### 1.7.1 Main techniques for Double Beta Decay searches

The experimental signatures of nuclear double beta decays are in principle very clear: in the case of the neutrinoless decay, one should expect a peak (at the $Q_{\beta\beta}$ value) in the two–electron summed energy spectrum, whereas a continuous spectra will feature the two–neutrino decay mode. In spite of such characteristics, their identification is very difficult. The search for the $0\nu$DBD decay is a search for a peak superimposed on a continuum. Therefore good energy resolution is a must. Not only does it improve the signal to background in the peak search, but poor resolution would result in the $2\nu$DBD tail extending up into the peak region to become a background itself. Natural radioactivity is present in all materials at some level. Thus the source and detector must be very low in such impurities. Furthermore, the detector must be shielded from the environment and its associated radioactivity. This shielding must also be radiopure. Since the total activity of an impure material will scale as its volume, it is usually an advantage to minimize the detector size. This can be most readily accomplished by employing a detector that also plays the role of the source. Cosmogenic activities build up in materials through nuclear reactions of cosmic ray muons and their secondary products, especially neutrons. These can be a signicant background contribution both for the source and for the shielding material. Some materials have no long–lived isotopes and thus have a built–in safeguard against cosmogenics. For experiments that must fight this problem, fabricating the apparatus underground and storing materials underground can greatly reduce this background. Unlike solid sources, a gaseous or liquid source can be continuously purified from such contamination.

To measure double beta decays, three general approaches have been followed: geochemical, radiochemical, and direct counting measurements [56, 81].

The radiochemical experiments search for DBD by noticing that when the daughter nuclei of a double beta emitter are themselves radioactive, they can be accumulated, extracted and counted. If the daughter has a half–life much smaller than $10^9$y and has no other long–lived parents, its presence can be only due to $\beta\beta$. This technique is not able to distinguish the $2\nu$ contribute from the $0\nu$ one. The quoted rates refer therefore to the sum of all possible transitions to ground or excited levels, with or without the emission of neutrinos.

In the geochemical experiments, isotopic anomalies in daughters of $\beta\beta$ decaying nuclei over geological time scales are looked for. These experiments are very sensitive, due to the long exposure time, but, like the radiochemical ones, indicate only the presence of the daughter nucleus and cannot therefore discriminate between lepton conserving and non conserving processes or between decays to the ground or excited states of the daughter nucleus. For this reason, the results obtained with radio– and geo–chemical techniques cannot provide new discoveries in particle physics directly.

Most of the recent experiments use direct measurement approaches that allow measurement of the $\beta\beta$–electron energy, their spectral shape and, sometimes also permit event reconstruction. Direct experiments are based on two different methods. In the source$\neq$detector approach a double beta active material is inserted, normally in form of thin sheets, in a suitable detector. In the

source=detector or "calorimetric experiments" the detector itself is made of a material containing the double beta active nuclei.

Well–known examples of $\beta\beta$ emitters measured in direct counting experiments are $^{48}$Ca, $^{76}$Ge, $^{96}$Zr, $^{82}$Se, $^{100}$Mo, $^{116}$Cd, $^{130}$Te, $^{136}$Xe, $^{150}$Nd.

Calorimeters can achieve good energy resolution and almost 100% efficiency. They normally lack the tracking capabilities to identify the background on an event–by–event basis but they have, in their favor, that their sharp energy resolution does not allow the leakage of too many counts from ordinary double beta decay into the neutrinoless region, and so the sensitivity intrinsic limitation is not too severe. In the other case, the identification capabilities make them very well suited for $2\nu$DBD experiment, but, having low energy resolution their $0\nu$DBD regions can be dominated by the $2\nu$DBD background events. For this reason, at least in principle, calorimetric experiments are preferred to search for $0\nu$DBD .

Several types of conventional devices have been used in DBD direct searches: solid state devices (Germanium spectrometers and Silicon detector stacks), gas counters (time projection chambers, ionization and multiwire drift chambers) and scintillators (crystal scintillators and stacks of plastic scintillators).

In order to understand the general strategy to follow to perform a neutrinoless double beta decay experiment, the sensitivity to the $0\nu$DBD half life has to be introduced. In general this quantity is expressed as:

$$T_{1/2}^{0\nu} \simeq ln2 \times \frac{N \cdot t}{S} \tag{1.61}$$

where $N$ is the number of emitter nuclei used as source, and $S$ is the number of observed decay counts recorded during the time $t$. When no evidence of decays is found, this expression represents the limit on the decay half–life; in this case $S$ is the background fluctuation in the energy region studied. Using eq. 1.61 it is possible to obtain the so called *neutrinoless sensitivity (1 $\sigma$)* or factor–of–merit for homogeneous (source=detector) devices, for which the background rate scales with the detector mass:

$$F_D = 4.17 \times 10^{26} \left(\frac{f}{A}\right) \sqrt{\frac{M \cdot t}{B \cdot \Gamma}} \cdot \epsilon_\Gamma \qquad \text{years} \tag{1.62}$$

where $f$ is the isotopic abundance and $A$ the mass number, $B$ is the background rate (in c/(keV kg y)), $M$ the mass of the $\beta\beta$ emitter (in kg), $\epsilon_\Gamma$ the detector efficiency in the energy interval $\Gamma$ around the energy transition of the searched decay, and $t$ the running time measurement in years.

Thus in order to obtain powerful $0\nu$DBD experiments it is necessary

- to work with very large source masses, of order of one ton or larger in the next generation experiments;
- to use good energy resolution and high efficiency detectors;
- to perform the experiment in "clean" conditions from the point of view of radioactivity background; to perform an effective background suppression strategy, it is useful that the detectors provide much information. For

| Emitter | Experiment | $T^{0\nu}_{1/2} >$ | *C.L.%* |
|---|---|---|---|
| $^{48}$Ca | HEP Beijing | $1.8 \times 10^{22}$ y | 68 |
| $^{76}$Ge | MPIH/KIAE | $1.9 \times 10^{25}$ y | 90 |
| | IGEX | $1.6 \times 10^{25}$ y | 90 |
| $^{82}$Se | UCI | $2.7 \times 10^{22}$ y | 68 |
| | NEMO 3 | $4.7 \times 10^{22}$ y | 90 |
| $^{96}$Zr | NEMO 2 | $1.3 \times 10^{21}$ y | 90 |
| $^{100}$Mo | LBL/MHC/UNM | $2.2 \times 10^{22}$ y | 68 |
| | UCI | $2.6 \times 10^{21}$ y | 90 |
| | Osaka | $5.5 \times 10^{22}$ y | 90 |
| | NEMO 3 | $6 \times 10^{22}$ y | 90 |
| $^{116}$Cd | Kiev | $1.7 \times 10^{23}$ y | 90 |
| | Osaka | $2.9 \times 10^{21}$ y | 90 |
| | NEMO 3 | $1.6 \times 10^{22}$ y | 90 |
| $^{130}$Te | Milano | $2.1 \times 10^{23}$ y | 90 |
| | CUORICINO | $5.5 \times 10^{23}$ y | 90 |
| $^{136}$Xe | Caltech/UN/PSI | $4.4 \times 10^{23}$ y | 90 |
| $^{136}$Xe | Rome | $1.2 \times 10^{24}$ y | 90 |
| $^{150}$Nd | UCI | $1.2 \times 10^{21}$ y | 90 |
| | NEMO 3 | $1.4 \times 10^{21}$ y | 90 |

Table 1.3 - Limits on Neutrinoless Decay Modes

example if detector permits an event topology reconstruction it is possible to perform an event–by–event background rejection.

- to have long data taking periods.

Table 1.3 summarizes the current experimental situation. Here more attention is devoted to the Heidelberg–Moscow (HM) experiment that presently gives the best limits on the effective neutrino mass, and on the Neutrino Ettore Majorana Observatory (NEMO), a modern tracking experiment operating for a few months, which has the potential to improve the HM results. Complete reviews on $0\nu$DBD experiments are found in Refs. [81, 56]

### 1.7.2 The Heidelberg–Moscow experiment

The best limit on $0\nu$DBD comes from the Heidelberg–Moscow (HM) experiment [82, 83] using $^{76}$Ge source: $^{76}Ge \rightarrow^{76} Se + 2e^-$. This experiment operates five enriched (to 86%) high–purity $^{76}$Ge detectors, with a total mass of 11.5 kg, the active mass of 10.96 kg being equivalent to a source strength of 125.5 mol of $^{76}$Ge nuclei. The experiment is installed in the Gran Sasso underground laboratory under heavy shields for gamma and neutron environmental radiation. Extremely low background levels are achieved thanks to a careful selection of the setup materials and further improved by the use of Pulse Shape Discrimination (PSD) techniques. In the $0\nu$DBD region the background level is $\sim 0.06 \pm 0.02$ c/keV/kg/year. The limit obtained is $T^{0\nu}_{1/2} = 1.9 \times 10^{25}$ years at 90% of C.L., corresponding to $< m_\nu > < 0.35$ eV.

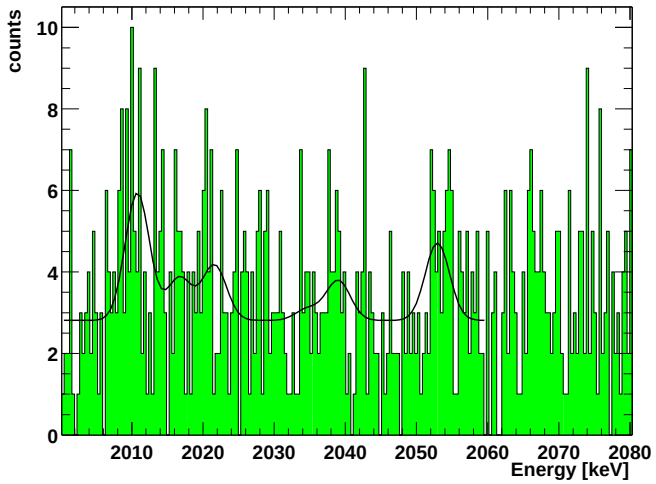


Figure 1.14 - Analysis of measured spectrum of HM experiment. The total data taken time is of 54.9813 kg y. The probability that a line is located at 2039.0 keV is 86%.

In January 2002, a few members of the HM collaboration claimed evidence for $0\nu$DBD peak with $T^{0\nu}_{1/2} = 1.5\ 10^{25}$ years as a best value corresponding to a $< m_\nu > = 0.39$ eV [84]. Fig. 1.14 shows the $0\nu$DBD spectrum region collected by HM.

The result stemmed from a reanalysis of the HM data based on:

- an automatic peak detection method;
- identification of the observed lines;
- narrowing of the fit interval to exclude any contribution from recognized lines.

This claim raised skepticism in most of the scientific community and a controversy followed which is still open [85, 86, 87]. In particular, a strong criticism is due to the fact that the lines identification is still weak: some recognized line have not been yet identified while the others are still inconsistent or just compatible with expectations. It is probable therefore that a definite answer to the correctness of the claim will be given only by the very sensitive next generation $0\nu$DBD projects.

A future upgrade of the HM experiment has been proposed, with the acronym GENIUS (GErmanium NItrogen Underground Setup). The main idea is to use a large amount of enriched $^{76}$Ge (about 1 ton), in the form of an array of about 300 naked Ge detectors suspended in liquid nitrogen, which provides simultaneously cooling and shielding. The anticipated background is 0.04 counts/(keV·yr·ton), i.e., about 1000 times lower than the best existing backgrounds. Such a detector could reach a half–life limit of about $6\times10^{27}$ years within one year of operation, thus improving the neutrino mass limit by an order of magnitude.

| | 7 kg $^{100}$Mo | 1 kg $^{82}$Se |
|---|---|---|
| $T^{0\nu}_{1/2}$ [years] | $> 4 \times 10^{24}$ | $> 1.5 \times 10^{24}$ |
| $\langle m_\nu \rangle$ [eV] | $< 0.25 - 0.7$ | $< 0.6 - 1.2$ |

Table 1.4 - Expected sensitivities (90% C.L.) for the NEMO–3 experiment after 5 years.

### 1.7.3 The neutrino Ettore Majorana Observatory experiment

The NEMO (Neutrino Ettore Majorana Observatory) collaboration is working with NEMO–3 detector at Frejus underground labs (4800 m.w.e.) with the primary goal of studying different isotopes DDB0$\nu$ (decay) with big $Q_{\beta\beta}$ values. The NEMO–3 detector can contain at least 10 kg of different decaying $\beta\beta$ isotopes. The biggest effort has been dedicated to $^{100}$Mo ($Q_{\beta\beta}$ = 3034 keV) and $^{82}$Se ($Q_{\beta\beta}$ = 2995 keV). Compared to Heidelberg–Moscow, NEMO is an experiment where the source is separated from the detector and for this reason it is possible to measure $\beta\beta$ decay for different nuclei simultaneously.

This experiment is based on the direct detection, by a tracking set–up, of the two electrons resulting from the decay and on the direct measurement of their energy with a calorimeter. NEMO–2, a smaller prototype of such a system, operated until 1999 with promising results.

The detector has a cylindrical shape and is divided in 20 identical parts. The source consists of thin layers ($\sim 50\mu$m thick) vertically fixed that separate the tracking volume made of Geiger counters cells. In order to minimize multiple scattering effects the tracking element is filled with helium and 4% ethyl alcohol. The cells give a 3D tracking of the particles recording for each cell both drift time and the two propagation times of the plasma.

The tracking volume is covered by very low activity scintillators coupled to photomultipliers. In total the final detector is made of 6180 counters and 1940 scintillators.

A solenoid surrounds the detector. It produces a 30 Gauss magnetic field in order to separate ($e^+e^-$) couples produced in the thin source foils. An external 20 cm thick shield of low activity iron reduces the thermal neutrons and the $\gamma$ ray flux.

The background contaminating the DDB0$\nu$ measurement in the 3 MeV region is mainly caused by the presence in the source of the $^{214}$Bi and $^{208}$Tl deriving from the U and Th chains. A special treatment, limiting the concentration of these isotopes to a value for which the only contribution to the background is given by the DDB2$\nu$ tail, is thus required. The expected number of backgrounds events, caused by such effects and by neutrons, has been estimated [88] to be less than 0.18 c/(kg y) for the $^{100}$Mo and 0.01 c/(kg y) for the $^{82}$Se. Both values refer to the 2.8 and 3.2 MeV region.

The sensitivity that the NEMO–3 experiment will reach after five years of data taking has been estimated [88] to be 7 kg of $^{100}$Mo and 1 kg of $^{82}$Se. In the energy range between 2.8 and 3.2 MeV, 6 background events are expected for 7 kg of $^{100}$Mo and no background is expected for 1 kg of $^{82}$Se, corresponding to a detector efficiency of 14%. In table 1.4 the planned sensitivities are reported.

### 1.7.4 The low Temperature Detector technique

New techniques based on the use low temperature true calorimeters have been proposed and developed in order to improve the experimental sensitivity and enlarge the choice of candidates investigable with an active source approach. The use of low temperature calorimeters to study nuclear phenomena was proposed by Simon about 60 years ago [89]. Andrews obtained the first $\alpha$ particle detection using superconductive bolometers in 1949 [90]. Large mass thermal detectors have been suggested since 1984 for searches on rare decays [91]. Over the last few years, low temperature detectors have provided better energy resolution, lower energy thresholds and wider material choice than conventional detectors for many applications. It is impossible to review briefly this exploding research field. A complete overview is offered by the proceedings of the specific low temperature detectors conferences [92].

The Milano group started some years ago a program to develop both large mass bolometers to search for $0\nu$DBD of various isotopes and microcalorimeters for X–ray and $\beta$–spectroscopy. A series of bolometric experiments have been carried out by the Milano group since 1989 in the Gran Sasso Laboratory, searching for the double beta decay of $^{130}$Te. The working principle of these thermal detectors is explained in the next chapter. The most recent developments and achievements of these devices will be detailed in next chapters, while here the main experimental steps that lead this group to propose a new generation large mass experiment are summarized:

- the preliminary experiment on $^{130}$Te $0\nu$DBD was performed with 73 g and 334 g single $TeO_2$ crystals. The latter has been operated for 10508 hour live time, allowing to set a $T^{0\nu}_{1/2}$ limit of $2.1 \times 10^{22}$ years at the 90% confidence level.

- 4 detectors, 340 g each, where then operated simultaneously to study the feasibility of a large mass experiment consisting of an array of many identical bolometers. The obtained average energy resolution was 11.0 keV at 2.5 MeV. A cumulative limit of $2.39 \times 10^{22}$ y at the 90% of C.L was achieved [93].

- at the end of September 1997, a new 20 $TeO_2$ detector (340 g each) array was operated in the Gran Sasso underground laboratory [94, 95]. This experiment is named MiDBD and the new limit on $T^{0\nu}_{1/2}$ achieved was 9.5 $\times 10^{22}$ years at the 90% confidence level. This phase of the Milano group experimental work is detailed in chapter 3.

- at the beginning of 2000, to improve the performance of MiDBD experiment the $TeO_2$ detector array was remounted [96]. This phase of the MiDBD experiment, usually referred to as MiDBD-II, is described in chapter 4.1.

- a new experiment named Cuoricino was proposed and implemented [97]. It is the natural expansion of the MiDBD experiment. The Cuoricino array consists of 44 cubic crystals of natural $TeO_2$ of 5 cm side and by 18 crystals

of 3x3x6 $cm^3$. Operated for the first time only a few months ago, it has already been able to set a $T^{0\nu}_{1/2}$ limit of $5.5 \times 10^{23}$ years at 90 % C.L. The corresponding limit for the effective neutrino mass ranges between 0.37 to 1.9 eV depending on the theoretically calculated nuclear matrix elements used. This limit is the best after the results obtained by the HM collaboration (and is already very close to it). Cuoricino is presently taking data and its sensitivity surpasses the HM present limits. The development, the test, the results and the modelling of the Cuoricino single module are the main topics of this thesis and will be reported in chapters 5, 6 and 7. As shown in this thesis, Cuoricino is both a self-consistent experiment and a general test for a future large mass project.

- in October 2003, the Milano group has proposed a new generation large mass experiment named CUORE (Cryogenic Underground Observatory for Rare Events) [98]. It is based on the experience collected with the previous experimental steps but important innovative modifications have been suggested. In chapter 8 these innovations are presented.

# Chapter 2

# Bolometric Technique

## 2.1 Introduction

The expression "bolometer" is normally used to indicate a Low Temperature Detector (LTD) sensitive to single particle interactions. With the bolometric technique it is possible to obtain a wealth of information, at least in principle, on the interacting particle, such as deposited energy, arrival time, quantum type, impact point and initial momentum.

In this chapter, after a short exposition of the basic operation principles and an introduction to the main detector components, the theoretical detector energy resolution will be compared with the one obtained from conventional detectors. The detector and the main noise sources will then be described. A complete overview of bolometric detectors is provided by the proceedings of the specific low temperature detector conferences [92].

## 2.2 Operation Principles of phonon mediated particle detectors

A LTD consists normally of two main components: the *energy absorber*, where the particles to be detected deposit their energy, and the *sensor*, which collects the excitations produced by the particle interaction in the energy absorber and develops a signal. In fig. 2.1 a simple scheme of a bolometric detector is shown.

LTDs can be classified according to the type of elementary excitations (phonons, quasi-particles, ...) which mediate the detection of particles. Here the attention is focused on the LTDs that are sensitive to phonons. These devices are named Phonon Mediated particle Detectors (PMDs) and their sensitive element is consequently a *phonon sensor*.

As the elementary excitation energy is very low, less than 10 meV, the bolometers have to work at low temperatures, so as to prevent the thermal generation of excitations that could hide the particle signals. Therefore, the detector is coupled to a heat bath that is usually maintained at a temperature in the range between 10 and 100 mK.

When a particle interaction occurs in the energy absorber, the phonons produced are out of equilibrium; in fact they have about the Debye energy, of the

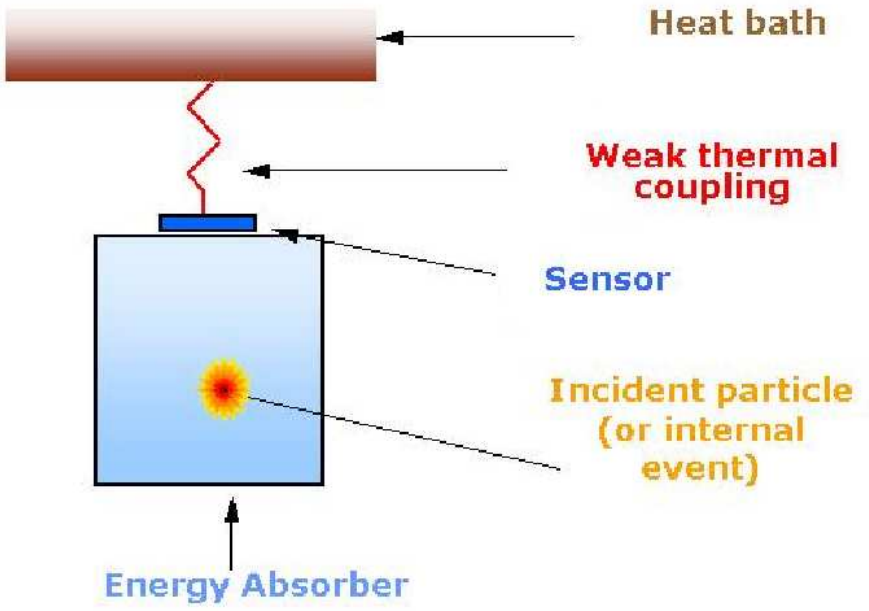


Figure 2.1 - Scheme of a bolometric detector.

order of tens of meV, while the thermal energy is orders of magnitude lower, given the very low operation temperature. So these phonons are named athermal phonons.

Normally the athermal phonons degrade their energy and relax onto a new equilibrium distribution by interacting with the surface of the crystal absorber, with the defects of the crystal lattice and with the different isotopes present in the absorber (see section 2.3.1).

According to which type of phonon sensor is used, the PMDs can be fast or slow, of course in the context of bolometric detectors. In the first case they have a response time of the order of microseconds and can be sensitive to athermal phonons. If the phonon sensor response time is slow and longer than the thermalization time of the non-equilibrium phonons produced by the particle interaction, it will be sensitive mainly to thermal phonons. In the latter case the sensor measures the temperature of the detector and is a thermometer. The PMD works then as a perfect calorimeter. In many experimental situations, it is difficult to distinguish between these two extreme cases, and the nature of the detection mechanism is still poorly known.

## 2.3 The energy absorber

A scheme of a very simple thermal model for a PMD is reported in fig. 2.2. The calculation of thermal equations referring to this model will be detailed in chap. 7, but the main results are that the height of the PMD thermal signal, when operated as a perfect calorimeter, corresponds to the ratio between the

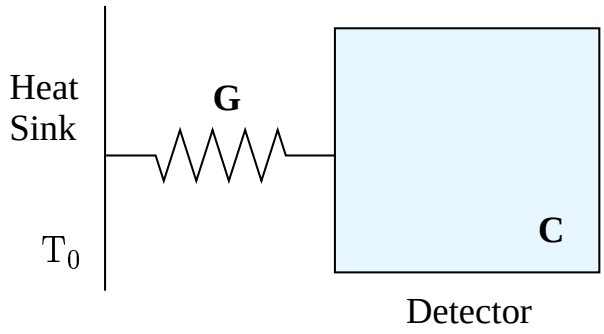


Figure 2.2 - Monolithic thermal model. Here the detector is modeled as a unique system weakly coupled to the heat sink.

energy E deposited by the particle and the heat capacity C of the detector, E/C, and that the time constant of the signal is equal to the ratio between the heat capacity and the thermal conductance G to the bath, C/G. The most important parameter of the detector is then the heat capacity that has to be small to achieve big and fast signals. This condition is not very difficult to meet and therefore there is a wide choice for the energy absorber materials.

At low temperatures the specific heat of a crystal can be expressed as:

$$c(T) = c_r(T) + c_e(T) \tag{2.1}$$

where $c_r$ represents the lattice contribution to the specific heat and $c_e$ the electron one. Dielectric diamagnetic materials are preferred as energy absorbers, as only the lattice contribution is present and furthermore it is proportional to the cube of the temperature over the Debye temperature (Debye law) at low temperatures:

$$c_r(T) = \frac{12}{5}\pi^4 k_B N_A \left(\frac{T}{\Theta_D}\right)^3 \tag{2.2}$$

where $k_B$, $N_A$ and $\Theta_D$ are the Boltzmann constant, the Avogadro number and the Debye temperature respectively. This contribution can be written in terms of heat capacity as

$$C(T) = \beta \frac{m}{M}\left(\frac{T}{\Theta_D}\right)^3 \tag{2.3}$$

where $\beta$=1944 J $K^{-1}mol^{-1}$, $m$ is the absorber mass, and $M$ is the molecular weight. In metals the specific heat is dominated by the electron contribution

$$c_e(T) = \frac{\pi^2}{\Theta_D} Z R \frac{T}{\Theta_F} \tag{2.4}$$

where $Z, R$ and $\Theta_F$ are the conduction electron number for each atom, the gas constant and the Fermi temperature respectively. However, if the metal is in superconductive state, then the electron contribution to the specific heat at T « $T_c$ is

$$c_e(T) = K_s e^{-2(\frac{T_c}{T})} \tag{2.5}$$

where $K_s$ is a constant depending on the material characteristics.

The above considerations lead to prefer diamagnetic or superconductors as energy absorber materials.

Absorber dimensions usually depend on the type of LTD applications and can range from micrograms, in case of X-ray spectroscopy [99], to kilograms in case of Gamma-ray spectroscopy, DBD and Dark Matter searches [100].

### 2.3.1 Thermalization processes of the deposited energy

In this section, in order to understand better the detector operation, the processes that allow the conversion of the deposited particle energy into thermal phonons will be introduced. The main thermalization processes occur through the nuclear and electronic channels [101].

**Nuclear channel**: the particle interactions with the crystal lattice produce vibrational excitations thanks to the nuclear scattering, but could also produce structural damages of the lattice, where the energy can be stored. If this energy is not converted into phonons, the statistical fluctuation of the number of the produced defects can worsen energy resolution. The fraction of lost energy depends on the incident particle: for electrons and photons it is negligible, whereas for $\alpha$ particles having some MeV of energy it can cause a FWHM resolution of hundreds of eV.

**Electronic channel**: let's take into consideration the kinetic energy transfer from a charged particle produced by a nuclear process to a semiconductor crystal. The particle is slowed down in few $\mu$m (heavy particles) or mm (electrons) from its interaction point and normally it stops in the crystal. Along its track it produces many electron–hole pairs having at the beginning very high spatial density and energy. These charge carriers interact first with each other and spread very quickly in the crystal. As a quasi–equilibrium situation is reached, they undergo their final degradation via direct interaction with the lattice site: these interactions produce phonons.

During this step undesirable processes could take place, indeed a fraction of the pair energy can leave the crystal or can be stored in stable or metastable states instead of going into the crystal lattice. It is possible to have: *radiative recombinations* of e–h couples with the escape of the emitted photon, *non-radiative recombinations* that take too long time compared to signal development, *trapping* of electrons and holes in impurity sites or lattice defects. A large fraction of the initial energy is transferred to the lattice as vibrational excitations (phonons), through different mechanisms depending on the e–h pair density and on their energy.

Let's consider now the phonon thermalization processes. To explain what happens, it is useful to use the mono-dimensional representation of the phonon dispersion curves. The e–h pair recombination, across conduction and valence bands, produces high energy and low momentum phonons on the optical branch. Then these primary phonons depart from the particle interaction region. The optical phonons decay in the *longitudinal acoustic* (LA) branch in a very short time ($10 - 100$ ps). Obviously, the decay obeys the energy and momentum con-

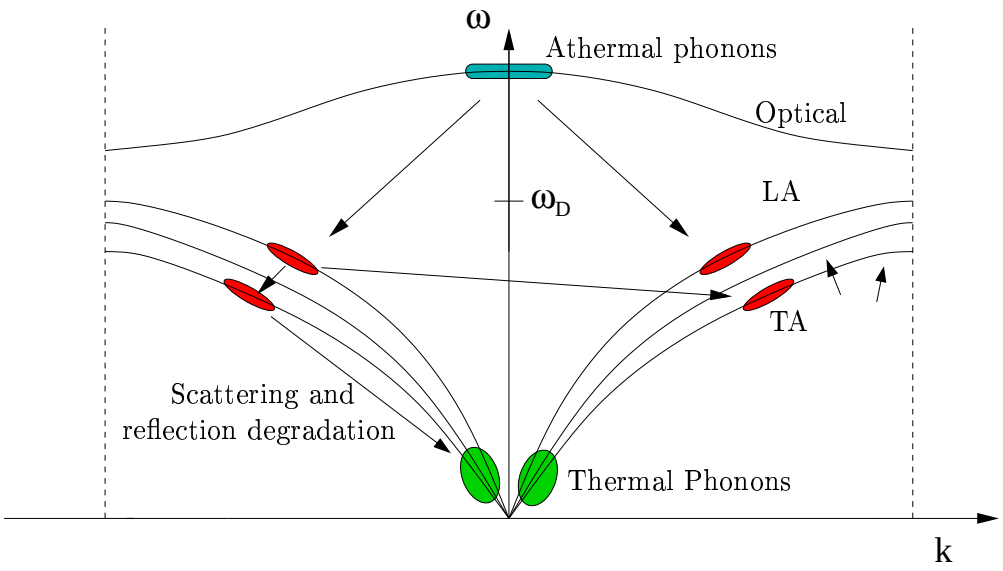


Figure 2.3 - Athermal phonon thermalization model

servation laws, and it produces mainly two phonons each having half the energy of the initial one (of the order of the Debye energy) and opposite momentum. Also the e–h recombinations that happens on impurity levels contribute to this phonon population. Therefore the final result is a phonon system, mainly belonging to LA branch, having energy of the order of $\hbar\omega_D$ (where $\omega_D = 2\pi\nu_D$, and where $\nu_D$ is the Debye cut–off frequency of the crystal). This energy is much higher than the average energy of thermal phonons at the bolometer working temperature (for example, at T= 10 mK, the average energy is $\sim\mu$eV). At this point new phenomena of phonon energy degradation occur, so that phonons become thermal phonons. These processes can be classified in three channels: phonon–phonon interaction, scattering on impurities and reflection on crystal surfaces. The first channel is possible thanks to the an-harmonicity of the lattice potential, however this an-harmonicity is less important when the crystal temperature and the phonon energy decrease. Moreover, if the LA phonon decay is possible and it is also responsible for the *transverse acoustic* (TA) phonon production, the decay of the TA phonons is forbidden by the momentum conservation law. From these two considerations it is easy to understand that other energy degradation mechanisms must exist to permit, in a reasonable time, the thermalization of the energy trapped in the athermal phonons. These mechanisms were named before: they are able to degrade phonon energy and also to induce the conversion of the TA phonons, otherwise stable, into LA phonons so that they can be thermalized. The conversion towards low energies is a very slow process, but it is difficult to make a quantitative estimation due to the complication of the involved mechanisms.

Let's go back to the decay process. After a certain number of the decays, the mean free path becomes larger than crystal dimensions. At this point in pure crystals, there is a ballistic propagation of phonons until they reach the crystal

surfaces [102]. Using several fast sensors (able to detect athermal phonons) it is possible in principle to determine the particle interaction point using the phonon signal relative time [103]. Phonons that are not absorbed by a sensor will be reflected by surfaces and therefore they can undergo decay processes. At the end they interact with the background thermal phonons and they thermalize.

For superconductor materials, the thermalization processes could be longer. This happens in particular when the Debye temperature $\theta_D$ for the material is large and the critical temperature $T_c$ is low. In fact, in this case, phonons that are generated by particle interactions easily break the Cooper pairs and cause an energy storage in the quasi–particle system. For this reason, even in the case when superconductive materials present lower heat capacity at the same temperature, the diamagnetic dielectric materials are to be preferred.

### 2.3.2 Intrinsic energy resolution

By thermodynamic considerations that will be explained in sec. 2.5.2 it is possible to express the intrinsic energy resolution $\Delta$E for a bolometric detector sensitive to thermal phonons as

$$\Delta E = \sqrt{k_B C(T) T^2} \tag{2.6}$$

where $k_B$ and C are the Boltzmann constant and the energy absorber heat capacity respectively.
To give an idea of the potentiality of these devices we can calculate that for 1 kg of $TeO_2$ working at 10 mK the intrinsic energy resolution is about 10 eV. Once again we see that a crucial parameter of the energy absorber is its Debye temperature, $\theta_D$, which has to be as high as possible in order to reduce the specific heat. For this reason, light materials with a small mass number are better energy absorbers in terms of heat capacity. Even superconductors are in principle suitable, since the electronic contribution to the specific heat vanishes exponentially below the critical temperature, but the *caveats* exposed in the previous section have to be taken into account.

It should be stressed that, according to eq. 2.6, $\Delta$E is *independent* of E.

However, even in the case of athermal phonons, it is possible to see the advantage of PMDs over conventional devices for radiation spectroscopy as the energy resolution is concerned. In fact the energy interaction generates a number of elementary excitations, N, equal to

$$N = \frac{E}{\epsilon}$$

where $\epsilon$ is the energy to produce an elementary excitation. The intrinsic energy resolution is limited by the statistic fluctuation of the produced elementary excitation number. So the theoretic energy resolution $\Delta$E is

$$\frac{\Delta E}{E} = 2.35 \cdot \frac{\Delta N}{N} \tag{2.7}$$

that is proportional to the $\sqrt{\epsilon}$. In a scintillator detector $\epsilon$ is about 100 eV, in a gas detector $\epsilon$ is about 30 eV whereas in a solid state detector $\epsilon$ is around 3 eV.

As already said, in a PMD the energy of an elementary excitation is less than 0.01 eV even in the case of athermal phonons, so, at least in principle, energy resolutions more than an order of magnitude better than to conventional devices are possible.

## 2.4 The phonon sensor

In order to achieve good signal-to-noise ratio a PMD neeeds a high sensitivity phonon sensor. The phonon sensor is a device that collects the phonons produced in the absorber and generates an electrical signal, usually proportional to the energy contained in the collected phonons. A simple realization of this device can be accomplished through the use of a thermistor whose resistance, as a function of the temperature, has a steep slope. In practical devices, there are two main classes of thermistors which give the best results: semiconductor thermistors (STs) and transition edge sensors (TESs). Thermistors are usually characterized by their "logarithmic sensitivity" A, defined as

$$A = \left| \frac{d \log R(T)}{d \log T} \right| \tag{2.8}$$

The value of the sensitivity is usually in the range $1 \div 10$ for STs and in the range $10^2 \div 10^3$ for TESs.

Here the two approaches are introduced, but in the next part of the chapter the attention will be focused on STs.

### 2.4.1 Transition Edge Sensors

The TESs are superconductive films kept around the critical temperature ($T_C$). They are intrinsically fast, and so they can detect athermal phonons. Their working point lies in a narrow range of temperature. A typical example of a resistance-temperature curve for a TES is shown in fig. 2.4. The superconductive film is deposited on the absorber crystal, with typical thickness of a few hundred nanometers [104]. This technique can take advantage of the SQUID technology as read-out. TESs are made normally only of a single superconductor, but it is possible also to use a bilayer film formed by a normal metal and a superconductor. In the latter case, because of the proximity effect, the normal metal is driven superconductive and the resulting $T_C$ can be much lower than that of the pure superconductor. In this way it is possible to tune the $T_C$ by adjusting the thickness of the layer.

### 2.4.2 Semiconductor Thermistors

As the STs are intrinsically slow, they are probably sensitive mainly to thermal phonons in a PMD. In this context, they give information about systems in thermal equilibrium, and could be thought as temperature sensors. However, it must be remarked that there are clear indications that also athermal phonons can be detected by STs; in this case the collected pulses contain non thermal

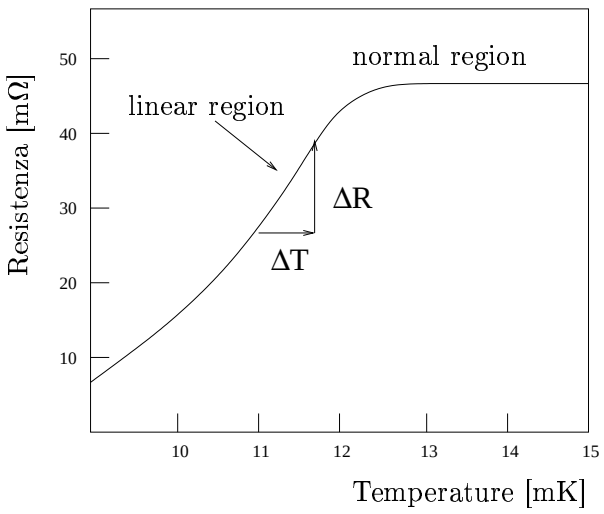


Figure 2.4 - Resistance of a W TES thermistor as a function of the temperature.

components. STs consist normally of Ge or Si small crystals with a doped region. A very useful technique to uniformly dope large volumes is the Neutron Transmutation Doping (NTD). In this approach the semiconductor sample is bombarded by neutrons, which induce nuclear reactions on the various target isotopes leading to the formation of n- and p-dopants. On the other hand, small low-heat-capacity thermistors can be obtained by ion implantation in Si, according to the procedures of the standard planar Si technology.

### Conduction processes

For both the previously described approaches, the results is a strong dependence of the sensor resistance on the temperature as follows:

$$\rho \simeq \rho_0 \cdot \exp\left(\frac{\epsilon(T)}{k_B T}\right)^{1/2} \tag{2.9}$$

where $k_B$ is the Boltzmann constant, $\epsilon(T)$ is the activation energy and $\rho_0$ is a parameter depending on the doping conditions.

Semiconductors are covalent solids that may be regarded as insulators because the valence band is completely full and the conduction band is completely empty at the absolute zero. They present an energy gap between the valence and conduction bands of no more than 2 eV. For silicon the energy gap is 1.14 eV and for germanium the gap is 0.67 eV. So, for intrinsic semiconductors, i.e. for a semiconductor without impurities, the conduction can happen only with an activation energy equal or larger than the energy gap. This mechanism is possible if the T working temperature is T » $T_{amb}$, since $kT \simeq 0.025$ eV at room temperature.
If impurities are present in the semiconductor lattice (extrinsic or doped semiconductors) then it is possible to have electronic conduction also at lower tem-

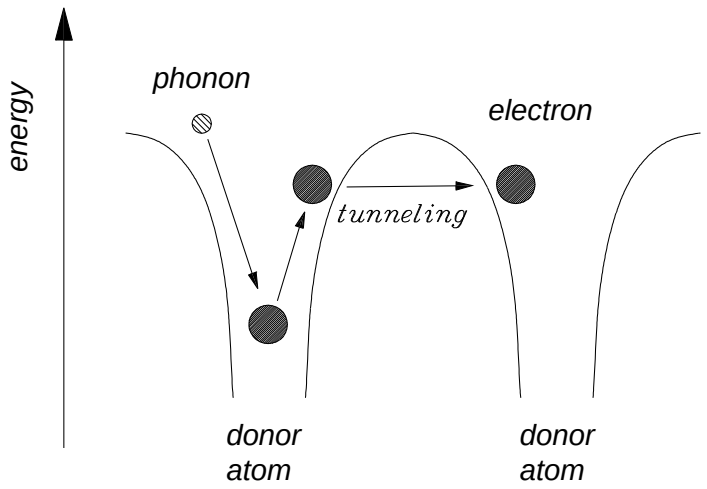


Figure 2.5 - Schematic representation of hopping conduction mechanism.

peratures. In this case in fact, the impurities introduce discrete levels slightly above the top of the valence band or under the bottom of the conduction band, depending on the type of atoms inserted in the semiconductor. For low impurity concentrations, the localized energy levels of dopant atoms are not broadened into bands because these atoms are many lattice spacings apart and they interact with each other very weakly. The energy difference, $\Delta\epsilon$, between the donor impurity energy levels and the conduction band and between the acceptor impurity energy levels and the valence band, is small; for instance if a small amount of arsenic impurities is introduced in a germanium crystal, a energy activation equal to $\Delta\epsilon = 0.0127$ eV is obtained. So the conduction mechanism due to dopant sites dominates the conduction at room and lower temperatures. Depending on the number of dopant atoms, the semiconductor, also near the zero temperature, can behave as an insulator or a metal. So, there exists a critical concentration $N_c$ that characterizes the transition from the insulator to the metallic behavior of the semiconductor. The region near this concentration is named metal-insulator transition region (MIT) [105].

At temperatures lower than 10 K, the conduction is due to the migration of charge carriers from an impurity site to another. When the donor concentration is increased, the wave function of the external electron of the donor atom overlaps with the external electron wave function of the neighboring atoms. In this situation the electrons are not localized and the conduction happens when electrons jump from a donor site to another (*hopping mechanism*) without using the conduction band. This migration is due to quantum-mechanical tunneling through the potential barrier which separates the two dopant sites. The conduction is activated by phonon mediation as schematically described in fig. 2.5, in which the tunnelling process is also shown.

If $T \ll 10$ K and if the net doping atom concentration is slightly lower than $N_c$, then the resistivity is strongly dependent on the temperature. For this reason, usually, it is chosen to operate semiconductor thermistors slightly below

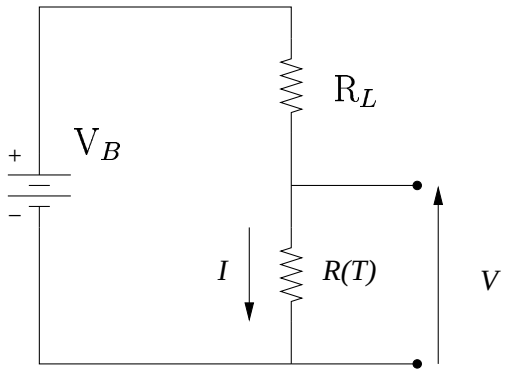


Figure 2.6 - Electric scheme of the bias current circuit used for the read-out of a bolometer. $R_L$ is the load resistance

the MIT region. The dominant conduction mechanism in these conditions of temperature and dopant level is named "Variable Range Hopping" (VRH) and the carriers can migrate also on far sites if their energy levels are located in a narrow range around the Fermi energy. As the state density near the Fermi energy in the semiconductor is determined by compensation level K, it plays a fundamental role in the VRH process. Let's recall that K is equal to the ratio between the acceptor concentration $N_A$ and the donor concentration $N_D$.

For VRH, the resistivity depends on the temperature in the following way:

$$\rho = \rho_0 \cdot \exp\left(\frac{T_0}{T}\right)^{\gamma} \tag{2.10}$$

where $\rho_0$ and $T_0$ are parameters depending on the doping and compensation levels. The exponent $\gamma$ in the Mott model, for a three-dimensional system, is equal to $\frac{1}{4}$ for low compensation levels. For larger values of K, the Coulomb repulsion among the electrons leads to the formation of a gap (Coulomb gap) in the electron state density near the Fermi energy. The value of $\gamma$ in this case becomes $\frac{1}{2}$.

In the following sections, attention will be focused on the case of bolometers using STs as sensors.

## 2.5 Detector operation

From the considerations in the previous section, it is clear that the sensor converts thermal pulses into electrical signals. To obtain a voltage signal a steady current (bias current) I is sent trough the thermistor by means of the bias circuit shown in fig. 2.6, where $R_L$ is the load resistance, R(T) is the sensor resistance and $V_B$ is a constant voltage generator. In these conditions a voltage $V(T) = I \cdot R(T)$ appears across the sensor. This produces a power dissipation P which increases the temperature and acts back on the resistance $R(T)$, until an equi-

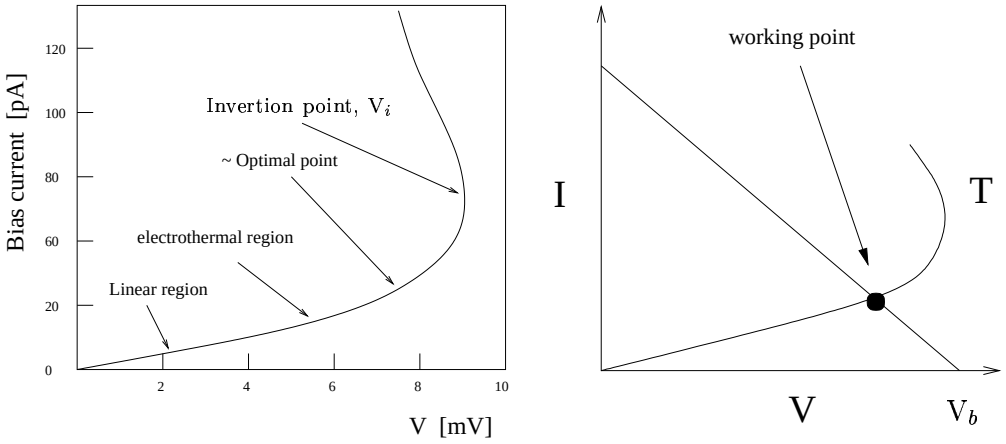


Figure 2.7 - Typical current–voltage characteristics of a semiconductor thermistor: load curve.

librium is reached. In static conditions the absorber temperature $T_b$ is

$$T_b = T_0 + \frac{P}{G} \tag{2.11}$$

where $T_0$ is the heat sink temperature and G the conductance to the bath. This phenomenon makes the V-I relation deviate from linearity and leads to a non-ohmic behavior. This characteristic behavior of bolometers is often referred to as "electrothermal feedback". The static resistance is simply the ratio V/I while the dynamic resistance is the tangent at the V-I curve. By further increasing the bias current the dynamic resistance crosses the so called inversion point (where it vanishes) and becomes negative. For semiconductor thermistors, a typical V-I curve, usually referred to as *load curve*, is represented in fig. 2.7(left). In static conditions the thermistor electric and thermal parameters are described by a load curve point. The intersection of the straight line of equation $V = V_b$ - I $R_L$ and the load curve I = I(V) determines the working point of the sensor, as described in fig. 2.7(right). Usually the working point is chosen in such a way that the signal amplitude or the signal-to-noise ratio is maximum (optimal working point). By a combined fit to a set of load curves at different base temperatures, all the thermistor parameters ($R_0$, $T_0$, $\gamma$) are evaluated as it can be seen in fig. 2.8 where R-P load curves for the same Si-ST at different base temperatures are shown with their corresponding fits.

### 2.5.1 Detector signal amplitude

In the first approximation the thermal pulse produced by an energy release in the absorber is characterized by a very fast rise time, that in monolithic approximation is instantaneous if the thermalization time is assumed negligible, and by an exponential decay time depending on the physical characteristics of the individual detector (equal to the ratio between the heat capacity and the conductance to the bath in case of the monolithic model assumption). Such a thermal pulse is then converted into an electrical one by means of the thermistor

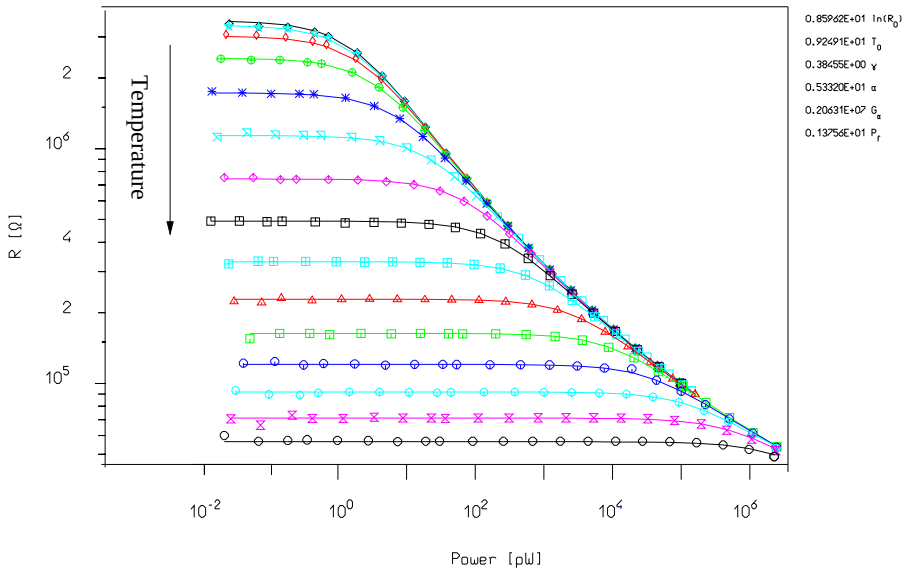


Figure 2.8 - Typical P-R characteristics of a semiconductor thermistor.

bias circuit and the detector optimization is achieved by finding the best configuration for a maximum pulse amplitude. Considering the basic circuit shown in fig. 2.6, it's straightforward to obtain the relationship between the maximum voltage signal ($\Delta$V), the thermistor parameters and the deposited energy E:

$$\Delta V = \frac{R_L}{R_L + R} \cdot V \cdot A \cdot \frac{\Delta T_b}{T_b} \sim \frac{E}{C \cdot T_b} \cdot A \cdot \sqrt{P \cdot R} \qquad (2.12)$$

where $T_b$ is the static detector temperature, $\Delta T_b$ is the increase of detector temperature, A is the sensor logarithmic sensitivity of eq. 2.8, P is the power dissipated in the thermistor by Joule effect and R is the sensor resistance. This expression vanishes both in the limit $P \to 0$ and $P \to \infty$. To increase the signal amplitude, a higher V operation point could be chosen, but normally without surpassing the inversion point $V_i$ on the load curve. Usually the best working point doesn't correspond to the $V_i$ voltage, as the increase of the applied voltages determines higher temperatures and so lower $\Delta T/T$ ratios. For each detector, it is necessary to determine the optimal working point experimentally.

### 2.5.2 Detector noise

In this section the principal noise sources of a bolometric detector using a ST sensor will be presented. These sources can be classified as generating intrinsic and extrinsic noise.

- It is not possible to totally eliminate intrinsic noise source that provide energy resolution limit of detector. As these sources depend on detector parameters, they have to be analyzed to achieve the optimal experimental configuration.

- The extrinsic noise sources usually depend on the cryogenic, electronic and read-out set-ups. In the bolometers described in this thesis they dominate

the intrinsic noise source, so they are the real limits to the energy resolution. Other sources of noise can be included in this category, such as a electric microphonic noise, electromagnetic interferences, and mechanical microphonic noise. These aren't classifiable as intrinsic noise of the detectors or as consequence of the electronic read-out of bolometers but can seriously impact detector performance.

The extrinsic noise sources are characteristic of different experimental set-ups, and will be analyzed in detail in the next chapters. Here the description of the two main intrinsic noise sources follows:

**Johnson Noise:** Every resistance R working at a temperature $T_b$ generates a white noise having a power spectrum equal to:

$$e_R = \sqrt{4k_B R T_b} \tag{2.13}$$

If the monolithic model is used it is possible to demonstrate that the Johnson noise at low frequency is reduced by the electrothermal effect. The scheme in fig. 2.6 shows that the sensor is biased using a $R_L$ load resistance that in general is at a temperature $T_L$ different from $T_b$. (For instance, at room temperature, as in most of the devices described in the following chapters.) So also the Johnson noise of the load resistance $R_L$ has to be taken into account, but it is possible to demonstrate that this can be made negligible with respect to the detector noise; in fact the load resistance contribution to the detector noise $e_{det}$ is

$$e_{det} = e_{R_L} \left( \frac{R}{R_L + R} \right)^2 \tag{2.14}$$

This contribution can therefore be reduced *ad libitum* by choosing a large enough value for $R_L$.

$$\frac{e_{det}}{e_R} = \frac{e_R}{e_{R_L}} \left( \frac{R}{R_L} \right)^2 = \frac{R}{R_L} \cdot \frac{T_L}{T} \tag{2.15}$$

**Thermodynamic Noise:** As already anticipated in sec. 2.3.1, in case of complete energy thermalization, the intrinsic energy resolution is limited by the thermodynamic fluctuations of the number of thermal phonons exchanged with the heat bath through the conductance G. This produces energy fluctuations and therefore temperature fluctuations in the absorber, i.e. an intrinsic detector noise. An estimate of this noise can be obtained by the following simplified argument. The number of phonons contained in the absorber at thermal equilibrium can be estimated as

$$N = \frac{E}{\epsilon_a} = \frac{C(T) \cdot T}{k_B \cdot T} = \frac{C(T)}{k_B} \tag{2.16}$$

where the mean phonon energy $\epsilon_a$ is expressed as equal to $k_B \cdot T$ and $E$ is the internal energy of the absorber [106]. If Poisson statistics is assumed

then it is possible to estimate the fluctuations of the internal energy of the absorber in the following way:

$$\Delta E = \Delta N \cdot k_B T = \sqrt{N} \cdot k_B T = \sqrt{\frac{C(T)}{k_B}} \cdot k_B T = \sqrt{k_B C(T) T^2} \quad (2.17)$$

that is the expression already presented in sec. 2.3.1. In the monolithic bolometer model case, a detailed calculation of noise due to intrinsic sources shows that a dimensionless factor $\xi$ has to be introduced as a multiplier for eq. 2.17. The $\xi$ value depends on the details of the temperature sensor, of the thermal conductance and of the heat capacity temperature dependences, and can be made of the order of unity with a proper optimization work.

# Chapter 3

# Search for Neutrinoless Double Beta Decay of $^{130}$Te with bolometric technique

## 3.1 Introduction

In the '80s the Milano group published the first papers on massive bolometric detectors to search for rare events [107, 108, 109, 110]. The experiments made with these devices have the detection of the neutrinoless double beta decay as a main goal. The experimental activity of this group is mainly carried out in the Laboratori Nazionali del Gran Sasso where the mountain provides a 3500 m.w.e. shield against cosmic rays. After successfully using $TeO_2$ crystals of 73 g and 340 g, as well as a set of four of these large crystals, a tower–like array of 20 crystals of 340 g in a copper frame at about 10 mK was installed and operated. This is the so–called MiDBD experiment, that is now over, and successfully produced the second best neutrino mass bound (after the $^{76}$Ge result). In this chapter the bolometric detectors developed by the Milano group will be introduced.

As pointed out in section 1.7.1, the search for $0\nu$DBD with calorimetric techniques requires to work with low radioactive levels and with good energy resolution detectors. This has many implications for the design of the detectors and their construction. Furthermore, additional constraints are involved if it is required to work at very low temperatures, as in the case of the Milano group experiments. The choices regarding the detector construction, the MiDBD experiment made by the Milano group and the results obtained will be presented in the following sections. In this chapter the panorama in which my PhD–work began is described.

## 3.2 The energy absorber

As explained in sec. 1.7.1 the use of bolometric detectors is well coupled with the searching for $0\nu$DBD; in fact, the calorimetric approach provides good energy resolution and thus an increase of the signal–to–background ratio. As already mentioned the Milano group developed large mass bolometers using $TeO_2$ crystals. In this section the reasons will be presented that lead to the choice of these crystals as energy absorbers.

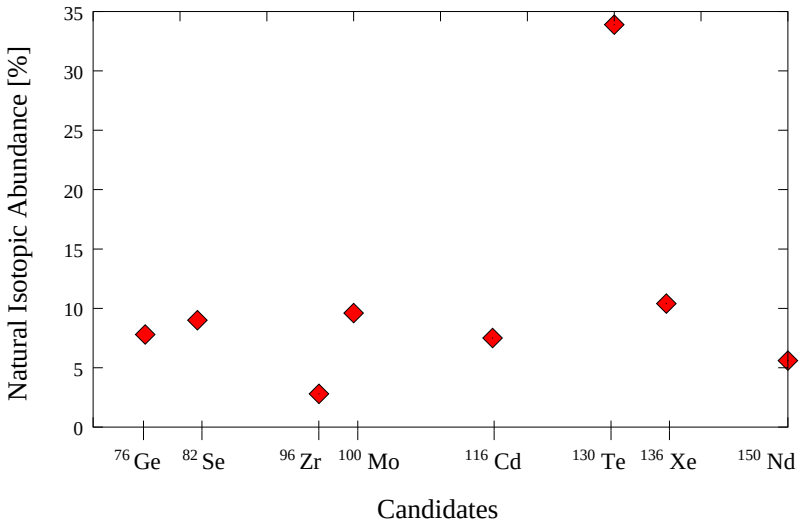


Figure 3.1 - Comparison of the natural isotopic abundance of the candidates to $0\nu$DBD sources. It is possible to observe that the $^{130}$Te has the highest value.

### 3.2.1 The choice of the $0\nu$DBD source: why $^{130}$Te ?

There are different candidates as $0\nu$DBD source (as, for istance, $^{48}$Ca, $^{76}$Ge, $^{82}$Se, $^{92}$Zr, $^{100}$Mo, $^{116}$Cd, $^{130}$Te and $^{150}$Nd). The Milano group has chosen the $^{130}$Te as source, so the sought for decay is

$$^{130}Te \rightarrow ^{130}\ Xe + 2e^- + 2\overline{\nu}_e. \tag{3.1}$$

There are various properties of $^{130}$Te that confirm this as a good choice of $0\nu$DBD source:

- An important issue in the choice of the $0\nu$DBD source candidate regards its **high natural isotopic abundance**. In fact, by using eq. 1.62, and reasonable values of the experimental parameters, as for example a radioactive background level B equal to 1 c/keV/kg/years, an energy resolution $\Delta$E = 10 keV, and a detector efficiency $\epsilon$ equal to 1, then, to achieve half life sensitivities higher than $10^{26}$ years it is necessary to study at least $5 \times 10^{27}$ active nuclei for one year. For this reason, a few per cent of natural isotopic abundance are unacceptable. Furthermore this is particularly important in experiments where the experimental space is limited, as the cases where cryogenic detectors are used. For the $^{130}$Te the natural isotopic abundance is rather high, about 33.8% [111]. Another possibility to obtain high sensitivities is to work with isotopic enriched source, but the use of this technique is sometimes impossible and anyway often very expensive. Fig. 3.1 shows a comparison of the natural isotopic abundance of the various candidates to $0\nu$DBD sources.

- A second reason to choose $^{130}$Te as $0\nu$DBD source concerns the **energy transition Q** of the decay searched for, that in the case of $0\nu$DBD of

$^{130}$Te is equal to 2528.8 ± 1.3 keV [112]. In fact, the higher the energy transition values, the larger the phase space for the decay. This means that high Q–values are preferred since they are associated with high probabilities for the decay. Furthermore the Q–value is important with respect to the natural radioactive background. The $^{130}$Te Q–value is placed in a fortunate position of the natural radioactive background, in fact it is located in a window of the spectrum characterized by low radioactivity between the full energy and the Compton edge of the 2615 keV photon peak ($^{208}$Tl due to the Th chain), and out of the $^{248}$U background.

- Another important reason that lead to the choice of $^{130}$Te regards the **encouraging theoretic calculations** of the $0\nu$DBD mean life. Of course, isotopes with low mean life values are preferred. As said in the first chapter, these calculations involve the nuclear matrices of the transition nuclei which are model dependent. So all these calculations have spreads due to the different possible models. The tab. 1.7 contains the theoretic half lives for various $0\nu$DBD candidates, and it can be observed that the theoretic $^{130}$Te $T^{0\nu}_{1/2}$ is compatible with the lower ones.

- The last reason to choose the $^{130}$Te is connected to the contradictory issue of various geochemical experiments on $^{130}Te$. Inclusive Double Beta Decay for this nuclide has already been observed with geochemical techniques but there are some disagreements in the results. The measured values with the geochemical approach for DBD lifetimes range from $(7\pm2) \times 10^{20}$ to $(2.7\pm0.1) \times 10^{21}$ years. This disagreement has stimulated some speculation on the possibility that the weak interaction constant could change with time. The geochemical technique simply indicates the presence of the (A,Z+2) nucleus in the sample containing (A,Z) and could be affected by badly known systematic errors. An exploration of the range of these results using a different approach is therefore necessary.

### 3.2.2 The choice of the energy absorber: why $TeO_2$ ?

Once it was decided to use $^{130}$Te as a $0\nu$DBD source, the Milano group chose $TeO_2$ crystals as energy absorbers. This choice was determined by the properties of the $TeO_2$ crystals:

- the straightforward solution would be pure tellurium but crystals grown with this material evidenced poor mechanical properties and they break after a few thermal cycles. On the contrary with $TeO_2$ **large single crystals** with excellent properties **can be grown**;

- furthermore, the **Debye temperature** of $TeO_2$ is higher than that of pure Te and so, at the same temperature, the $TeO_2$ crystals have a lower specific heat and then higher pulses can be achieved;


Figure 3.2 - Example of $TeO_2$ crystal used in the Milano group. The crystals are produced by Shanghai Institute of Ceramics (Shanghai, China).

- in addition, **Te dominates the compound with respect to the mass** (about 80%) permitting to work with large quantity of tellurium, and the radiopurity of the crystals is high ($<$ 1pg/g in $^{232}$Th and $^{238}$U).

Fig. 3.2 shows an example of a $TeO_2$ crystal of 3x3x6 cm$^3$ size.

## 3.3 The sensor

The Milano group decided to work with NTD–Ge thermistors, working in the Variable Range Hopping (VRH) conduction regime with Coulomb gap as sensors. As described in section 2.4.2, this kind of thermistor can work as a perfect thermometer and it converts the thermal pulse into an electrical signal thanks to the temperature dependence of its resistivity. The resistance behavior follows the relation

$$R = R_0 \exp(T_0/T)^{\gamma} \tag{3.2}$$

where $\gamma = 0.5$ in the MIT region and at a working temperature lower than 1 K, and where the parameter $R_0$ depends on the sensor geometry as

$$R_0 = \frac{l}{S} \cdot \rho_0 \tag{3.3}$$

where $l$ indicates the distance between the electrical contacts, $S$ is the area of the pad where the contacts are made and $\rho_0$ is the electric resistivity that is described by eq. 3.2.

In sec. 2.4.2 the logaritmic sensitivity $A$ was introduced, that depends on the neutron irradiation dose. For this reason each thermistor must be characterized at the operating temperatures, as described for $Si$ thermistors by Alessandrello *et al.* [113]. For the NTD thermistors used by the Milano group (belonging

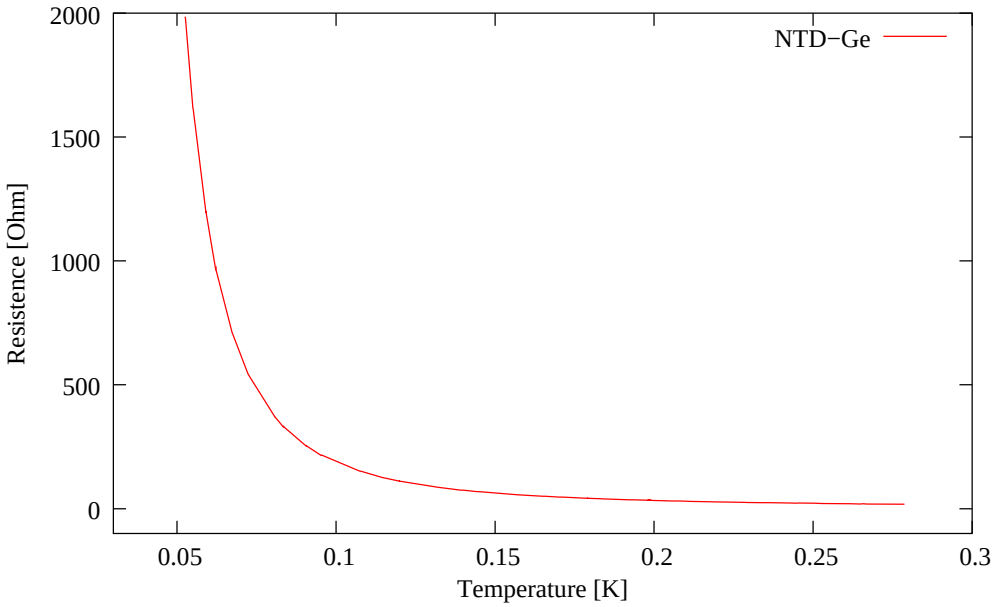


Figure 3.3 - Resistance of a NTD-Ge thermistor of the Milano-Como group as a function of temperature.

to series #31 according to the Berkeley group classification), the $T_0$ value is around 3 K and so this parameter ranges between 7 and 10. A typical resistance vs. temperature curve, for these detectors, is reported in fig. 3.3.

These sensors are realized by neutron transmutation doping of ultra–pure Ge in a nuclear reactor to obtain the proper characteristics of both the resistance and the variation of resistance with temperature.

Melt–doped Ge crystals cannot achieve the necessary uniformity due to a variety of dopant segregation effects. The only technique available for producing such uniform doping is NTD. In typical applications, the neutron absorption probability for a 3 mm thick wafer of Ge is small, on the order of 3 %, leading to a very homogeneous, uniform absorption process. The most important aspect of this process is that $^{70}$Ge transmutes into Ga, an acceptor, and $^{74}$Ge transmutes into As, a donor, the primary active dopant in NTD Ge. In this process, one places the Ge in a nuclear reactor where the following reactions take place:

$$\begin{aligned} {}^{70}Ge\ (21\%) + n &\rightarrow {}^{71}Ge\ (\sigma_T = 3.43 \pm 0.17b,\ \sigma_R = 1.5b) \\ {}^{71}Ge &\rightarrow {}^{71}Ga\ (t_{1/2} = 11.4\text{day}) \qquad \text{Acceptor} \end{aligned} \tag{3.4}$$

$$\begin{aligned} {}^{74}Ge\ (36\%) + n &\rightarrow {}^{75}Ge\ (\sigma_T = 0.51 \pm 0.08b,\ \sigma_R = 1.0 \pm 0.2b) \\ {}^{75}Ge &\rightarrow {}^{75}As\ (t_{1/2} = 83\text{min}) \qquad \text{Donor} \end{aligned} \tag{3.5}$$

$$\begin{aligned} {}^{76}Ge\ (7.4\%) + n &\rightarrow {}^{77}Ge\ (\sigma_T = 0.16 \pm 0.014b,\ \sigma_R = 2.0 \pm 0.35b) \\ {}^{77}Ge &\rightarrow {}^{77}Se\ (t_{1/2} = 38.8\text{hr}) \qquad \text{DoubleDonor} \end{aligned} \tag{3.6}$$

where $\sigma_T$ and $\sigma_R$ refer to the thermal and resonance neutron capture cross sections respectively.

Since the doping level of the Ge needs to be on the order of $1 \times 10^{17}$ atoms/cm$^3$, a very high flux reactor, such as that at the University of Missouri or the Massachusetts Institute of Technology, is necessary to do the doping in a reasonable time. Even more important is stability in the flux and stability in the neutron energy distribution as measured by the Cd ratio.

It is very important to optimize the neutron irradiation exposure and to make the exposures as uniform as possible. It is not possible to evaluate the thermistor material directly from the reactor because of the long half life of $^{71}$Ge (11.43 days). A delay of several months is required to see if the Ge needs more exposure. To overcome this difficulty, the Ge material is accompanied by foils of metal with long-lived $(n, \gamma)$ radioactive daughter nuclei. Accordingly, the neutron exposure of the Ge can be determined accurately, and uniformity of exposure is achieved. This technique was developed recently by the Lawrence Berkeley National Laboratory group [114]. Following the neutron exposure and radioactive decay period, the NTD germanium is first heat treated to repair the crystal structure then cut to obtain strips of the desired geometry.

## 3.4 The other detector components

The other components of the detector are the heat bath and the mechanical and electrical connections:

- the **heat bath** corresponds with the copper frames of the detector, in fact they are in good thermal contact with the coldest part of the dilution refrigerator, named *mixing chamber*.

- the **mechanical holder** of the crystal and its main thermal connections to the heat bath are made with PTFE pieces. At low temperature the PTFE contracts significantly. Therefore if the Teflon pieces are appropriately designed, they could hold the crystals in a safe mode. Furthermore PTFE is not so hard as a metal and keeps some elasticity even at the lowest temperatures; so it can touch the crystals without breaking it. The PTFE isn't a good heat conductor at low temperatures. The geometry of PTFE pieces needs to be optimized to obtain a correct conductance to the bath, in fact too low thermal conductances would mean too long thermal pulses, otherwise too big thermal conductances to the bath would mean that the energy released by the particle would flux through the PTFE pieces to the bath producing a loss in the signal amplitude. Also the heat conductance of the PTFE was measured in Milan and the phenomenological relation was found to be $\sim 4 \times 10^{-5}$T[K]$^2$ W/K .

- the **electrical contacts** are obtained with gold wires of 25 or 50 $\mu$m diameter bonded on the lateral golden sides of the thermistor. Of course these connections are also thermal links to the thermal bath. Dedicated

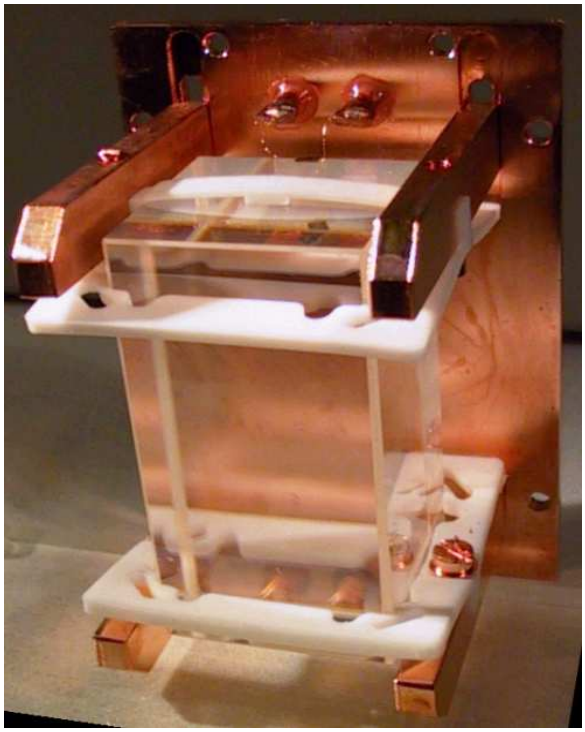

Figure 3.4 - Example of bolometric detector. It is possible to see the copper frame (heat bath), the PTFE pieces (mechanical and main thermal connections) and the gold wires (electrical and thermal connections).

measurements have provided a temperature behavior for the gold wires heat conductances equal to $\sim 0.8 \times 10^{-5} \mathrm{T[K]}^{2.4}$ W/K .

- the **coupling between the thermistor and energy absorber** is made by some spots of Araldit rapid, Ciba Geigy (now Novartis) epoxy, of 0.4 to 0.7 mm deposited on the crystal surface by an array of pins. The height of each spot is 50$\mu$m, and normally this is obtained by putting a mylar mask providing the requested thickness between the thermistor and the crystal until the solidification of the glue spots is achieved. This procedure was found to be reasonably reliable and reproducible in the Milan experiments. The heat conductance of the epoxy spots was measured in Milan and the phenomenological relation was found to be $\sim 2.6 \times 10^{-4}$ $(\mathrm{T[K]})^3$ W/K/spot;

Figure 3.4 shows a bolometer used until 2001 in MiDBD–I experiment that will be presented in detail in section 3.9.

I would like to remark that usually all the materials used in the detector construction are to be measured from the point of view of the radioactivity and that only radiopure materials could be used. Copper has the advantage to have a good heat conductance and that it is relatively easy to obtain batches of copper reasonably "clean". Also Teflon has the characteristics to have low level

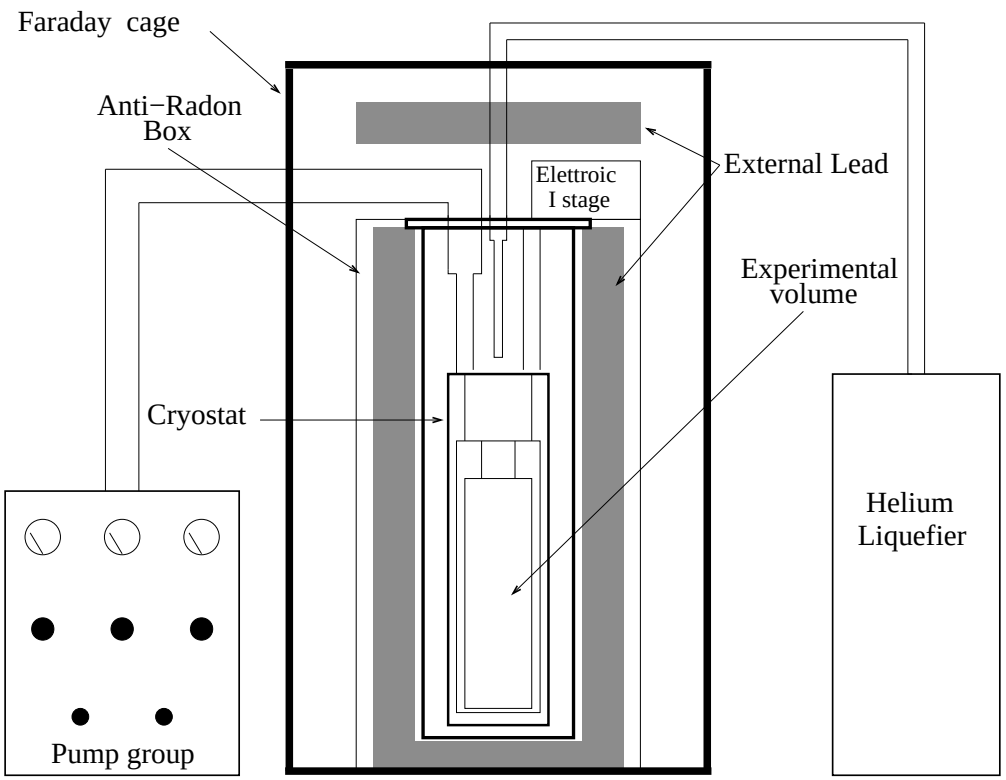


Figure 3.5 - Scheme of the cryogenic set-up.

of radioactivity, and it is used when contacts with poor heat conductances are needed.

## 3.5 The experimental set-up

### 3.5.1 The cryogenic set-up

As already said, to achieve low heat capacities and then high pulses, it is necessary to work at very low temperatures. For this reason the Milan detectors work between 7 and 12 mK, placed in the experimental space of an Oxford Instruments dilution refrigerator. The Milan experiments are realized in Hall A of the LNGS, whereas the R&D of the detectors is made in Hall C of the same laboratories. In these halls two dilution refrigerators, with a cooling power respectively of 1000 $\mu$W and 200 $\mu$W, are installed. They allow cooling down the detectors in the experimental space by means of the thermodynamic proprieties of the $^3$He–$^4$He mixture. The two apparatus, although having different purposes, are similar. The experimental set–up is described in fig. 3.5. Due to the low background constraint, the refrigerators were built with a contamination level lower than 100 mBq/kg for materials used in quantity lower than 1 kg and a contamination level lower than 1 mBq for materials used in quantity higher than 1 kg.

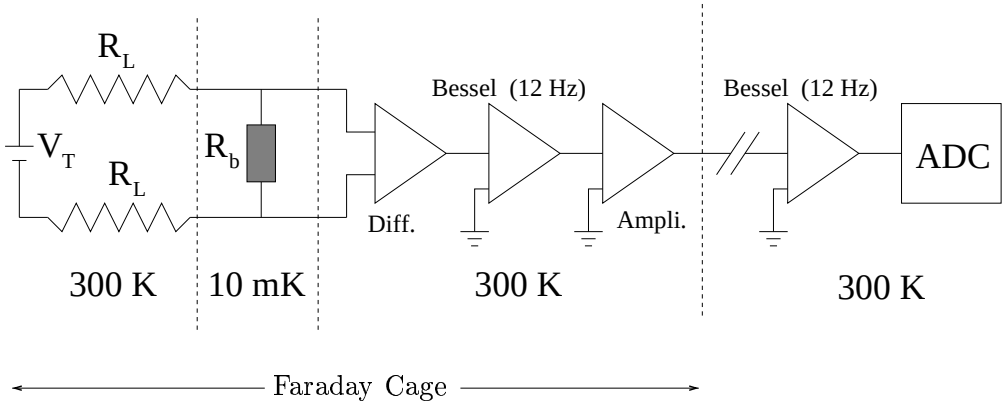


Figure 3.6 - Scheme of the electrical read–out set–up.

Furthermore, to reduce the background due to the inner rocks of the laboratory, each refrigerator is shielded with two layers of lead, 10 cm thick each. The external layer is composed by normal lead whereas the internal one is composed by a special lead with a radioactivity level lower than 16±4 Bq/kg in $^{210}$Pb. As it is shown in fig. 3.5, the refrigerator is coupled with a liquefier, which permits to maintain a constant level of the liquid helium to be mantained in the Main Bath. This is important to reduce the variation of detector temperature that is correlated with the levels of the cryogenic liquids. The refrigerator and the lead shields are enclosed in a Plexiglas box where a pure nitrogen atmosphere is maintained to eliminate the natural radon of the tunnel. To reduce the noise due to the electromagnetic interferences the Plexiglas box is surrounded by a Faraday cage.

### 3.5.2 The electrical read-out and DAQ

In fig. 3.6 the electronic configuration normally used for the detector read–out is shown. The bolometers are polarized in a symmetric way through two so called load resistances, $R_L$ (usually having some GΩ of value). The thermistor resistance at the working temperature $R_b$ is between 1 and some hundreds of MΩ, so the relation $R_L \gg R_b$ is realized and therefore the signal amplitude can be maximized (see sections 2.5 and 2.5.2).

The first differential preamplifier stage could be at room temperature, as in the figure, or cooled down to 120 K. The cold electronics has the purpose to reduce the microphonic noise. This could help at low energy, whereas at large energies the resolution is worse than the one expected from the signal–to–noise ratio, and the two set–ups are expected to give equivalent performances. So the cold electronic set up could be used to achieve an improvement of the energy threshold, useful for experiments that search for Dark Matter. The total gain of the electrical system is G=218.

After the preamplifier stage, the signal is sent to the antialising Bessel filter. As the signal has no frequency components higher than 10 Hz, it is possible to use a 4 pole low pass filter with a frequency cut at 12 Hz and unitary gain.

The connection from the thermistors and the first stage of the electronics is obtained via a twisted pair from one meter (when the cold stage is present) to five meters (when the cold stage is not present) in length. At this point the signal is sent simultaneously to the Analog to Digital Converter (ADC) and to the trigger that commands the ADC.

If the pulse amplitude is higher than the trigger threshold the signal is digitalized and then transmitted to a PC–VXI that works as a memory of the system. The ADC parameters depend on the pulse characteristic, but usually a voltage range of 0 – 10 V and 16 bits are used. The sample time is 2 ms and the number of samples of the pulse is 1024, so that the base–line is recovered.

## 3.6 Data analysis

The data analysis is completely performed off–line: as said in the previous section, pulses exceeding a given threshold amplitude, depending on the noise RMS, are fully sampled and recorded on a hard disk. The main goals to be achieved are:

- a good evaluation of the pulse amplitudes;
- rejection of spurious pulses;
- correction for system instabilities;
- possible identification and rejection of background pulses.

In order to maximize the signal–to–noise ratio and to estimate at best its amplitude, each recorded pulse is Optimally Filtered (OF).

This technique is frequently used with bolometers to evaluate the amplitude of a signal superimposed on stochastic noise. This algorithm has proved to provide the best estimate of the pulse amplitude under general conditions. Relative to a simple maximum–minimum algorithm, this technique allows the evaluation of the signal amplitude with much higher efficiency resulting in an improvement in energy resolution by as much as a factor of two. To use the OF technique, it is necessary to obtain the noise power spectrum and the response function (i.e. the shape of the signal in a zero noise condition).

The noise power spectrum is periodically evaluated by randomly acquiring a few hundreds of noise pulses. The expected response function of the system (Reference Pulse; RP) is obtained by averaging over a large number of "true" pulses acquired with an external calibration source. In order to distinguish actual pulses from randomly acquired ones induced by microphonic or electronic noise, a pulse shape analysis is performed. Each optimally filtered pulse is compared, after proper normalization and time shift, with the optimally filtered RP.

The sum of their point by point squared differences is assumed as shape parameter. Since noise frequencies are suppressed by Optimum Filter, this parameter is very effective and noise pulses are always fully identified and rejected for energies higher than 50 keV (the software threshold used in MiDBD–I).

An important step of the data analysis consists in the production of the so called "n–ple" (a shortening for *entuple*). The idea is to convert the main

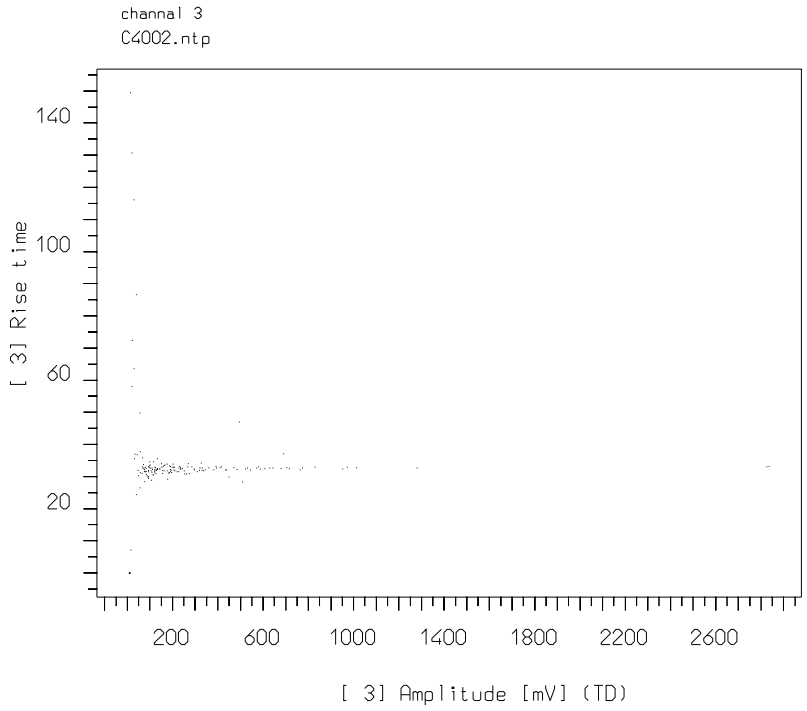


Figure 3.7 - Example of bidimensional representation: the rise time vs. the pulse amplitude.

characteristics of the pulses in simple and readly–understandable information. A fraction of 5% of the total events were identified as noise pulses and therefore rejected by pulse shape analysis in the $0\nu$DBD region.

With each recorded pulse is associated to a set of parameters that represents their principal variables. In this way for each pulse a vector is produced, n–ple, that contains for example the OF amplitude, the rise time, the decay time, and other parameters associated with the shape of the recorded signal. The next step consists on the selection of the pulses. To do this it is useful to analyze the n–dimensional space of parameters. This permits identification regularity and to select only the pulse fraction with the desired characteristics. In fig. 3.7 and 3.8 two bi–dimensional plots are reported as examples. In the first figure the pulse rise time is plotted versus the OF pulse amplitude. A main class of pulses with about the same rise time is visible. At low pulse amplitude some points with different rise times are present; these points are probably related with noise pulses.

### 3.6.1 Coincidence analysis

A powerful tool of the data analysis is represented by the coincidence analysis. In fact coincidence spectra between different detectors are used to identify background sources. Part of the continuous radioactive background is due to degraded alpha particles that left energy in more than one single crystal. If the energy of simultaneous pulses in two adjacent crystals are plotted it is possible

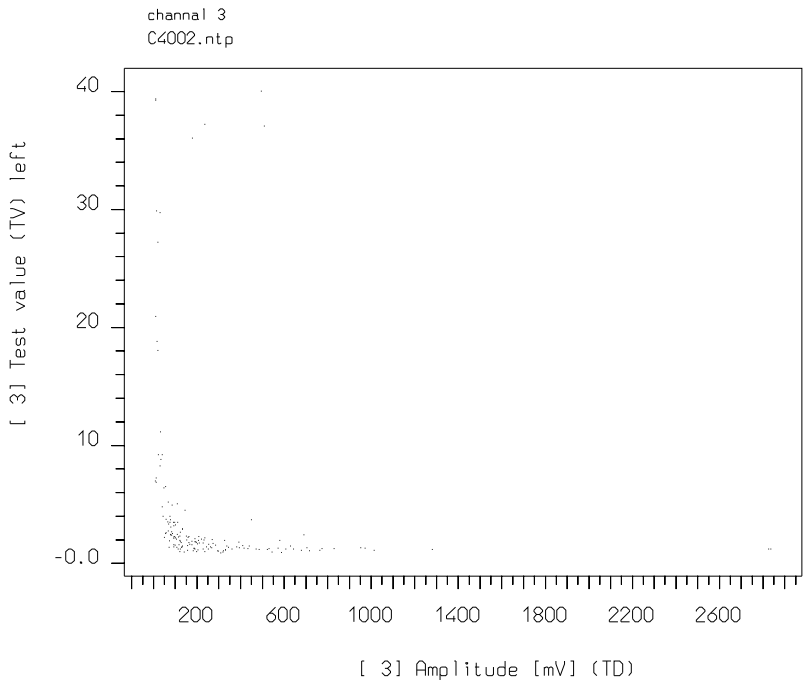


Figure 3.8 - Example of bidimensional representation: the TV left parameter vs. the pulse amplitude.

to obtain the graphic shown in fig. 3.9. Each line in the plot corresponds to an alpha decay and the alpha transition energy is equal to the sum of the energy released in the two detectors. These events are rejected and so the background is reduced.

## 3.7 Thermal instabilities and off–line stabilization

In chapter 2 various noise sources of the bolometric detectors have been discussed. Another source of noise, which is particularly fastidious, is discussed in this section: the thermal instabilities. This is an important problem of cryogenic experiments. In fact, changes for the base temperature even at the 0.1% level may have a negative effect on detector performances. Usually thermal instabilities are correlated with intrinsic instabilities of the cryogenic setups, and experience shows that in long measurements one has to cope with thermal fluctuations, mainly because variations of liquid bath levels (at 4.2 and 1.5 K) determine small changes in the flow rate of the $^3$He–$^4$He mixture in the refrigerator, that influence base temperature. The problem can be minimized by directly stabilizing the main cryogenic parameters as much as possible, but often this is a difficult, and sometimes impossible, task.

An obvious approach to the response stabilization consists in delivering periodically to the detector one (or more) fixed amount of energy generating a detector response as similar as possible to the signal of interest. The energy injection can occur in the form of

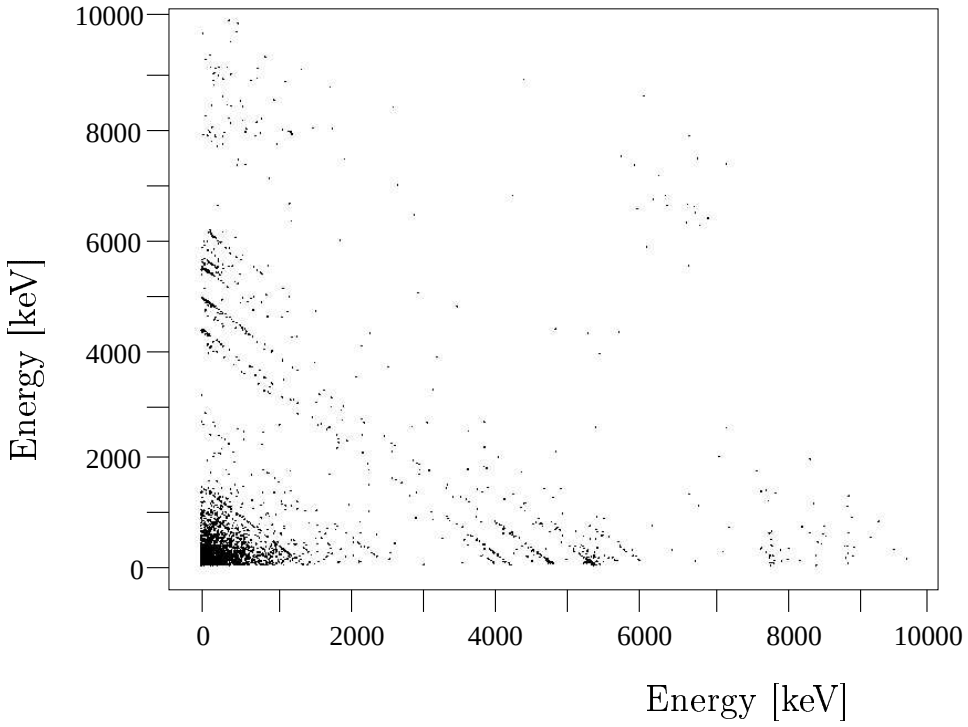


Figure 3.9 - Coincidences between adjacent crystal detectors.

- energetic particle absorptions;
- Joule pulses delivered by a proper heating element thermally coupled to the crystal;
- light pulses transmitted through optical fibers.

The Milano group has studied all of the above solutions, and has chosen to work with the second one. This solution consists in using a resistive element thermally coupled to the crystal to inject calibrated amounts of energy through Joule heating. The advantage of this solution is of course the complete control of the calibration mechanism that it would offer: the pulses would be equally spaced in time. The rate and amplitudes could easily be tuned to the necessity of the experiment. However, such a heating element must satisfy some non–obvious requirements:

- its resistance must be reasonably independent of temperature and applied voltage;
- its heat capacity must be negligible with respect to the detector one;
- in order to provide an almost instantaneous energy release, the relaxation time of the developed heat in the crystal must be much shorter than all the typical thermal time constants;

- the signal formation mechanism for particle interactions and for Joule heating must be similar enough to assure that the pulse amplitude dependences on time, baseline level and other operation conditions are the same for the two processes;

- the heater resistance must be much higher than the connection wire resistance through the cryostat in order to represent the main point of power dissipation, but not so high to require excessive voltage pulses to develop the required calibration energy.

The most natural approach would be to register the pulse amplitudes $V_h$ given by the pulser together with their arrival times and then to reconstruct the function $V_h(t)$, which represents the detector response as a function of time: it can be used off–line to correct the amplitudes of every pulse whose arrival time is known. Unfortunately, this method has an intrinsic limit: the function $V_h(t)$ is sampled with a certain rate that cannot be too high for obvious reasons of dead time. Therefore, fast variations of the detector response could not be registered and pulses occurring during these variations would be erroneously corrected.

There exists a much more powerful approach to the problem. The amplitudes $V_h$ can be correlated with the baseline level $V_b$ (or $T_b$) immediately preceding the pulse development: $V_b$ can be inspected for every pulse, as our ADCs register a baseline segment of about 100 ms before pulse onset. It is possible to plot $V_h$ as function of $V_b$, as in fig. 3.10, and to see that $V_h(V_b)$ can often be successfully approximated with a negative slope straight line. When the function $V_h(V_b)$ is known, it is possible to choose an arbitrary reference value $V_b^{ref}$ corresponding to a $V_h^{ref} \equiv V_b^{ref}$. It is possible, then, to find the function

$$\alpha(V_b) = \frac{V_h^{ref}}{V_h(V_b)} \tag{3.7}$$

that represents the multiplicative factor that gives the value $V_h^{ref}$ at the amplitude $V_h$ when the baseline has the value $V_b^{ref}$. If it is supposed that the $\alpha(V_b)$ is linear with the energy, it is possible to correct the energy pulses. With this procedure stabilized pulses are obtained.

The heaters used in the Milano group [115] experiments are realized by the IRST (Istituto per la Ricerca Scientifica e Tecnologica) by using the well known microelectronic technique. The heaters are obtained by doping a silicon substrate with a high concentration of As ions. After the implantation, a heavily–doped diode, well above the MIT region and with $6\mu m \times 120\mu m \times 0.5\mu m$ size, is obtained. The dimensions of the silicon substrate are $2\times2\times2$ mm$^3$. The heaters have about $100 - 200$ k$\Omega$ of resistance at low temperature and they are attached to the crystals by means of a 50 $\mu$m thick spot of Araldit rapid, Ciba Geigy (now Novartis) epoxy glue. With a programmable pulse generator a square voltage pulses is injected in the heating element, tuning the amplitude and the time width (always much shorter than the thermal pulse rise time) so as to develop a few MeV thermal energy in the heater . The results are summarized in the following points:

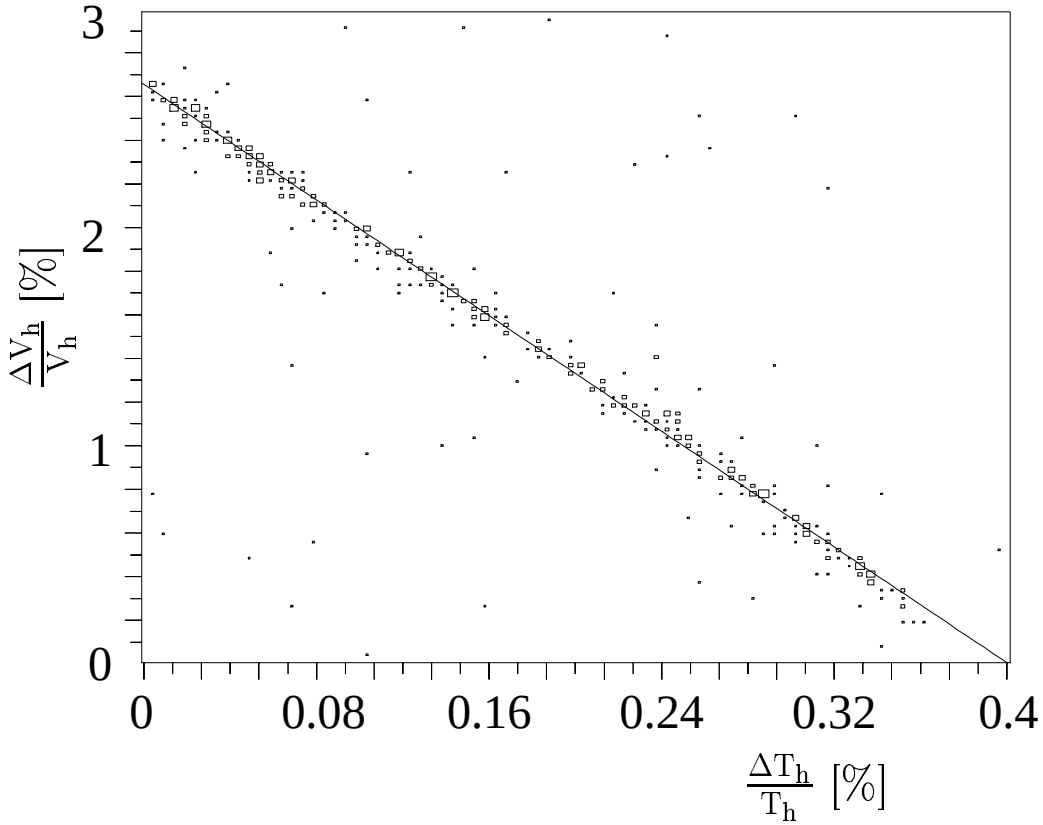


Figure 3.10 - Percentage variation of heater signal amplitude as function of percentage variation of the detector temperature.

- Heater–generated pulses are almost indistinguishable from particle pulses. This is not surprising, since the heat capacity of the device should not be higher than $10^{-13}$ J/K (assuming that the constant resistance doped region can be described as an ideal Fermi gas) which, combined with the $10^{-10}$ W/K glue spot thermal conductance, leads to the typical time necessary to achieve thermal equilibrium between heater and detector $\tau_h$ of about 1 ms, much shorter than the $\sim$ 50 ms thermal rise time of the detector.

- Heater pulse amplitudes scale as $V^2$ and as $\Delta t$, where V and $\Delta t$ are the amplitude and the time width of the voltage square pulses applied at the heating element respectively; this shows that the bolometer is really sensitive to an energy E given by

$$E \propto \frac{\Delta t}{R_h} \cdot V^2 \tag{3.8}$$

  where $R_h$ is the heater resistance.

- The crucial point is that the signals generated in the detector by the heater pulse have the same time and baseline dependence as the particle

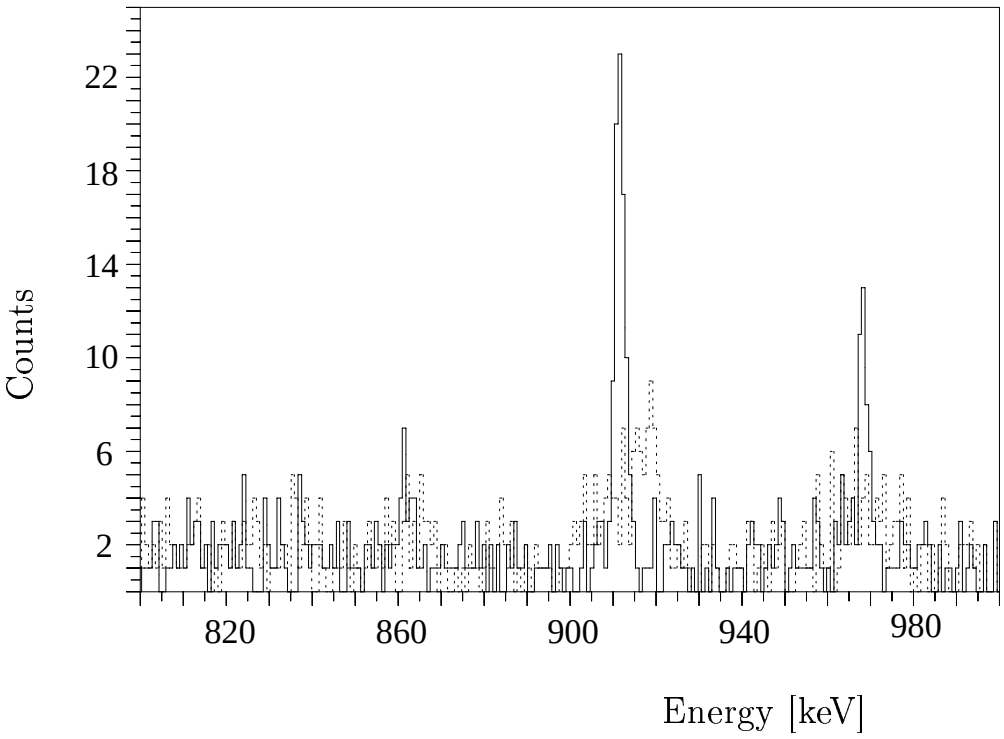


Figure 3.11 - Calibration spectrum obtained with a $^{232}$Th source. The dashed line is the spectrum without stabilization whereas the continuous is stabilized.

signals; this allows an effective stabilization using the heater pulses, which furthermore can be easily identified and selected by software;

- The contemporary recording of the pulses developed on the heater itself could also allow compensation for possible time width and amplitude drifts of the calibration signals.

In fig. 3.11 a spectrum is shown before (dashed line) and after (continuous line) the stabilization procedure. It is possible to note the difference due to the stabilization in the shape of the gamma peaks at 911 and 968 keV generated by the calibration source of $^{232}$Th.

## 3.8 Calibration and linearization

To obtain an energy spectrum from the recorded pulses it is necessary to convert their signal amplitudes into energy. The naive bolometer model used in chapter 2 assumes the linearity of the OF pulse $\Delta$V with energy; however, several parameters depend on the crystal temperature, rendering the corresponding equation nonlinear. Accordingly, the relation between $\Delta$V and E is obtained periodically by the use of radioactive calibration sources. $^{238}$U and $^{232}$Th sources are introduced into the lead shields, near the cryostat, to calibrate the spectrum. The ratio $\Delta$V/E is measured for several gamma lines, and the data are fitted taking

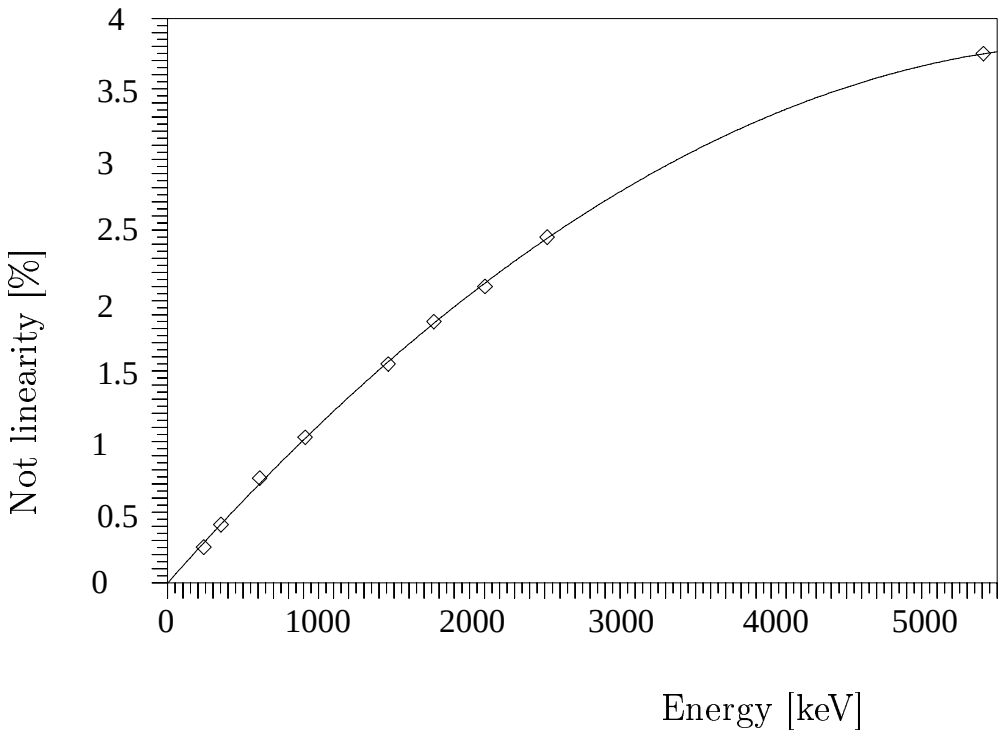


Figure 3.12 - Percentage deviation of the linearity versus the energy.

into consideration the fact that the bolometer resistance and the crystal heat capacity are temperature dependent. This provides the calibration functions of E versus $\Delta V$ , that are then used to convert the OF amplitudes into energy values. It is possible to verify that the relation between the pulse amplitude $\Delta V$ and the released energy of the particles is not linear by observing fig. 3.12. In this figure the percentage deviation of the linearity versus the energy is shown. The fit is performed by using a second order polynomial.

## 3.9 MiDBD experiment: I phase

The MiDBD experiment, carried out in Hall A of LNGS, was only the last of a series of experiments on neutrinoless DBD of $^{130}$Te, based on the bolometric technique. In fact, the improvements in the detector performances obtained in the course of years of measurements with detectors of constantly increasing mass, lead finally to a large mass, low background experiment whose results demonstrated the competitiveness of low temperature calorimeters.

The MiDBD experiment consists of an array of twenty cryogenic detectors. The set–up is made with crystals of $TeO_2$ for a total mass of 6.8 kg. Four crystals are made with isotopically enriched materials: two at 82.3 % in $^{128}$Te and two others at 75.0% in $^{130}$Te . By mass spectrometer measurements we found that these enrichments are lower than the original ones (94.7% and 92.8%, respectively). This is due to the process of crystallization which is more complex

when isotopically enriched powder is used, and requires seeds of natural tellurite. The remaining ones are made with natural tellurium. The detectors are placed in a tower–like structure with five planes of 4 detectors each. The 20 absorbers are crystals of $TeO_2$ of 3x3x6 $cm^3$ volume. The experiment could be subdivided in two main steps performed in different configurations. The two phases are usually indicated as MiDBD–I and MiDBD–II. In this section the first phase configuration and its results, are discussed whereas the characteristic of the second phase will be detailed in the next chapter.

### 3.9.1 The MiDBD–I detector characteristics

MiDBD took data from April 1998 until the end of 2000, and it recorded about 4000 hours of measurements. The tower is connected via an OFHC (Oxygen Free High Conductivity) copper cold finger to the mixing chamber of the dilution refrigerator, and the tower was surrounded by an internal shield of Roman lead of 2.2 cm minimum thickness.

The read–out wires were made of a constantane wire with a diameter of 60 $\mu$m. Each pair of wires are twisted together, in order to minimize the possibility of cross–talk and microphonic noise. Each wire connecting the detectors to the room temperature electronic system is thermalized at 5 different stages of temperature (4.2 K, 1.2 K, 600 mK, 50 mK, 7 mK). Only the room temperature electronics was used in this experimental phase. Each thermistor is read–out independently, whereas the heaters are connected in parallel, in groups of five, along the tower walls. The copper used for the construction of the tower and of the detectors is OFHC and is welded by an electron beam, in order to prevent the contamination due to the introduction of external radioactive materials. The single module is composed of a single $TeO_2$ crystal, so each plane contains 4 modules. The single crystal is held by two Teflon masks that touch the crystal surfaces in 14 points each.

The sensor dimensions are $3 \times 1.5 \times 0.4$ $mm^3$, and the heater (see section 3.7) is 2 $mm^3$. 6 glue spots are used to attach the sensors to the crystals, whereas for the heater only one glue spot is used. A picture of a detector used in this experimental phase was already shown in fig. 3.4, whereas in fig. 3.13 the design of the tower and of the single crystal module are reported.

### 3.9.2 Results and problems

The MiDBD experiment demonstrated that it is possible to operate with an array of bolometric detectors. In table 3.1 the performances of the twenty detectors are shown. The working temperatures, third column, are rather homogeneous and, for each detector, near the optimal working value. In the second column the bolometric resistances $R_b$ are reported at the working point. In the fourth column the voltage pulse amplitudes A for the various detectors are listed for an energy deposition of 1 MeV. The resolutions in tab. 3.1 are referred to the FWHM of the $^{208}Tl$ peak obtained during a calibration measurement as described in section 3.8, whereas in the last column of the same table the reported values correspond to the intrinsic energy resolution of the bolometers. The en-

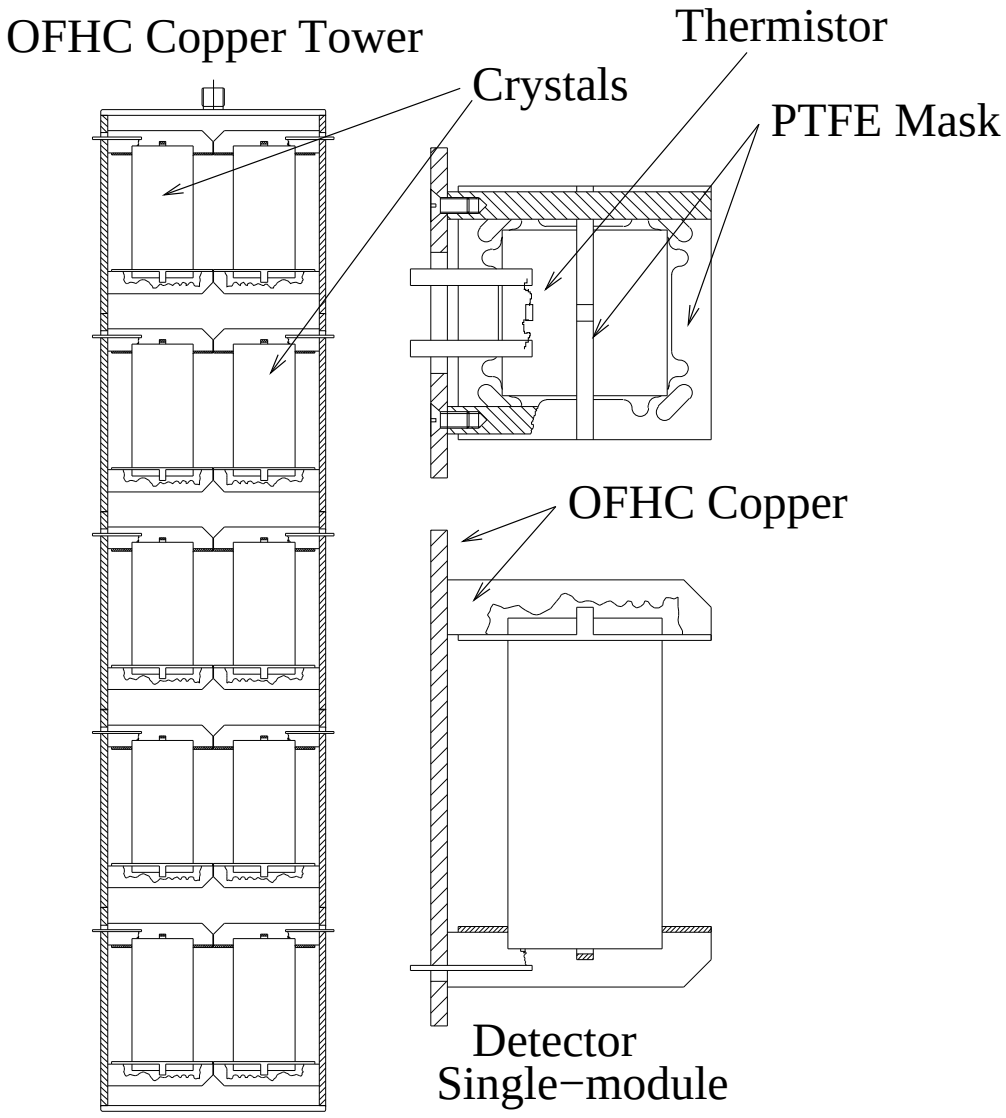


Figure 3.13 - Design of the tower detector used in MiDBD–I.

| *DET.* | $R_b$ $[M\Omega]$ | $T$ $[mK]$ | Amp. [$\mu$V/MeV] | $\tau_D$ $[ms]$ | FWHM @ 2615 $[keV]$ | FWHM *F.O.* $[keV]$ |
|---|---|---|---|---|---|---|
| 1 | 133 | 12.3 | 330 | 250 | 7.4 | 2.3 |
| 2 | 80 | 11.8 | 200 | 220 | 5.7 | 3.3 |
| 3 | 130 | 11.9 | 300 | 355 | 16.2 | 8.6 |
| 4 | 133 | 12.4 | 285 | 135 | 6.9 | 2.4 |
| 5 | 95 | 12.9 | 190 | 180 | 8.4 | 3.7 |
| 6 | 148 | 11.7 | 230 | 235 | 5 | 3.1 |
| 7 | 89 | 12.4 | 210 | 140 | 10.5 | 2.7 |
| 8 | 117 | 12.1 | 350 | 160 | 6.9 | 6.7 |
| 9 | 187 | 11.5 | 420 | 150 | 5.7 | 3 |
| 10 | 140 | 12.8 | 390 | 345 | 4.8 | 3.8 |
| 11 | 296 | 10.8 | 385 | 120 | 9.1 | 2.2 |
| 12 | 86 | 12.1 | 320 | 235 | 8.2 | 1.8 |
| 13 | 67 | 13.1 | 160 | 125 | 7.9 | 2.8 |
| 14 | 61 | 12.7 | 210 | 215 | 6.4 | 2.2 |
| 15 | 55 | 13 | 130 | 230 | 8.9 | 2.4 |
| 16 | 81 | 12.7 | 200 | 205 | 5.8 | 2 |
| 17 | 108 | 12.4 | 310 | 160 | 8.5 | 1.9 |
| 18 | 152 | 13.5 | 240 | 265 | 9 | 3 |
| 19 | 56 | 13.6 | 200 | 210 | 5.5 | 2.2 |
| 20 | 98 | 12.8 | 225 | 130 | 5.6 | 2.3 |
| **Mean** | **115** | **12.4** | **265** | **200** | **7.6** | **3.1** |

Table 3.1 - Performances of the MiDBD detectors obtained in the sixth run, with the experiment in the first configuration.

ergy resolution at the $^{208}$Tl line is important as it is near to the $0\nu$DBD region. In the table 3.1 it is possible to observe the good mean energy resolution obtained at low and high energy, but it is also possible to note that there is a non-negligible dispersion of the detector performances. These variations are better observed in fig. 3.14. In the first one, the distribution of the signal amplitude for a deposited energy of 1 MeV of the various detectors is reported, whereas in the second one the dispersion of the energy resolution at 2615 keV is plotted.

The data analysis also shows that the energy resolution increases with the energy. This behavior is not completely understood, though it might be due to gain fluctuations of the detectors, i.e. to not completely recovered instabilities. In fig. 3.15 the energy resolution of the twenty detectors at various energies is shown. As will be shown in the next chapters, this behavior is observed also in the present experiment.

In fig. 3.16 a calibration spectrum is reported. In the figure only the $\gamma$ region is shown. The most common natural $\gamma$ radioactivity has the $^{208}$Tl line at 2615 keV as the upper limit. The upper part of the spectrum is characterized by the $\alpha$ or $\alpha + \gamma$ radioactivity. The $\alpha$ region of a $TeO_2$ bolometer spectrum is dominated

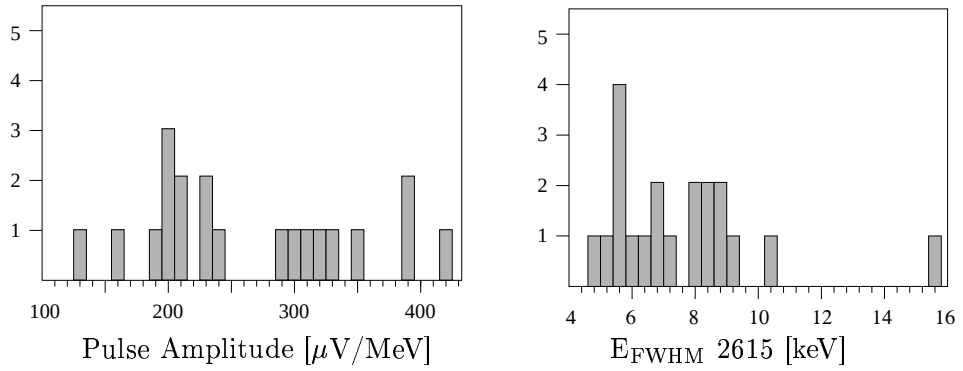


Figure 3.14 - Detector performance, it is possible note the spreads in the detector parameters.

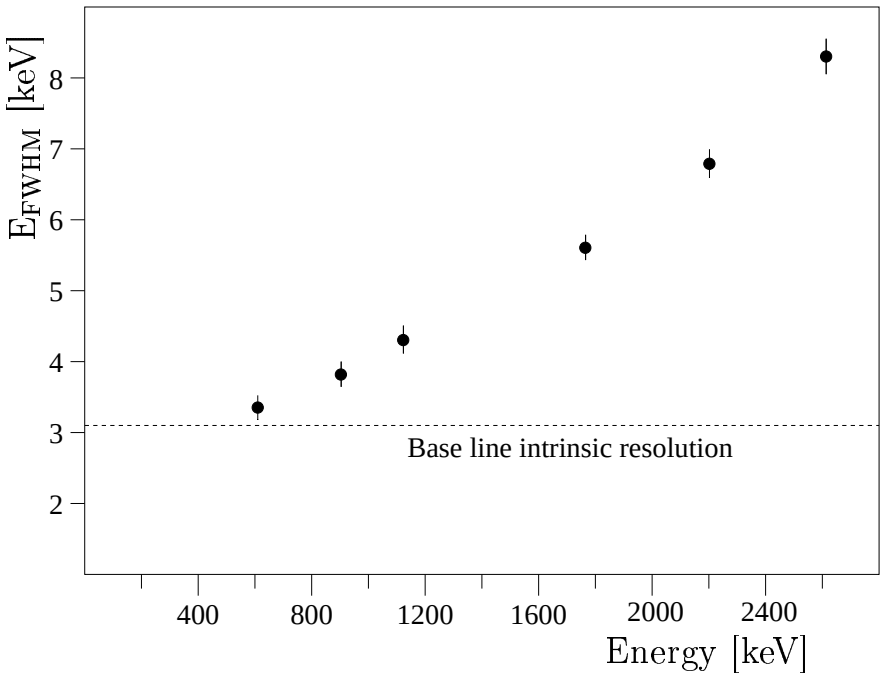


Figure 3.15 - Behavior of the energy resolution with the energy for the 20 bolometric detectors

by the 5407 keV peak of the $^{210}$Po. Fortunately the $^{210}$Po has a short half life of 138 days. Even though the MiDBD–I experiment has taken data about 5 years after the growth of the crystal, the $^{210}$Po peak is still present in the spectrum, as is shown in fig. 3.18. Furthermore the two lines due to the $^{210}$Po do not present temporal variations, so the most probable explanation of these lines regards the $^{210}$Pb contaminations. In any case it is not clear if these contaminations are due to the existence of $^{222}$Rn in the laboratory, implanted in the copper or absorber surfaces, or to the intrinsic contaminations of the crystals.

Fig. 3.16 shows the spectra obtained with 70 hours of calibration running

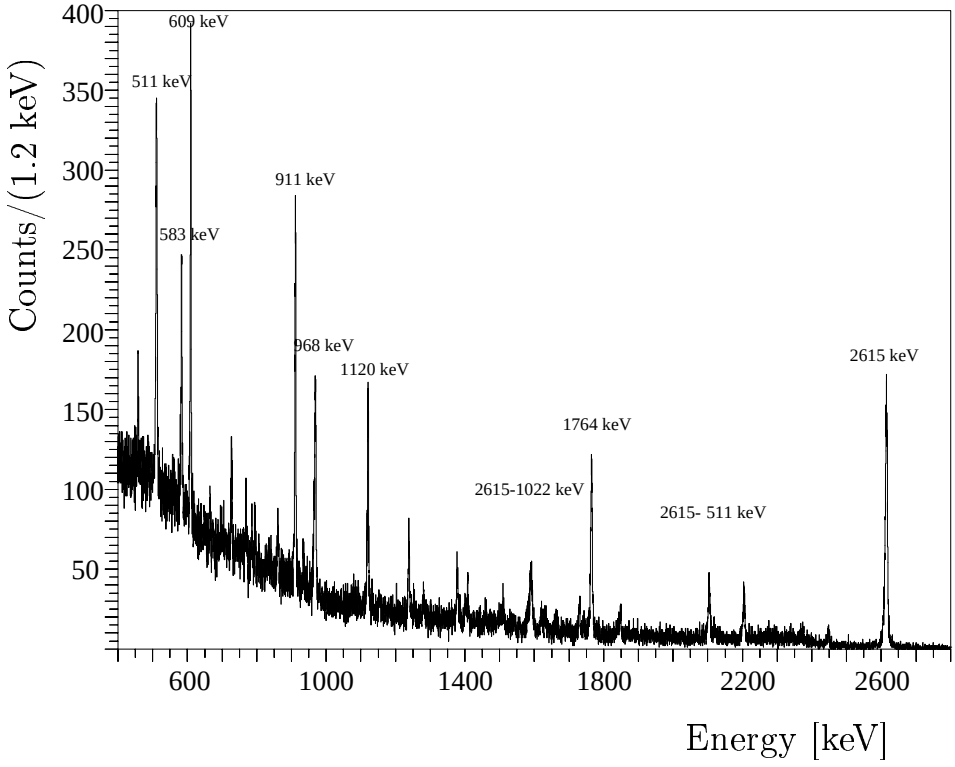


Figure 3.16 - Calibration sum spectrum obtained with 70 data hours and with a source of $^{238}$U and $^{232}$Th.

time.

Fig. 3.17 shows the background spectrum obtained with 63000 hours × crystal of measurements in the first configuration of MiDBD, whereas in fig. 3.18 the background spectrum in the $\alpha$ region is shown. The FWHM at the $^{208}$Tl line is 9.3 keV and the background level in the $0\nu$DBD region is 0.5 counts/keV/kg/year, and is principally due to the degraded Th and U chains alpha particle with energy higher than the $0\nu$DBD transition. In other words the superficial contaminations located at a depth of a few $\mu$m from the copper and crystals surfaces, produce alpha particles that release only a part of their energy in the absorber. Therefore higher energy than $0\nu$DBD transitions produce a continuous level of counts in the $0\nu$DBD energy region.

As said in sec. 3.9, since 1999, four isotopically enriched crystals were added to the tower. The objective is to search for the $2\nu$DBD by using the comparison of their radioactive background spectra. The behavior of these 4 crystals is rather different from those of natural crystals. In fact they have a worse thermal response of a factor 2 – 4 with respect the other MiDBD–I crystals. Furthermore, their thermal pulse shape is different from the other one. In fig. 3.19 the normalized pulse of the enriched crystals is shown and compared with a "normal" pulse of a natural crystal. It is possible to observe that the enriched crystal

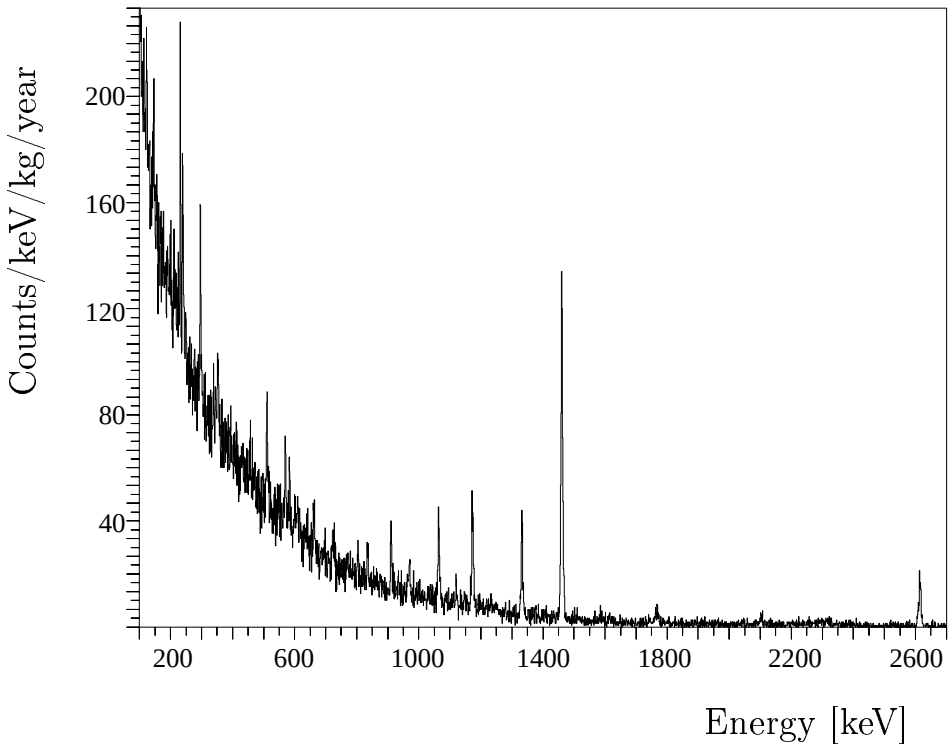


Figure 3.17 - Background spectra, in the $\gamma$ region, obtained with 63000 hours×crystal of measurements of MiDBD–I experiment

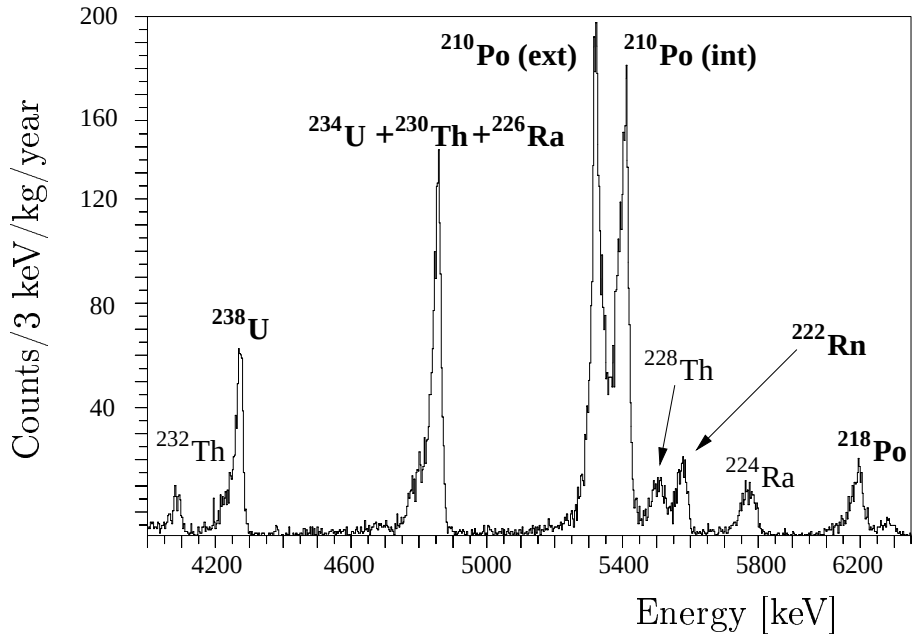


Figure 3.18 - Background spectra, in the $\alpha$ region, obtained with 63000 hours×crystal of measurements of MiDBD–I experiment.

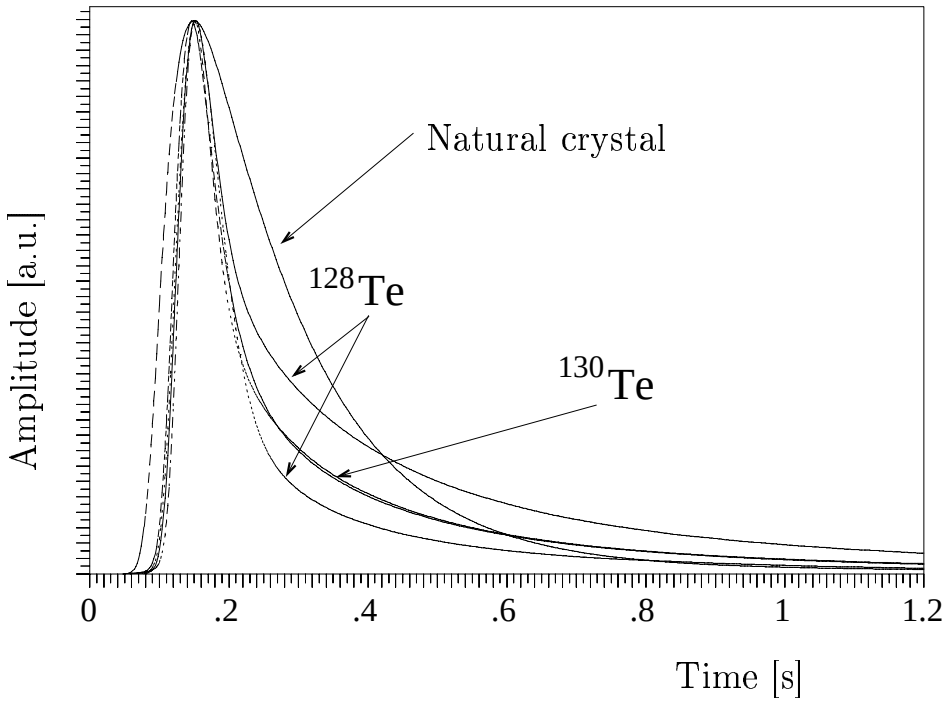


Figure 3.19 - Comparison between the pulse shapes obtained with enriched crystals and one obtained with a natural crystal.

| DET | R [MΩ] | T [mK] | Amp. $\mu$V/MeV | $\tau_D$ [ms] | FWHM @ 2615 [keV] | FWHM F.O [keV] |
|---|---|---|---|---|---|---|
| 128-1 | 109 | 12.1 | 60 | 150 | 16 | 6.5 |
| 128-2 | 135 | 13.7 | 185 | 60 | 8 | 5.5 |
| 130-1 | 69 | 12.8 | 70 | 80 | 15 | 6.5 |
| 130-2 | 67 | 13.1 | 160 | 80 | 8 | 6 |
| Mean Naturals | 115 | 12.4 | 265 | 200 | 7.6 | 3.1 |

Table 3.2 - Thermal characteristics and performances of the 4 enriched cristals.

pulses have two time constants in the decay phase. The faster one is about 80 ms whereas the slower one is about 300 ms. Also the rise time is different, it is, in fact, about 30% faster than the natural crystal pulses ones. A possible explanation is imputed to a contamination of silicon in the enriched powder used to grow the crystals. In table 3.2 the performances of the enriched crystal are listed.

From a scientific point of view, the MiDBD experiment has achieved an upper limit of $8.6 \times 10^{22}$ and $1.44 \times 10^{23}$ years on $0\nu$DBD of $^{128}$Te and $^{130}$Te respectively at 90% confidence level. The detail of the final spectrum in the $0\nu$DBD region is shown in fig. 3.20 Unfortunately, regarding the search

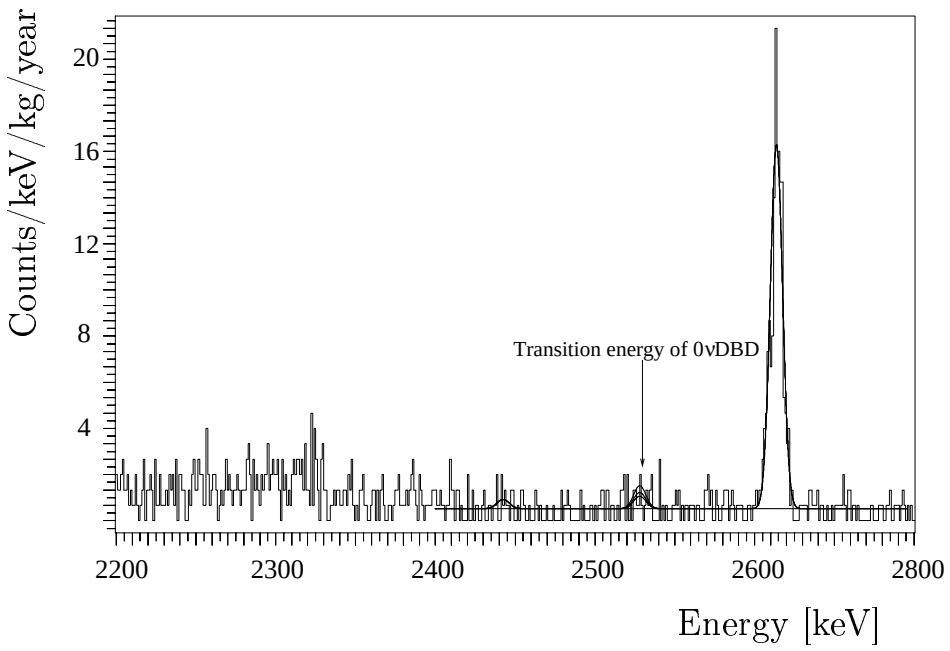


Figure 3.20 - The final spectrum (63000 hours per detector of effective running time) in the region of neutrinoless double beta decay.

for the $2\nu$DBD by using the enriched crystals, the present background is radically different between crystals of $^{128}$TeO and $^{130}$TeO, and considerably larger than for crystals made with natural tellurium. In addition the knowledge of the background, even for the enriched crystals, was not such to allow a safe subtraction of it from the measured spectrum, as made for instance, in the Germanium experiments. For these reasons only a conservative upper limit was obtained: $\tau^{2\nu}_{\rm halflife} = 3 \times 10^{20}$ years at 90% confidence level.

To summarize, apart from the new limits on the DBDs, the main result of the first phase of the MiDBD experiment is the demonstration of the feasibility of experiments with bolometric array detectors. This experiment has also shown the necessity to spend effort in order to achieve a narrow spread in the detector performances. Furthermore, it was evident that improvements from the point of view of the radioactivity background level are needed to achieve good sensitivity on $0\nu$DBD .

# Chapter 4

# MiDBD-II as a general test for Cuoricino

## 4.1 Main ideas for a new 20 detector array: MiDBD–II

In section 3.9.2, the different problems in the MiDBD-I experiment and their interpretations were described. The second phase of the MiDBD experiment goal was to modify the detectors and the experimental set-up in order to achieve an improvement in the signal to noise ratio and in the reduction of the radioactive background level in the $0\nu$DBD region. These modifications were made to increase MiDBD statistics, but above all they were used as a test for the Cuoricino experiment: that is, a new step towards the CUORE project. In fact, the R&D work carried out in Hall C has two limits:

- a low sensitivity in the $0\nu$DBD region due to a background level higher than that of Hall A. This is caused by the lower radiopurity of the materials used for the refrigerator.
- the small experimental space of the refrigerator doesn't allow us to test a sufficient number of detectors.

At the beginning of 2001, the MiDBD detector was completely dismounted and remounted in a new configuration. Here the outline adopted in the construction of MiDBD-II follows:

- to clean crystal surfaces in order to reduce their radioactive contamination;
- to clean the copper surfaces in order to remove contamination due to the production process and to reduce the reactivity of these surfaces: indeed they are chemically active and could fix radioactive elements present in the air, as $^{210}$Pb and other $^{222}$Rn daughters;
- to reduce the amount of Teflon used in every single detector module to perform a better anti–coincidence analysis;
- to reduce the tower size in order to add a shield against the external radioactive sources.

- to reduce the electrical noise introducing, for some detectors, cold electronic stages;
- to reduce the mechanical noise testing an anti–vibration damping method.

The previous points will be detailed in the next sections.

## 4.2 The compact holder and four detector module

The new holder has been realised to obtain a reduction of its dimensions. Indeed the aims of this operation were:

- increasing the fraction that each crystal sees of its neighbour. This aspect is important to perform an efficient anticoincidence analysis.
- improving the tower shielding as for the reduction of the background due to external sources.

Fig. 4.1 shows a single module of MiDBD second phase and in fig. 4.2 a schematic diagram of the new module is shown. The new aspects of this configuration are:

- every single module holds four crystals instead of one.
- the PTFE masks are replaced by PTFE pieces with a L– and T–shape. In this way it is possible to reduce the crystal areas hidden by Teflon (about 10% both for the top and the bottom surfaces, and a not negligible part of the lateral surfaces).
- limitation of the amount of copper used to hold crystals.
- new electric connections instead of the old ones made with indium. In fact the most abundant isotope of indium is the $^{115}$In which has a life time of $4.4 \times 10^{14}$ years. These new connections were obtained introducing the sensor and heater gold wires in copper pins. The pins were glued in the copper frames in order to thermalize the wires and avoiding short–circuit with ground. The gold wires are fixed to them by crimping.

This new configuration was designed considering also the CUORE project: thanks to this new module structure, detectors can be seen also by other crystals in case of more than one tower. In fig. 4.3 a comparison between the old and new configuration of the holder is shown.

The four detectors of the MiDBD–II first plane have two thermistors each. The idea was to obtain an improvement of the signal to noise ratio: in case of uncorrelated noise in two channels, a reduction of $\sqrt{2}$ is expected by summing up the two thermistor outputs. The "double read–out" of the detectors has been already tested in Hall C of the LNGS: the results were so appreciable to stimulate the testing of the same configuration of some detectors of the MiDBD–II experiment. In tab. 4.1 the results obtained in the Hall C, during the R&D for MiDBD–II, with a double read–out detectors are reported. Ch 1 and Ch 2 represent the two sensors.

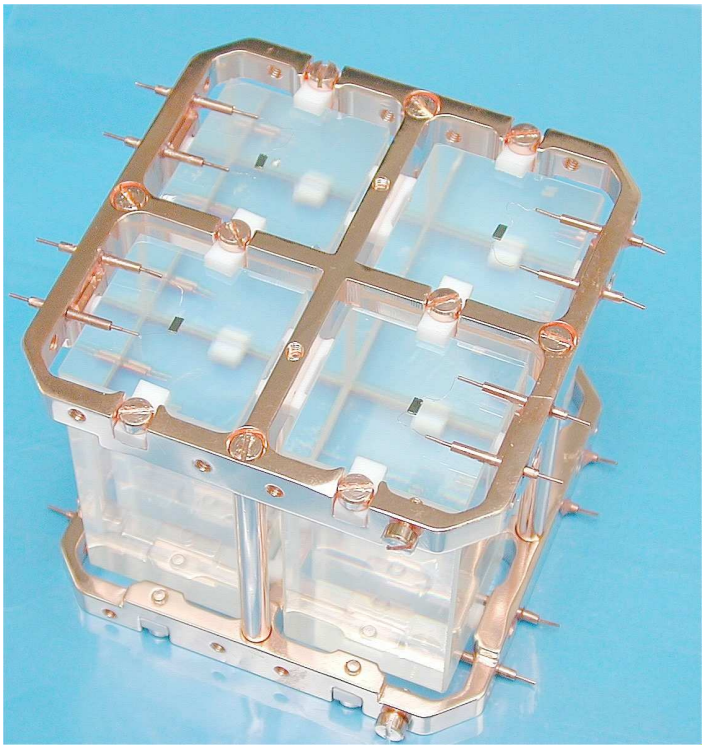

Figure 4.1 - Example of a new module of MiDBD-II.

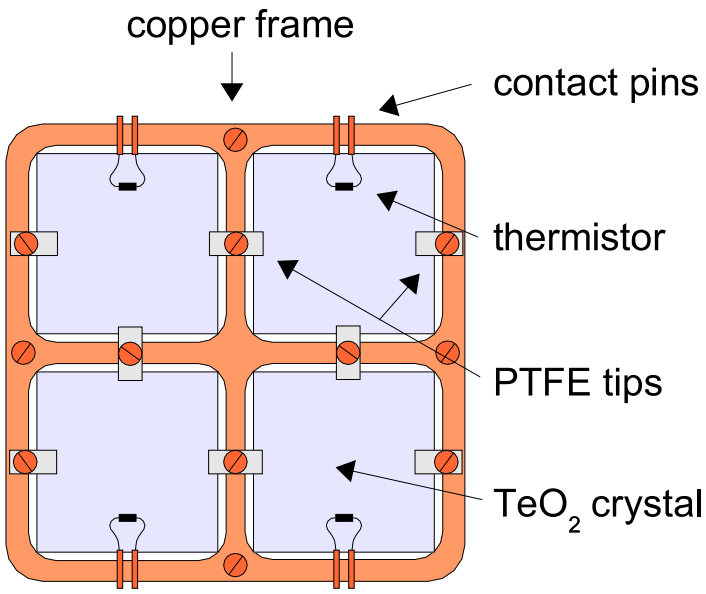


Figure 4.2 - Scheme of the new module of the MiDBD experiment seen from the top view.

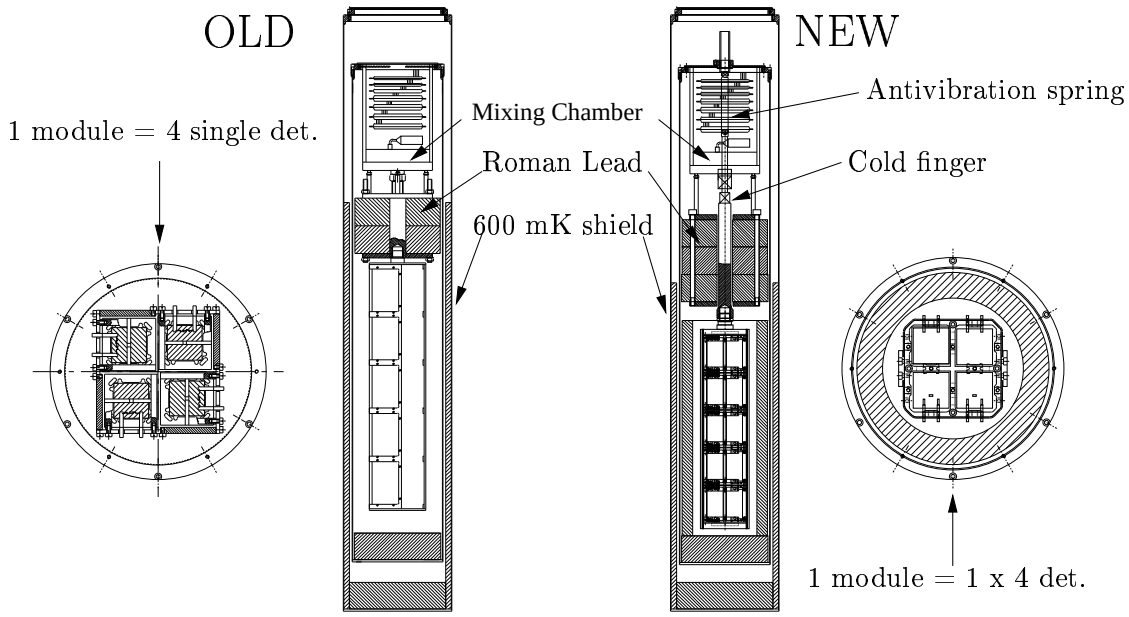


Figure 4.3 - Comparison the old and new experimental configuration.

| | $N_{rms}$ | FWHM FO | FWHM @ 238 Kev |
|---|---|---|---|
| Ch1 | 1.3 | 1.8 | 1.9 |
| Ch2 | 1.4 | 2.1 | 2.3 |
| Ch1+Ch2 | 0.9 | 1.6 | 1.6 |

Table 4.1 - Resolution and noise of the two sensors and of their analogic sum.

In the new configuration the tower is more compact, as can be seen in fig. 4.3. Each module contains 4 crystals and the frames are made in copper. The five single modules are hold by 2 copper bars, and the tower is closed with 2 copper covers having a C–shape. Thanks to these covers detectors are shielded from the 50 mK screen. These new tower and module designs permit the addition of an additional internal roman lead shield 2 cm thick around the tower and a roman lead layer 5 cm thick upper the tower to shield the bolometers against the radioactivity coming from the refrigerator upper parts.

## 4.3 The reduction of the radioactive background

What has been done in order to achieve a reduction of the background level, is:

- a treatment of the crystal surfaces;
- a treatment of the copper surfaces of the holder;
- the introduction of a new shield to reduce neutron–induced background.

| | $^{238}$U CHAIN | | | | $^{232}$Th CHAIN | | | |
|---|---|---|---|---|---|---|---|---|
| | $^{234}$Pa | $^{226}$Ra | $^{214}$Pb | $^{214}$Bi | $^{228}$Ac | $^{217}$Pb | $^{212}$Bi | $^{208}$Tl |
| $Al_2O_3$ | 3.8 | 24.8 | 11.7 | 8.2 | 6.4 | 5.2 | 4.6 | 3.2 |
| $Ce0_2$ | 14.3 | <4 | 0.8 | 0.6 | 44 | 82 | 63 | 50 |

Table 4.2 - $\gamma$ analysis of powders used in the crystal polishing procedure. The contamination is expressed in Bq/kg

### 4.3.1 The treatment of the crystal surfaces

A straightforward explanation of the reason why the surface crystal is contaminated is the contaminated powders used during the cleaning procedure. Once grown, $TeO_2$ crystals are cut and then polished in two steps: in the first step alumina powder ($Al_2O_3$) is used, in the second one the crystals are polished with $CeO_2$. Thanks to this second step a better optical quality of the surface is obtained. Samples of powders used by the Shanghai Institute of Ceramics (SICCAS), which has produced these crystals, were requested and analysed. These powders samples are analysed through $\gamma$ spectroscopy with germanium detectors. The results, after this analysis, are reported in table 4.2 where it is shown that there are rather large contaminations. So it is possible that some remainder of powder left on the surfaces could contaminates the detectors.

The Milano group decided to lap these crystals again in order to remove from the surfaces a thin layer of $TeO_2$ material. This operation was realised in a clean room at LNGS with powders that were previously tested as having low radioactivity. For this operation, a machine with a rotating wheel having a ranging velocity of 100–200 turns per second was used. A nylon cloth is attached on the wheel. A mixture of powder and clean water is put on the cloth. When the crystal is pushed on the wheel the friction between granules and crystal removes material whose quantity depends on the dimensions of the granules. The lapping procedure is divided in two steps: during the first step a lot of material, about $40 \div 70 \mu$m, was removed using a powder of $7 \mu$m. During the second one, an almost optical finishing of the surface was achieved using $0.7 \mu$m powder. It is not clear if optical finishing is really important for bolometric performance. What is sure is that transparent sides allow the inspection of the crystal quality and of the glue–spots for the coupling between crystal and sensor.

### 4.3.2 The treatment of the holder surfaces

Contamination of the copper frames is dangerous because the anticoincidence analysis can not be applied to degraded alphas involving inactive surfaces. Many tests were performed to achieve a reproducible and reliable procedure to clean the copper surface. The technique used was studied and developed at Laboratori Nazionali of Legnaro. Indeed people working in these laboratories are expert as far as cleaning operations of resonant cavities for accelerators. Final procedures include polishing, chemical etching and passivation of the copper surfaces.

A dedicated measurement was performed in Hall C to test the copper cleaning procedure. Four $3 \times 3 \times 6$ cm$^3$ crystals, held by copper frames treated in Legnaro, have been used for the test. The integral of number of counts obtained

| Holder | Integral 3-4 MeV c/keV/h $\cdot 10^{-5}$ | Integral 4-5 MeV c/keV/h$\cdot 10^{-5}$ | Integral 5-6 MeV c/keV/h$\cdot 10^{-5}$ |
|---|---|---|---|
| cleaned in Milan | 4.0±0.4 | 8.1±0.7 | 15.2±0.8 |
| cleaned in Legnaro | 5.1±0.5 | 8.4±0.7 | 15±1 |

Table 4.3 - Comparison of the integrals obtained with four 3×3×6 $cm^3$ crystals with copper frames cleaned with Milan or Legnaro procedure.

in a background measurement are compared with ones obtained using copper frames etched by the Milano group. The results are reported in table 4.3. The results are compatible with the best ones obtained in Milano.

### 4.3.3 The anti-neutron shield

Another possible component for the observed background level in $0\nu$DBD region could be due to neutrons coming out from the rocks of the laboratory. The neutron flux was measured in various energetic regions: its value is:

$$\begin{array}{ll} \phi = 1.08 \pm .002 & 0 - 0.05 \text{ eV} \\ \phi = 1.98 \pm .005 & 0.05\, eV - 1 \text{ keV} \\ \phi = 0.23 \pm .007 & > 2.5 \text{ MeV} \end{array} \qquad (4.1)$$

where the unit used is $10^{-6}/\text{cm}^2\text{s}$, [116]. This flux causes a continuous background spectrum due to neutron capture on components of the system. In case of suppression of the neutron flux, an improvement of a factor $1 \div 10$ has been estimated.

For this reason in May 2001 measurements stopped to permit the introduction of a borated polyethylene shield (the concentration of B is about 10%) to reduce the interaction among neutrons and detectors. This shield is composed by panels of 100 × 200 × 2.5 $cm^3$ size, in order to form a 10 cm thickness around the refrigerator. The manipulation of the valves of the cryogenic circuits on the top of the refrigerator was allowed through a shield characterized by bags containing 2 mm diameter balls of borated polyethylene.

## 4.4 The vibration damping method

One of the main sources of mechanical microphonic noise in MiDBD–II was due to the cryogenic experimental apparatus. This problem was already clear during the first data run: the noise level increased 100 times with respect to MiDBD–I, so that measurements stopped to do set–up modifications. Reasons for this noise are not completely clear, but probably are due to a larger mutual influence of the crystals permitted in these new modules. Furthermore the use

of Teflon pieces, instead of Teflon masks, could decrease the mechanical stability of the detector, as the thermal contractions tend to increase the gaps between crystals and Teflon blocks.

To control this vibrational noise, various methods were tested in Hall C to mechanically decouple detectors from the vibrating parts of the refrigerator (main helium bath, 1 K pot, dilution unit). This goal is normally achieved by installing mechanical filters, consisting of a proper combination of intermediate masses and springs or wires, which anchor the detector at a low-vibration point, sometimes at temperatures higher than the pne of the mixing chamber.

In fig. 4.4, the scheme of the solution tested in the Hall C is shown: a stainless–steel helicoidal spring was introduced between the cold finger and the array. This solution was adopted also in the MiDBD–II experiment. A detail of the Hall A refrigerator set–up is shown in fig. 4.5. Thanks to this method the spring suspends the array from the 50 mK stage of the dilution refrigerator damping the vibration. Furthermore the spring decouples the detectors from the 50 mK plate, as steel is a very poor thermal conductor.

To avoid too long vertical oscillations of the tower and to forbid transversal ones, the spring is put in a damping Teflon tube. The thermal connection between the array and the mixing chamber was realised through four copper strips. Of course, using copper strips as thermal connection between the mixing chamber and detectors produces a partial by–pass of the damping spring system and causes an attenuation of the filtering of the vibrations. For this reason an optimization of the copper strips is required in order to find a compromise among thermal and mechanical constraints. This optimization work has been carried out for the Cuoricino experiment (see sec. 4.7).

The time required to cool the array from 4.2 K to a temperature useful for the detector operation (below 10 mK) depends on the thermal link conductance, on the detector total mass and on the parasitic power on the whole tower. Most of this power can be generated through the slow ortho–para conversion of the molecular hydrogen trapped in the copper elements of the detector holder.

The copper strips used in MiDBD–II for the thermal link were not chosen after previous measurements and no effort was done to control the hydrogen problem. The tower cooling time from 1.5 K to less than 10 mK took 25 days. The tower total mass was 15 kg inclusive of 7.5 kg copper. Below 10 mK, a long temperature drift was observed, which went on for several months.

In october 2001, near the end of the MiDBD experiment, the copper strips were replaced with new ones: 40 mm long, 12 mm wide and 50 $\mu$m thick. These new copper strips were thicker than the previous ones, but longer: as a whole, the rigidity of the thermal link was substantially reduced. This operation was made to decrease the annoying vibrational noise level that prevented the acquisition of 3 detector signals. This procedure permitted the recover of these three detectors and allowed the improvement of the signal to noise ratio of the others.

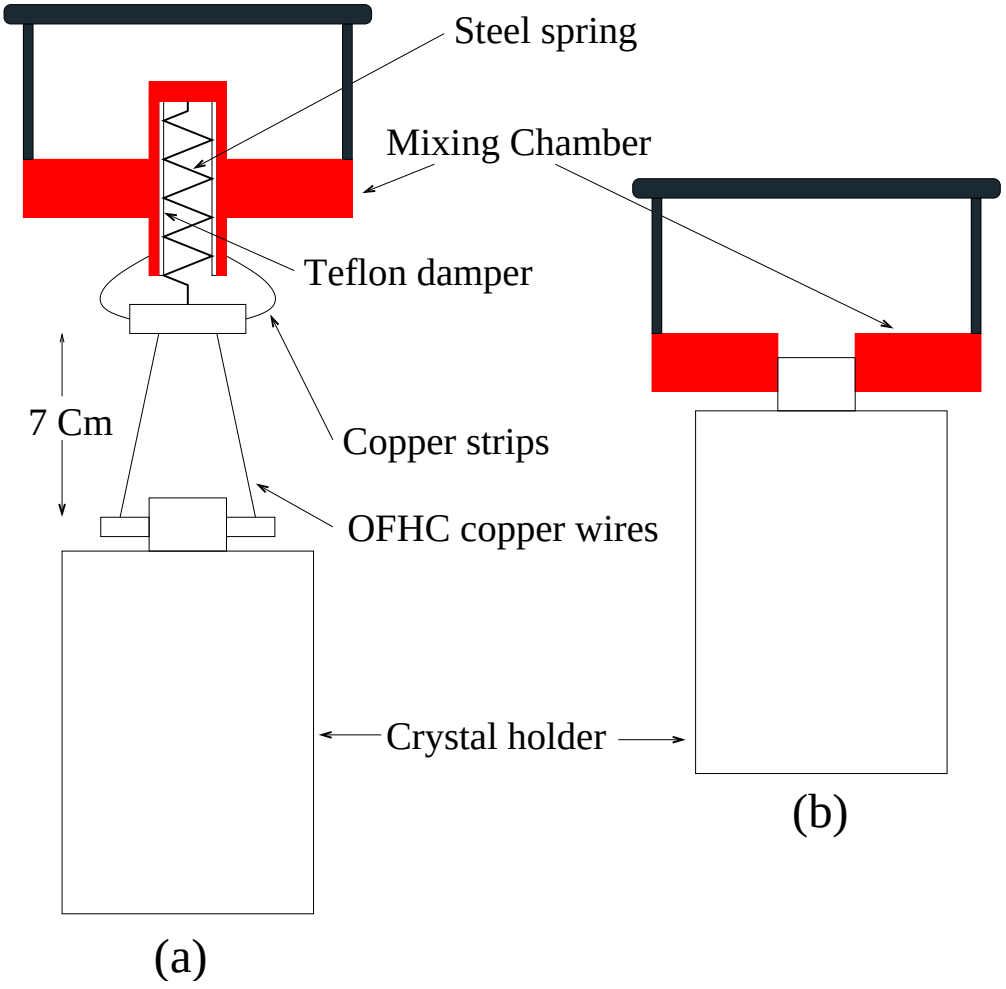


Figure 4.4 - Comparison between the old and new connection of the tower to the cryogenic set-up.

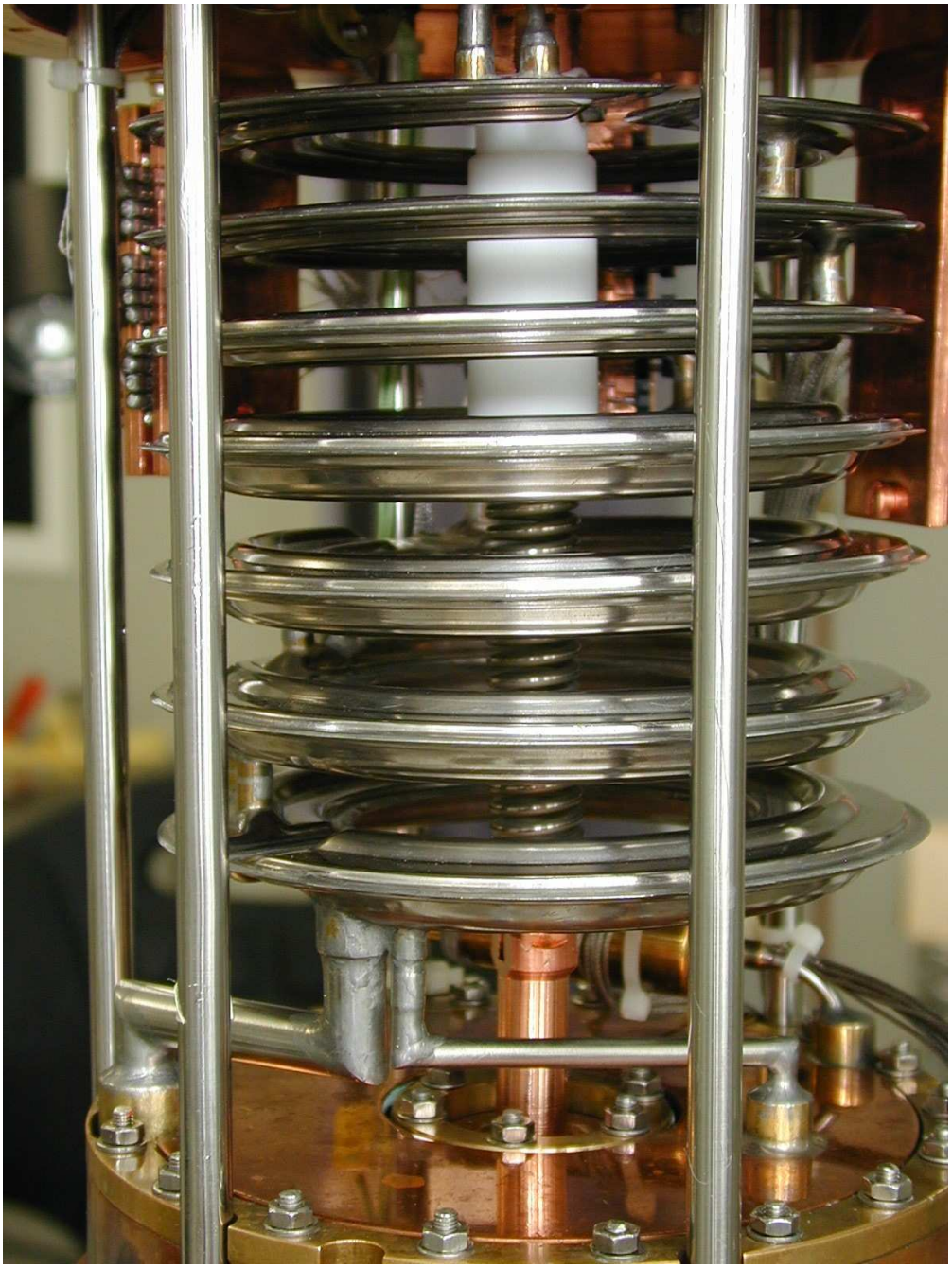

Figure 4.5 - Detail of the damping method used in the MiDBD-II experiment. It is possible to see a part of the steel spring and of the damping Teflon ring.

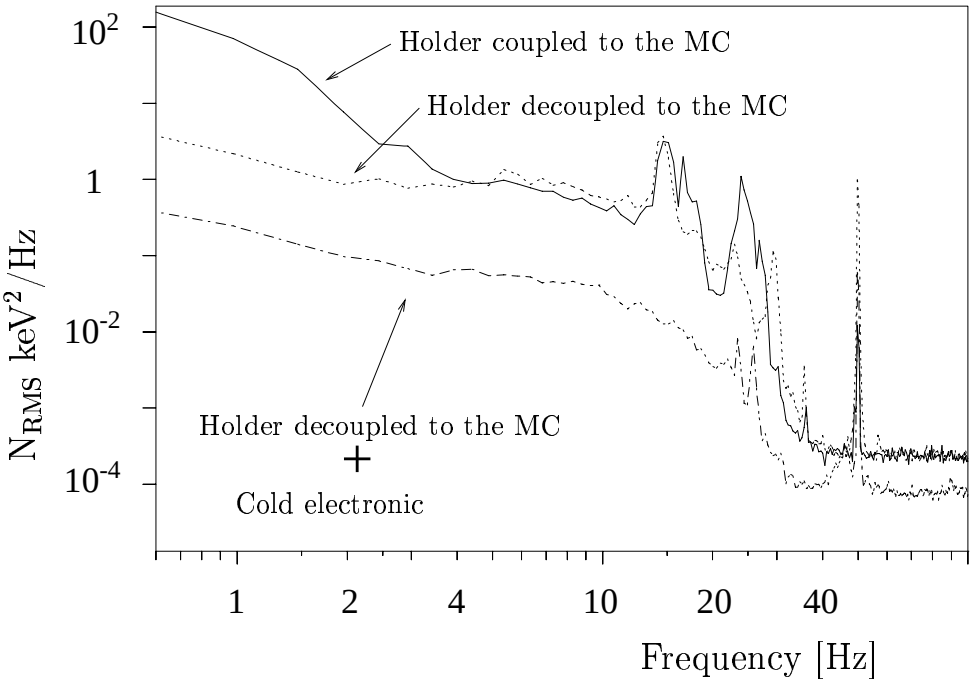


Figure 4.6 - Noise spectra registred in Hall C in the same detector with different configurations.

## 4.5 The cold electronics

As the microphonic noise, due to the read–out wires, is proportional to their length, a cold preamplifier stage was introduced for some channels. 10 JFETs in differential configuration were placed between the 1 K–pot and 600 mK plat in thermal contact with the 1 K–pot. As the JFETs working temperature is 120 K, it is important to thermally isolate the box containing the cold electronic stage, in order to prevent the experimental space from warming up and moreover to avoid thermal noise on the detectors.

In fig. 4.6 the noise spectra of the detectors tested in hall C in the R&D phase are reported. The comparison among these spectra shows a noise reduction in the configuration with the mechanical decoupling and the cold electronic stage.

In spite of that, the effects of cold electronic channels in the MiDBD–II experiment are not yet clear. In fact, a number of spurious noise sources important especially at low energies (microphonic effects, electric interferences) seem to be an individual feature of each detector and therefore appreciable differences among channels with or without cold electronic stage are not easy to evaluate.

## 4.6 The MiDBD–II results and problems

In fig. 4.7 two pictures of the MiDBD–II detector are shown. In picture (a) it is possible to see the lead shield placed on the top of the array, in (b) the open tower of MiDBD–II.

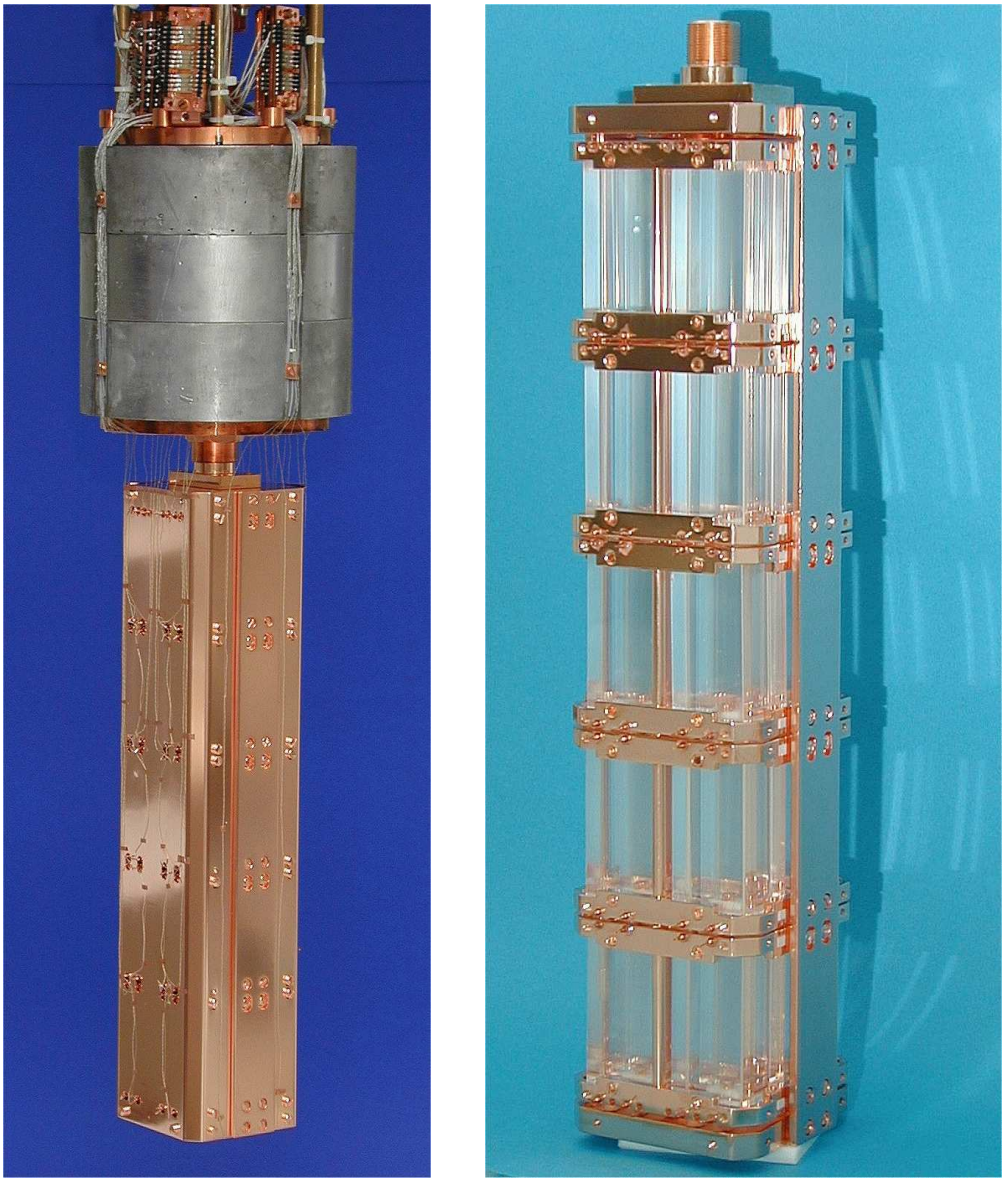

(a) (b)

Figure 4.7 - Pictures of the MiDBD-II tower detector. In figure: (a) tower closed with lateral copper plates; (b) tower without copper plates

From the beginning of the first data taking run three big problems appeared: (i) some thermistors were impossible to read out, probably because of the breakage of some wires; (ii) the breakage of four heater connections caused the impossibility to stabilize the corresponding detectors, therefore they could not be used to increase the statistics; (iii) some detectors had too high a noise level to acquire their signals. A lot of changes were made in order to solve the last problem; main operations were the introduction of the anti–vibration spring and the substitution of the copper strips that thermalize the detectors.

| U+Th Sum Calib. of the natural crystals | $^{208}$Tl | $^{228}$Ac | $^{214}$Bi | $^{208}$Tl |
|---|---|---|---|---|
| Energy [keV] | 583 | 911 | 1764 | 2615 |
| FWHM Old configuration | 3.6 | 4.3 | 5.9 | 8.1 |
| FWHM New configuration | 3.9 | 5.7 | 6.8 | 8.7 |

Table 4.4 - Comparison among energy resolutions obtained during the calibration in two configurations

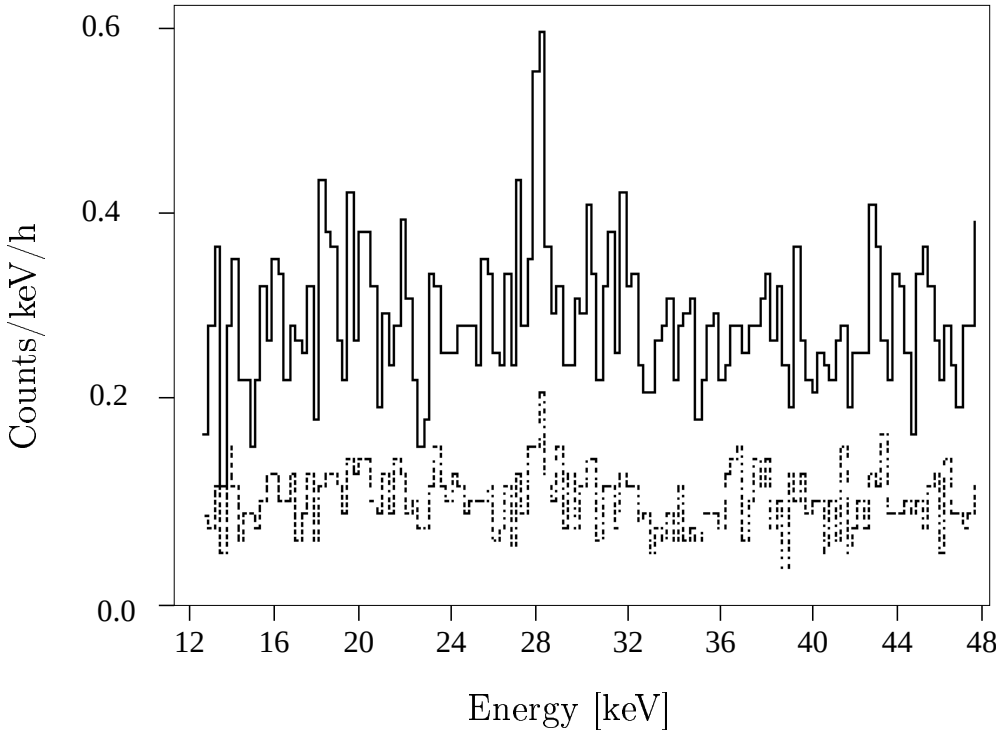


Figure 4.8 - U+Th calibration: the line at 27 keV is due to the Te X–rays, with a FWHM resolution of 1 keV. The continuous line represents the total spectrum, whereas the dashed one represents the spectrum obtained with the anticoincidence analysis.

In tab. 4.4 the comparison among main energy resolutions, obtained through all the natural crystals during MiDBD–I and MiDBD–II calibration, is reported. This table shows a little worsening in MiDBD–II compared to the first phase of the experiment, though they are similar.

Fig 4.8 shows the power of the anticoincidence analysis, that permits descrimination of spurious pulses especially at low energy; the continuous line represents the total spectrum, whereas the dashed one represents the spectrum obtained with the anticoincidence analysis.

In tab 4.5 the energy resolutions and the pulse amplitudes normalized to 1 MeV of deposited energy are reported; these values were obtained during the last MiDBD-II run with the working detectors. It can be observed that the detector performance have big variations. In tab. 4.6 the total resolution obtained from the analysis of the background during these three years of MiDBD

| DET | A [$\mu$V/MeV] | FWHM @ 2615 KeV |
|---|---|---|
| F | 523 | 7.2 |
| O | 394 | 11.0 |
| 11 | 439 | 12.4 |
| 2 | 513 | 8.0 |
| 8 | 404 | 7.7 |
| E | 416 | 8.8 |
| 4 | 379 | 8.1 |
| B | 543 | 11.7 |
| 9 | 546 | 6.5 |
| 13 | 416 | 8.1 |
| F | 469 | 16.1 |
| 2 | 504 | 8.3 |

Table 4.5 - Resolutions and 1 MeV pulse amplitudes obtained during the last MiDBD–II measurement with natural crystals.

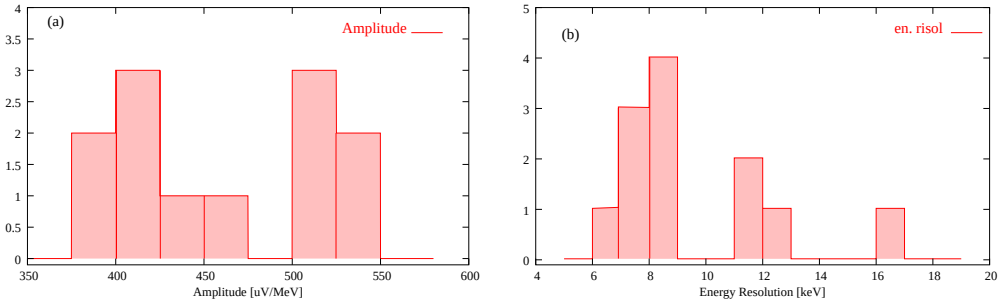


Figure 4.9 - Spread of the detector perfomance: (a) signal amplitude in $\mu$V/MeV, (b) energy resolution in keV.

running is summarized. The 20 detector statistics was collected in 8 different data runs. Fig. 4.9 reports the signal amplitude (a) and energy resolution (b) distributions of the MiDBD–II detectors.

The 20 detector spectra are summed together and it has been observed that the obtained resolution in the various runs are compatible. In tab. 4.7 we report the performance of the enriched crystal detectors and the mean values of the natural ones obtained with the second configuration. The table below shows that in the detector performance no big variations have been introduced after the array remounting.

As pointed out in sec 4.2, every first plane detectors of MiDBD tower had two sensors in order to achieve an improvement of the signal to noise ratio. Unfortunately the MiDBD–II resolution limit was due to common mode noise: in other words the dominant noise sources on the two thermistors were correlated, and so no improvements are achieved.

Yet results as far as the radioactive background is concerned are encouraging. In fig 4.10 the comparison between the old and new configuration of the MiDBD

| Energy [keV] | 511 | 911 | 1460 | 1764 | 2615 |
|---|---|---|---|---|---|
| OLD configuration | | | | | |
| run 1 11 days | - | - | 7.9 | - | - |
| run 2 28 days | 4.4 | - | 5.5 | - | 6.8 |
| run 3 20 days | 4.0 | - | 5.2 | - | 9 |
| run 4 35 days | - | 4.5 | 5.6 | - | 10 |
| run 5 20 days | 3.0 | 4.3 | 6.0 | - | 10 |
| run 6 34 days | 3.9 | 4.0 | 4.9 | - | 7.4 |
| run 7 44 days | 5.2 | 5.4 | 7.1 | 9.2 | 9.6 |
| NEW configuration | | | | | |
| run 8 32 days | 3.9 | - | 10.7 | - | - |
| sum 8 runs | 4.8 | 5.5 | 6.7 | 9.2 | 9.5 |

Table 4.6 - Partial and total resolution of the MiDBD experiment.

| DET | R [MΩ] | T [mK] | $\mu$V / MeV | $\tau_D$ [ms] | FWHM @ 2615 [keV] | FWHM F.O [keV] |
|---|---|---|---|---|---|---|
| 128-1 | 298 | 10.8 | 95 | 114 | 15.9 | 10.26 |
| 128-2 | 135 | 13.7 | 185 | 60 | 8.0 | 5.50 |
| 130-1 | 270 | 10.9 | 116 | 90 | 18.7 | 9.11 |
| 130-2 | 352 | 12.2 | 293 | 70 | 10.4 | 6.92 |
| Mean Naturals | 177 | 11.7 | 391 | 190 | 7.9 | 1.32 |

Table 4.7 - Thermal characteristics and performance of 4 enriched crystals. The mean values corresponding to natural crystals are reported.

experiment both in gamma and beta region is shown. The main result is the factor 2 reduction in the continuous background. Fig. 4.11 shows the background level in the $\alpha$ region: the continuous line represents MiDBD–I background and the dashed the MiDBD–II one. A strong reduction of the peaks is evident.

In the second run spectrum both peaks and continuum decreased of a factor 2 with respect to the first run. According to the results obtained from the background analysis and supported by the detector Monte Carlo simulation it is clear that these reduction factors, although similar, are due to two different effects. The peaks were due to sources outside the detector and consequently they were reduced putting an additional lead shield, whereas the continuum was mainly reduced through crystal and copper frame lapping and cleaning.
The introduction of the anti–neutron shield did not improve the radioactive background level; indeed the ratio between the continuous background before and after the introduction of this shield has been estimated of $1 \div 1.5$. However, thanks to this operation it was possible to clarify that neutrons were not the dominant cause of the background.

The two set–ups have been operated for an effective running times of 31508 and 5690 hours $\times$ kg, respectively. The sum spectra have been obtained both

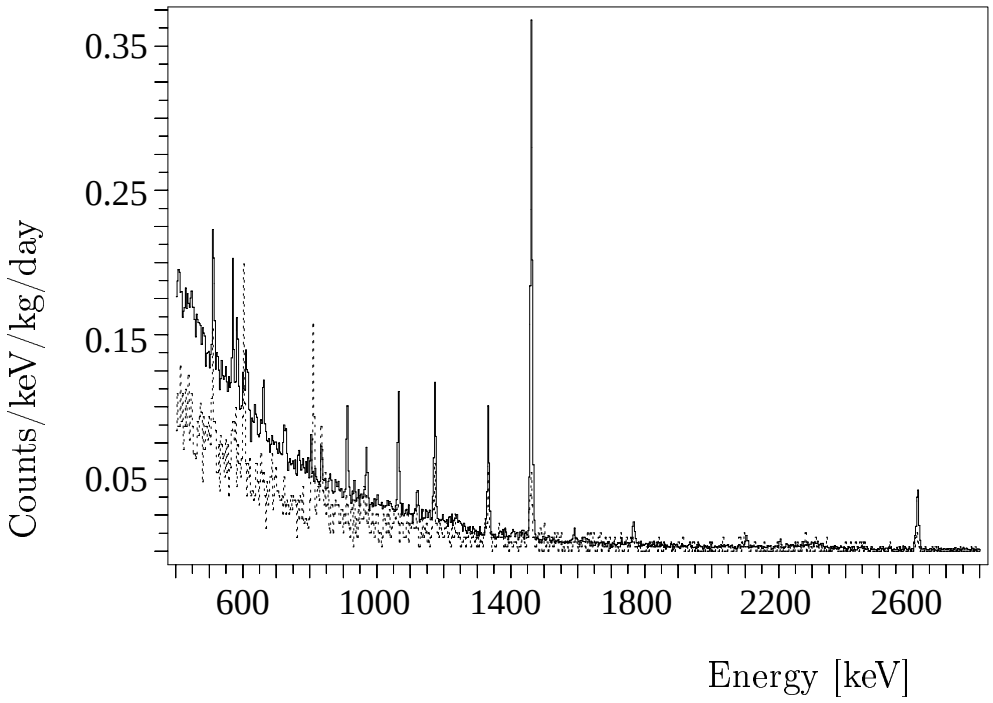


Figure 4.10 - The MiDBD experiment background level in the $\gamma$ and $\beta$ region.

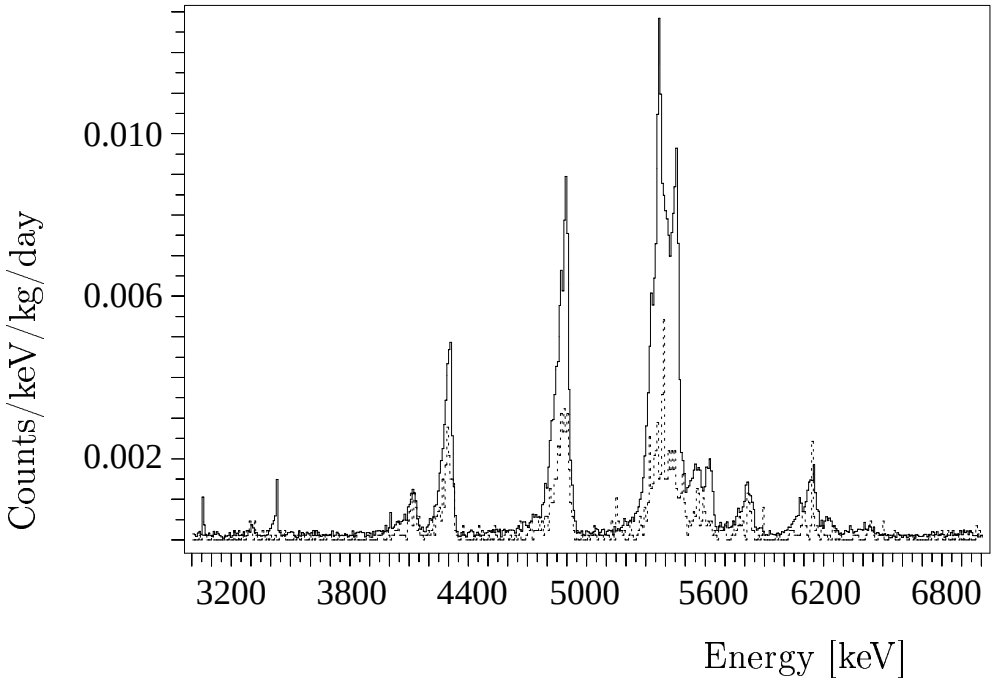


Figure 4.11 - The MiDBD experiment background level in the $\alpha$ region in the first (continuous line) and second (dashed line) configuration.

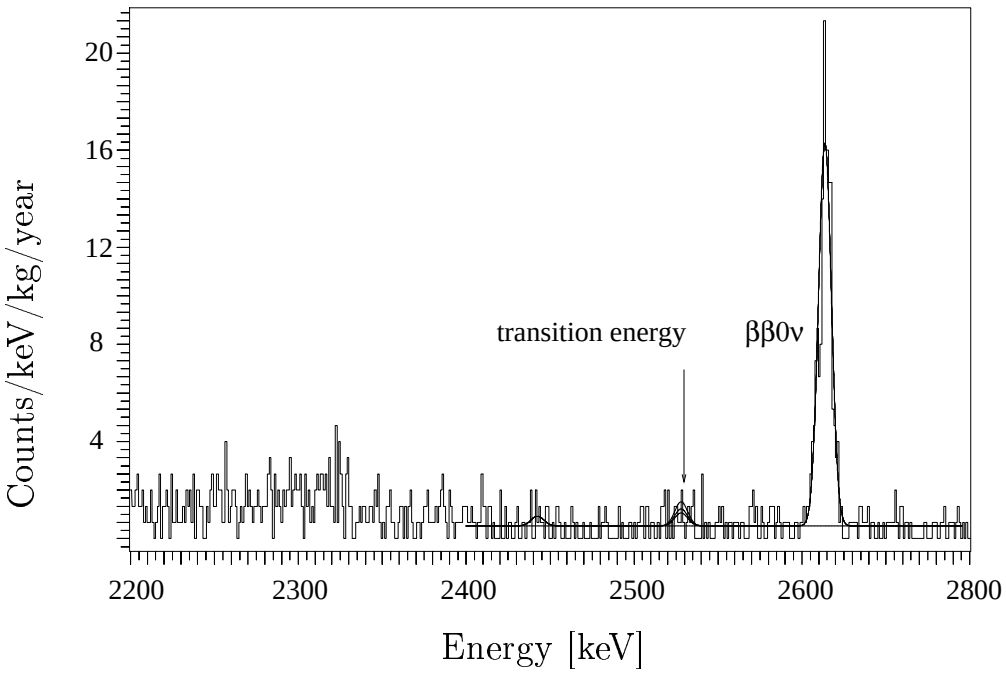


Figure 4.12 - Background spectrum in the $0\nu$DBD region obtained with the 20 $TeO_2$ detectors.

with no anticoincidence cut and making each detector operate in anticoincidence with the others. In all these spectra it is possible to observe the main lines due to the natural activity of $^{232}$Th and $^{238}$U chain, $^{40}$K and lines at 1173 and at 1332 keV due to cosmogenic $^{60}$Co.

In fig. 4.12 the background total spectrum in the $0\nu$DBD of $^{130}$Te region obtained in the 20 crystal detectors is shown.

This statistics corresponds to 1.57 kg $\times$ year. No peak appears in the region of neutrinoless DBD of $^{130}$Te, where the rates are, respectively, of $0.59 \pm 0.06$ and $0.33 \pm 0.11$ counts keV $^{-1}$ kg $^{-1}$ year $^{-1}$ for the former and latter run, when they operated in anticoincidence. No peak also appears at that energies corresponding to $0\nu$DBD of $^{130}$Te to excited levels of $^{130}$Xe, and at the energy of 867 keV corresponding to $0\nu$DBD of $^{128}$Te. Results about double beta decays are reported in tab. 4.6. Fit parameters and 90 % C.L. limits for the various decay processes were evaluated with a Maximum Likelihood procedure.

An evaluation of the rate for the lepton conserving process was attempted analyzing the difference between the sum of the two spectra as for crystal isotopically enriched in $^{130}$Te and the sum of those of crystals enriched in $^{128}$Te. (Fig. 4.13). These differences are positive in $2\nu$DBD region having an excess of $269 \pm 60$ counts corresponding to $T_{1/2} = (6.1 \pm 1.4\, stat.) \times 10^{20}$ years. However a precise evaluation of the half life is not straightforward because the background differs among four enriched crystals. In particular different rates were observed for the $^{40}$K 1460 keV gamma line and for alpha lines in the 4-6 MeV energy region.

Thanks to a Monte Carlo simulation reproducing the contributions of the

| Isotope | Transition | Cuts | $E_0$ (keV) | Efficiency (%) | $T_{1/2}$ (years) |
|---|---|---|---|---|---|
| $^{130}$Te | $0\nu : 0^+ \to 0^+$ | a.c. | 2528.8 | 84.5 | $> 2.1 \times 10^{23}$ |
| $^{130}$Te | $0\nu : 0^{+*} \to 0^+$ | none | 1992.8 | 7.9 | $> 3.1 \times 10^{22}$ |
| $^{130}$Te | $0\nu : 0^{+*} \to 2^+$ | none | 1992.8 | 37.5 | $> 1.4 \times 10^{23}$ |
| $^{130}$Te | $2\nu : 0^+ \to 0^+$ | a.c. | | | $(6.1 \pm 1.4^{+2.9}_{-3.5}) \times 10^{20}$ |
| $^{130}$Te | $1\chi : 0^+ \to 0^+$ | a.c. | | | $> 2.2 \times 10^{21}$ |
| $^{130}$Te | $2\chi : 0^+ \to 0^+$ | a.c. | | | $> 0.9 \times 10^{21}$ |
| $^{128}$Te | $0\nu : 0^+ \to 0^+$ | a.c. | 867.2 | 97.9 | $> 1.1 \times 10^{23}$ |

Table 4.8 - Half lifetime limits (90 % C.L.) on lepton violating and conserving channels deduced from the MiDBD data analysis. $E_0$ is the energy at which $T_{1/2}$ was obtained whereas *a.c.* represents anticoincidence among different detectors.

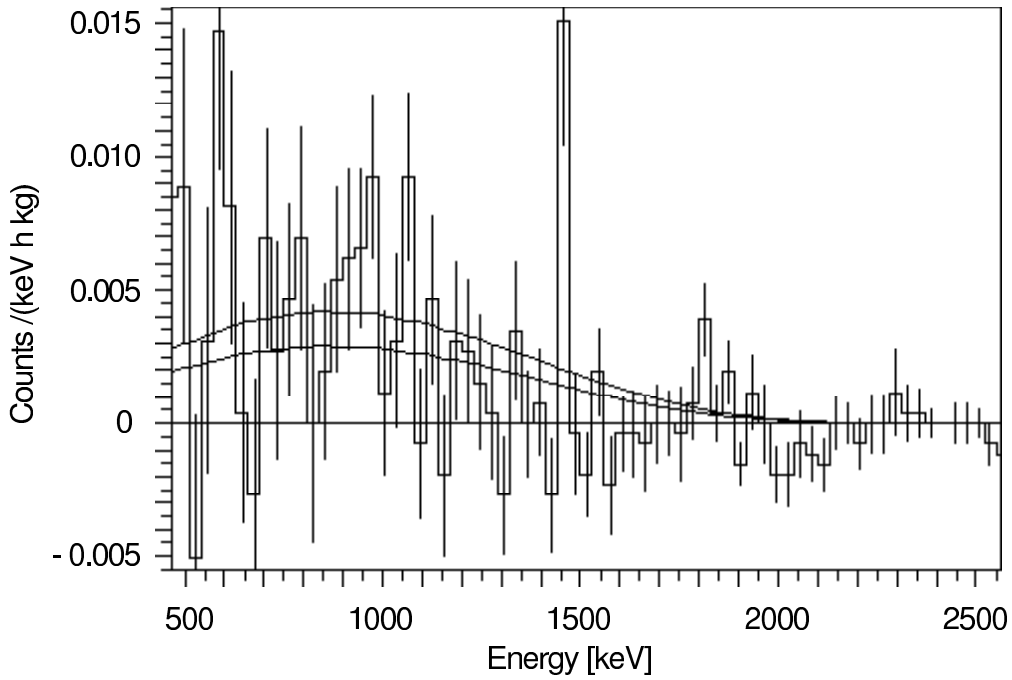


Figure 4.13 - Total difference spectrum between $^{130}$Te and $^{128}$Te detectors (no background subtraction). The solid curves represent the best fit (lowest curve) and the 90 % C.L. excluded signal.

probable background the possible sources causing these lines were determined. Probably the 1460 keV gamma peak was due to an accidental $^{40}$K contamination localized on the bottom surface of the detector copper holder (as suggested by a Monte Carlo simulation), whereas the alpha lines are clearly due to $^{238}$U and $^{232}$Th surface contamination of crystals. A similar - though lower - surface contamination was observed also for all natural crystals.

Taking into account different rates observed in the lines of the isotopically enriched detectors, the contribution to the $^{130}$Te - $^{128}$Te spectra produced by such contamination in the two neutrino DBD region is extrapolated. The expected maximum of the difference due to $^{238}$U and $^{232}$Th contamination is negative and corresponds to 380 counts, which should therefore be added to the actually found signal. On the other side the corresponding expected maximum of the difference due to background from $^{40}$K (86 counts) is positive and should therefore be subtracted. Slightly different values are obtained changing the contamination location. However in every case negative values are obtained for the $^{238}$U and $^{232}$Th contribution (responsible for the differences in alpha counting rates) and positive for the corresponding $^{40}$K ones. In conclusion, the difference in crystal background rates introduces a large systematic uncertainty in the half life evaluation.

Assuming the above quoted background rates as possible maximum contributions to the systematic error, the final result is $T_{1/2} = (6.1 \pm 1.4\, stat.^{+2.9}_{-3.5}\, sys.) \times 10^{20}$ years. This value, in agreement with most (but not all!) of the geochemical results, looks higher than most of those predicted theoretically [117]. The already running NEMO 3 experiment [118], as well as the improved search carried out through Cuoricino, will soon allow a deeper insight into the $^{130}$Te two neutrino DBD controversy.

Summarizing, during the second phase of the MiDBD experiment many modifications were introduced to study the radioactive background and to understand which are the main contributions.

The importance of the obtained results consists in the demonstration that the radioactive level measured in the previous runs was mainly due to the superficial U and Th contamination and not to bulk contamination that would be not easily removed. Anyway it is clear that much more work is needed to obtain an improvement of the background level. New configurations of a single module and of an array were studied for a larger experiment.

The solutions adopted as far as the vibrational noise is concerned got good results even if optimization work is needed, for example a different choice of copper strips. Modifications in the configuration where the crystal absorbers are held must be carried out, in order to improve the signal to noise ratio and the reproducibility of detector performance.

## 4.7 The future: Cuoricino.

Proposed as an intermediate step to demonstrate the feasibility of a large mass high sensitivity cryogenic experiment to search for rare events (CUORE), Cuoricino is now a true experiment.

The Cuoricino set-up has been already installed in Hall A at the Gran Sasso National Laboratories, in the same dilution refrigerator that housed the MiDBD array and it is taking data.

It consists of an array of 44 cubic crystals of 5 cm side and 18 of the already measured $3 \times 3 \times 6$ cm$^3$ of natural TeO2 crystals having a mass of 790 g and 330 g respectively. The total mass of $TeO_2$ in Cuoricino is 40.7 kg. Similar to MiDBD detector, the Cuoricino array has a tower-like structure too. The main advantage of such an array is that each plane of the tower can be considered as an elementary module and can be optimised and tested independently. Cuoricino array has 13 planes, 11 are 4-crystal modules identical to those presently planned for CUORE. Two additional planes are made by 9-crystal modules housing small crystals. The enriched crystals already tested in the MiDBD experiment are placed in the corners of one of the 9-crystal modules. In fig. 5.27 the opened Cuoricino tower is shown. In the next chapter a detailed discussion of the new experimental set-up is given and the construction of the Cuoricino single modules will be described.

# Chapter 5

# Cuoricino single module: structure and construction techniques

## 5.1 Introduction: R&D for the Cuoricino experiment

During the data taking of the MiDBD experiment, a set of systematic tests were performed in order to decide the Cuoricino structure.
These tests were carried out in a specific refrigerator placed in Hall C at LNGS. As remarked in sec. 4.1, the Hall C set–up sensitivity is lower than the one of hall A as far as the radioactive background is concerned. This can be observed in fig. 5.1 where a background spectrum of hall C (dashed line) is compared to one obtained in hall A (continuous line). In particular, the higher $\gamma$ background in Hall C causes problems in the study of the $0\nu$DBD region. Indeed this region is populated by counts due to energy–degraded events of the $^{208}$Tl gamma line at 2615 keV.
In sec. 3.9.2 and 4.6 it was already explained that at the left and at the right of the $^{208}$Tl peak the same reduction factor of the continuous background was achieved. This fact supports that it is possible to achieve indications regarding the radioactive background level obtainable in the Hall C refrigerator studying the energy spectra in the 3-4 MeV region. In other words, reductions of the energy–degraded alpha background could correspond to reductions in the continuous background level in the $0\nu$DBD region in the Hall A set–up. Certainly, no strong indications could be obtained for gamma and beta radioactivity background in the hall C set–up. Moreover the two set–ups are almost equivalent as far as the possibility to study the other detector performance, like energy resolutions and pulse parameters, is concerned.

The aims of these tests were:

- to study a cleaning procedure for reducing the surface contaminations of the crystals;

- to try new ways to couple the sensor and the energy absorber to obtain a more reproducible thermal connection between them;

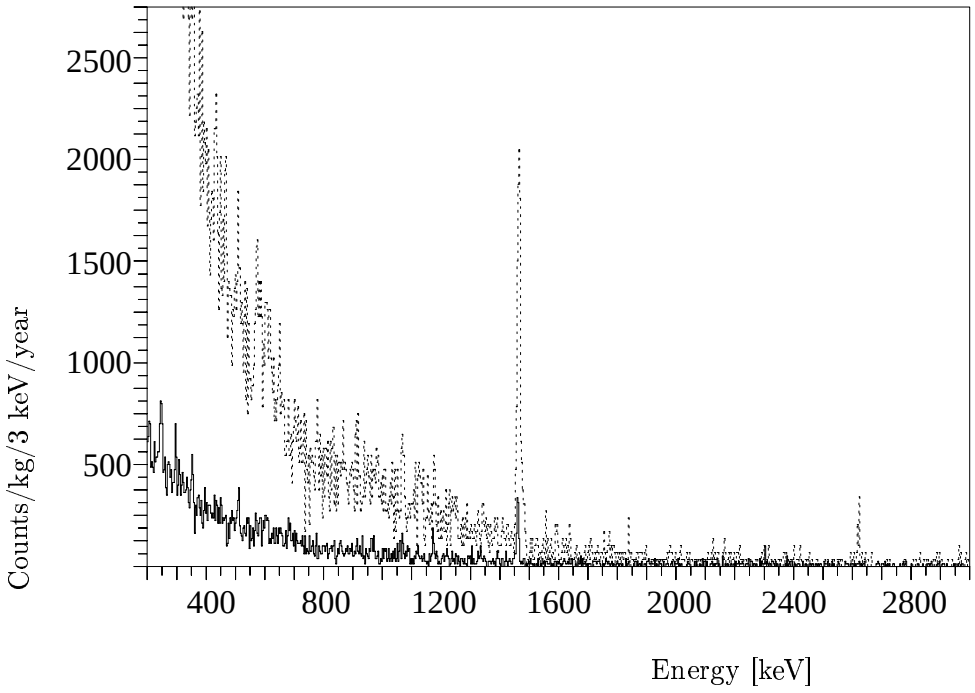


Figure 5.1 - Comparison between a background spectrum in hall A (continuous line) and a corresponding one in hall C (dashed line).

- to study a safer and more reproducible mechanical coupling system between the crystal and copper frame;
- to optimize the mechanical decoupling of the Cuoricino array from the refrigerator in order to obtain a reduction of vibrational noise.

In the next section, the R&D work to define the structure of the single module of the Cuoricino experiment is illustrated. The last section is dedicated to the description of the array construction and of the experimental set–up.

## 5.2 The treatment of the crystal surfaces

In the previous chapter the importance of using crystal absorbers with low radioactive contamination was stressed. Furthermore, thanks to Monte Carlo simulation and to the study of the MiDBD background spectral shape, it has been found out that the most probable source of radioactivity is due to copper and/or crystal surface contaminations.
The problem was faced in three ways:

- An operation that "easily" results in a reduction of the background level, involving the same quantity of active mass, consists in the use of a larger crystal absorber, so that the surface to weight ratio decreases. This is one of the main reasons why it was decided to use $5\times5\times5$ cm$^3$ size crystals for

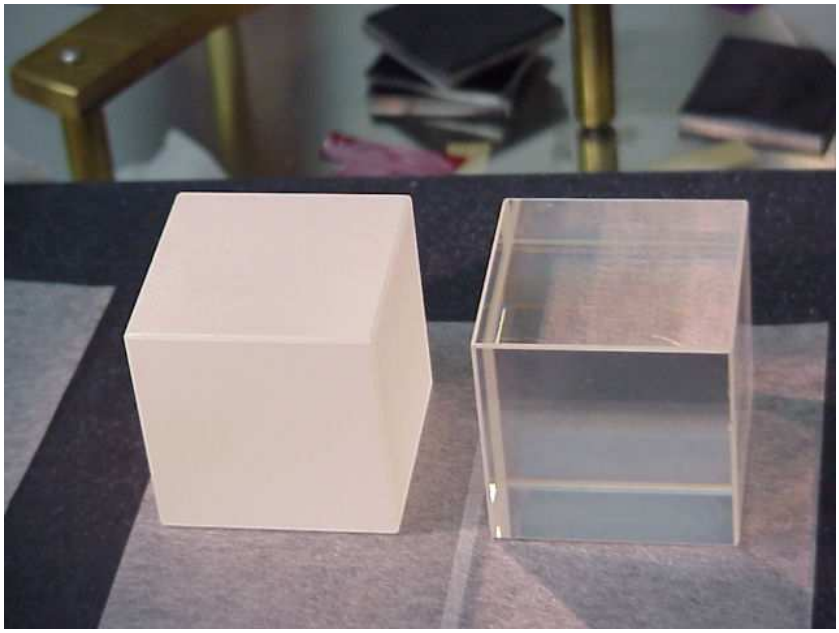

Figure 5.2 - Comparison among crystals polished with radiopure powder (right) provided by the Cuoricino collaboration and crystals polished following the usual SICCAS procedure (left).

the Cuoricino experiment. This crystal size is the maximum one produced by the Shanghai Institute of Ceramics (SICCAS) and it is compatible with our experimental set–up.

- To reduce the problem of contamination it was required that the polishing procedure, performed by SICCAS , should be done only with 11 $\mu$m size radiopure Sumitomo powder delivered and previously tested by the Cuoricino collaboration. The nominal grain size of this powder is 7 $\mu$m, but a specific measurement performed at SICCAS showed that the actual average grain diameter is 11 $\mu$m. Because this powder is not as fine as that used by SICCAS in the last polishing step and has a broad distribution of grain size, crystals are not transparent and has big scratches on the surface. In fig. 5.2 crystals treated by SICCAS with radiopure (right) and standard (left) powders are shown.

  In November 2000, four crystals treated with the radiopure powder arrived at LNGS. They were immediately tested in order to investigate their radioactive background level and their signal shapes. Unfortunately only two among these four detectors worked properly. Probably this partial failure was caused by the poor quality of glue spots. Results as for the working detectors are reported in tab. 5.1. Using limits on the $^{232}$Th $< 0.006$ c/kg/h $^{238}$U $< 0.006$ c/kg/h, the obtained values of crystal bulk contamination are

$$^{232}\mathrm{Th} < 3 \cdot 10^{-12}\ \mathrm{g/g} \quad ^{238}\mathrm{U} < 1 \cdot 10^{-13}\ \mathrm{g/g} \tag{5.1}$$

| | integral 3-4 MeV c/keV/h | integral 4-5 MeV c/keV/h | integral 5-6 MeV c/keV/h | integral 6-10 MeV c/keV/h |
|---|---|---|---|---|
| B38 | $(3\pm2)\cdot10^{-5}$ | $(24\pm4)\cdot10^{-5}$ | $(1820\pm35)\cdot10^{-5}$ | $(2.2\pm0.6)\cdot10^{-5}$ |
| B40 | $(2\pm1)\cdot10^{-5}$ | $(4\pm2)\cdot10^{-5}$ | $(180\pm10)\cdot10^{-5}$ | $(0.2\pm0.1)\cdot10^{-5}$ |

Table 5.1 - Calculated integral for two 5×5×5 $cm^3$ crystals B38 and B40, lapped in China with large grain powder (11 $\mu$m).

These limits are in agreement with the previous results obtained with 340 g crystals.

- Different tests have been performed to find a good procedure for cleaning crystal surfaces. In these tests a big problem has to be taken into consideration: the final quality of the treated surface. This characteristic indeed could influence the coupling between the energy absorber and sensor and consequently the detector performance and its pulse parameters. In addition, it is often speculated that the surface quality could play a crucial role in the mechanism of pulse formation, due to its influence on the phonon spectrum evolution. In the next subsection the various tests performed are described.

### 5.2.1 Tests to determine a final cleaning procedure

Here the description of the tests that lead to the formulation of the final cleaning procedure is reported.

- For the MiDBD experiment, the Milano group tested a **chemical etching procedure** for removing nearly 10$\mu$m of $TeO_2$ from the crystals. These crystals were immersed into a 1 molar solution of ultra–pure nitric acid for 30 seconds. The surfaces of the two tested crystals looked milky and rough. Their pulses had long rise and decay time constants. For example, the decay time increases of about a factor 3÷4. Furthermore, the signal amplitude changed too, decreasing of nearly 30%. In fig 5.3 the comparison among pulses obtained in crystals before and after the etching procedure, are reported. This effect can be attributed to the modification of the absorber–sensor coupling due to the different roughness of the surface, but other explanations are possible, invoking the role of surfaces in the pulse formation mechanism. As reported in sec. 4.3, the cleaning procedure executed in MiDBD experiment uses radiopure powders in order to remove by friction the superficial $TeO_2$ material.

- In **August 2001** a dedicated run was carried out to test the effects of the cleaning procedure used in the MiDBD on the 5×5×5 $cm^3$ absorbers. This run was mainly a "thermal" test whose aim was to study pulse properties. For this reason, four of the old 5×5×5 crystals provided by SICCAS

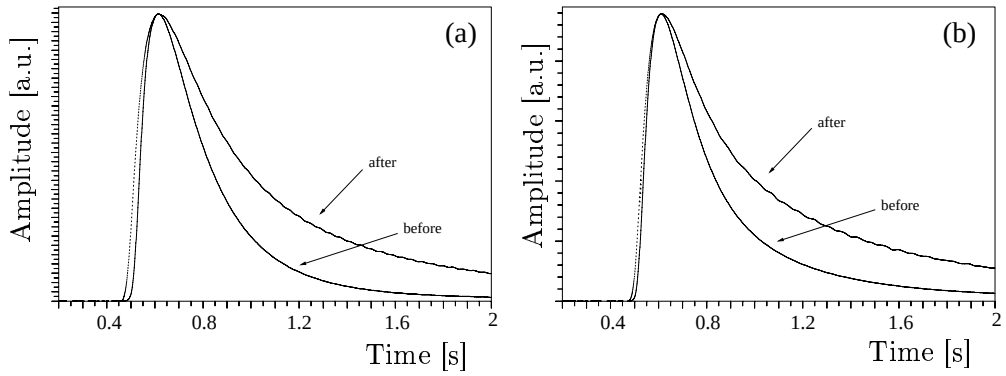


Figure 5.3 - Mean pulses obtained in the same crystal before and after the etching procedure.

| | sensor | $R(T_{work})$ [MΩ] | $t_{rise}$ 10-90% [ms] | $t_{dec}$ 90-10% [ms] | $t_{dec}$ 90-30% [ms] | $T_{work}$ [mK] | Ampl. [μV/MeV] | FWHM @2615 [keV] |
|---|---|---|---|---|---|---|---|---|
| B1 | L | 117 | 71 | 390 | 320 | 8.9 | 220 | 4.5 |
| B2 | S | 88 | 88 | 410 | 340 | 8.7 | 107 | 24 |
| B4 | S | 43 | 86 | 1120 | 790 | 9.2 | 73 | 9 |
| B5 | L | 99 | 105 | 1190 | 860 | 9.5 | 85 | 9 |

Table 5.2 - Summary of detector performance obtained during the August data taking.

were used, even though they were produced with no care about possible radioactive contamination and though they had optical surfaces. Three of these crystals were cleaned through the procedure explained in sec. 4.3 whereas the last one, named B1, was used as a reference, so its optical surfaces were not treated at all. The fragility of these crystals showed up immediately: indeed during the cleaning operation substantial internal cracks were produced.
The obtained results are summarized in tab. 5.2. In this table performance of the four detectors are reported.
The sensors on these detectors were attached with 12 glue spots. The "L" type sensors have $3\times3\times1$ mm$^3$ size whereas the "S" ones are $4\times3\times1.5$.

The comparison among detector decay times points out that the cleaning procedure produces slower pulses. It has to be underlined that, in all these measurements, the detector having B1 crystal as an energy abosrber achieved the best performance even if it worked in different conditions. The reasons why the B1 results are so good are not understood yet.
The comparison among sample pulses of the various detectors is shown in fig 5.4.
Because the polishing procedure tested in this run was very slow and requires a substantial manpower it is not conceivable to apply it like it is to at all crystals of CUORE. For this reason, the Berkeley group tested a new procedure for speeding up this crystal cleaning phase.

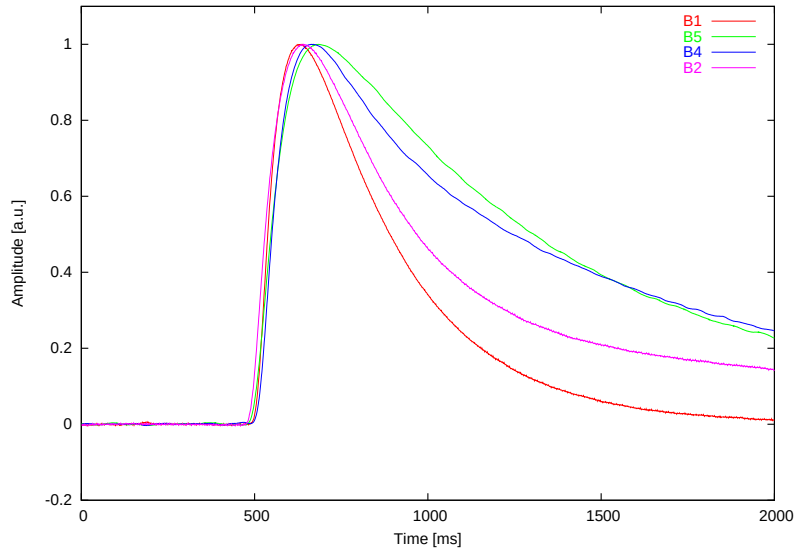


Figure 5.4 - Comparison among pulses measured in August 2001. B2, B4 and B5 crystal have been cleaned through the procedure described in sec. 4.3.

- In **November 2001** a new test for the lapping procedure developed by the Berkeley group was performed. During the first operation the already mention 11 $\mu$m Sumitomo allumina powder with Buehler nylon cloth was used to remove the main part of the material, whereas the final polishing step was achieved using the Sumitomo 0.7 $\mu$m silica powder and NaOH.
  It was decided to perform the crystal surface treatment at the Insubria University (Como). For this reason, the crystals were stored in a low radioactivity laboratory situated under the Baradello hill. This laboratory is not far from the Insubria University and the rock cover provides about 300 m.w.e against cosmic rays. The cleaning operations were carried out in a clean room (class 1000) built at this university just for that occasion. Each batch of crystals was brought from the Baradello laboratory to University where they underwent the cleaning procedure.
  Unfortunately, this polishing did not give the planned results. One of the main causes of this issue was that crystals were sent from Shanghai in a different condition from that supposed. They were supposed to have been polished with 11 $\mu$m size Sumitomo alumina powder, which should have produced a scratch–free surface. Instead of that the surfaces were covered with 50 $\div$ 100 $\mu$m deep scratches that were straight, curved, squiggled (see fig. 5.5). The following analysis, as already pointed out, showed that the average size of Sumitomo powder particles provided by Cuoricino collaboration for SICCAS have a mean size of 11.6 $\mu$m and that there were also larger particles up to 50 $\mu$m. The big spread in the powder size was probably the source of deep scratches, joined with the use of a hard glass lapping pad in Shanghai. The consequences of this situation were:

  – plans for the crystal polishing had to be modified. Furthermore some

| | detail | sensor | $R(T_{work})$ [MΩ] | $t_{rise}$ 10-90% [ms] | $t_{dec}$ 10-10% [ms] | $t_{dec}$ 90-30% [ms] | Ampl. [μV/MeV] | FWHM @2615 [keV] |
|---|---|---|---|---|---|---|---|---|
| B19 | perfect | L | 37 | 73 | 1230 | 660 | 64 | 7 |
| B20 | crack | S | 126 | 58 | 870 | 320 | 118 | 9 |
| B21 | big crack | S | 22 | 62 | 620 | 220 | 35 | 9 |
| B22 | big crack | L | 107 | 73 | 1770 | 870 | 140 | 10 |

Table 5.3 - Summary of detector performance obtained in November during tests using Berkeley cleaning procedure. Resistances are measured at the working point. In the second column the presence of cracks in crystals is reported.

crystals seemed to be well polished in an hour, while others took up to three hours before getting a reasonable surface;

- several big cracks appeared inside the crystals. The fig. 5.6 shows a crystal after the polishing procedure, representing an example of the deep fractures. There are indications that, at least in some cases, the cracks appear in correspondence with a large surficial scratch.

Certainly, the biggest problem was the latter. Its cause is not completely clear yet. Perhaps thermal shocks due to the temperature difference between the underground laboratory and clean room, contributed to the crystal breakage. However, it was decided to test in Hall C four cleaned crystals in order to understand:

- the effects on the pulse shape due to the above procedure; in fact using NaOH, the surface role could change;
- the effects on radioactive levels;
- the effects on pulses due to the internal cracks; indeed there is the possibility that the broken crystal works as a composite structure implying worse energy resolution or even double peaks in the energy spectra.

B19, B20, B21 and B22 lapped crystals were tested. Each detector has an "L" type sensor attached with 9 glue spots. The fig. 5.7 shows the tested crystal module. The obtained results are presented in tab. 5.3

As it can be noted, detectors worked well, and the presence of breakage does not seem to have influenced energy resolution. It seems that the pulses of this run present a longer decay time constants. In fig. 5.8 the obtained pulses are compared. As for radioactivity levels, the results obtained were comparable with the previous measurements.

- In order to solve the problem of crystal fractures (come out in November), it was useful to ask SICCAS for some help. Thanks to their and our experience a new procedure was developed; it can be divided into three steps:

  1. the first step is the removal of deep surface scratches using 10 μm Chinese alumina powder for 3 minutes on hard surfaces and 5 on soft

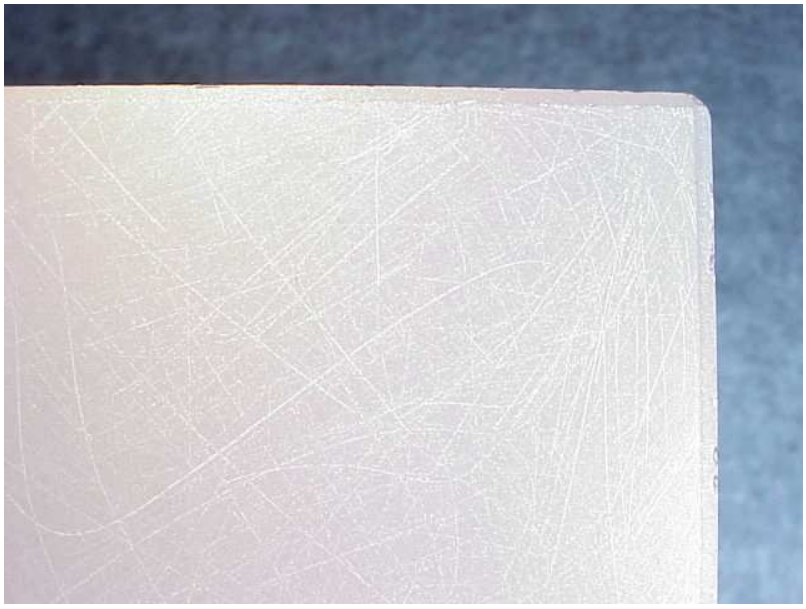

Figure 5.5 - Detail of a $TeO_2$ crystal received from China. It is possible to see the deep scratches on the surface.

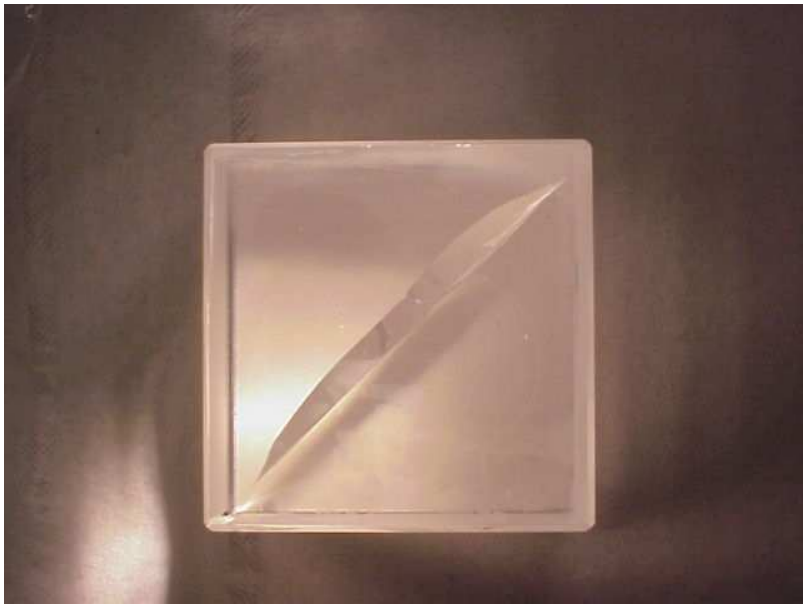

Figure 5.6 - Picture of a polished crystal. It is possible to see the big internal fracture.

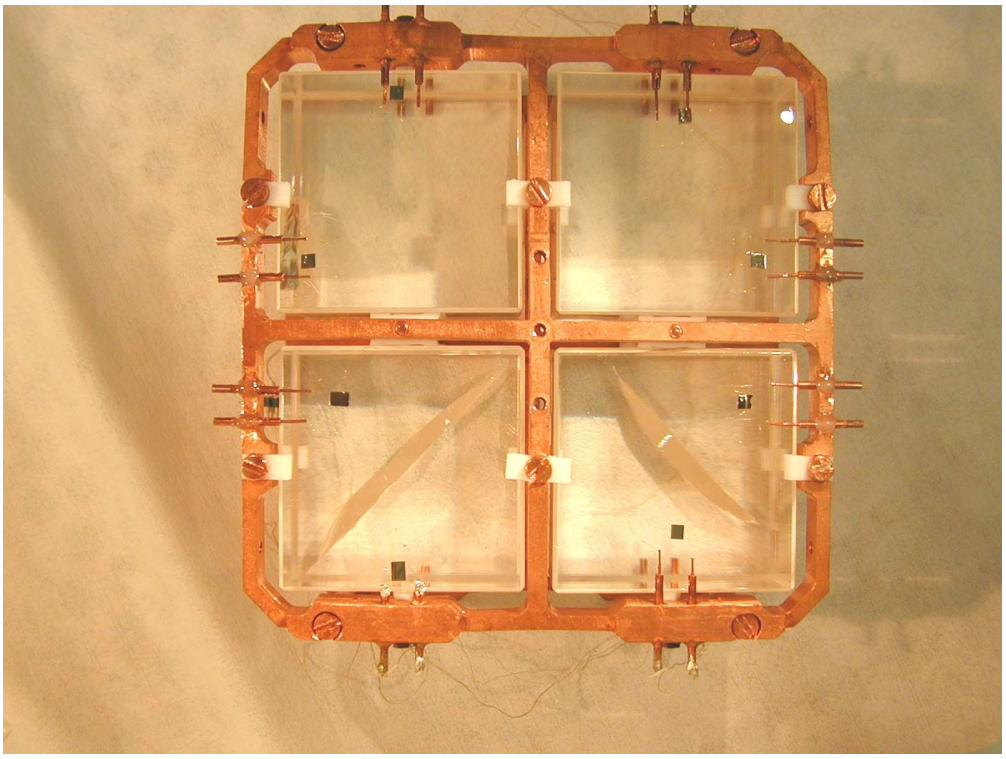

Figure 5.7 - Picture of the four crystal module tested in November 2001 in Hall C. All the crystals have been used to test the Berkeley polishing procedure.

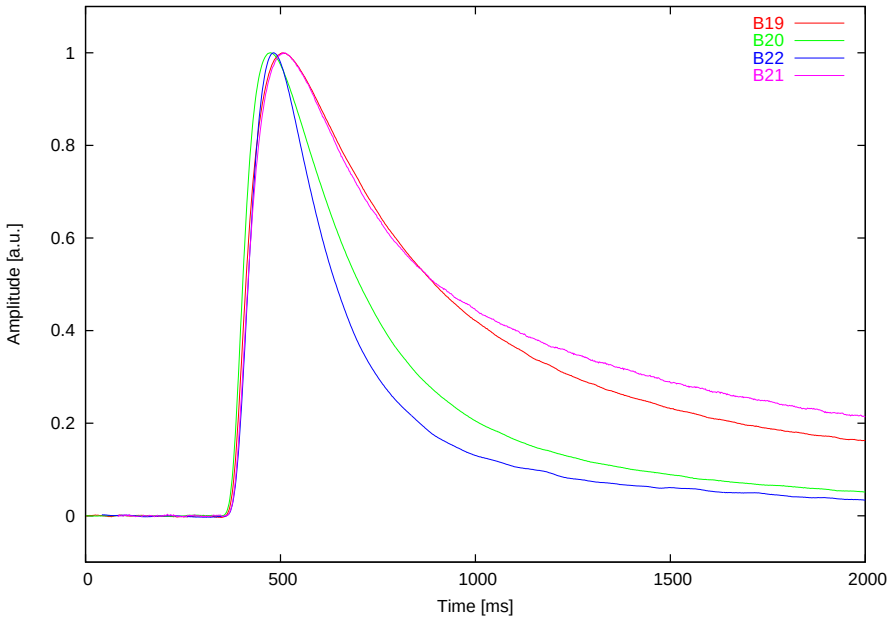


Figure 5.8 - Comparison among pulses measured in November 2001.

| | sensor | $T_{base}$ [mK] | $T_{work}$ [mK] | $R(T_{work})$ [MΩ] | $t_{rise}$ 10-90% [ms] | $t_{dec}$ 90-10% [ms] | $t_{dec}$ 90-30% [ms] | Ampl. [$\mu$V/MeV] |
|---|---|---|---|---|---|---|---|---|
| B8 | L | 8.9 | 10.1 | 44 | 59 | 830 | 290 | 130 |
| B8 | L | 9.1 | 10.2 | 20 | 57 | 930 | 250 | 65 |
| B21 | L | 8.4 | 9.3 | 84 | 69 | 830 | 300 | 130 |
| B11 | L | 8.6 | 9.5 | 100 | 65 | 870 | 430 | 140 |
| B11 | S | 9 | 10.1 | 61 | 76 | 960 | 570 | 175 |

Table 5.4 - Summary of the detector performance obtained during the test of December on the cleaning procedure. Resistances reported are measured at the working point. In the second column the presence of cracks in the crystals is reported.

ones. For this operation a glass disk is used. The thickness of the material removed in this way ranges between 50 and 130 $\mu$m for each face. The powder used is contaminated with U and Th, so the only aim of this step is to obtain workable crystals for the next operation;

2. this second step represents the real cleaning procedure, whose aim is the removal of surface contamination, including the one possibly introduced during the previous step. This goal was achieved using for 5-8 minutes the usual 11 $\mu$m radiopure Sumitomo alumina powder, depending on the surface hardness. In this step, initially an ULTRA–PAD (Buehler) cloth is used. ULTRA–PAD is a hard woven aggressive cloth pad for rough grinding, which allows a quick removal of substantial amount of material. For the final polishing step a soft LAM 450 (Lamplan) cloth is used for few minutes in order to achieve a better quality of the surface. The use of these pads, based on a plastic texture, does not produce the big scratches that appeared when the same powder was coupled to the hard glass pad. The amount of material removed in this operation is 30-35 $\mu$m;
3. the third and last step is the lapping of crystal edges for 30 seconds with 11 $\mu$m radiopure Sumitomo alumina powder. This operation does not produce appreciable variations in the weight of crystals since very little material is removed from crystal edges.

In **December 2001** in Como, 2 crystals, named B8 and B11, underwent the previous cleaning procedure. After this treatment they did not become transparent. Therefore, a question came out: could the quality of the surfaces influence the pulse shape and the performance of the detectors? This question is particularly relevant at this point, since the procedure described above could be adopted for all the CUORICINO crystals. To clarify this point, the two crystals B8 and B11 were tested with crystal B21, used as a reference, in hall C of LNGS. The results obtained are summarized in tab. 5.4.

As for the energy resolution, the FWHM of every detector is nearly 10-15 keV at the $^{210}$Po line. The comparison among signal shapes demonstrates that signals are not influenced by the lack of polishing. The signals obtained with detectors with the same type of thermistor in this test are

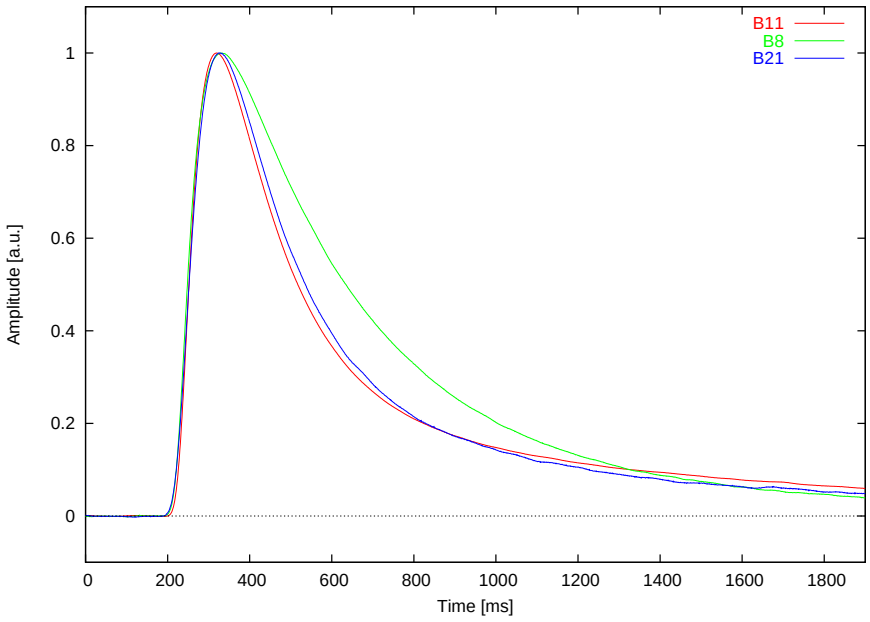


Figure 5.9 - Comparison among pulses measured in December 2001.

| | 3-4 MeV [c/keV/hour] $\times 10^{-5}$ | 4-5 MeV [c/keV/hour] $\times 10^{-5}$ |
|---|---|---|
| B8 | 2±1 (3) | 9.5±2.5 (15) |
| B21 | 5±2 (8) | 6.5±2 (10) |
| B11 | 5±2 (8) | 7.5±2 (12) |

Table 5.5 - Counting rate in an energy region between 3 and 5 MeV obtained through measurements performed in December 2001 using crystals lapped in Como after the suggestion of SICCAS people. In the brackets, integral counts are reported.

compared in fig 5.9.
As far as the radioactivity level is concerned, results, referred to the interesting energy region, are reported in tab. 5.5.

The Cuoricino collaboration was afraid that step 1 of the procedure, described above, could introduce not easily removable contamination, but as it can be noted in tab. 5.5 this did not happen.

It was decided to use the cleaning procedure tested in December for all the Cuoricino crystals. Step 1 was performed (on the 5×5×5 $cm^3$ crystals) by SICCAS's expert technicians in Como. On the other hand 3x3x6 $cm^3$ crystals did not undergo the first step as their surfaces did not present deep scratches. The last two steps were accomplished in Como for 5×5×5 $cm^3$ crystals, whereas 3×3×6 $cm^3$ ones were treated at LNGS. The detailed procedure executed by the Cuoricino collaboration in order to clean both smaller and bigger crystals is described in tab. 5.6. We report this table to stress that the polishing procedure is rather cumbersome and surely not applicable as it is to a larger scale experiment. Furthermore, at LNGS this cleaning procedure was executed in an

| | OPERATIONS |
|---|---|
| ULTRA-PAD | Weigh the crystal<br>Mark faces with an arrow–shaped piece of tape (to be moved if necessary)<br>Change the cloth every two crystals<br>Lap faces with Sumitomo 7 $\mu$m alumina powder, ULTRA–PAD cloth and white polisher<br>2 min. for soft face - 3 min. for hard face (new cloth)<br>3 min. for soft face - 5 min. for hard face (cloth already used for one crystal)<br>Hard faces are identified via lapping<br>Goal: remove 30-40 $\mu$m per face: weigh the crystal after each face is lapped<br>Lap edges: 30 sec. for each edge<br>Time required per crystal: 75 min. |
| LAM 450 | Weigh the crystal<br>Lap faces with Sumitomo 7 $\mu$m alumina powder, LAM 450 cloth and yellow polisher<br>Change the cloth for every crystal<br>3 min. per soft face - 5 min. per hard face<br>Goal: get reasonably smooth surfaces<br>Mark a hard face with an araldit in a corner<br>Time required per crystal: 75 min. |
| Assistance | Write in the run book<br>Help washing the crystals before and after lapping<br>Prepare lapping water and keep it at the right temperature<br>Prepare the powder–water mixture (the ratio is not critical: save powder!)<br>Help putting the mixture on the wheel during lapping<br>Prepare arrow–shaped pieces of tape and araldit to mark hard faces<br>Measure crystal dimensions with a caliber<br>Help packing the crystals (optical paper + kim wipes + plastic bag)<br>Help putting the crystals in the pot - Trips to the cave<br>General cleaning |

Table 5.6 - Final lapping procedure carried out by the Cuoricino collaboration for the detector crystals. Three operators are always involved during this procedure. The first one works on the lapping machine that uses the ULTRA–PAD cloth, the second one minds the polishing machine that uses the LAM 450 cloth and the third one assists them. The different operations every person has to do are reported in the second column.

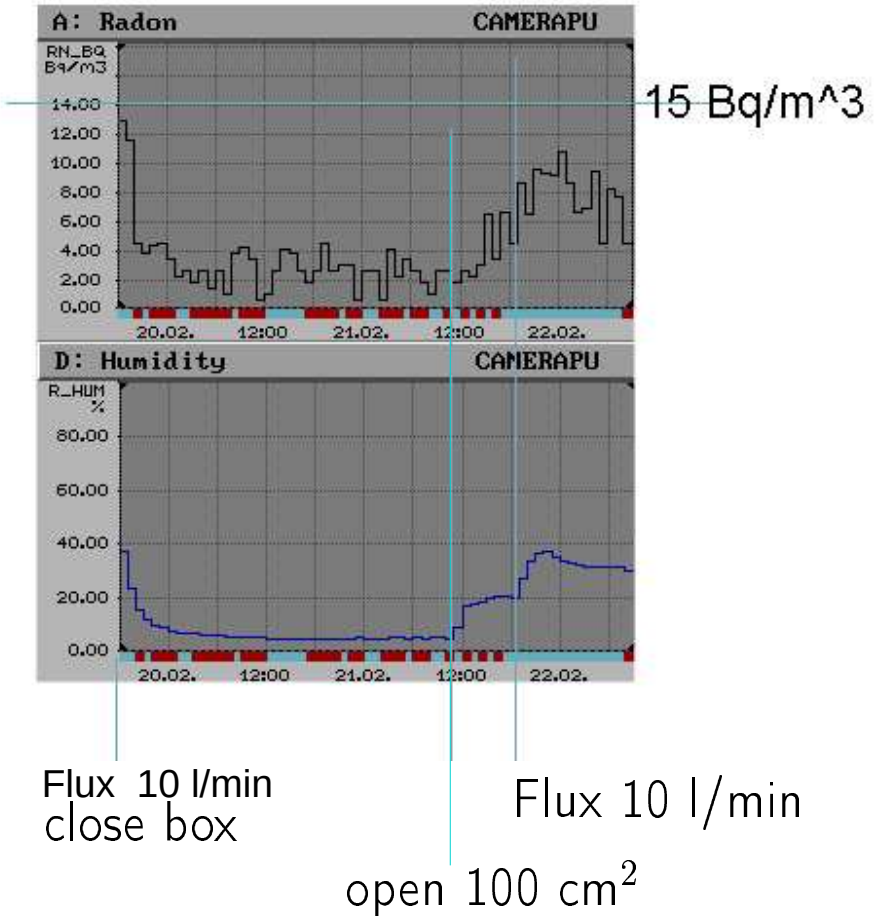


Figure 5.10 - Measurement of the radon and humidity performed into the anti-radon box.

anti–radon box where a saturated atmosphere of pure nitrogen is maintained. A picture of the anti–radon box is shown in fig. 5.11. In fig. 5.10 we report the measurements of the radioactivity due to radon and of the humidity performed into the anti–radon box at different conditions of nitrogen fluxed in the box. It is evident that when the ports for the operator's hands are open the radioactivity increases.

## 5.3 The coupling between NTD–Ge thermistors and $TeO_2$ crystals

As mentioned in the previous chapter, in MiDBD $3\times1.5\times0.4$ mm$^3$ size NTD–Ge thermistors were used as sensors. To improve electron–phonon coupling and then the signal amplitude, it was decided to use larger thermistor size. The larger sensor size allowed on increase in the number of glue spots. The next chapter will describe the expected effects of increasing both the sensor size and the glue spot number.

Figure 5.11 - Picture of the anti-radon box placed in the white room of Hall A at LNGS. The silicon tubes flux pure nitrogen in the chamber.

As shown in sec. 4.6, the quality of the coupling between the thermistor and absorber is an important source of spread in the detector performance. Furthermore, in the previous section, it was pointed out that, because of thermal stresses and probable bad qualities of crystal surfaces, it is possible that sensors came off crystals, as happened in the November 2000 test. For these reasons, many efforts were devoted to develop a reliable and reproducible procedure for attaching the sensor to the crystal.

It has been already explained that joining a thermistor to the crystal with an homogeneous layer of glue could cause problems due to differential thermal contractions. In the R&D phase of the Cuoricino experiment, two different approaches were tested:

- the use of special NTD–Ge thermistors with pedestals (standoff) and legs in order to reduce the surface that touches the crystals. This reduction will allow the use of a glue veil on the interface in spite of the big difference among the thermal contraction coefficients of glues and crystalline solids;
- the variation of the number of glue spots between sensor and crystal in order to obtain an optimal configuration;
- the study of a more reproducible procedure for gluing thermistor to crystals.

During runs performed in **August 2001** in Hall C, three detectors were tested with two thermistors each; the first one was attached using 12 standard glue

| | Sensor coupl. | $R(T_{work})$ [MΩ] | Amplit. [$\mu$V/MeV] | $t_{rise}$ 10-90% [ms] | $t_{dec}$ 90-10% [ms] | $t_{dec}$ 90-30% [ms] | stand./glue ampl. ratio |
|---|---|---|---|---|---|---|---|
| B1 | 12 | 117 | 220 | 71 | 390 | 330 | 0.24 |
| B1 | standoff | 92 | 53 | 85 | 690 | 430 | |
| B2 | 12 | 88 | 107 | 88 | 410 | 340 | 0.19 |
| B2 | standoff | 55 | 20 | 90 | 1650 | 1130 | |
| B4 | 12 | 43 | 73 | 86 | 1120 | 790 | 0.53 |
| B4 | standoff | 53 | 39 | 71 | 990 | 580 | |

Table 5.7 - Results obtained in August using 3 crystals with two thermistors each. These thermistors are coupled to the crystal using either 12 glue spots ("12" in the second column) or a small pure Ge crystal ("standoff" in the second column).

| | Sensor coupl. | $R(T_{work})$ [MΩ] | Amplit. $\mu$V/MeV | $t_{rise}$ 10-90% [ms] | $t_{dec}$ 90-10% [ms] | $t_{dec}$ 90-30% [ms] | leg/glue ampl. ratio |
|---|---|---|---|---|---|---|---|
| B19 | 9 | 37 | 64 | 73 | 1230 | 660 | 0.42 |
| B19 | table–leg | 35 | 27 | 82 | 1190 | 1000 | |
| B20 | 9 | 126 | 118 | 57 | 870 | 320 | 0.52 |
| B20 | table–leg | 58 | 61 | 74 | 1400 | 470 | |

Table 5.8 - Results obtained in November using 2 crystals with two thermistors each. The thermistors are coupled to the crystal using either 9 glue spots ("9" in the second column) or thermistors cut in such a way to replace the small Ge–crystal used in tests of August ("table–leg" in the second column).

spots whereas the second one by interposing a small standoff of pure Ge, glued to the crystal and to the thermistor with two very thin Araldit films. The standoff had a surface of $1\times1$ mm$^2$ and it was 75 $\mu$m thick. In tab. 5.7 the results obtained through the two thermistor configurations are reported. It must be underlined that the $TeO_2$ crystals were lapped in a different way. Yet, because on each crystal two thermistors were glued, the comparison between signal amplitude and decay time constant obtained with thermistors on the same crystal, is an indication of the goodness of the used approach. From the table above, it can be seen that the standoff–signal amplitude was systematically lower than the 12–spot–signals, this means that bigger contact surfaces are needed. In fig. 5.12 the comparison between the standoff–signal and the 12–spots–signal arrived in coincidence on the B1 crystal is reported as an example. In this case the amplitude of stand-off signal is 1/4 of the 12–spot–signal one, however the signal shape is not very different.

After these results, in **November 2001**, a new technique to couple the sensor to the absorber was studied. The thermistors were micro–machined in such a way that it was not necessary to glue the standoff. This new thermistors are named "table–leg sensors". Only 2 detectors with 2 thermistors each were tested. One of the two thermistors was glued as usual using 9 Araldit glue spots and the second one was the "table–leg thermistor". In tab. 5.8 the results of the test are summarized. Also in this run the amplitude of the table–leg signals were smaller than the 9–spot signals by a factor of 2. In fig. 5.13 the comparison be-

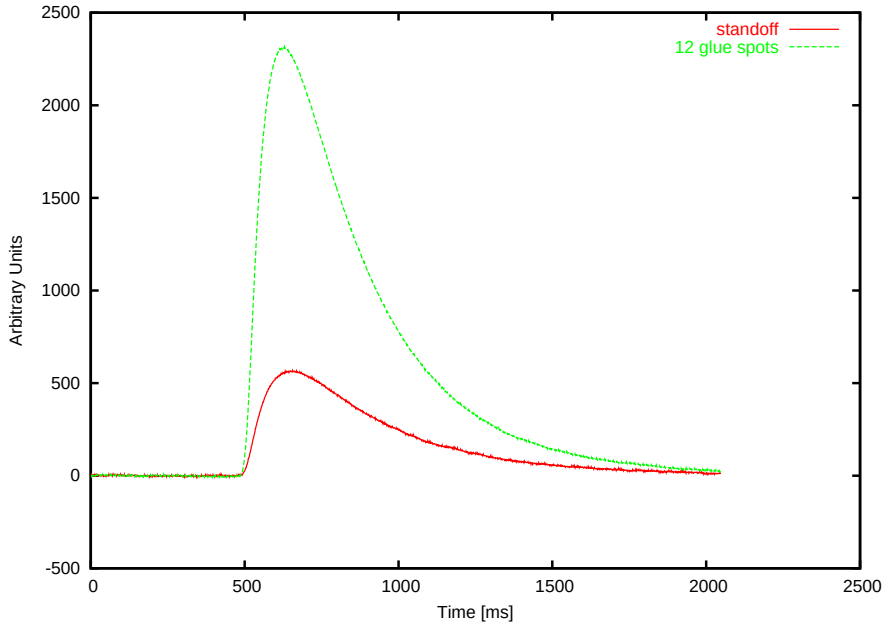


Figure 5.12 - Comparison between the standoff–signal and 12–spots–signal obtained with B1 crystal detector.

tween the signal obtained with a thermistor coupled as usual and one obtained with a table–leg sensor on the crystal B20, is shown. It can be noted that the difference between amplitudes persists but has been reduced. A still open problem concerns the decay time. Equal decay times are expected for thermistors on the same detector; indeed according to a naive approach it should be equal to detector heat capacity (C) and conductance to the bath (G) ratio (C/G). It is clear that the standoff and table–leg sensors need optimization work.

As shown in the previous paragraph, the study of new types of sensor–absorber coupling was developed simultaneously with the study of the effects of increasing the number of glue spots. Moreover in tab. 5.7 and 5.8 it can be noted that the glue spots approach gives better results, at least now, with respect to the standoff and table–leg method.
It must be remarked that it is not easy to make comparisons among different test runs. The main reason is that experimental conditions usually change from run to run. For example, the spurious noise, which is due to the cryogenic set–up and is often unstable and different from run to run, could cause an increase of temperature in the detector holder and consequently a loss of detector sensitivity. It is therefore convenient to compare detector performance obtained in the same run. Furthermore, the detector performance are often influenced by the coupling of the crystal to the bath. For example, if the crystal is not well fixed to the copper frame, it could be more sensitive to the vibrational noise and it could give bad performance. For this reason the most significant test on the sensor coupling is performed by gluing two thermistors on the same energy absorber.

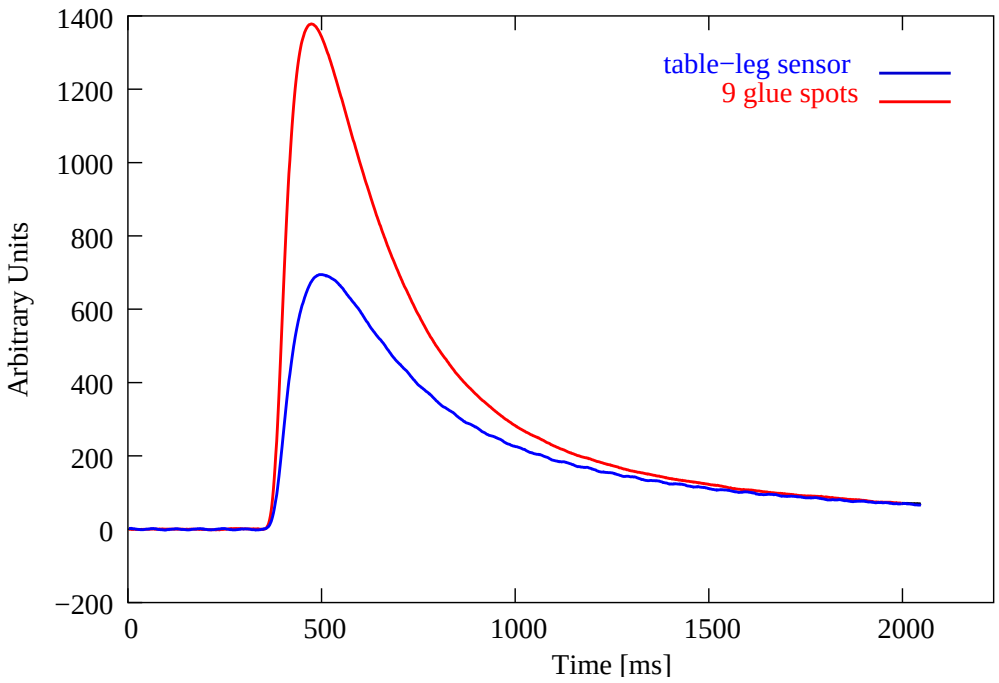


Figure 5.13 - Comparison between the table–leg signal and 9–spots signal obtained with the B20 crystal detector.

However, since the experimental set–up does not permit to test many read–out channels and also because each experimental run takes a long time, comparisons among detectors in different runs are taken into account but assigning to them a lower degree of reliability.

In tab. 5.9 the results obtained in different runs involving the study of sensors and their coupling to the absorber are summarized. Each box corresponds to a single run. In the third column sensor sizes are reported and in the fourth column the number of glue spots can be found.

As shown in tab. 5.9, in November two different numbers of glue spots were tested on the same crystal absorber. The results obtained are not very clear yet, as they give contradictory indications; probably this is due to the quality of glue spots. The gluing operation, indeed, is not easy and many differences could be introduced in the coupling. For this reason it was decided to realize the sensor–absorber coupling of the Cuoricino detectors using 9 glue spots instead of 12. A higher sensor–absorber conductance could improve the signal amplitude, but it is easier to achieve more reproducible couplings by restricting the glue spot number, since the 9 glue spots are made using a single 9–pin–tool, while the 12 glue spots are obtained by using twice the same 6–pin–tool in shifted positions. The repeated application of the same tool introduces problems in gluing duration (the resin life, once the two components are mixed, is a few minutes) and in the calibration of the amount of glue deposited on the pins. A 12–pin–tool, at least with the technique used at the moment, is unpractical because of the dif-

| Run 2001 | Crystal | sensor type | spots number | $R(T_{work})$ [MΩ] | $t_{rise}$ 10-90%[ms] | $t_{dec}$ 90-10%[ms] | $t_{dec}$ 90-30%[ms] | Amplitude [$\mu$V/MeV] | en. resol. [keV] |
|---|---|---|---|---|---|---|---|---|---|
| 7 | B8 | L | 6 | 41 | 100 | 1020 | 490 | 24 | 28 |
| (Jun.) | B11 | S | 12 | 121 | 112 | 1490 | 840 | 54 | 15 |
| | B14 | S | 9 | 30 | 109 | 1310 | 600 | 72 | 10 |
| | B9 | L | 9 | 49 | 112 | 1130 | 590 | 97 | 24 |
| | B37 | L | 12 | 48 | 64 | 1520 | 700 | 27 | 20 |
| | B40 | L | 12 | 91 | 86 | 1060 | 490 | 119 | 14 |
| | B39 | L | 6 | 55 | 65 | 830 | 750 | 41 | 18 |
| | B38 | L | 12 | 43 | - | - | - | 68 | 13 |
| 8 | B1 | L | 12 | 117 | 71 | 390 | 320 | 220 | |
| (Aug.) | B2 | S | 12 | 88 | 88 | 410 | 340 | 107 | 29 |
| | B4 | S | 12 | 43 | 86 | 1120 | 790 | 73 | 50(pulser) |
| | B5 | L | 12 | 99 | 105 | 1190 | 860 | 85 | 8 |
| 9 | B19 | L | 9 | 37 | 73 | 1230 | 660 | 64 | 5 |
| (Nov.) | B20 | L | 9 | 126 | 57 | 870 | 320 | 118 | 6 |
| | B21 | L | 9 | 22 | 73 | 1770 | 870 | 35 | 8 |
| | | L | 12 | 42 | 68 | 1840 | 700 | 61 | 5 (1764) |
| | B22 | L | 9 | 107 | 62 | 620 | 220 | 140 | 15 |
| | | L | 12 | 75 | 67 | 860 | 280 | 107 | 7.7 (1764) |
| 10 | B8 | L | 12 | 44 | 65 | 870 | 430 | 130 | - |
| (Dec.) | | S | 12 | 20 | 75 | 960 | 570 | 65 | - |
| | B11 | L | 12 | 61 | 58 | 830 | 290 | 170 | - |
| | B21 | L | 12 | 84 | 68 | 830 | 300 | 140 | - |

Table 5.9 - Results obtained in different runs performed to test sensors and in particular their coupling to the energy absorber. Here only the coupling realized by using glue spots is taken into account. In the first column the month when the test was made is obtained.

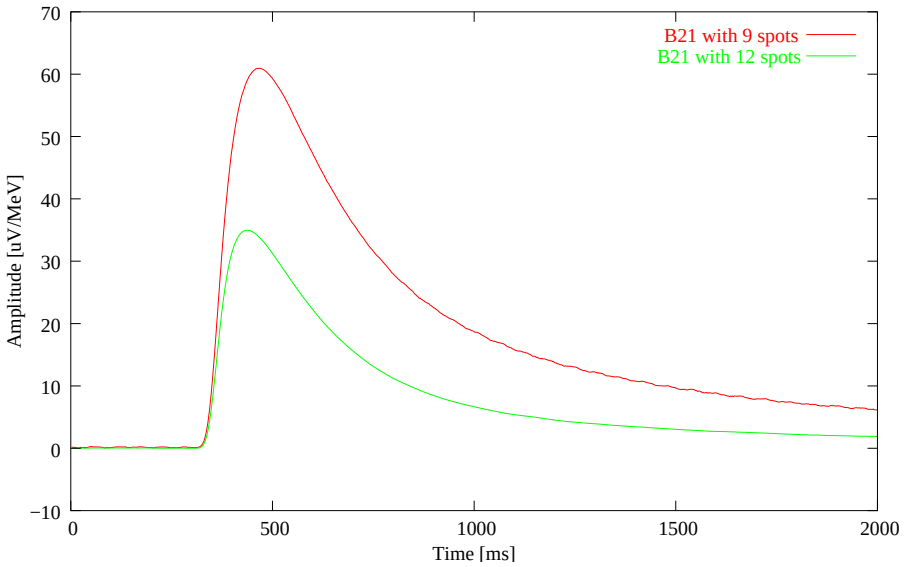


Figure 5.14 - Comparison of the 9–spot–signal and 12–spot–signal shapes obtained with the same absorber (B21).

ficulty to set the pins at the same level and to machine their tips with the same curvature. In fig. 5.14, 5.15 and 5.16 the signal shapes obtained with sensors glued with different glue spot numbers on the same crystal, are compared.

In run 8 and 10 different sensor sizes were tested; also in this case, a not clear result was achieved. The most probable cause could be again the glue spot quality. However it was decided to use the L thermistor size: as will be explained in chap. 7, an increase of the sensor volume implies an increase of the electron–lattice sensor coupling, and a resulting increase of the signal amplitude. This is true however only if the sensor size does not increase too much, otherwise the heat capacity of the sensor limits the thermal pulse. In fig. 5.18 and 5.17 the signal shapes obtained on the same crystal with sensors with different sizes are compared.

To obtain more reproducible and faster gluing operations, a new gluing method was developed in Como. Let's first describe the old one. As reported in sec. 3.4, in the MiDBD experiment and in the test runs, the following operations are carried out in order to glue the sensor on the crystal surface:

- a mylar mask is placed on the crystal area where the sensor should be attached. The mask has a horseshoe–like shape and it is 50 $\mu$m thick;

- using pins displaced in a matrix-like configuration, it is possible to obtain the desired number of glue spots on the crystal surface; these spots are placed in the middle of the mask, so that they are surrounded by the mylar;

- the sensor, picked up by a small vacuum tube, is directed upon the glue spots in such a way that the thermistor edges could touch the mylar mask.

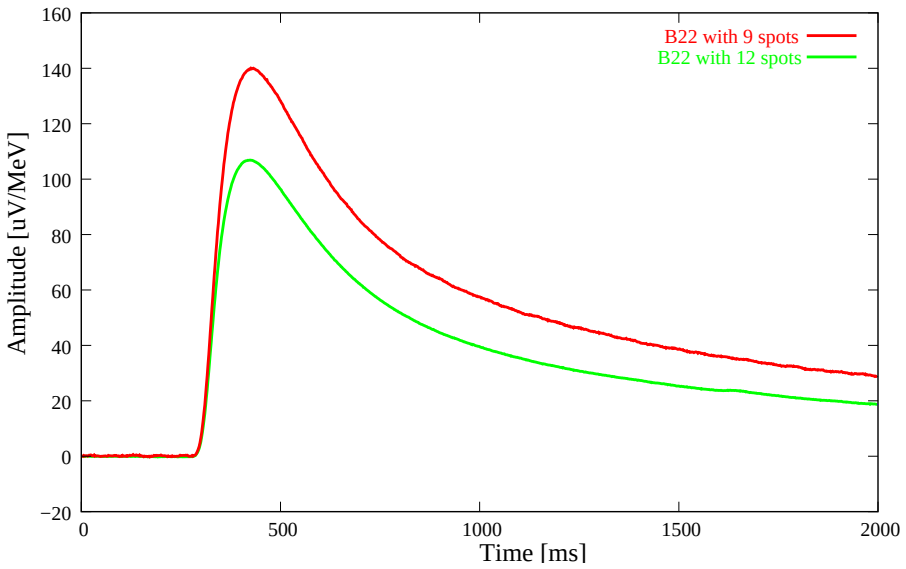


Figure 5.15 - Comparison of the 9–spot–signal and 12–spot–signal shapes obtained with the same absorber (B22).

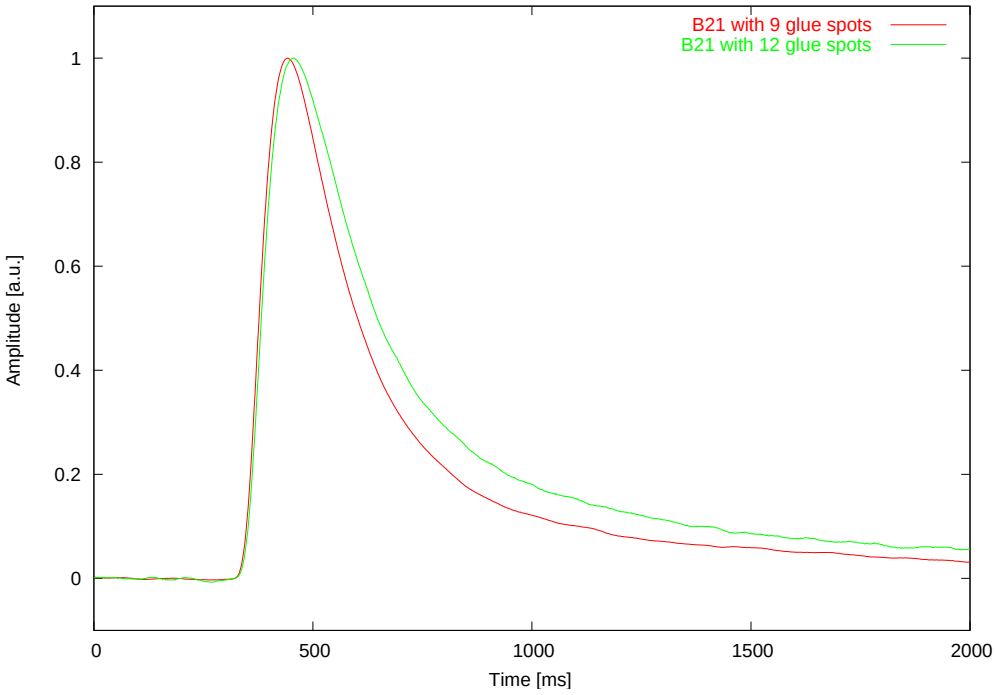


Figure 5.16 - Comparison of the 9–spot–signal and 12–spot–signal shapes obtained with the same absorber (B21). The pulses have been normalized.

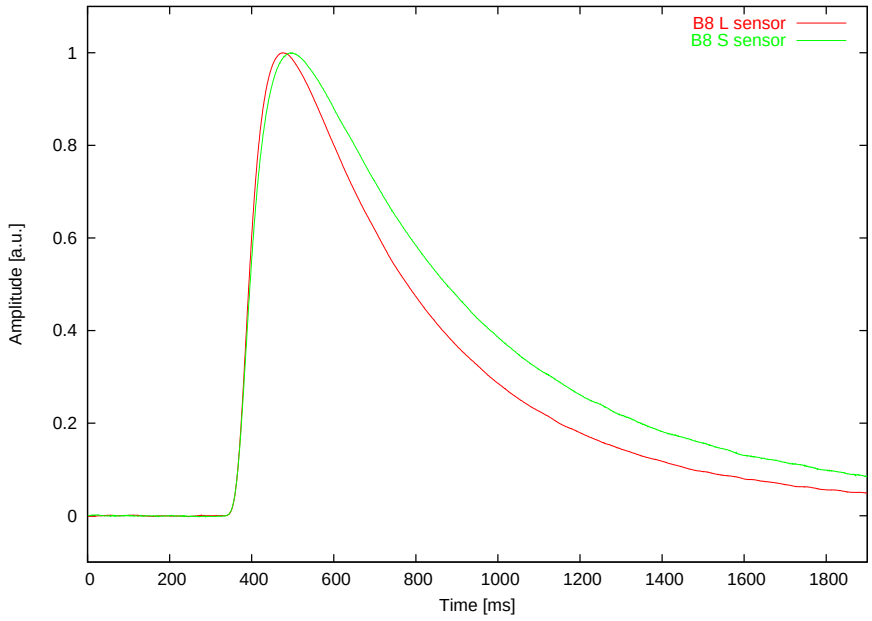


Figure 5.17 - Comparison of the signals obtained with L–type and S–type thermistors on the crystal B8. The pulses have been normalized.

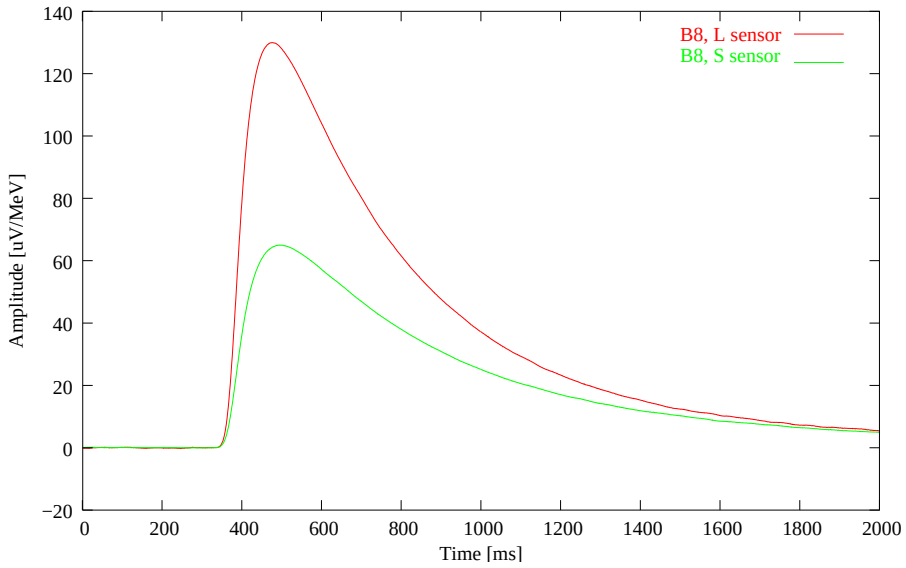


Figure 5.18 - Comparison of the signals obtained with L–type and S–type thermistors on the crystal B8.

In this way the glue spots, left after the removal of the mask, are 50 $\mu$m high. The sensor can be positioned using a micro–manipulator.

It is necessary to do all these operations very quickly because the properties of Araldit epoxy deteriorate in about 3 minutes. Not only the preparation of these operations is very long but also the last step is particularly delicate: sometimes, the procedure has to be repeated many times because of some failure in the spot formation or in the sensor positioning. In fig. 5.19 a picture taken during the gluing operation performed with the old method is shown.
The main idea concerning the new gluing method is to deposit glue spots on the sensor instead of putting them on the crystal. Indeed the positioning of the sensor on the glue spots, placed on the crystal, is difficult. Moreover a new tool was designed to avoid the use of the mylar mask; in fact the removal of the mask often causes the sensor gold wires breakage. A picture of this gluing tool is shown in fig. 5.20. The fig. 5.20 (a) shows the main component of the gluing tool, where the sensor is placed. To permit sharp and fast operations, the thermistor is put in an indentation that fixes the sensor position, and is held through vacuum. A detail of the indentation is shown in 5.20 (b). In this method too, glue spots are obtained using a set of pins. The central part of the main component can move up and down; it is possible to fix this part using a positioning–tool so that the sensor upper surface is 50 $\mu$m under the external ring of the gluing tool. By producing glue spots on the sensor and resting the crystal on the external ring it is possible to obtain glue spots 50 $\mu$m high. Fig.5.21 shows the scheme reproducing the gluing tool way of working. Pins are placed in the tool shown in fig.5.20 (c). These pin-tool works like a cap: it is bound in such a way that when it falls down the pins are able to touch the sensor in the right position.

The gluing procedure is divided in different steps:

- to position the sensor on the indentation in the central part of the gluing tool paying attention that also the sensor gold wires are into the indentations made for them;
- to put the sensor in the correct position, i.e. at 50 $\mu$m under the external ring hight, using the specific positioning–tool;
- glue spots are produced on the sensor using the "cap" shown in fig. 5.20 (b);
- the $TeO_2$ crystal is rested on the gluing tool, in particular the crystal bottom touches the external ring of the gluing tool.

An example of the 9 glue spots obtained with this method is shown in fig. 5.22, here spots are seen through a transparent crystal.

This new method has been used for all the Cuoricino $5\times5\times5$ cm$^3$ bolometers, whereas the old one has been used to glue sensors on $3\times3\times6$ cm$^3$ crystals. These two gluing operations are performed in the anti–radon box placed in the clean room of hall A at LNGS. Unfortunately gluing operations were more difficult than thought because crystals were not transparent in consequence of their cleaning procedure. For this reason it was impossible to assess the quality of glue spots by looking at them through the crystal. It was necessary to redo again

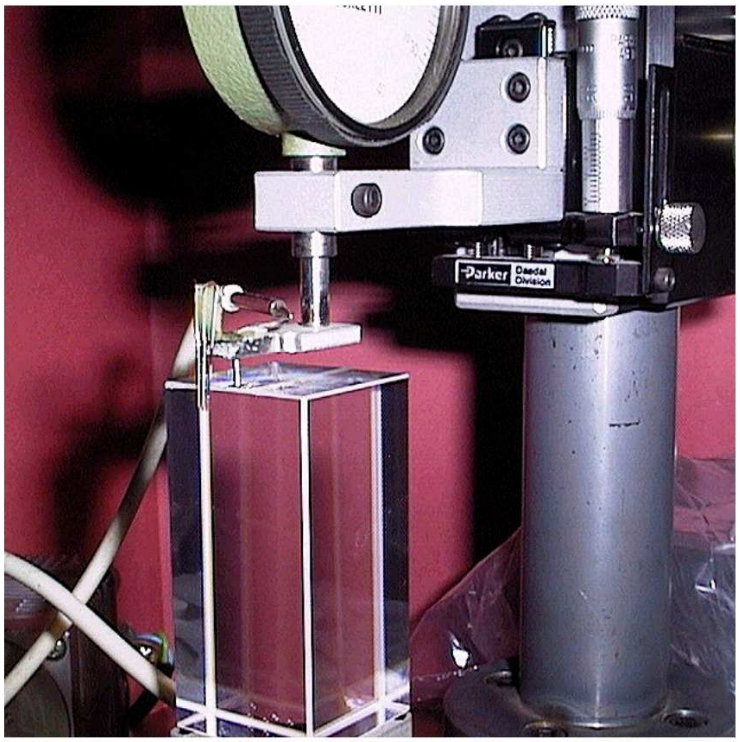


Figure 5.19 - The tool used in the MiDBD experiment to attach the sensor to the energy absorber with glue spots.

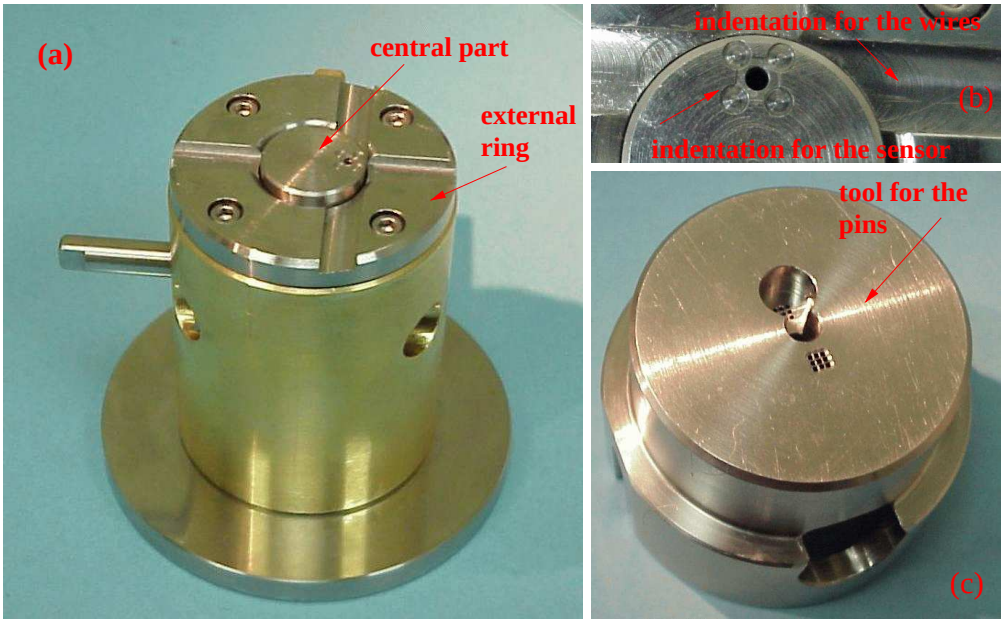


Figure 5.20 - The tool produced in Como to obtain fast and reproducible sensor–absorber coupling. In fig. (a) the main component of the gluing tool is represented, in fig. (b) a detail of the gluing tool upper side is shown. It is possible to see the indentation for the sensor and the one for its gold wires. In fig. (c) the “tip”, where the pins are held, is shown.

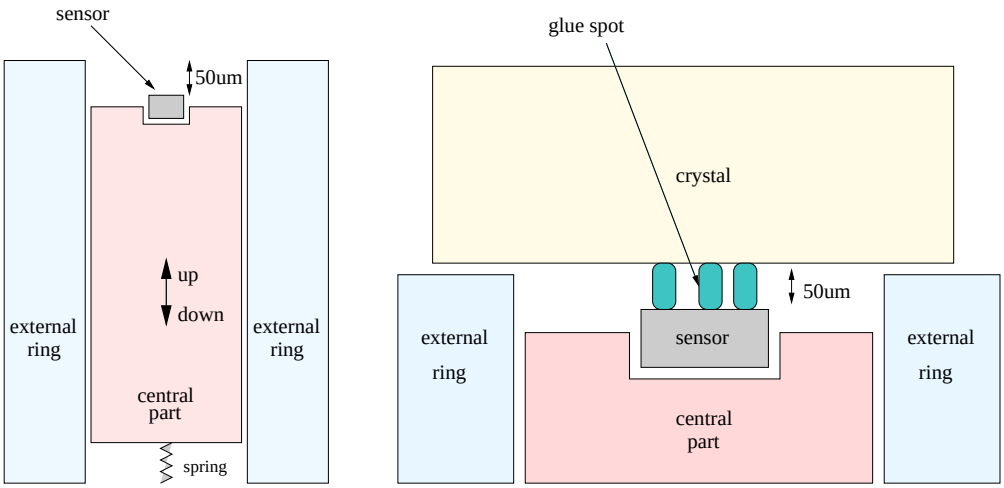


Figure 5.21 - Schematic drawing of the way the gluing tool works.

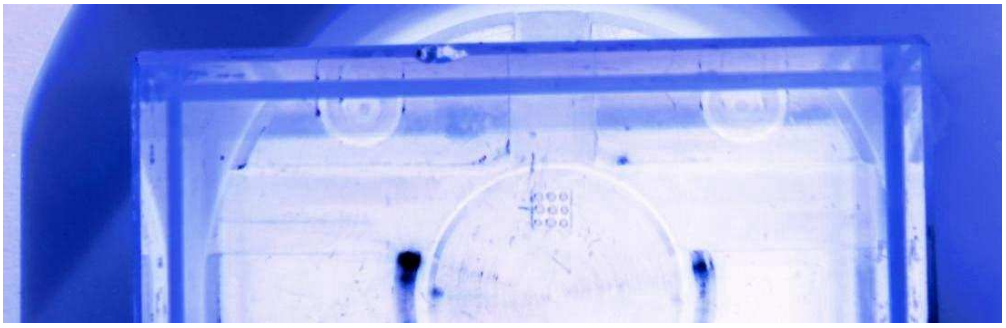

Figure 5.22 - Example of glue spots obtained with the new method developed in Como. Glue spots are visible through the crystal.

some sensor–absorber coupling because some glue spots were characterized by dark blobs. These blobs were probably due to a reaction between the glue and the humidity in the anti–radon box, humidity that has been produced by the ultrasound bath used to clean the pins after each gluing operation.

## 5.4 The coupling between the crystals and the heat sink

As pointed out in sec. 4.4 during the first run of MiDBD it was impossible to measure detector signals because of the high vibrational noise. For this reason the anti–vibrational method detailed in sec. 4.4 was introduced. In order to clarify the causes of this effect, different tests have been performed in hall C at LNGS. In particular it was not clear if this problem was due to the modification of the mechanical coupling between the crystal and the copper frame.

- First of all two modules, using Teflon pieces to hold the crystal, were tested without the spring. Because these modules were tested during the previous run, a comparison between results recorded with and without the anti–vibrational system was made. Results obtained without the spring showed that the vibrational noise on the detector was so high that it was impossible to perform measurements.

- During the second test (in May 2001) two other modules were measured in hall C. The aim of these measurements was to study the possibility that the vibrational noise on the crystal depended on the holding system used. For this reason the first module was composed by 4 5×5×5 $cm^3$ crystals held by the MiDBD–II–style Teflon pieces, whereas the second one was composed by 4 5×5×5 $cm^3$ crystals held with the Teflon masks (a picture of crystals held with teflon mask is reported in fig. 5.23). This run was performed again without the spring. In this case too, the noise was too high on both modules.

- To complete the tests to solve this problem, in June 2001 the same array was measured with the anti–vibrational system. Results have been already presented in tab. 5.9. They show that the vibrational problem is mainly an intrinsic feature of the detector module that contains more than one crystal. Therefore the main source of this noise does not depend on the Teflon holding system.

The design of the PTFE pieces is a source of irreproducibility of the MiDBD–II as remarked in sec. 4.6. In fact their thermal contractions work in opposite directions of their elastic contractions. For this reason detectors could be more sensitive to the vibrational noise, since crystals could get loose at low temperatures.
In September 2002 a new design of the PTFE pieces has been developed. In fig. 5.24 pictures of new and old PTFE pieces are reported. The novelty is the modification of the Teflon pieces so that their thermal contractions increase

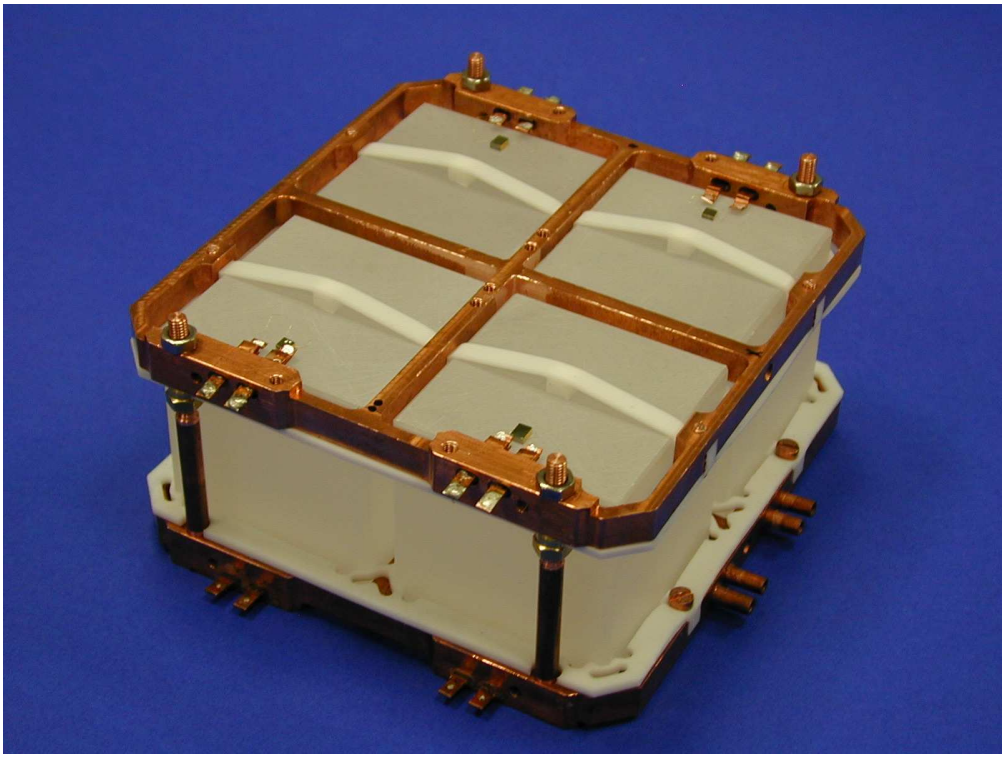

Figure 5.23 - Picture of the 4 cristals held with the Teflon mask instead of the Teflon pieces.

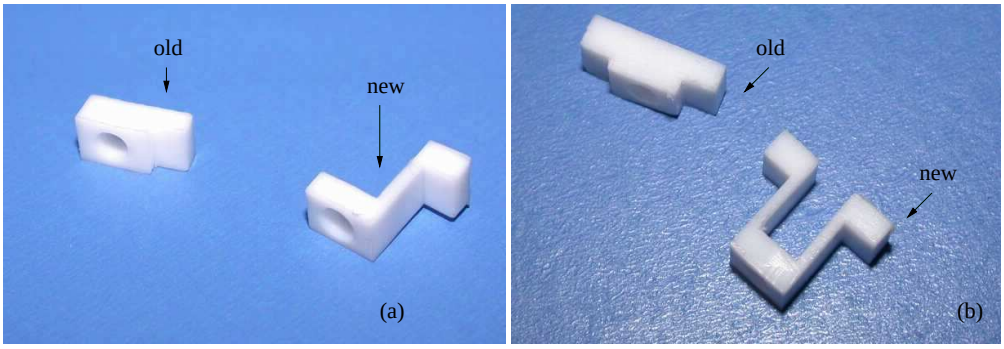


Figure 5.24 - Comparison of new and old PTFE pieces that hold $TeO_2$ crystals.

the pressure exerted on the crystal with decreasing temperature. A scheme of the way of working of both new and old Teflon pieces is shown in fig. 5.25. This crystal holding method was tested in Hall A after the dismounting of the MiDBD experiment. This test was performed in conditions as bad as possible, (i.e. without the anti–vibrating method), in order to see if this new method permits a lower mutual influence among crystals in the same Cuoricino module. Two Cuoricino modules were tested, one with old PTFE pieces and the second one with new pieces. Unfortunately the vibrational noise was so high that did not permit detectors to achieve the working temperature. The module contain-

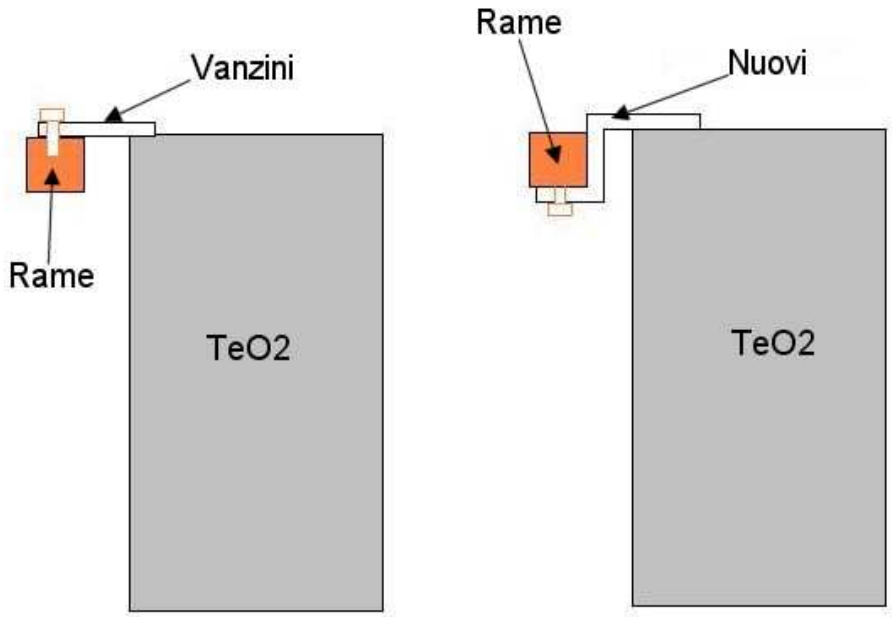


Figure 5.25 - Comparison between the holding method of old (a) and new (B) PTFE pieces.

ing new type PTFE pieces was cooler by severak mK than the other one; this effect was attributed to the fact that the new PTFE pieces design was more correct than the old one. Therefore, even if this proof is weak, it was decided to use them in the Cuoricino array.

## 5.5 Mechanical decoupling between of the array holder from the refrigerator

As remarked in the previous section and detailed in sec. 4.4, the vibrational noise could be reduced by introducing a mechanical decoupling between the cryogenic set–up and detector array. This method is used also in the Cuoricino experiment using simply a stainless–steel helicoidal spring which suspends the array from the 50 mK stage of the dilution refrigerator. The thermal link between the mixing chamber and the array holder has been realized by four copper strips, 40 mm long, 12 mm width and 50 $\mu$m thick.
The time required to cool the array from 4.2 K down to a temperature useful for detector operation (below 10 mK) depends on the conductance of the thermal link, on the total detector mass and on the parasitic power on the whole tower. A significant part of this power originate from slow ortho–para conversion of the molecular hydrogen trapped in the copper elements of the detector holder. In the Cuoricino experiment the total mass is about 60 kg, with a copper contribution of about 20 kg. To realize a good and fast thermal coupling of the tower

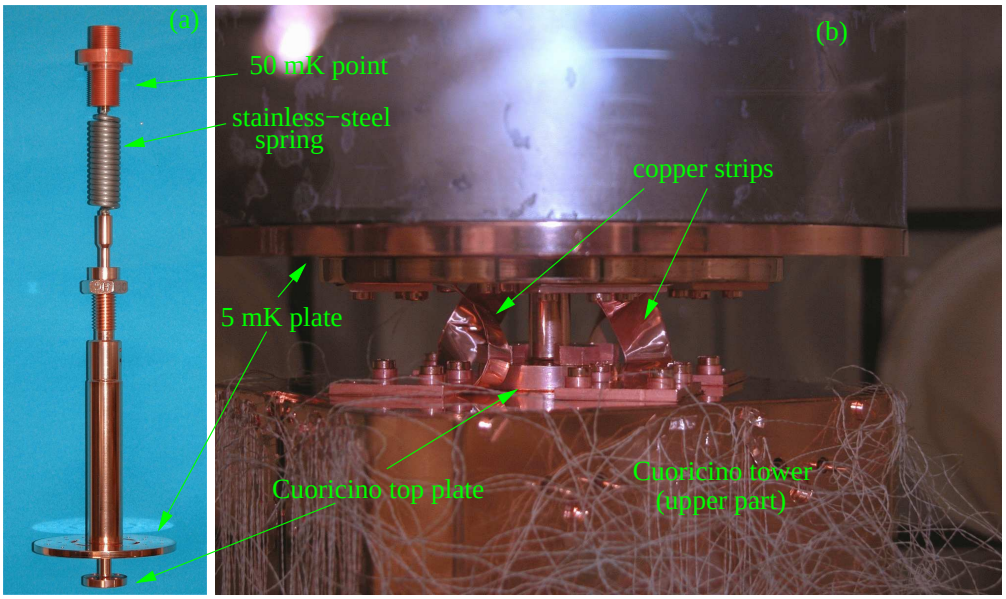


Figure 5.26 - (a) Suspension system of the Cuoricino tower. (b) Detail of the Cuoricino tower top side having a thermal link provided by four copper strips.

to the mixing chamber, various types of copper strips were measured, in order to test their thermal conductances. The copper chosen is CV 491 Cu OFHC, with a purity of 99:99%, produced by Goodfellow in bands with a thickness of $50\mu$m$\pm$15%. We performed annealing in vacuum for 12 hours at 450 C in order to increase its thermal conductivity.
The thermal conductance of these copper strips is $1.7\pm0.5$ W/cm K$^2$. In fig. 5.26 pictures of the suspension system of the Cuoricino tower and pictures of thermal coupling between the Mixing Chamber and the Cuoricino array are shown. Three measurements were taken in order to speed up the cool down and to get rid of the annoying temperature drift:

- The thermal link to the coldest fridge point was realized through strips made out of copper bands quoted above. The thermal link conductance increased by a factor 3 with respect to the MiDBD experiment.

- An important part of the copper used for Cuoricino had a very low hydrogen concentration.

- During the cooling down, the tower was kept for three days between 17 K and 22 K. In the cooling down curve the purpose of this plateau was to speed up the conversion from ortho– to para–hydrogen, which is catalyzed by inter–molecular interactions. The conversion time depends, therefore, both on the temperature and on the physical state of hydrogen inclusions. A temperature of 20 K is high enough to ensure the gaseous state of hydrogen, but it is also low enough to make para–hydrogen dominate over ortho–hydrogen at thermal equilibrium: this is, therefore, an ideal

condition to favour a quick and complete conversion from ortho– to para–hydrogen.

The tower cooling time from 1.5 K to less than 10 mK was shorter than 2 days, and no temperature drift was observed in the following period.

## 5.6 The array construction and the set up

Summarizing, the Cuoricino detector is a 13 plane CUORE–like tower; 11 of these planes are modules containing 4 $TeO_2$ crystals. Each crystal has a size of $5\times5\times5$ $cm^3$. It is lapped as explained in sec. 5.2 and held as detailed in sec. 5.4. Each crystal is coupled with a L–type NTD–Ge sensor using 9 glue spots as reported in sec. 5.3. Only four crystals were lapped in a different way and precisely with the Berkeley procedure. The other two planes of the Cuoricino tower are composed by 9 crystals each.
These crystals have a size of $3\times3\times6$ $cm^3$. They were already used in MiDBD and lapped again as described in sec. 5.2. One of these modules contains new PTFE pieces, whereas in the other one crystals are held through the MiDBD–II method. Four of these small crystals are the ones made with enriched Tellurium and already used in the MiDBD experiment. The two central crystals (of the 9 crystal modules) were intended to disentangle the background contribution due to crystal surface contaminations from the one due to surface contaminations of the copper holder. Indeed the two central crystals face a copper surface that is 3 times smaller than the one faced by crystals placed at the edges of the modules. Besides they allow a test of the power of the anticoincidence analysis, giving important information for the CUORE project.
In Cuoricino the total mass of $TeO_2$ is 40.7 kg. The electrical connection system of gold wires is the same used in MiDBD–II. The array was finally assembled in an underground clean room having a $N_2$ atmosphere to avoid Rn contamination. Fig. 5.27 shows the Cuoricino tower just after the completion.

The preparation of the experimental set–up was particularly careful in order to select the material used, when it was possible. For example pins, used during different thermal steps of the refrigerator, were deprived of their rounded black plastic heads as it is radioactive. For the same reason, wires of the cold electronic box were substituted with clean ones.

The array is surrounded by 1 cm thick roman lead shield. Two roman lead disks, 7.5 cm and 10 cm thick, are positioned respectively just below and above the tower. As for MiDBD, the refrigerator itself is shielded by a 20 cm thick layer of low activity lead and by a 10 cm thick layer of borated PET. Nitrogen is flushed between the external lead shield and cryostat to avoid any Rn contribution to the detector background. Cuoricino was cooled at the beginning of 2003. Unfortunately during the cooling down some of the signal wires disconnected so that only 32 of the large size crystals and 16 of the small ones could be read–out. The technical problem causing the wires disconnection has been identified and soon the array will be warmed up to room temperature to allow the repair of the lost connections.

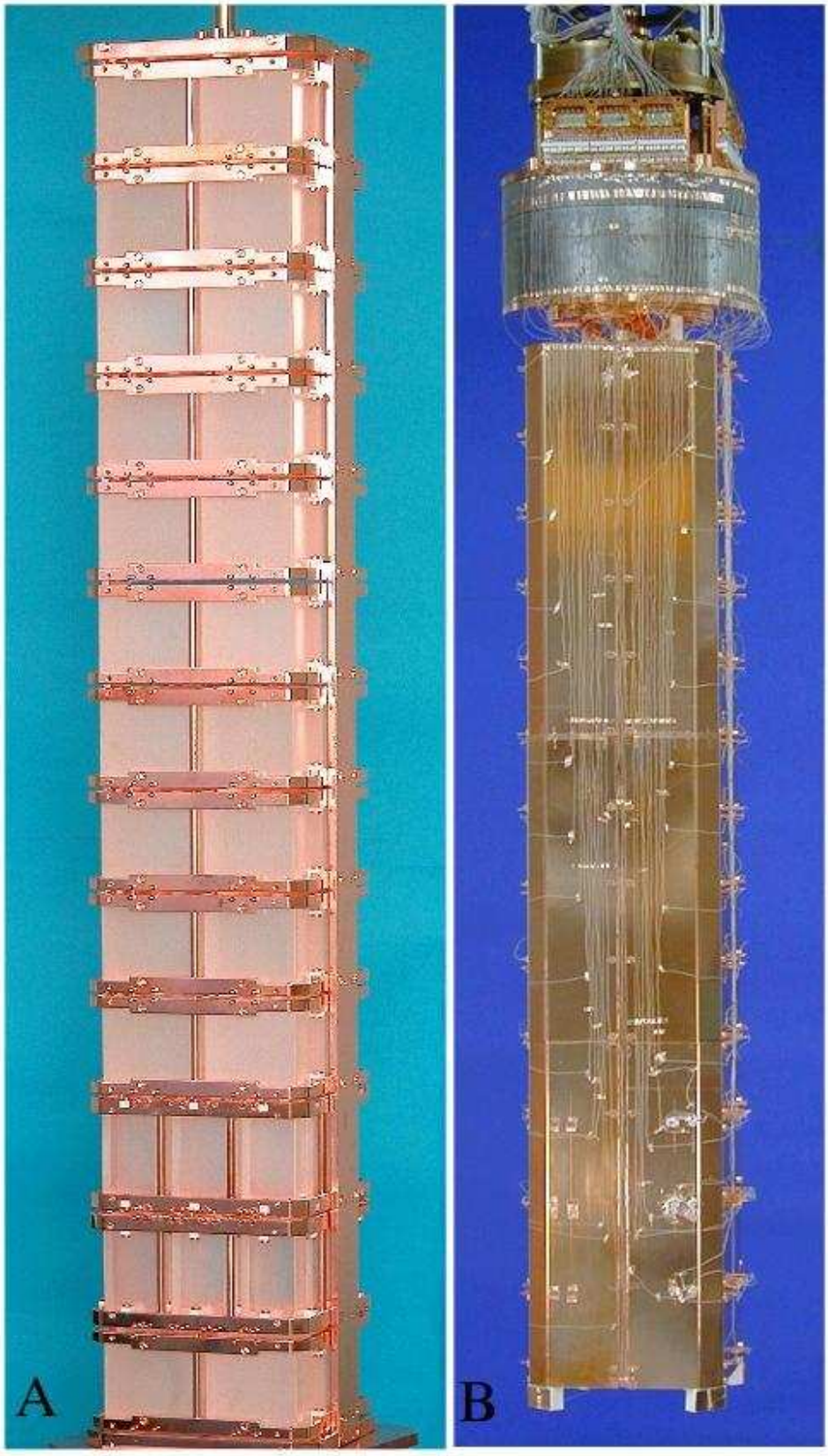


Figure 5.27 - Cuoricino tower opened (A) and closed (B). In picture A it is possible to see two of 9 crystal modules. In figure B it is possible to notice the upper roman lead shield and above the themalization stage on the Mixing Chamber.

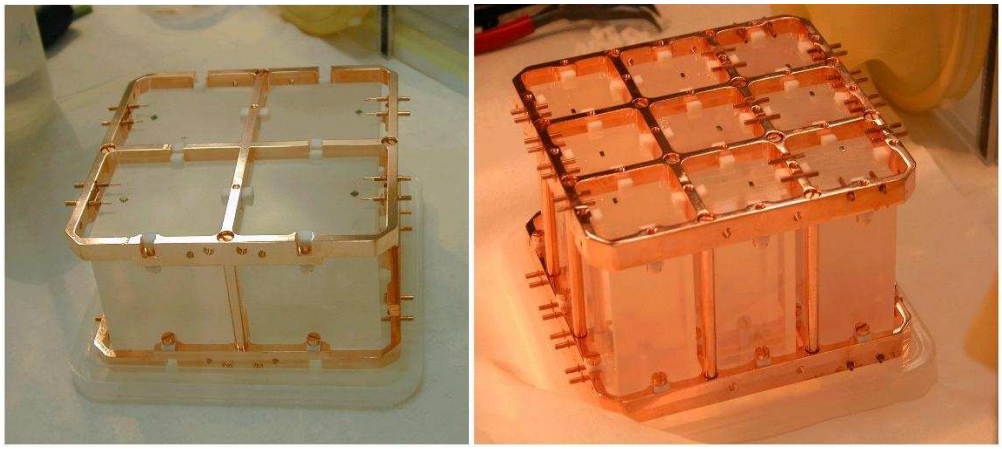

Figure 5.28 - Cuoricino modules. In the left picture a 4 crystal module is shown and in the right one a 9 crystal module is reported.

The mechanical structure of the array was made exclusively of OFHC copper and Teflon; both these materials have an extremely low radioactive content. Copper and Teflon parts were separately treated with acids to remove any possible surface contamination. In particular the copper holder was cleaned in Legnaro National Laboratory according to the MiDBD-II recipe (see sec. 4.3).

# Chapter 6

# The Cuoricino single module: detector performance and results

## 6.1 Introduction

The Cuoricino array was cooled in January 2003.
Two major phases characterized the data taking period:

1. **from January 22 until April 10**: the experimental set–up was optimized acting, for example, on the electronics and on the data acquisition stages. Furthermore a big effort was given to the characterization of high spurious noises and to the identifications of their sources. The preliminary results obtained during this period, the description of the spurious noises and of their sources and the operations carried out to reduce them are summarized in sec. 6.2;

2. **from April 19 until July 21**: the Cuoricino experiment took data giving relevant results. The detector performance description and the Cuoricino results analysis will be exposed in sec. 6.3 and sec. 6.4.

## 6.2 The first run: preliminary results

As reported in sec. 5.5, the cooling of the Cuoricino array was very fast, the detectors quickly reached the base temperature and no more annoying temperature drift of the operating points was observed. The first pulse was acquired on January 17 and is shown in fig. 6.1.

Unfortunately during the cooling procedure some of the signal wires got disconnected so that only 32 of the large size crystals and 16 of the small ones could be read. The technical problem responsible for the wire disconnection has now been identified: it was due to the thermal contractions of the wires at the various thermalization stages. On October 28 the array was warmed to room temperature in order to allow the lost connections to be repaired. The operations are still in progress.
A histogram of the detectors base temperatures, achieved in the first days of data taking, is reported in fig. 6.2. Obviously the detectors' working parameters

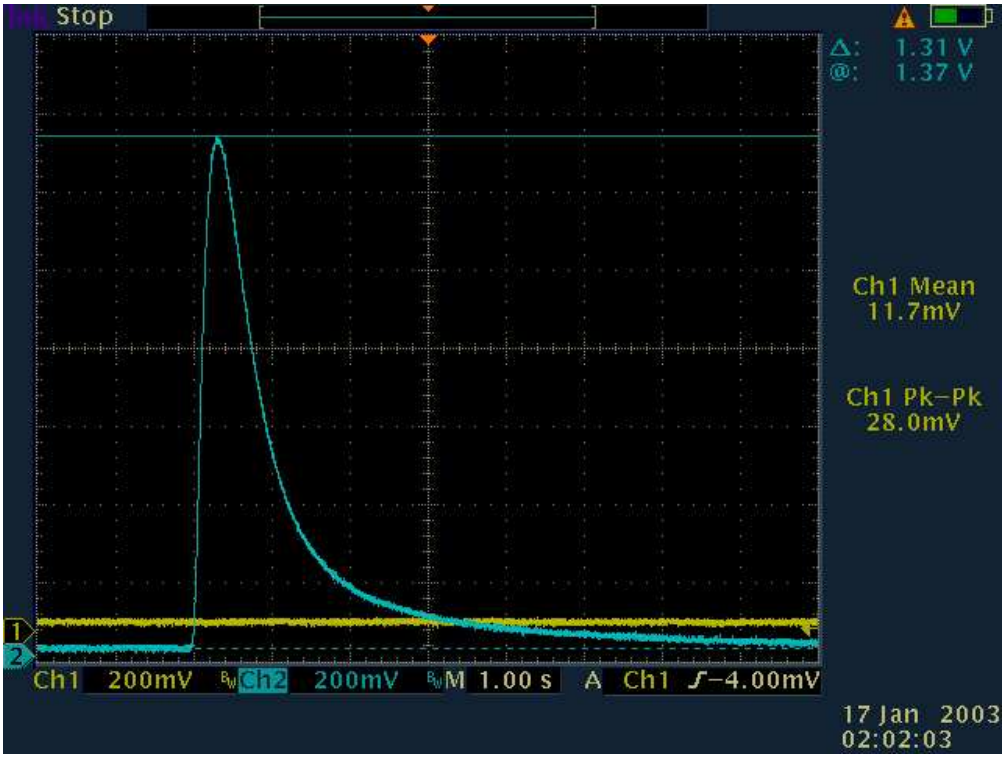


Figure 6.1 - The first Cuoricino pulse obtained in January 2003 and recorded by using an oscilloscope.

weren't yet optimized. For this reason many detectors presented pulses with a "not–classical" shape. Some bolometers worked after the inversion point of the load curve and this fact combined with the inevitable parasitic capacitance of the read–out wires, produced pulses with undershoots in the decay phase of the signal (an example of these pulses is shown in fig. 6.3) or "triangular" signal shape (an example of these pulses is shown in fig. 6.4). For some detectors the "not–classical" shape of the pulse was present even if they were working at their optimum operating point; this problem will be detailed in the next section. Finally two crystals were affected by thermal cross talks and two by electric cross talks on their heater wires.

Despite these problems, it was clear since the beginning that the detectors performance was good. This is proven by the fact that in the first calibration week, the energy resolution FWHM at the $^{208}$Tl line was less than 10 keV for the 74% of the detectors and between 10 and 16 keV for the 17% of the detectors, whereas only the other 4 had higher resolutions. In tab. 6.1 the situation of the big size bolometers is summarized, whereas the results for the $3\times3\times6$ cm$^3$ ones is reported in tab. 6.2. The power on the Mixing Chamber was 233 nW.

The biggest and most tedious problem faced in the first measurements was the presence of noise pulses that sometime dominated the run making the data acquisition impossible even for long periods. The noise pulses were characterized by square shapes, as shown in fig 6.5, and random occurancy. Furthermore it

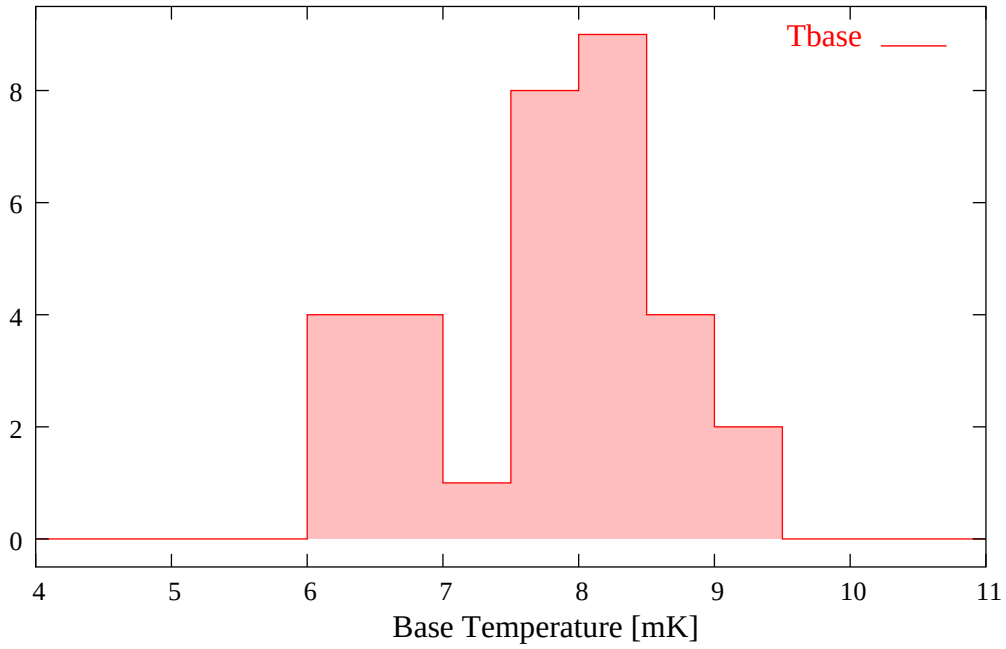


Figure 6.2 - Distribution of the base temperatures of the 5x5x5 $cm^3$ Cuoricino detectors during the first not optimized run.

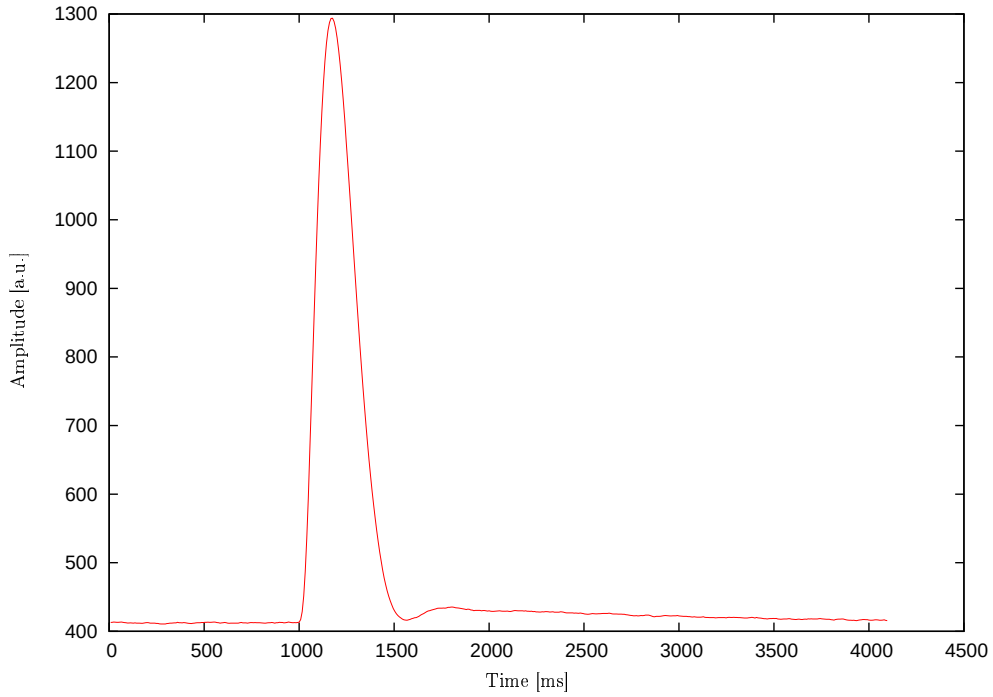


Figure 6.3 - Example of a signal obtained in a detector whose working point is placed after the inversion point of the load curve.

| Crystal | electr. ch. | state | R base [MΩ] | Amplitude [$\mu$V/MeV] | FWHM @ 2615 [keV] |
|---|---|---|---|---|---|
| B23 | 0 | dead | - | - | - |
| B15 | 1 | | 2,36G | 477 | 5.2 double |
| B38 | 2 | dead | - | - | - |
| B14 | 3 | dead | - | - | - |
| B24 | 4 | dead | - | - | - |
| B25 | 8 | dead | - | - | - |
| B47 | 11 | | 9,46G | 246 | 20 |
| B7 | 12 | | 1,34G | 415 | 18 |
| B60 | 13 | | 594M | 214 | 7 |
| B62 | 14 | dead | - | - | - |
| B56 | 15 | | 732M | 346 | 6.3 |
| B46 | 16 | | 792M | 159 | 8.9 |
| B28 | 17 | | 514M | 157 | 9.3 |
| B42 | 19 | | 276M | 148 | 8.4 |
| B29 | 20 | | 1,64G | 341 | 4 |
| B27 | 23 | | 210M | 137 | 5 |
| B39 | 24 | dead | - | - | - |
| B44 | 25 | | 6,6G | 524 | 5 |
| B51 | 26 | | 871M | 304 | 5 |
| B43 | 29 | dead | - | - | - |
| B36 | 36 | | 593M | 140 | 13 |
| B18 | 40 | | 1,28G | 286 | 7.3 |
| B13 (1) | 41 | | 695M | 167 | 32 |
| B35 | 42 | dead | - | - | - |
| B55 | 43 | | 841M | 321 | 11 |
| B16 (1) | 44 | ground | 3,6G | 489 | double |
| B30 | 45 | dead | - | - | - |
| B54 | 46 | | 4,2G | 546 | 4.8 |
| B32 | 50 | dead | - | - | - |
| B31 (1) | 53 | | 7,2G | 492 | 6.3 |
| B12 | 54 | | 275M | 147 | 8.6 |
| B52 | 55 | | 12,4G | 602 | 7.3 |
| B41 | 56 | | 6,2G | 470 | 10.2 |
| B57 | 57 | | 374M | 151 | 5.3 |
| B26 | 60 | | 859M | 241 | 4.5 |
| B10 | 61 | | 285M | 358 | 5.8 |
| B40 | 62 | | 449M | 191 | 4.7 |
| B37 (2) | 63 | | 1,12G | 97 | 9 |
| B49 | 64 | dead | - | - | - |
| B17 (2) | 65 | | 227M | 114 | 10 |
| B45 | 66 | | 576M | 159 | 4.7 |
| B61 | 67 | | 625M | 318 | 6.2 |
| B53 | 68 | | 12,7G | 586 | 5 |
| B34 | 69 | | 631 | 166 | 7 |

Table 6.1 - Summary of the detectors performance obtained with the $5\times5\times5$ cm$^3$ in the first step of the Cuoricino experiment. Note: (1) pulse has triangular shape - (2) pulse shows cross–talk on heater

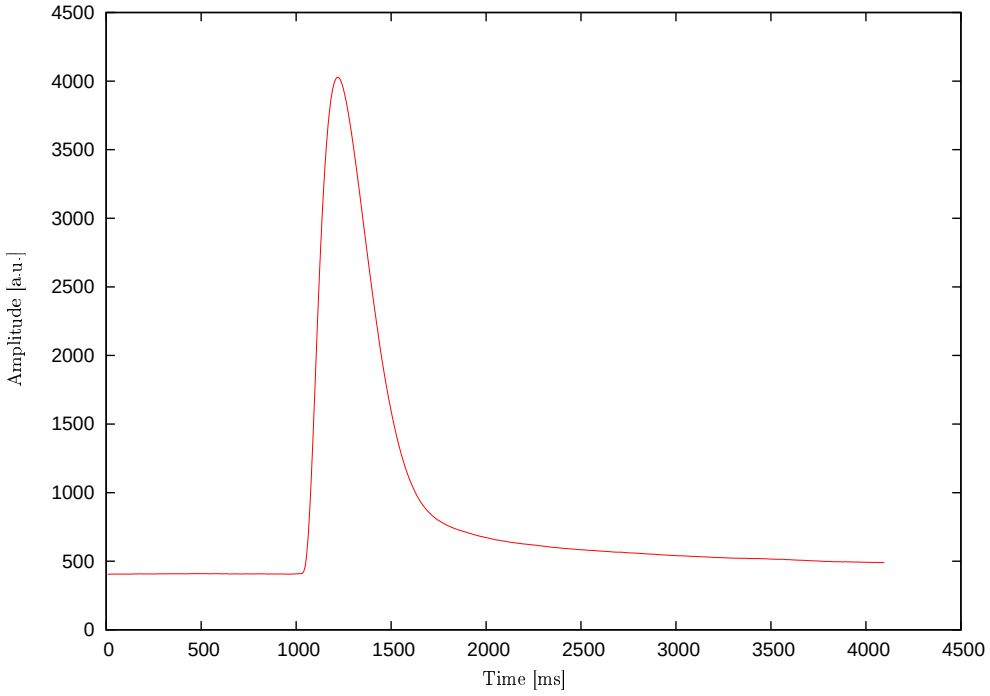


Figure 6.4 - Example of signal obtained in a detector whose working point is placed after the load curve inversion point. The signal has a triangular shape.

| Crystal | electr. ch. | state | R base [MΩ] | Amplitude $\mu$V/MeV | FWHM @ 2615 [keV] | note |
|---|---|---|---|---|---|---|
| H | 5 | dead | - | - | - | |
| 5 | 6 | | 650M | 418 | 9 | |
| F | 9 | | 2,24G | 589 | 7 | |
| 2 | 10 | | 514M | 409 | 9 | |
| 4 | 22 | | 1,02G | 712 | 5 | |
| 6 | 30 | | 1G | 751 | 10 | |
| B | 32 | | 1,97G | 491 | 12 | |
| 16 | 33 | | 1,2G | 325 | 30 | cross–talk |
| 0 | 34 | | 451M | 401 | 14 | cross–talk |
| I | 35 | | 791M | 731 | 4.3 | |
| E | 47 | | 895M | 546 | 5.5 | |
| 13 | 48 | | 1,4G | 427 | 7.5 | |
| 14 | 49 | no heater | - | - | - | |
| 9 | 52 | | 3,01G | 796 | 7.4 | |
| 128-1 | 51 | | 742M | 66 | 7.7 | enriched |
| 128-2 | 21 | | 790M | 175 | 12 | enriched |
| 130-1 | 18 | | 414M | 79 | 14 | enriched |
| 130-2 | 7 | | 950M | 74 | 20 | enriched |

Table 6.2 - Summary of the detector performance obtained with 3×3×6 $cm^3$ bolometers in the first step of the Cuoricino experiment.

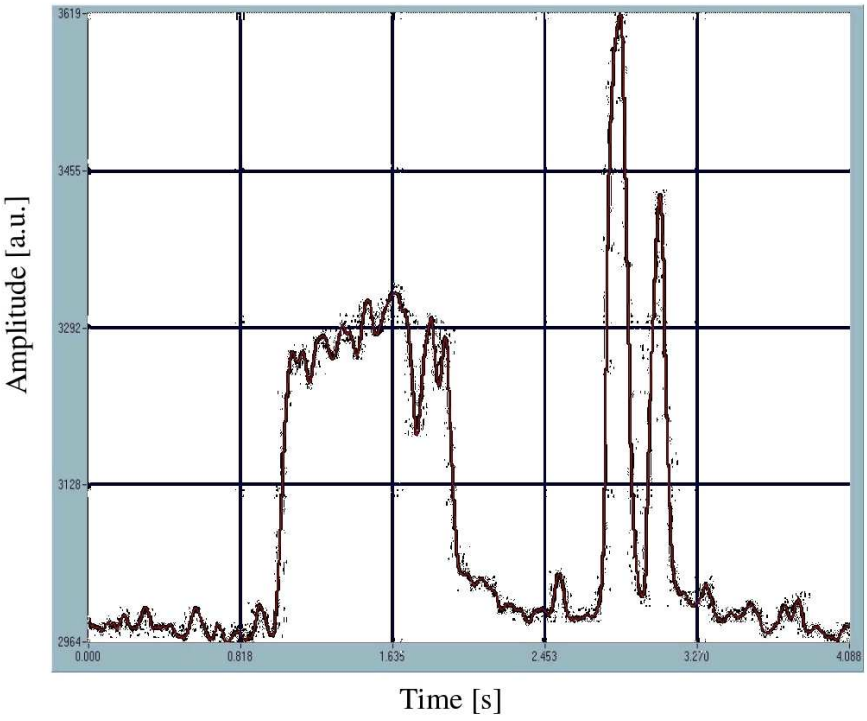


Figure 6.5 - Example of spurious noise square signal.

was observed that they were never acquired during the night. The noise event rate is shown in fig. 6.6. It has been discovered that the noise pulses were caused mainly by movements of the big crane used by another experiment in Hall A, probably interfering with our electric lines. The problem was solved by acting on the electric set–up and adjusting the grounding.

Another problem was linked to the presence of some helium in the IVC, i.e. in the experimental space of the refrigerator that should be kept in vacuum. Because of a very small leak, after several weeks of normal operation, $^4$He films grow on the detector surfaces and cause spurious noise. This type of noise consists of sequences of pulses with shapes very similar to ordinary pulses. It started from the top detectors of the array and during the measurement reached also the bottom ones. The only way to remove this noise was to stop the data taking and to pump the IVC. The fig. 6.7 shows the counting rate of two detectors; it is possible to observe that detector rates increase slowly. Since the problem was also present in the second phase of data taking, in order to reduce the measurement interruptions, it was decided to introduce a "getter" in the refrigerator. This element is composed by a copper frame that contains granules of charcoal powder that catch the helium atoms at temperature of a few K. In this way the measurements are not affected by this noise for longer periods, but as soon as the getter is saturated it is still necessary to warm it at a temperature higher than 70 K and pump the IVC. It is important to underline that this operation is made by using a heater located in the copper frame which is thermally isolated

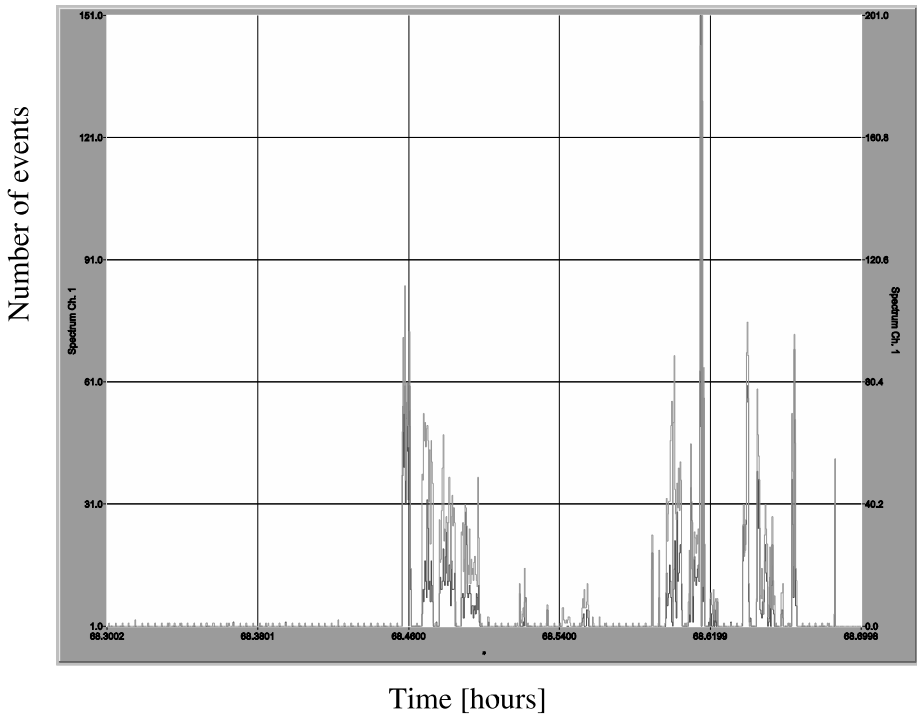


Figure 6.6 - Number of events as a function of time. It is clearly seen that there are periods characterized by high rates.

from the refrigerator and this implies that it is not necessary to warm up all the dilution unit.

## 6.3 The detector results at the optimum working point

In April 2003 the detectors were set in order to operate at their optimum working points.
First of all, since the base temperature of the previous run was so low that the detectors were too resistive, it was decided to dissipate on the Cuoricino array 466 nW instead of 233 nW. Then the optimum working points were searched for each detector. The optimum working point of a detector corresponds to the right values of bias voltage, current through the thermistor and sensor resistance that produces the maximum pulse amplitudes. For this reason, the signal amplitude corresponding to a fixed deposited energy was recorded for different biasing voltages. In this way a pulse is collected for each point of the detector load curve and then they are compared. Thanks to the very similar behavior of the Si heater pulses and the particles ones, at least at not too high energies, it is possible to perform this tuning of the detector working conditions dissipating a fixed power on the heaters. Examples of the load curve for a $5\times5\times5$ cm$^3$

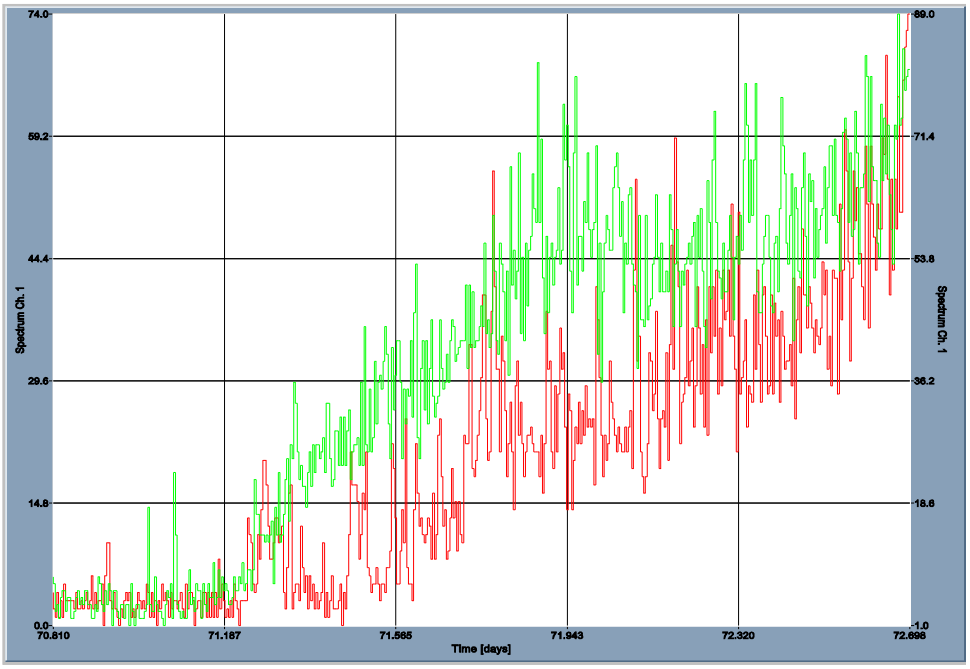


Figure 6.7 - Number of events as a function of time for two detectors: the rates increase due to the helium present in the IVC.

detector and of its heater pulse amplitude variation as a function of applied voltages are shown in fig. 6.8 and 6.9. Other load curves with the corresponding heater signal amplitudes versus total applied voltages are shown in fig. 6.10 and following. The optimum operation points can be estimated by the green curves and related to the load curves in blu remembering that $I_{bol} \simeq V_{tot}/R_{load}$, since $R_{load} \gg R_{bol}$ always.

On April 19 the first background measurement started and ran until July 21, when an interruption of the water supply, necessary to cool the compressors of the cryogenic system, occurred.
During this run the live time was 72%, including the time required for the periodic calibration (usually every 15 days) of the detectors. This percentage is considered excellent for thermal detectors.
The performance of the large size crystals during the entire run was quite good. We only had problems with 3 of the 32 detectors, once again due to the electrical connections: two detectors showed cross talk that prevented us from using them to compute the background while one had a too high spurious noise.
The performance of the electrically connected detectors was very good and is summarized in tab. 6.3 for the 5×5×5 $cm^3$ detectors, and in tab. 6.4 for the 3×3×6 $cm^3$ ones. In fig. 6.27 the distribution of the FWHM energy resolution of the 5×5×5 $cm^3$ crystals are compared with those of the 3×3×6 $cm^3$ ones. These value are normalized to 1 kg of $TeO_2$. It is possible to observe that even

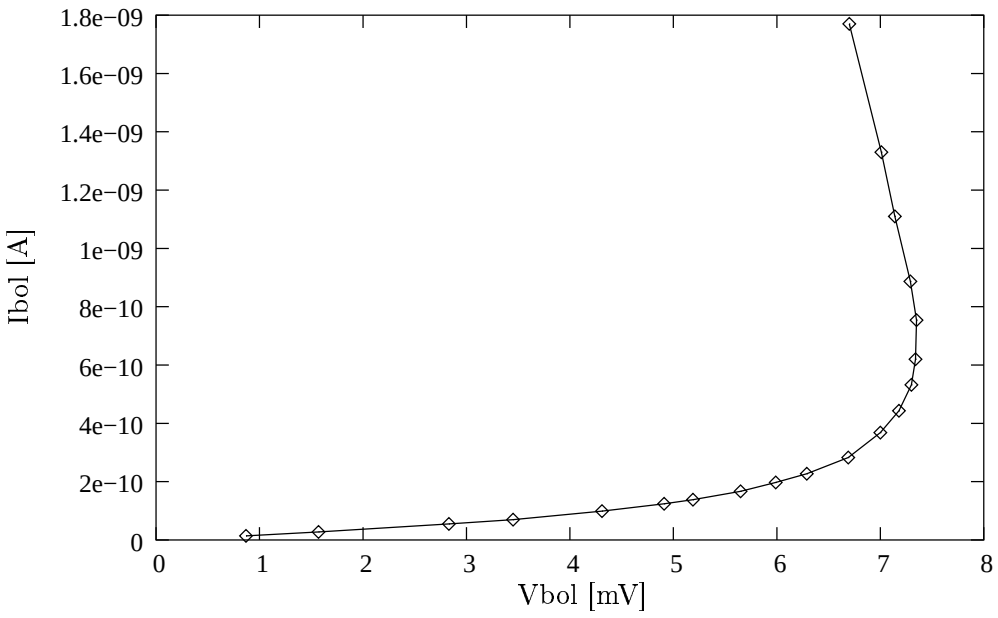


Figure 6.8 - Example of the experimental load curve for a 5×5×5 $cm^3$ detector.

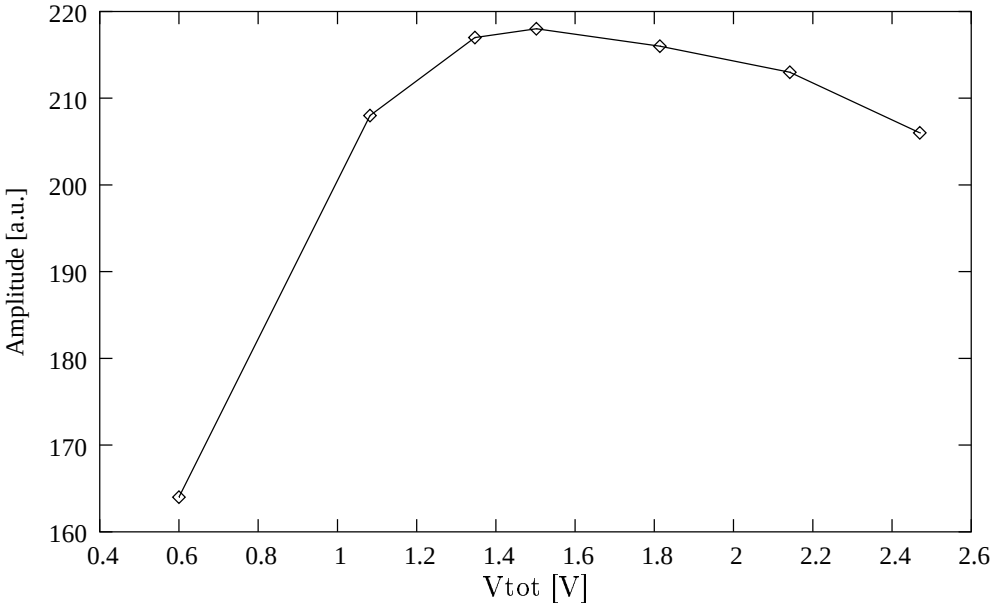


Figure 6.9 - Example of the variation of the pulse amplitude as function of the voltage on the thermistor, the signals are obtained dissipating fixed power on the Si heater. This curve was experimentally obtained using the same 5×5×5 $cm^3$ detector of fig 6.8.

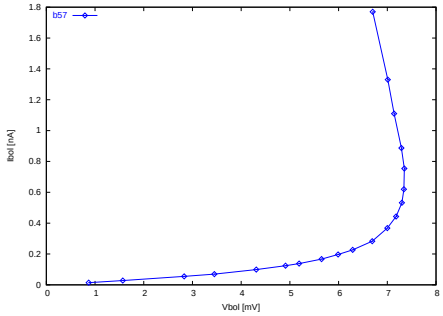


(a) plane 1, crystal B57

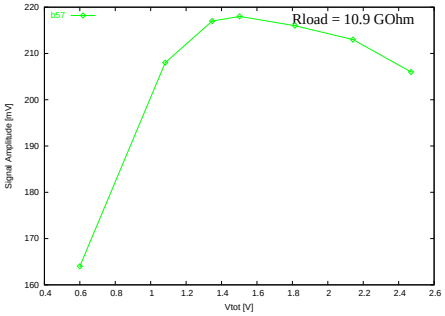


(b) plane 1, crystal B57

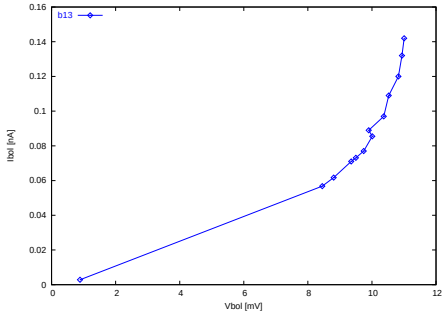


(c) plane 1, crystal B13

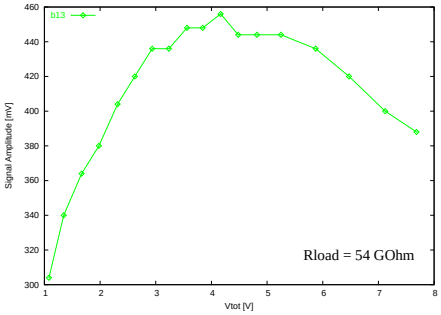


(d) plane 1, crystal B13

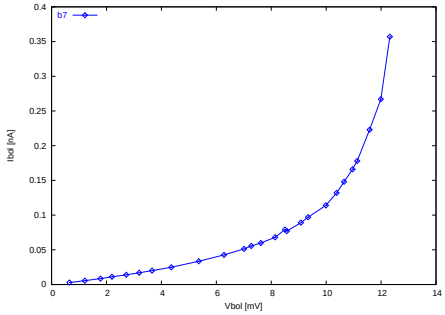


(e) plane 2, crystal B7

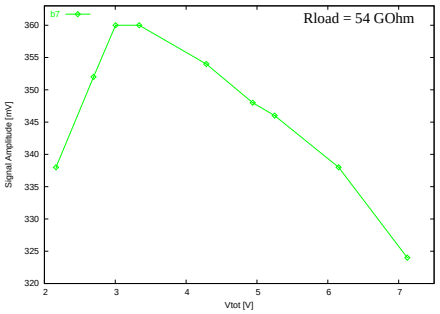


(f) plane 2, crystal B7

Figure 6.10 - The load curves and the Amplitude Optimization (AO) ones for the 5×5×5 $cm^3$ Cuoricino detectors are presented respectively in blue and in green.

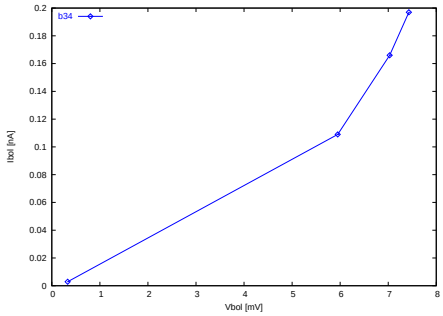


(a) plane 2, crystal B34

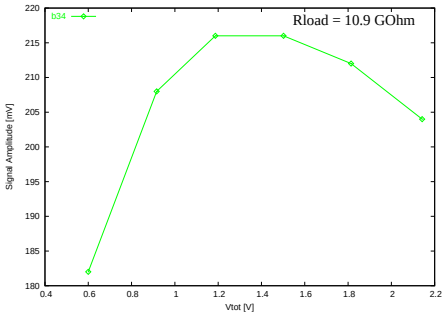


(b) plane 2, crystal B34

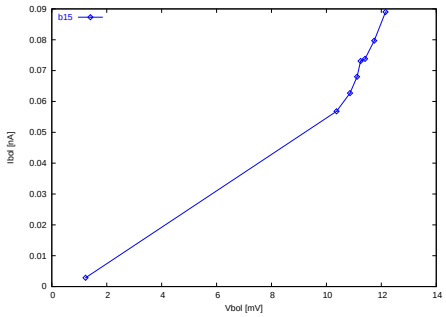


(c) plane 3, crystal B15

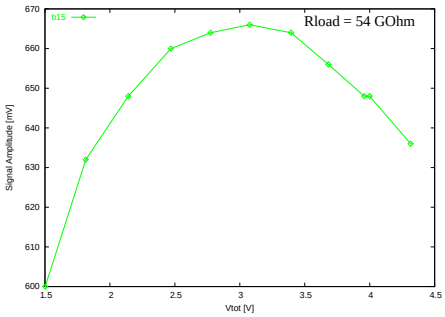


(d) plane 3, crystal B15

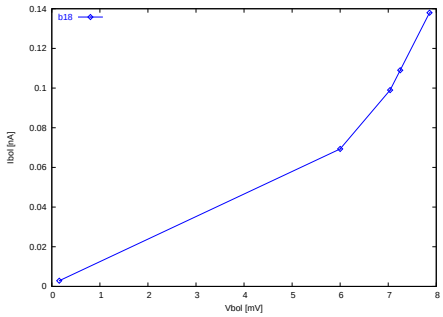


(e) plane 3, crystal B18

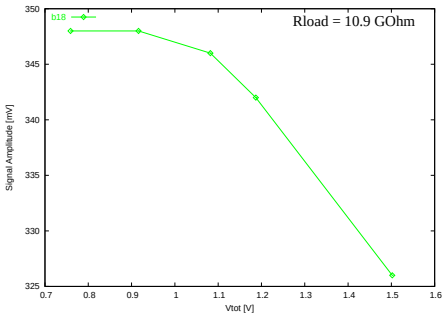


(f) plane 3, crystal B18

Figure 6.11 - In blue the load curves and in the green the amplitude optimization curves of $5\times5\times5$ cm$^3$ Cuoricino detectors.

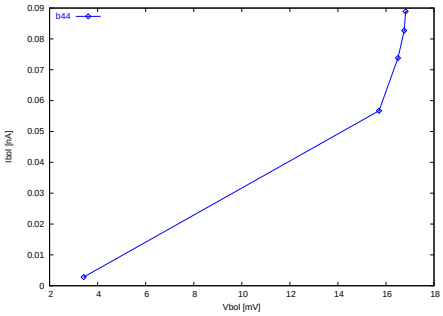


(a) plane 3, crystal B44

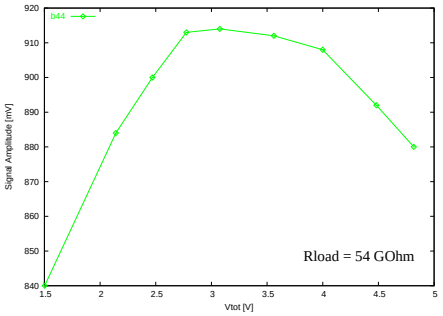


(b) plane 3, crystal B44

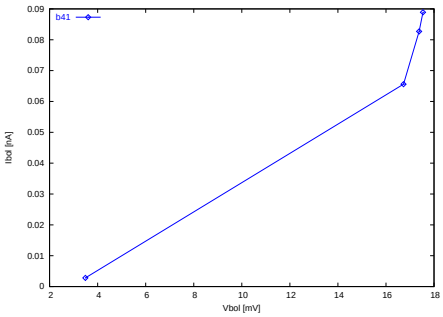


(c) plane 3, crystal B41

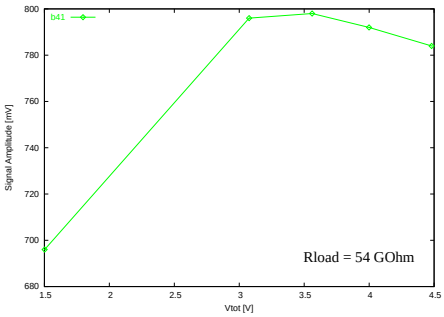


(d) plane 3, crystal B41

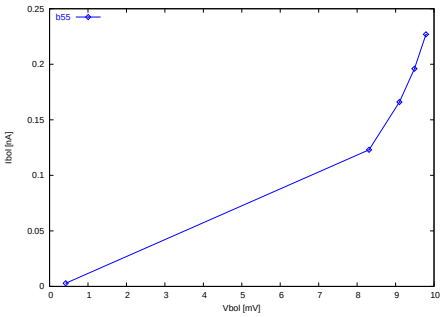


(e) plane 4, crystal B55

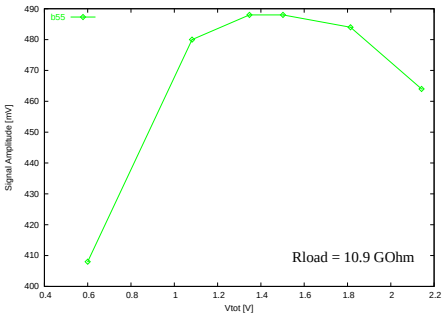


(f) plane 4, crystal B55

Figure 6.12 - In blue the load curves and in the green the amplitude optimization curves of $5\times5\times5$ cm$^3$ Cuoricino detectors.

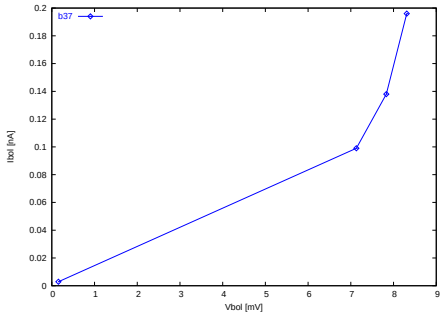


(a) plane 4, crystal B37

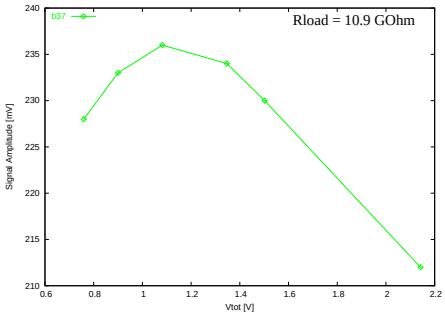


(b) plane 4, crystal B37

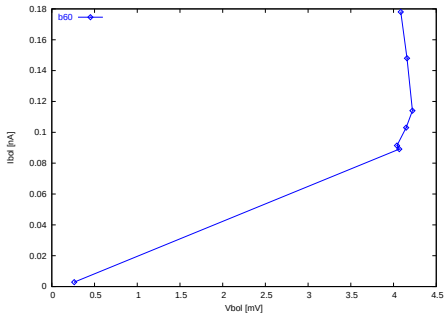


(c) plane 4, crystal B60

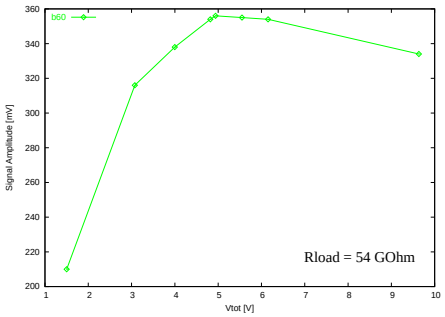


(d) plane 4, crystal B60

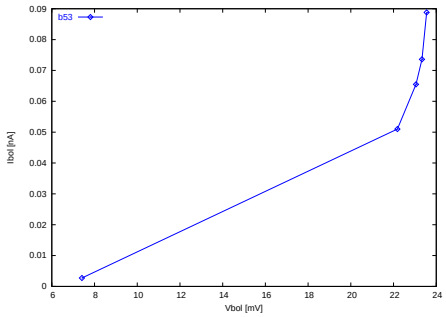


(e) plane 4, crystal B53

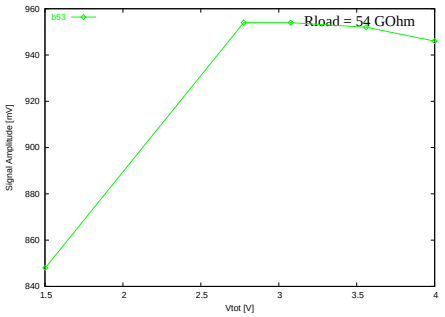


(f) plane 4, crystal B53

Figure 6.13 - In blue the load curves and in the green the amplitude optimization curves of $5\times5\times5$ cm$^3$ Cuoricino detectors.

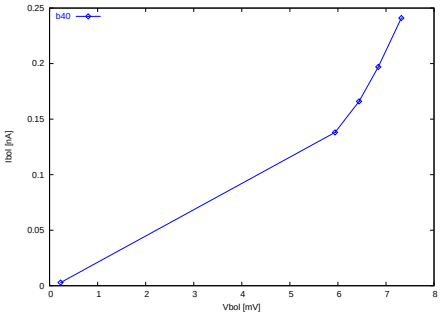


(a) plane 5, crystal B40

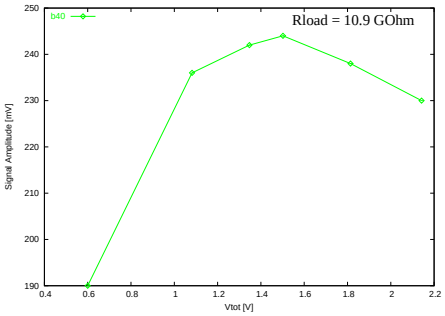


(b) plane 5, crystal B40

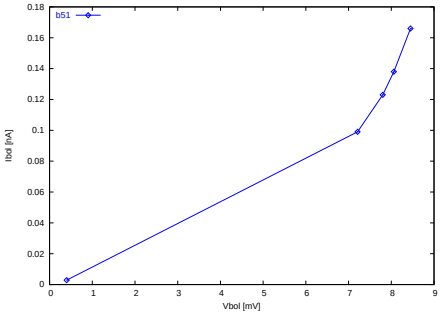


(c) plane 5, crystal B51

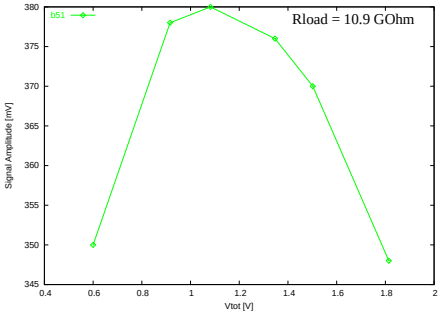


(d) plane 5, crystal B51

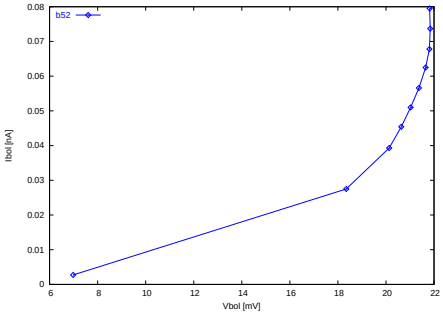


(e) plane 5, crystal B52

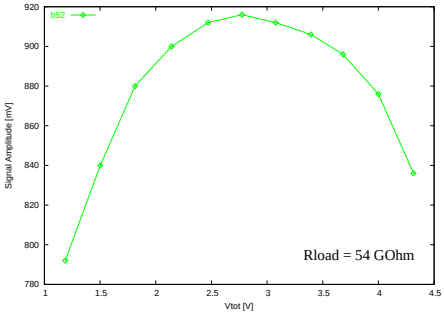


(f) plane 5, crystal B52

Figure 6.14 - In blue the load curves and in the green the amplitude optimization curves of $5\times5\times5$ cm$^3$ Cuoricino detectors.

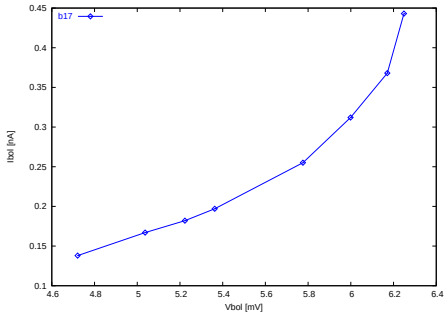


(a) plane 6, crystal B17

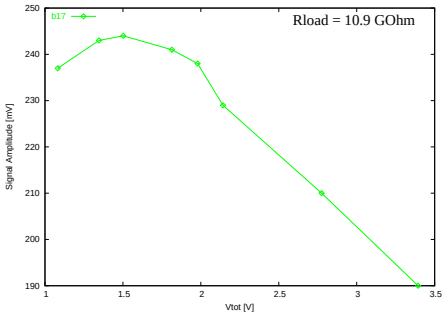


(b) plane 6, crystal B17

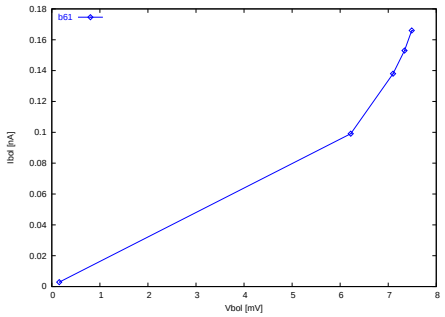


(c) plane 6, crystal B61

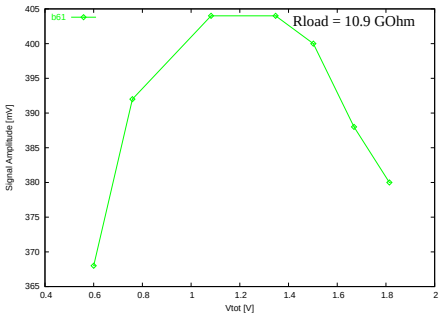


(d) plane 6, crystal B61

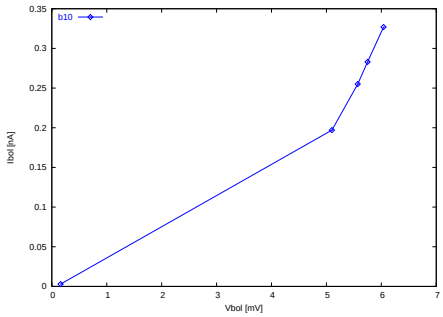


(e) plane 7, crystal B10

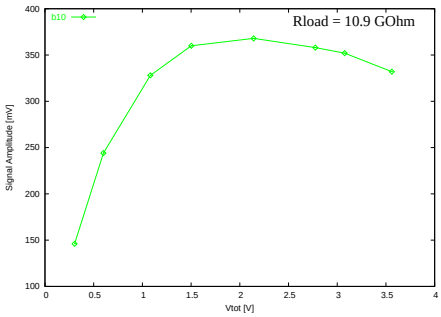


(f) plane 7, crystal B10

Figure 6.15 - In blue the load curves and in the green the amplitude optimization curves of $5\times5\times5$ cm$^3$ Cuoricino detectors.

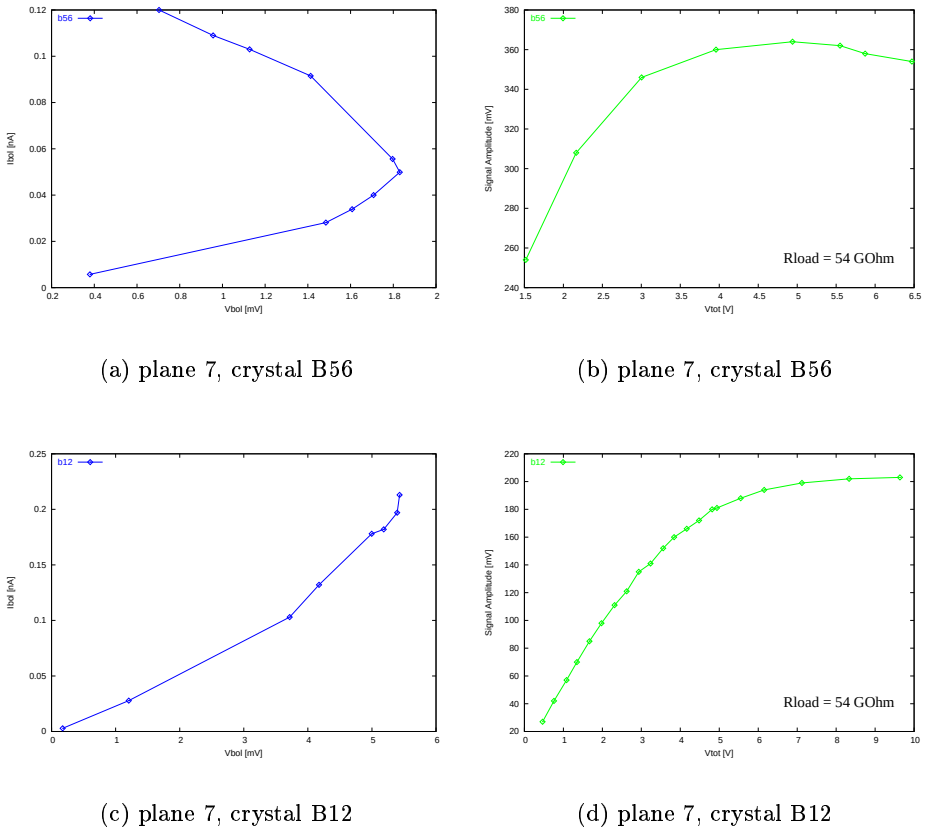


(a) plane 7, crystal B56

(b) plane 7, crystal B56

(c) plane 7, crystal B12

(d) plane 7, crystal B12

Figure 6.16 - In blue the load curves and in the green the amplitude optimization curves of 5×5×5 $cm^3$ Cuoricino detectors.

if the average detector performance is reasonably good, a large spread in the detector performance is still present. The fig. 6.28 shows the distribution of the Cuoricino detector energy resolutions for both the cristal sizes.

Even if the detectors performance is good (see tab. 6.3 and 6.4) their signals present different shapes from those obtained in previous experiments. In particular many detectors present pulses characterized by a double decay time constant. In fig. 6.29 a pulse with a "classical" shape produced with the B26 bolometer and a pulse with "long tail" obtained in the same measurement with the B57 detector, are compared. In fig 6.30 the pulse obtained with the B26 detector is compared, showing good agreement, with the one obtained with the historical B1 detector operating in hall C and considered as a benchmark. Examples of a signals for each working detector of the Cuoricino array are reported from fig. 6.33 to fig. 6.41. The pulses are presented with the same order in which the detectors are disposed in the array. The scheme of the tower is reported in fig. 6.32 where the detectors that for some reason aren't acquirable are colored in red, those producing normal pulses in white, and those producing pulses having long second decay time in blue. It is possible to see that about the 70% of the working 5×5×5 $cm^3$ crystal detectors present pulse shapes with a double

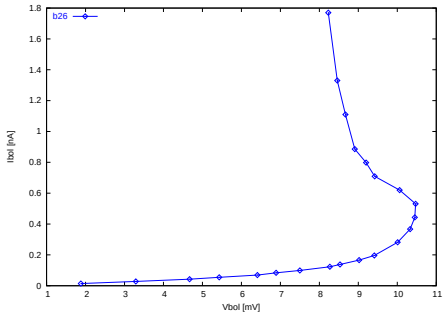


(a) plane 8, crystal B26

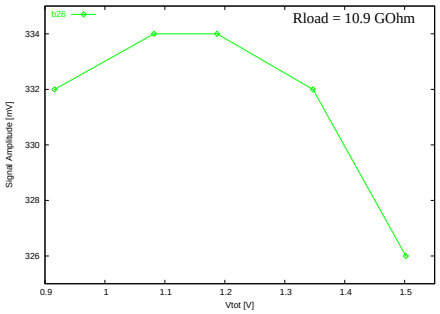


(b) plane 8, crystal B26

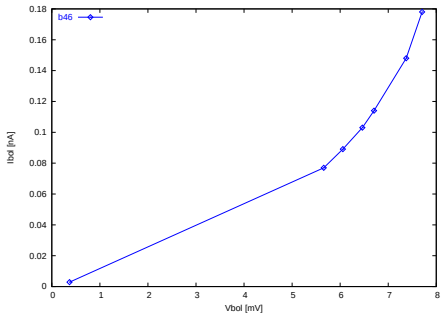


(c) plane 8, crystal B46

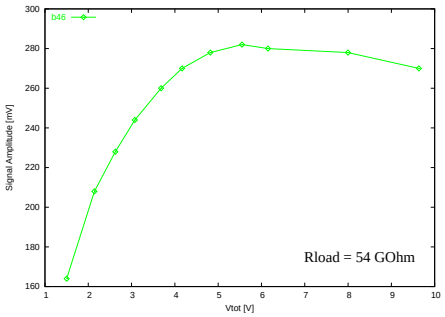


(d) plane 8, crystal B46

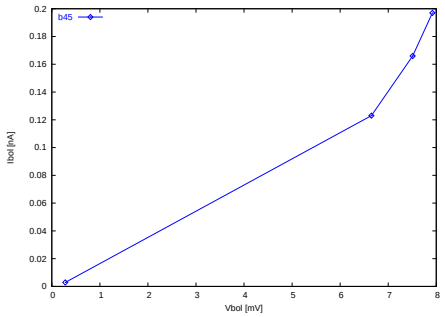


(e) plane 8, crystal B45

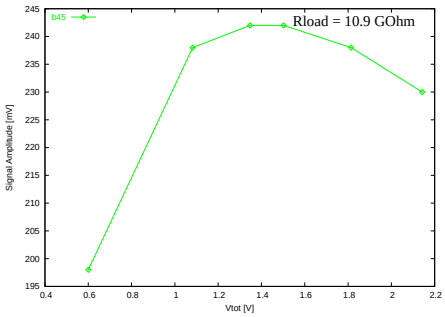


(f) plane 8, crystal B45

Figure 6.17 - In blue the load curves and in the green the amplitude optimization curves of $5\times5\times5$ cm$^3$ Cuoricino detectors.

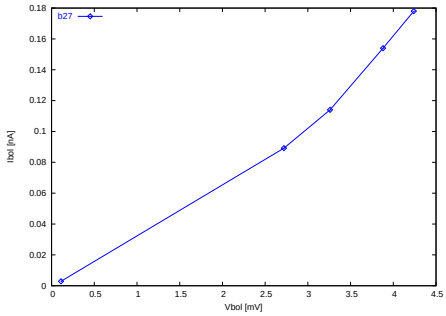


(a) plane 9, crystal B27

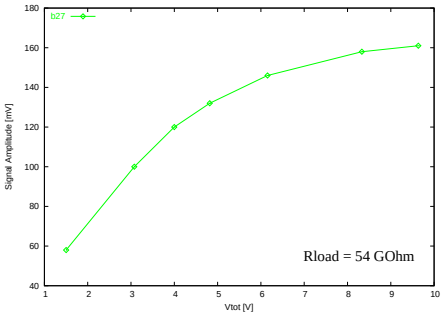


(b) plane 9, crystal B27

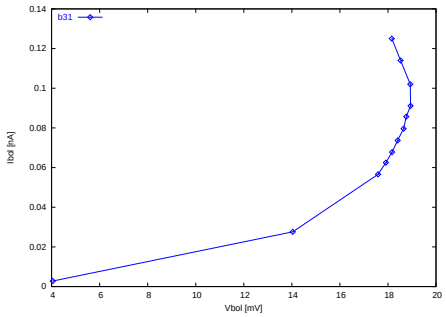


(c) plane 9, crystal B31

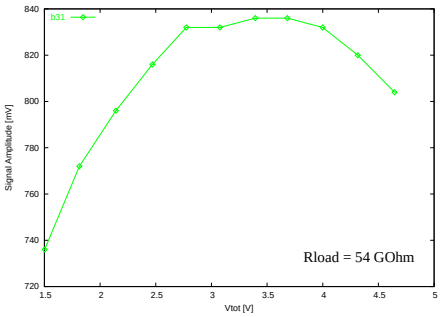


(d) plane 9, crystal B31

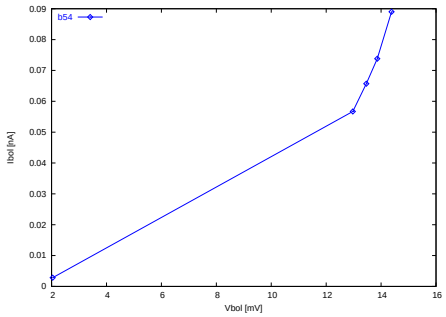


(e) plane 10, crystal B54

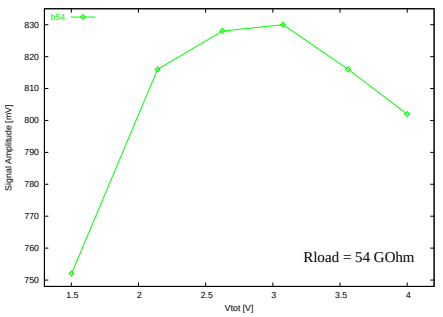


(f) plane 10, crystal B54

Figure 6.18 - In blue the load curves and in the green the amplitude optimization curves of $5\times5\times5$ cm$^3$ Cuoricino detectors.

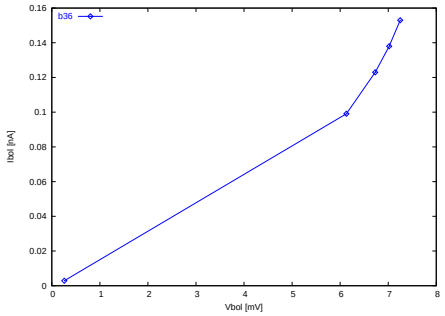


(a) plane 10, crystal B36

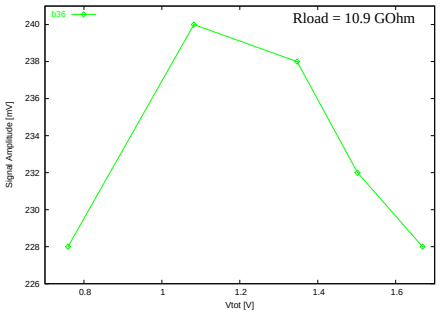


(b) plane 10, crystal B36

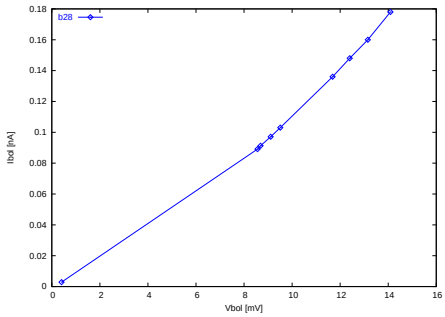


(c) plane 10, crystal B28

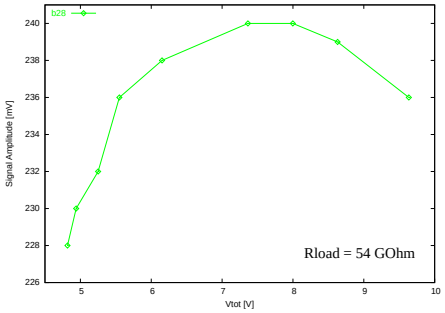


(d) plane 10, crystal B28

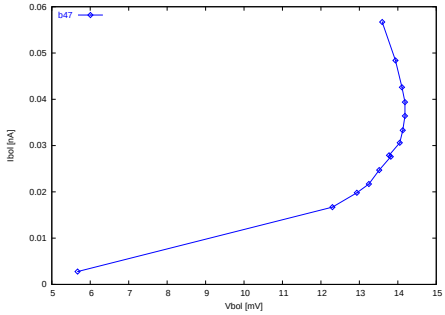


(e) plane 10, crystal B47

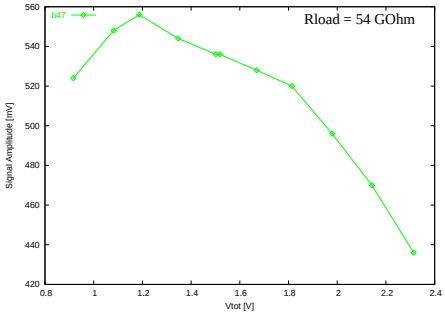


(f) plane 10, crystal B47

Figure 6.19 - In blue the load curves and in the green the amplitude optimization curves of $5\times5\times5$ cm$^3$ Cuoricino detectors.

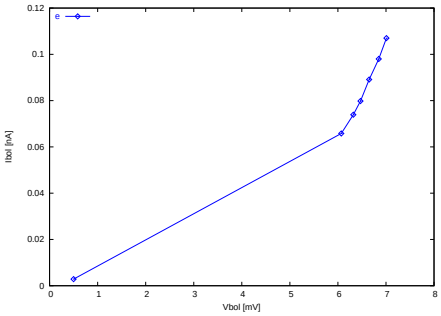


(a) plane 11, crystal E

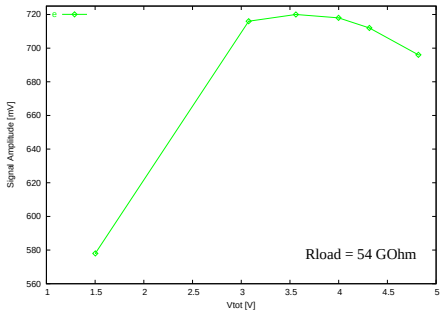


(b) plane 11, crystal E

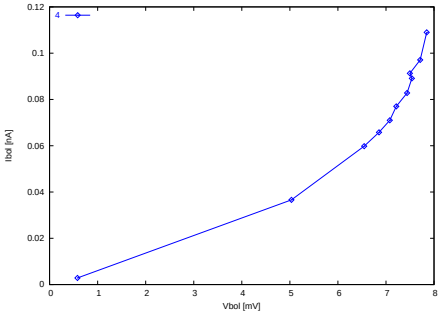


(c) plane 11, crystal 4

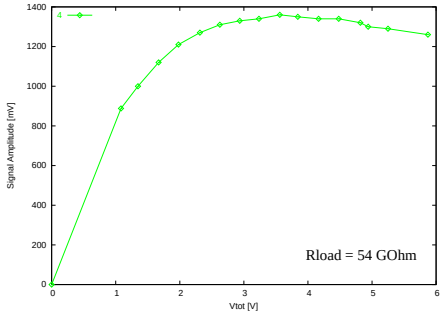


(d) plane 11, crystal 4

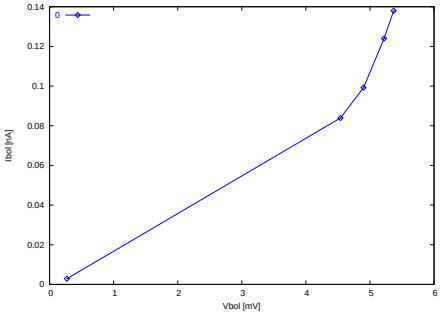


(e) plane 11, crystal 0

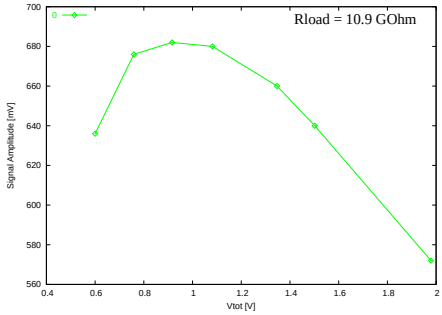


(f) plane 11, crystal 0

Figure 6.20 - In blue the load curves and in the green the amplitude optimization curves of $3\times3\times6$ cm$^3$ Cuoricino detectors.

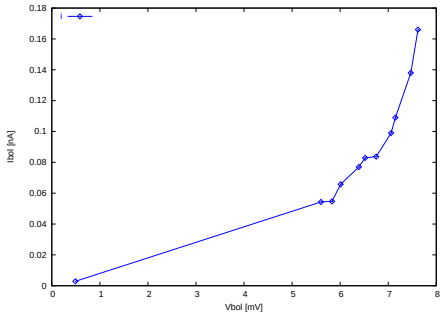


(a) plane 11, crystal I

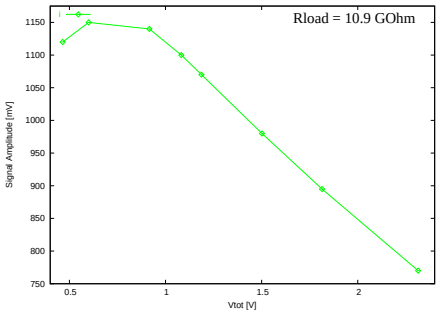


(b) plane 11, crystal I

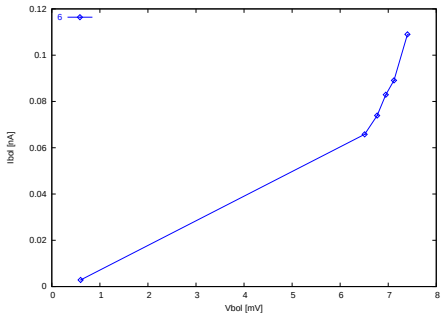


(c) plane 11, crystal 6

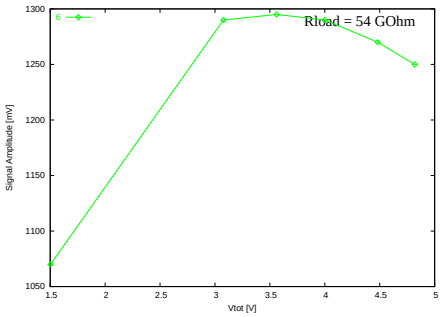


(d) plane 11, crystal 6

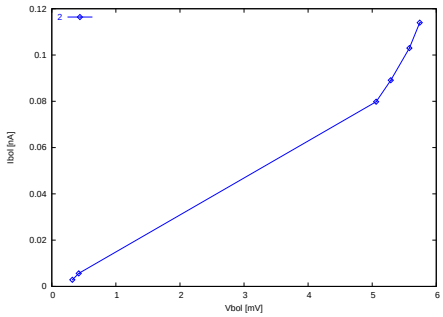


(e) plane 11, crystal 2

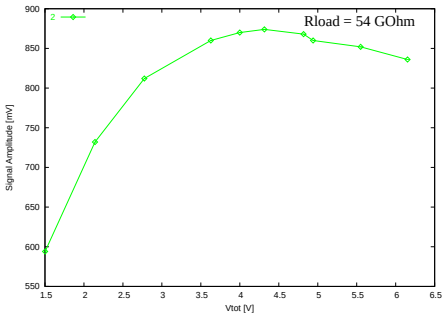


(f) plane 11, crystal 2

Figure 6.21 - In blue the load curves and in the green the amplitude optimization curves of $3\times3\times6$ cm$^3$ Cuoricino detectors.

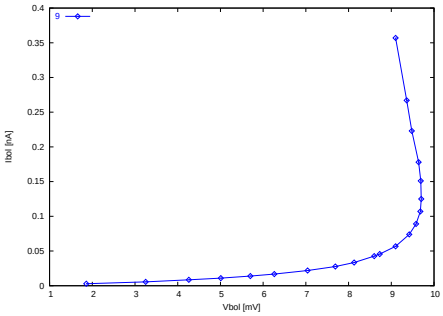


(a) plane 11, crystal 9

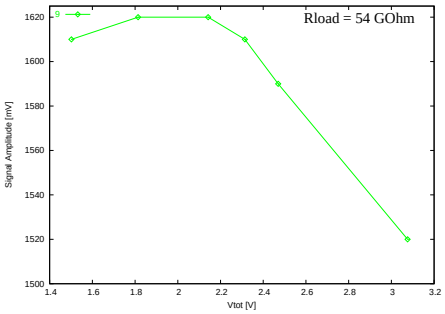


(b) plane 11, crystal 9

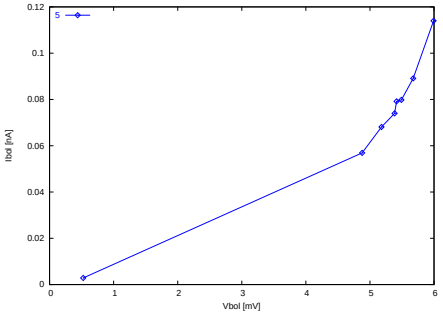


(c) plane 11, crystal 5

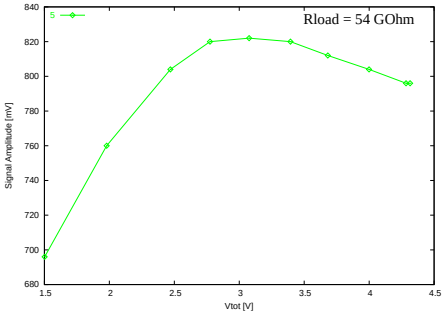


(d) plane 11, crystal 5

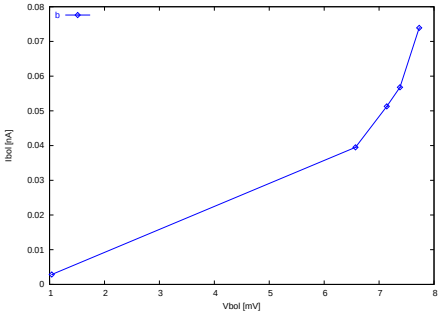


(e) plane 12, crystal B

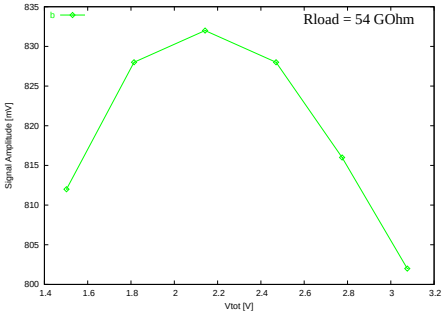


(f) plane 12, crystal B

Figure 6.22 - In blue the load curves and in the green the amplitude optimization curves of $3\times3\times6$ cm$^3$ Cuoricino detectors.

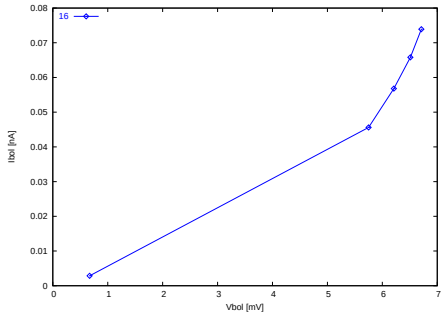


(a) plane 12, crystal 16

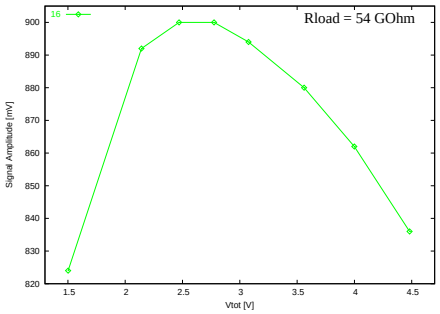


(b) plane 12, crystal 16

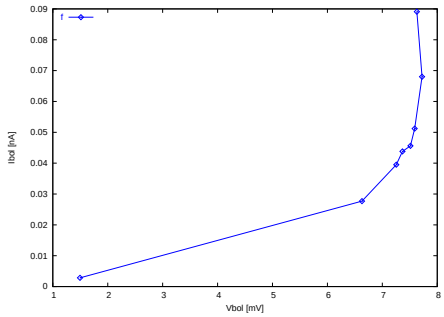


(c) plane 12, crystal F

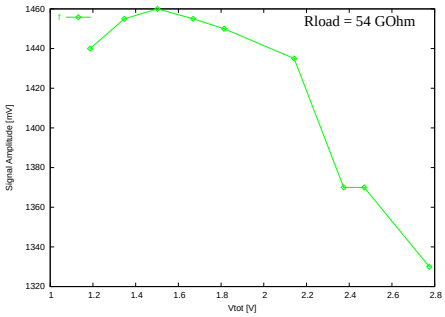


(d) plane 12, crystal F

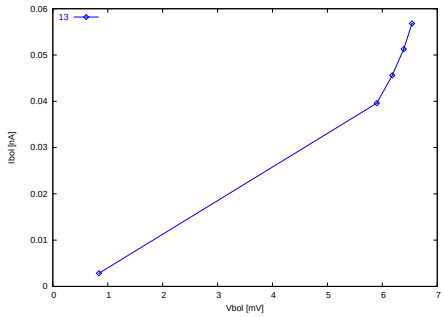


(e) plane 12, crystal 13

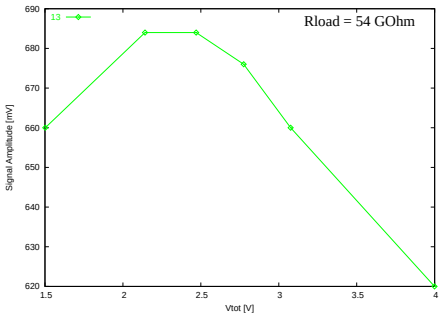


(f) plane 12, crystal 13

Figure 6.23 - In blue the load curves and in the green the amplitude optimization curves of $3\times3\times6$ cm$^3$ Cuoricino detectors.

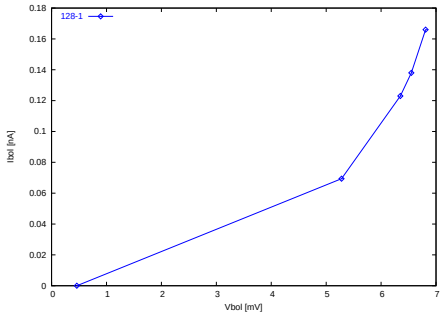


(a) plane 12, crystal 128-1

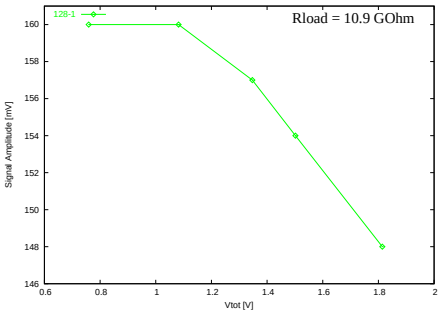


(b) plane 12, crystal 128-1

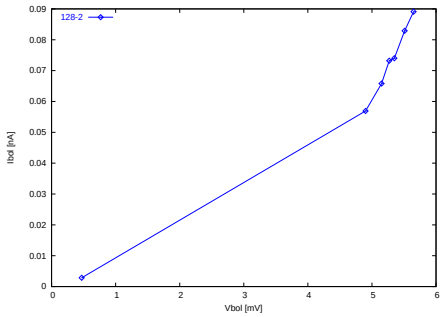


(c) plane 12, crystal 128-2

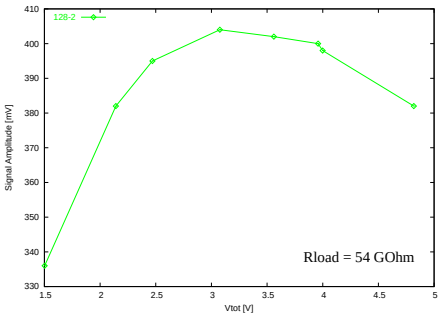


(d) plane 12, crystal 128-2

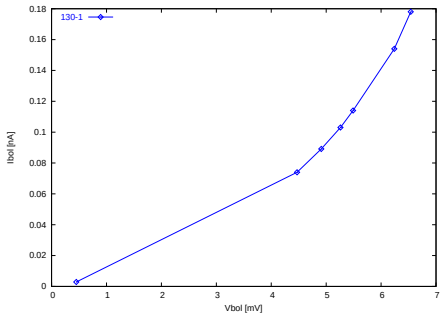


(e) plane 12, crystal 130-1

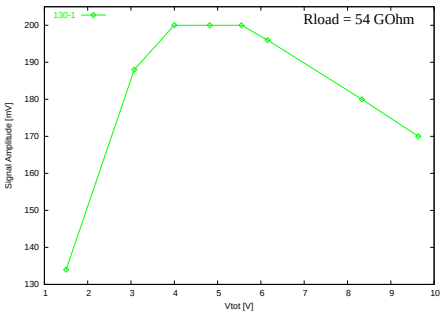


(f) plane 12, crystal 130-1

Figure 6.24 - In blue the load curves and in the green the amplitude optimization curves of $3\times3\times6$ cm$^3$ Cuoricino enriched detectors.

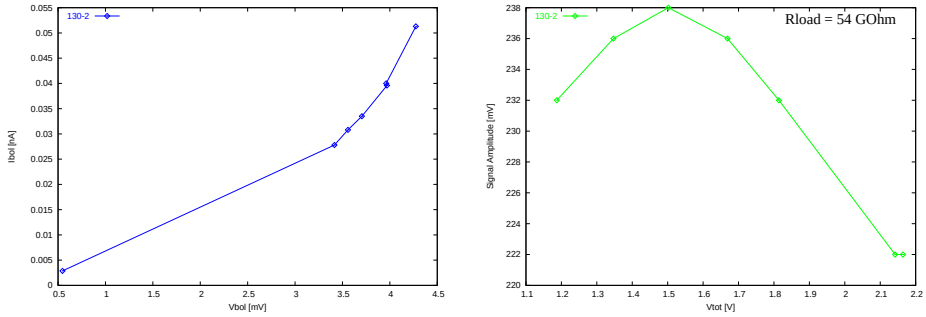


(a) plane 12, crystal 130-2 (b) plane 12, crystal 130-2

Figure 6.25 - In blue the load curves and in the green the amplitude optimization curves of $3\times3\times6$ cm$^3$ Cuoricino enriched detectors.

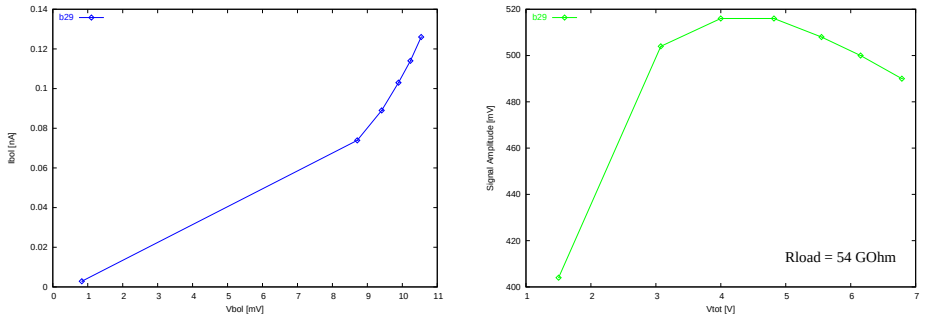


(a) plane 13, crystal B29 (b) plane 13, crystal B29

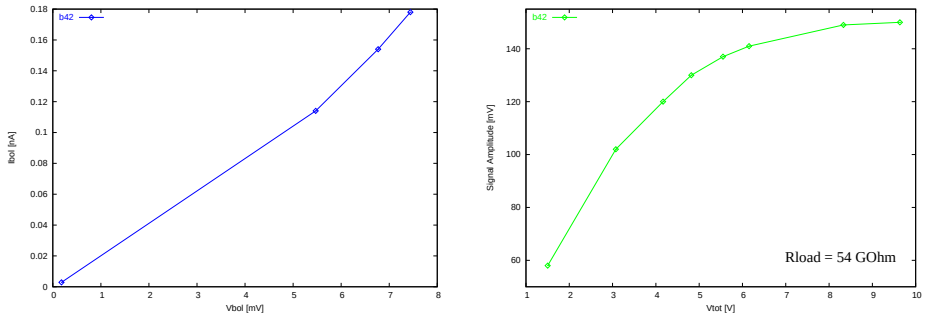


(c) plane 13, crystal B42 (d) plane 13, crystal B42

Figure 6.26 - In blue the load curves and in the green the amplitude optimization curves of $5\times5\times5$ cm$^3$ Cuoricino detectors.

| | DAQ ch | Floor | Bias [V] | R (working) [MΩ] | Amplitude [$\mu$V/MeV] | Risol. 2615 [keV] | Risol. old 2615 |
|---|---|---|---|---|---|---|---|
| B15 | 1 | 3 | 39.6 | 154 | 235 | 5.7 | 5.2 double |
| B47 | 11 | 10 | 15.2 | 494 | 164 | 18 | 20 |
| B7 | 12 | 2 | 42.8 | 10.7 | 192 | 8 | 18 |
| B60 | 13 | 4 | 55.5 | 40.7 | 98 | 7.7 | 7 |
| B56 | 15 | 7 | 21.6 | 42.6 | 129 | 6.4 | 6.3 |
| B46 | 16 | 8 | 80 | 49.8 | 76 | 6 | 8.9 |
| B28 | 17 | 10 | 96.4 | 79.1 | 63 | 6.1 | 9.3 |
| B42 | 19 | 13 | 96.4 | 41.7 | 58 | 6.2 | 8.4 |
| B29 | 20 | 13 | 55.5 | 96.4 | 168 | 5.6 | 4 |
| B27 | 23 | 9 | 96.4 | 23.8 | 48 | 8.7 | 5 |
| B44 | 25 | 3 | 39.6 | 224 | 279 | 6.8 | 5 |
| B51 | 26 | 5 | 73.6 | 58.6 | 131 | 13.5 | 5 |
| B36 | 36 | 10 | 73.6 | 51.0 | 71 | 10.7 | 13 |
| B18 | 40 | 3 | 52.5 | 71.1 | 131 | 6.7 | 7.3 |
| B13 | 41 | 1 | 49.4 | 111 | 126 | 7.2 | 32 |
| B55 | 43 | 4 | 89.6 | 54.7 | 174 | 12 | 11 |
| B16 | 44 | 6 | 33.4 | 190 | 351 | 6.4 | double |
| B54 | 46 | 10 | 39.6 | 188 | 281 | 6.4 | 4.8 |
| B31 | 53 | 9 | 42.8 | 234 | 250 | 5.4 | 6.3 |
| B12 | 54 | 7 | 96.4 | 27.4 | 58 | 7 | 8.6 |
| B52 | 55 | 5 | 30 | 378 | 362 | 7.1 | 7.3 |
| B41 | 56 | 3 | 46.3 | 210 | 268 | 12.2 | 10.2 |
| B57 | 57 | 1 | 96.4 | 30.5 | 64 | 8.6 | 5.3 |
| B26 | 60 | 8 | 67.9 | 67.1 | 103 | 5.1 | 4.5 |
| B10 | 61 | 7 | 96.4 | 21.8 | 130 | 6.9 | 5.8 |
| B40 | 62 | 5 | 96.4 | 34.8 | 74 | 6 | 4.7 |
| B37 | 63 | 4 | 73.6 | 56.9 | 52 | 10.7 | 9 |
| B17 | 65 | 6 | 96.4 | 28.7 | 55 | 8 | 10 |
| B45 | 66 | 8 | 89.6 | 45.1 | 66 | 5.3 | 4.7 |
| B61 | 67 | 6 | 73.6 | 51.6 | 124 | 7.4 | 6.2 |
| B53 | 68 | 4 | 36.3 | 352 | 300 | 6.1 | 5 |
| B34 | 69 | 2 | 89.6 | 42.2 | 73 | 5.2 | 7 |

Table 6.3 - Summary of detector performance obtained with the Cuoricino experiment 5×5×5 $cm^3$ crystals between April and July.

| | DAQ ch | Floor | Bias [V] | R (working) [MΩ] | Amplitude uV/MeV | Risol. 2615 [keV] | Risol. old 2615 |
|---|---|---|---|---|---|---|---|
| 5 | 6 | 11 | 42.8 | 68.4 | 244 | 7.9 | 9 |
| F | 9 | 12 | 23.7 | 168 | 488 | 7.4 | 7 |
| 2 | 10 | 11 | 61.5 | 50.4 | 229 | 9.1 | 9 |
| 4 | 22 | 11 | 49.4 | 82.1 | 395 | 5.9 | 5 |
| 6 | 30 | 11 | 49.4 | 79.9 | 312 | 7.8 | 10 |
| B | 32 | 12 | 26.9 | 139 | 257 | 11.4 | 12 |
| 16 | 33 | 12 | 36.3 | 99.0 | 312 | 14.2 | 30 |
| 0 | 34 | 11 | 67.9 | 42.2 | 165 | 13.2 | 14 |
| I | 35 | 11 | 46.3 | 80.6 | 382 | 47 | 4.3 |
| E | 47 | 11 | 49.4 | 74.7 | 248 | 6 | 5.5 |
| 13 | 48 | 12 | 26.9 | 125 | 250 | 8.6 | 7.5 |
| 14 (*) | 49 | 12 | 80 | - | 64 | | 18 |
| 9 | 52 | 11 | 23.7 | 191 | 501 | 13 | 7.4 |
| 128-1 | 51 | 12 | 67.9 | 51.4 | 35 | 11.7 | 7.7 |
| 128-2 | 21 | 12 | 39.6 | 73.2 | 111 | 8.7 | 12 |
| 130-1 | 18 | 12 | 61.5 | 48.2 | 44 | 15.6 | 14 |
| 130-2 | 7 | 12 | 21.6 | 99.0 | 62 | 33 | 20 |

Table 6.4 - Summary of detector performance obtained with the Cuoricino experiment 3×3×6 $cm^3$ crystals between April and July. (*) Crystal 14 has no heater.

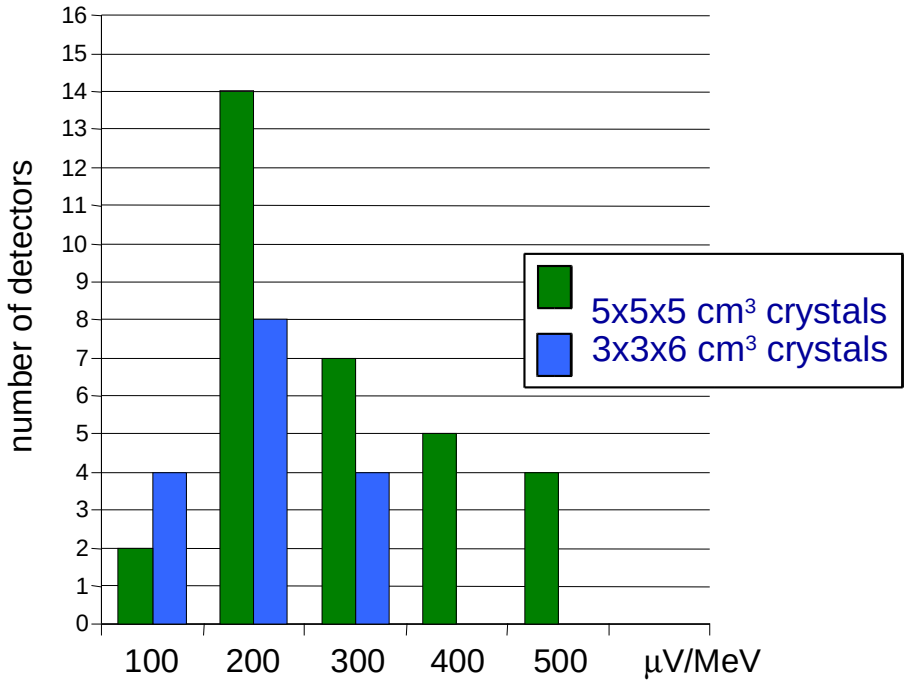


Figure 6.27 - The histogram contains the signal amplitude normalized to a 1 MeV deposited energy for the Cuoricino big and small size detectors. The detector energy responses are normalized to 1 kg of $TeO_2$ .

| Crystal | relative fall time index |
|---|---|
| B37 | 0.9501 |
| B55 | 0.9404 |
| B13 | 0.9383 |
| B53 | 0.9329 |
| B41 | 0.9310 |
| B44 | 0.9209 |
| B47 | 0.9197 |
| B60 | 0.9023 |
| B52 | 0.8991 |
| B28 | 0.8935 |
| B29 | 0.8934 |
| B17 | 0.8920 |
| B31 | 0.8848 |
| B57 | 0.8797 |
| B36 | 0.8774 |
| B51 | 0.8689 |
| B34 | 0.8650 |
| B42 | 0.8508 |
| B15 | 0.7322 |
| B18 | 0.7152 |
| B27 | 0.6776 |
| B46 | 0.6767 |
| B54 | 0.6256 |
| B45 | 0.5661 |
| B7 | 0.5543 |
| B12 | 0.4331 |
| B56 | 0.4089 |
| B26 | 0.3983 |
| B10 | 0.3972 |
| B61 | 0.3893 |
| B40 | 0.1892 |

Table 6.5 - Summary of detectors relative fall time indexes. The relative fall time index gives an idea of the existence of a second decay slope in the pulse.

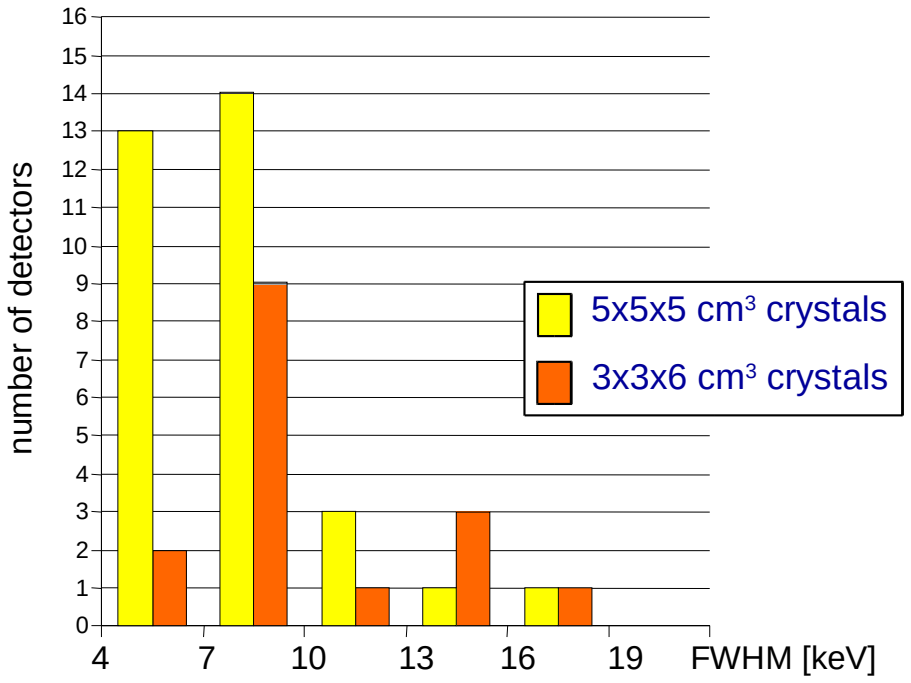


Figure 6.28 - The histogram contains the energy resolutions for the Cuoricino big and small size detectors.

decay time. The second decay "constants" are longer than those of the pulses obtained in the previous Cuoricino tests. To achieve this classification it was decided to introduce a new parameter: the relative fall time index. After converting the pulse amplitude in $\mu$V/MeV, the fall part of the signals has been fitted with two exponentials, in order to obtain an indication of their two decay time constants. If $\tau_1$ is assumed to be the decay time of the first slope of the pulse and $\tau_2$ of the second one, the relative fall time index is defined as $\tau_2 - \tau_1$ over $\tau_2$; its value is ranging from 0 to 1 and the closer it is to 1 the longer the second time constant is. The results are summarized in tab. 6.5. The line in the table divides the detector with pulses having long tails from those with "normal" ones. It is also clear from the value of the relative fall time index that there isn't a sharp distinction between the two classes and that the separation value was decided arbitrarily. In fig. 6.31 an example of the work performed to obtain the classification is reported. Tab. 6.6 and 6.7 show the (10-90%) rise times, the (30-90%) decay times and the (10-90%) decay times of all the Cuoricino detector pulses. The problem of the signal shapes is not present in the $3\times3\times6$ cm$^3$ natural $TeO_2$ crystal bolometers. Many hypotheses on the causes of this effect have been formulated, the principal are the following:

- This effect may be explained as a consequence of the surface polish, made for radioactive background reduction reasons. Indeed, the $3\times3\times6$ cm$^3$ crystals have a different axis of growth from those of $5\times5\times5$ cm$^3$ and this caused a different roughness of the crystal surfaces after the polish. Anyway this doesn't explain the fact that also some $5\times5\times5$ cm$^3$ detec-

| Crystal | rise time (10-90%) | decay time (10-90%) | decay time (30-90%) |
|---|---|---|---|
| B37 | 51 | 2598‘ | 172 |
| B55 | 65 | 1261 | 170 |
| B13 | 57 | 272 | 128 |
| B53 | 73 | 458 | 153 |
| B41 | 74 | 511 | 169 |
| B44 | 66 | 503 | 169 |
| B47 | 79 | 1095 | 195 |
| B60 | 53 | 1583 | 241 |
| B52 | 100 | 498 | 229 |
| B28 | 50 | 2069 | 295 |
| B29 | 54 | 692 | 206 |
| B17 | 48 | 999 | 165 |
| B31 | 88 | 324 | 186 |
| B57 | 64 | 1897 | 294 |
| B36 | 64 | 1527 | 245 |
| B51 | 73 | 1128 | 304 |
| B34 | 63 | 1891 | 327 |
| B42 | 57 | 2001 | 367 |
| B15 | 88 | 1021 | 440 |
| B18 | 89 | 1297 | 458 |
| B27 | 72 | 1950 | 598 |
| B46 | 43 | 484 | 164 |
| B54 | 100 | 1201 | 490 |
| B45 | 65 | 748 | 279 |
| B7 | 85 | 1310 | 523 |
| B12 | 74 | 1288 | 561 |
| B56 | 82 | 1208 | 538 |
| B26 | 71 | 544 | 260 |
| B10 | 66 | 1020 | 465 |
| B61 | 89 | 1868 | 784 |
| B40 | 68 | 495 | 260 |
| B16 | 79 | 470 | 249 |

Table 6.6 - Summary of the Cuoricino array large size detectors time constants. The rise time is calculated as the 10-90% of the pulse amplitude and is reported in the first column, whereas the 90-30% decay time and the 90-10% are reported in the second column and in the third one.

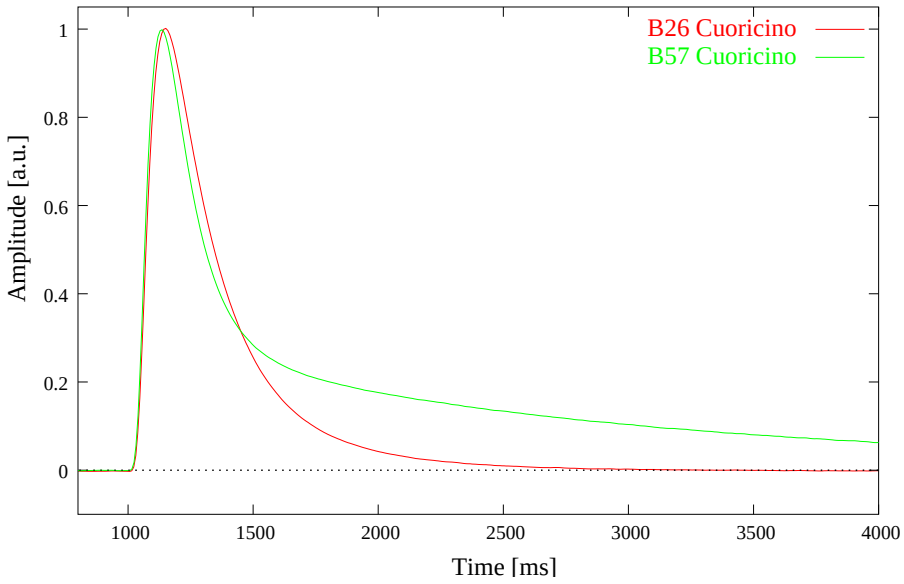


Figure 6.29 - Comparison between a "normal pulse" and a "pulse with tail"; both have been obtained with the Cuoricino detectors. The pulses are normalized.

tors produce signal with "classical" shape, and at the moment it is not possible to know if the 5×5×5 crystal that present classical shapes have a surface crystal quality better than the other ones and so it is difficult to demonstrate some correlation between these two characteristics.

- Another possibility concerns the impurities contained in the crystals. For example it is known that a contamination of platinum ($^{190}$Pt) is present in the bulk of the absorber. This contamination produces a line at ∼ 3300 keV giving an everage counting rate of ∼0.6e-2 c/h/crystal. This contamination is estimated to be located in the bulk as it was not changed in the 3×3×6 crystal after the cleaning procedure. It was estimated that the quantity of platinum contained is not negligible (of the order of $10^{-7}$-$10^{-6}$ g/g) and is probably due to platinum crucibles that are used by SICCAS to produce the crystals. For some detectors this contamination is more pronounced, as for the enriched crystals. It must be remarked that in the case of the Pt contamination there are contradictory indications: for example the estimated quantity of Pt in the enriched crystals is not compatible with the results obtained from the analysis made with a mass spectrometer.

The average FWHM resolution measured during the calibration of the detectors with a $^{232}$Th source is about 7 keV for the 5×5×5 cm$^3$ crystals and about 9 keV for the 3×3×6 cm$^3$ ones. Both these values are measured on the $^{208}$Tl gamma line at 2615 keV. The sum calibration spectra of the large size crystals and that of the small size ones are shown in fig. 6.42

Concerning the small size crystals, one of the two central detectors had its Si heater disconnected, while another detector showed a variation in the

| Crystal | rise time (10-90%) | decay time (10-90%) | decay time (30-90%) |
|---|---|---|---|
| 5 | 50 | 1007 | 481 |
| F | 61 | 839 | 386 |
| 2 | 46 | 1047 | 512 |
| 4 | 46 | 814 | 373 |
| 6 | 52 | 796 | 364 |
| B | 66 | 853 | 378 |
| 16 | 66 | 613 | 277 |
| 0 | 50 | 911 | 406 |
| I | 56 | 1055 | 498 |
| E | 65 | 898 | 392 |
| 13 | 62 | 832 | 337 |
| 9 | 62 | 968 | 446 |
| 128-1 | 48 | 1622 | 599 |
| 128-2 | 35 | 544 | 79 |
| 130-1 | 32 | 1215 | 351 |
| 130-2 | 42 | 903 | 184 |

Table 6.7 - Summary of Cuoricino array small size detectors time constants. The data in the upper part of the table correspond to the natural crystals whereas the last 4 rows correspond to the enriched ones. Again the rise time is calculated as the 10-90% of the pulse amplitude and is reported in the first column, whereas the 90-30% decay time and the 90-10% are reported in the second column and in the third one.

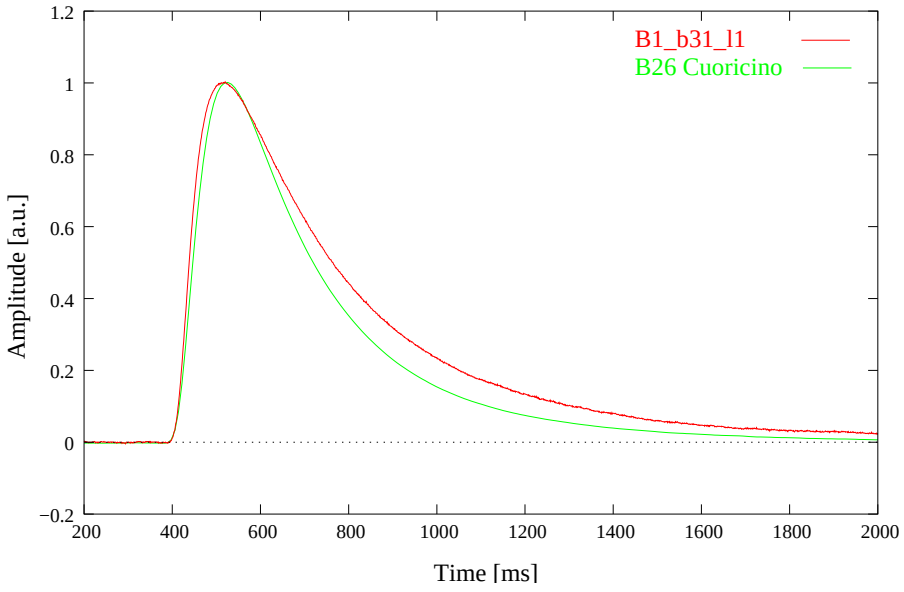


Figure 6.30 - Comparison between a “normal pulse” obtained with the historical B1 detector operated in hall C and a “normal pulse” obtained in the Cuoricino experiment with detector B26. The pulses are normalized.

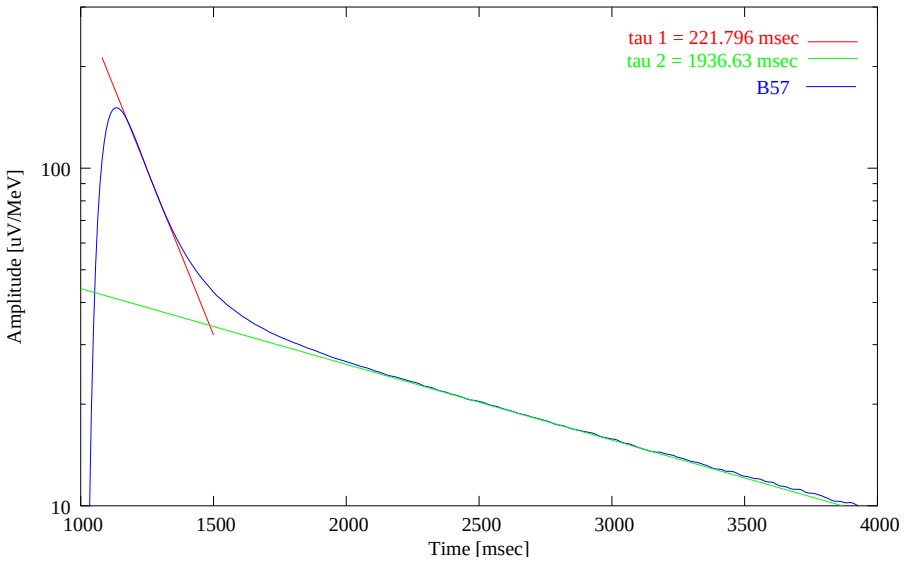


Figure 6.31 - Pulse of detector B57 plotted in semi-logarithmic scale. The two slopes of the decay pulse phase are fitted with exponentials in order to obtain their decay time constants. The relative fall time index of this pulse is equal to 0.8854.

reference pulse after some weeks of running: once again a problem with the electrical connections. The number of well–working $3\times3\times6$ cm$^3$ detectors was consequently reduced to 11 natural crystals and to 4 enriched ones. During the first part of the background measurements, a problem due to a change in the energy response of some of the small size crystals, was presented. In fact, a variation in the position of the gamma lines between the calibration measurements at the beginning of the run and the next ones, was observed. As a consequence the background statistics for these crystals are lower than expected. The reason for the detectors energy response variation was identified in the fact that their mounting structure is more sensitive to variations in the refrigerator conditions; in fact the only detectors that present this problem are those containing the old PTFE pieces. To avoid this problem we tried to have better control on the refrigerator conditions and to calibrate the detector more frequently with a higher intensity source. With this source a more frequent calibration will be possible without reducing the live time of the background measurement. In addition during the warm-up of the refrigerator, the Cuoricino tower will provided with special thermometers that will be allow the installation of apply a temperature stabilization system. This should further reduce any problem connected to thermal instabilities of the refrigerator.

## 6.4 Background levels and Cuoricino results

The evaluation of the possible background sources is affecteded by a large error since the statistics collected up to now are very low. All the results this paragraph have been obtained using the sum of all the detectors spectra since the

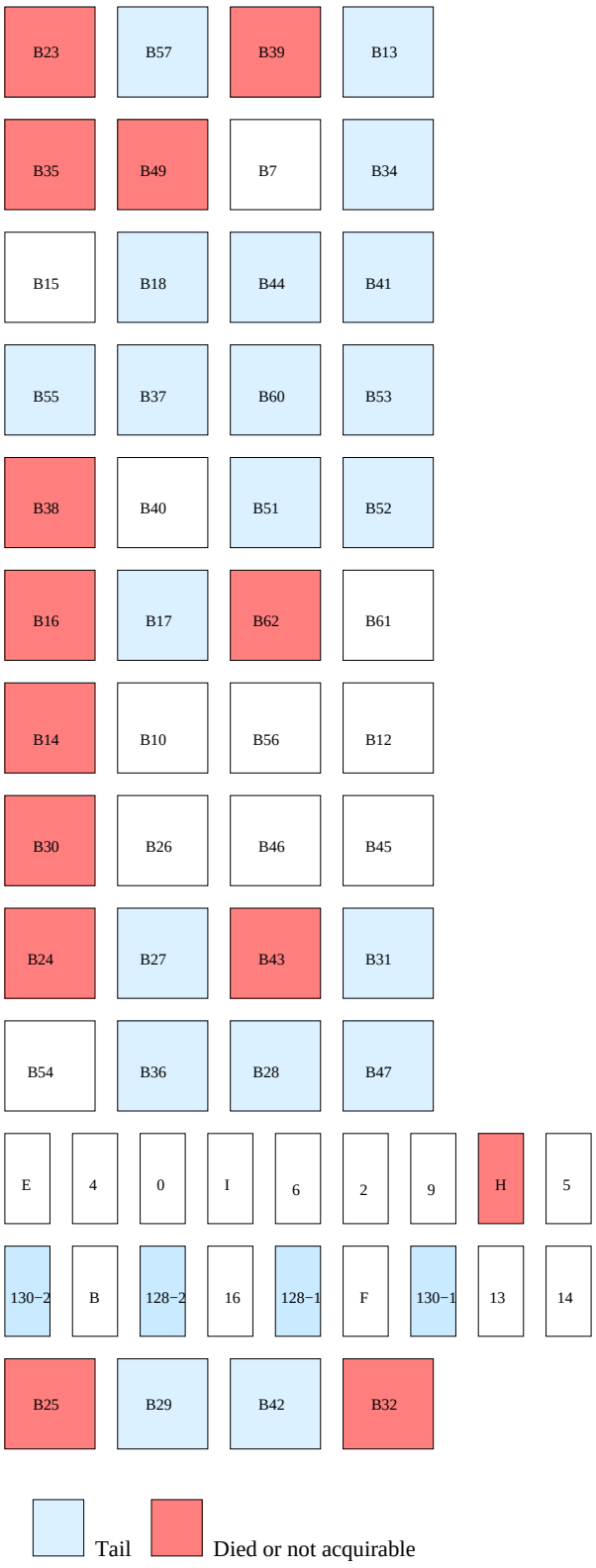


Figure 6.32 - Scheme of the Cuoricino tower. The blue color indicates detectors characterized by long tail signals; the red color indicates not acquirable detectors.

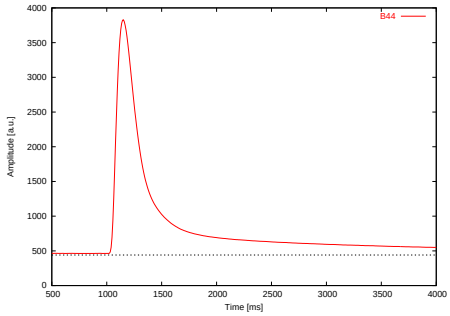


(a) plane 1, crystal B57

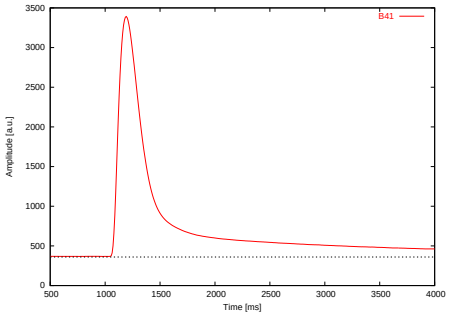


(b) plane 1, crystal B13

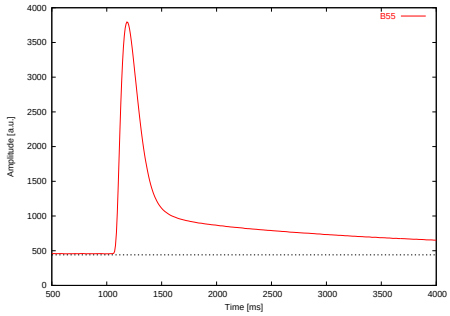


(c) plane 2, crystal B7

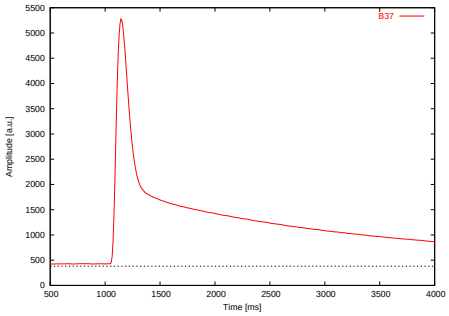


(d) plane 2, crystal B34

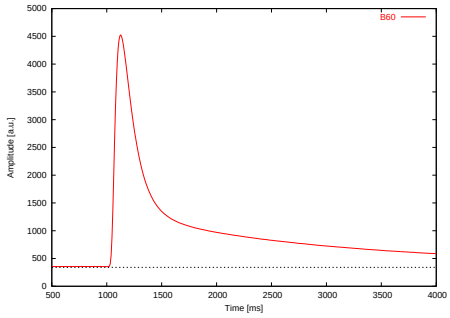


(e) plane 3, crystal B15

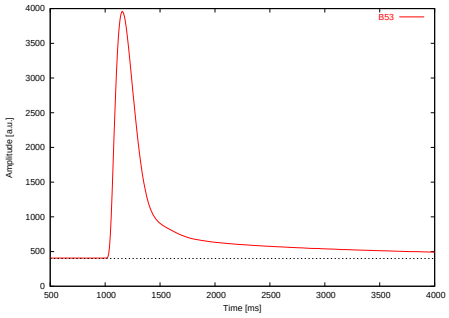


(f) plane 3, crystal B18

Figure 6.33 - Typical $5\times5\times5$ cm$^3$ Cuoricino bolometers pulses.

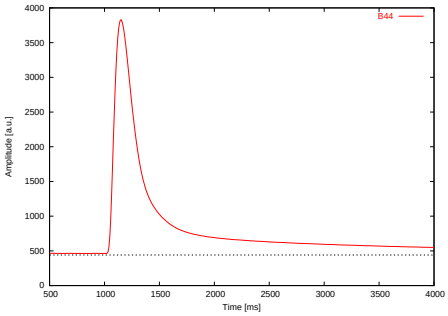


(a) plane 3, crystal B44

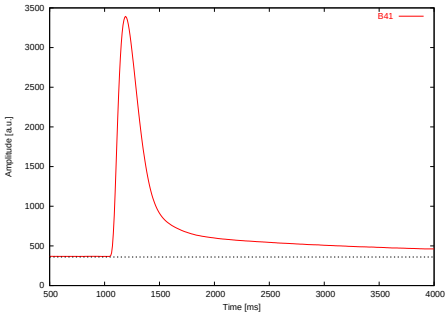


(b) plane 3, crystal B41

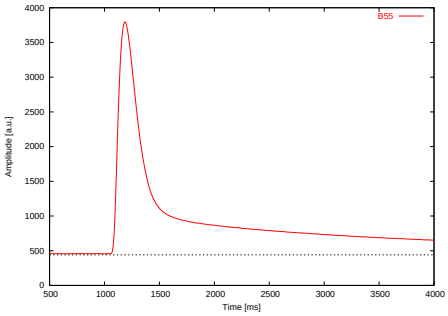


(c) plane 4, crystal B55

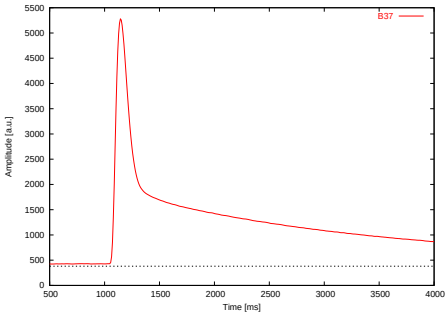


(d) plane 4, crystal B37

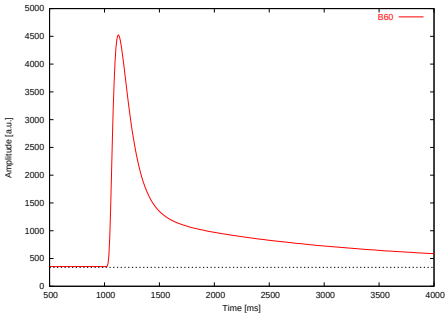


(e) plane 4, crystal B60

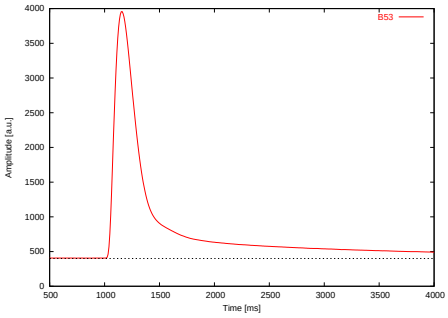


(f) plane 4, crystal B53

Figure 6.34 - Typical 5×5×5 $cm^3$ Cuoricino bolometers pulses.

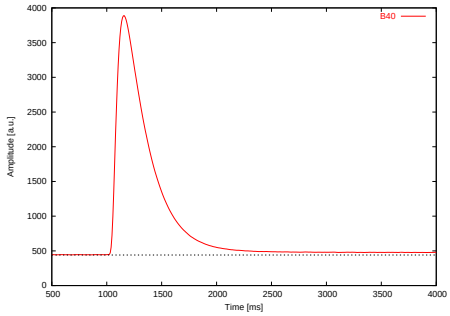


(a) plane 5, crystal B40

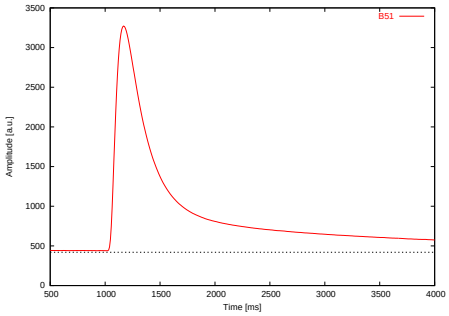


(b) plane 5, crystal B51

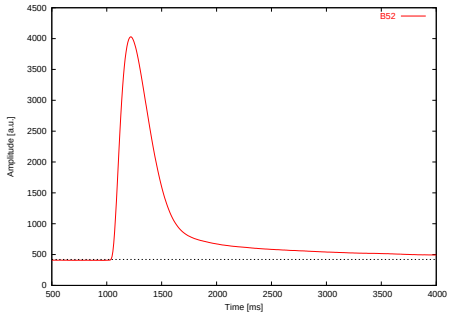


(c) plane 5, crystal B52

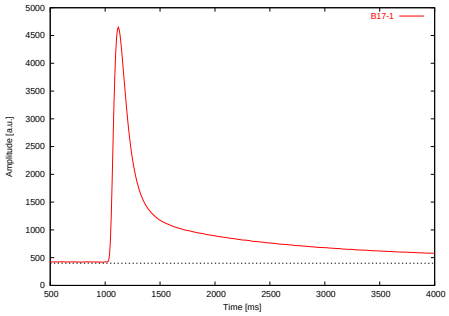


(d) plane 6, crystal B17

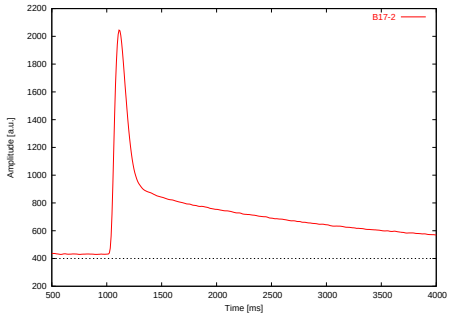


(e) plane 6, crystal B17

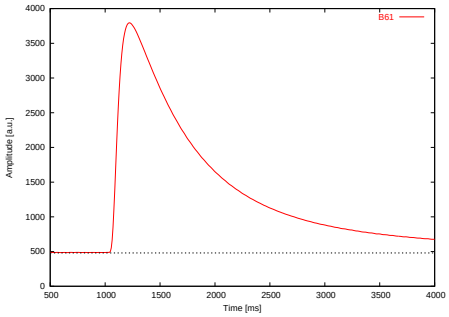


(f) plane 6, crystal B61

Figure 6.35 - Typical $5\times5\times5$ cm$^3$ Cuoricino bolometers pulses.

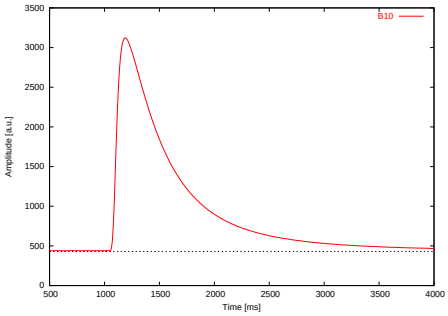


(a) plane 7, crystal B10

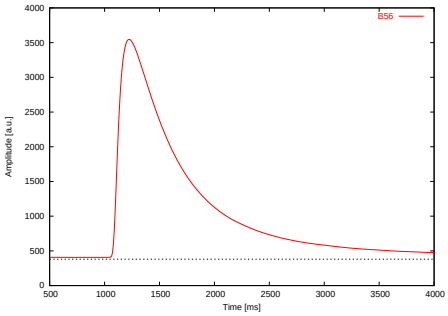


(b) plane 7, crystal B56

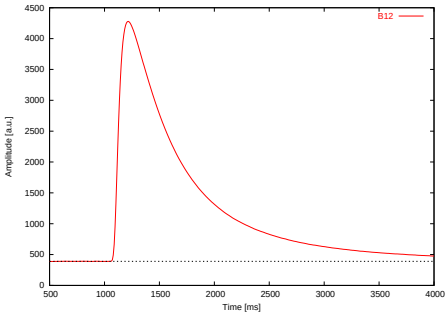


(c) plane 7, crystal B12

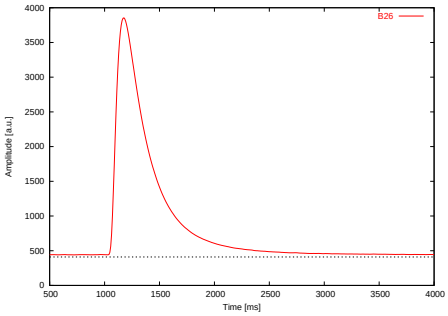


(d) plane 8, crystal B26

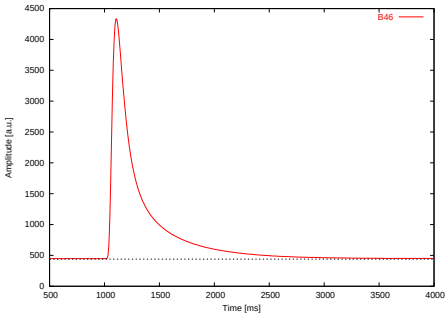


(e) plane 8, crystal B46

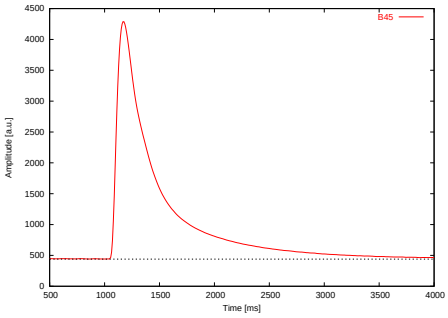


(f) plane 8, crystal B45

Figure 6.36 - Typical $5\times5\times5$ cm$^3$ Cuoricino bolometers pulses.

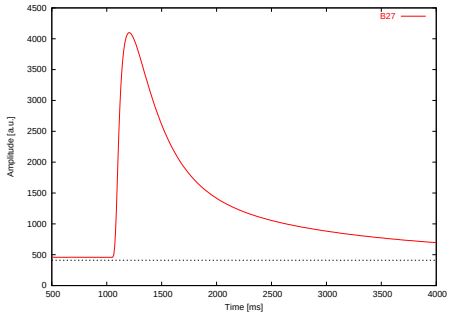


(a) plane 9, crystal B27

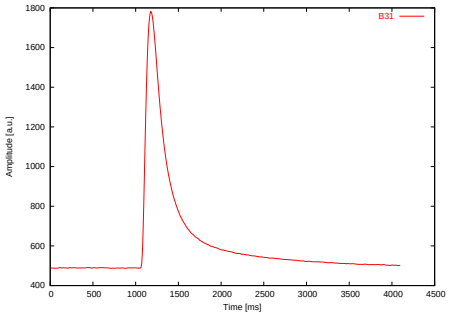


(b) plane 9, crystal B31

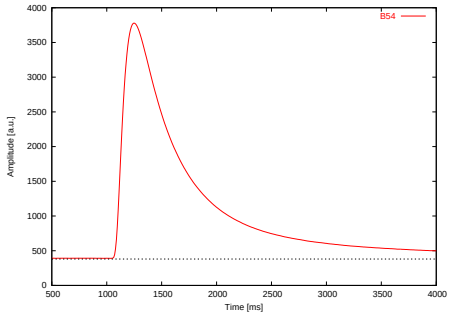


(c) plane 10, crystal B54

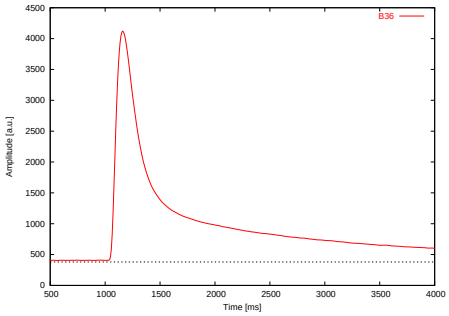


(d) plane 10, crystal B36

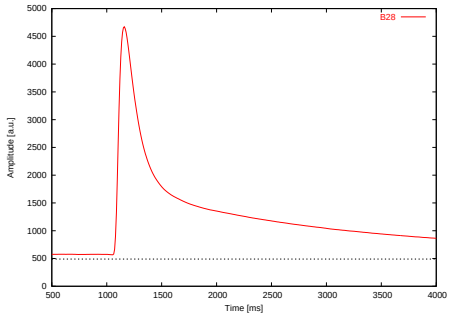


(e) plane 10, crystal B28

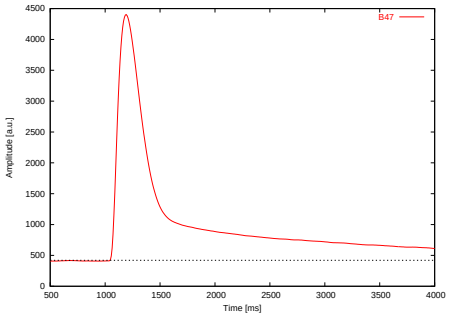


(f) plane 10, crystal B47

Figure 6.37 - Typical $5\times5\times5$ cm$^3$ Cuoricino bolometers pulses.

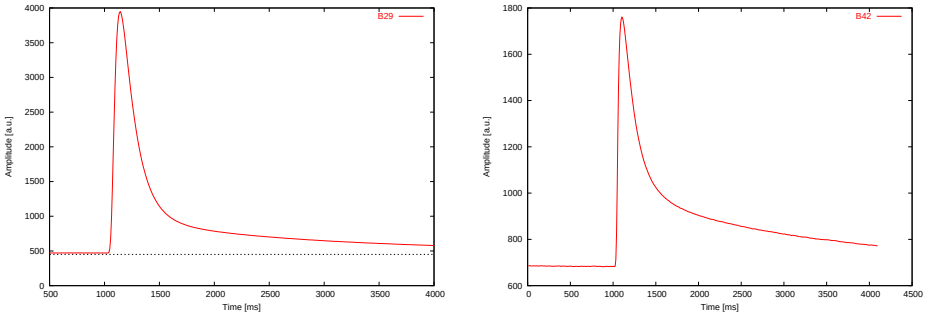


(a) plane 13, crystal B29 (b) plane 13, crystal B42

Figure 6.38 - Typical 5×5×5 $cm^3$ Cuoricino bolometers pulses.

statistics on each single one was so low.

The total collected running time on the background measurement was $\sim$ 31218 hours for 5×5×5 $cm^3$ crystals (thus corresponding to 25000 hours×kg) and $\sim$ 6975 hours for 3×3×6 $cm^3$ ones (corresponding to $\sim$ 2300 hours×kg).
The related background spectra are shown in fig. 6.43. The gamma lines due to $^{60}$Co, $^{40}$K and to the $^{238}$U and $^{232}$Th chains are clearly visible.

These lines, due to some contamination of the apparatus, are not visible in the spectra of each single detector: they appear only in the 29 detectors summed spectum and are a very good check of the detectors calibration and stability during the background measurements.

The FWHM resolution during the background measurements of the 5×5×5 $cm^3$ detectors at low energy, as evaluated at the 122 keV gamma line of $^{57}$Co, is 2.8 keV; the $^{208}$Tl gamma line FWHM at 2615 keV, clearly visible in the background summed spectrum and used to evaluate the energy resolution in the region of the double beta decay, is 8.7 keV and the background in the same region (i.e. 2510-2580 keV) is 0.20 $\pm$ 0.03 counts/keV/kg/y.
The statistics on the 3×3×6 $cm^3$ are much lower and the values are in this case respectively 1.5 keV FWHM for the gamma line of $^{57}$Co, 12 keV for the $^{208}$Tl and 0.2 $\pm$ 0.1 counts/keV/kg/y for the background in the $0\nu$DBD region.
The comparison between the background spectra of the small and the large crystal are reported in fig. 6.44 and 6.45.

The background spectra of the large and small size crystals in the region of neutrinoless double beta decay are compared in fig. 6.46. If they are normalized to the mass of the crystals, the two spectra shapes and their counting rates are quite similar. But on the other hand the intensities of the $\gamma$ lines do not show a clear behavior; the 1764 keV line (the only clearly visible of the U chain) and the 2615 keV line (the only clearly visible of the Th chain) seem to scale with the detectors efficiency (that is three times higher for the 5×5×5 crystals than for the 3×3×6 ones). The $^{40}$K line has the same intensity per unit mass

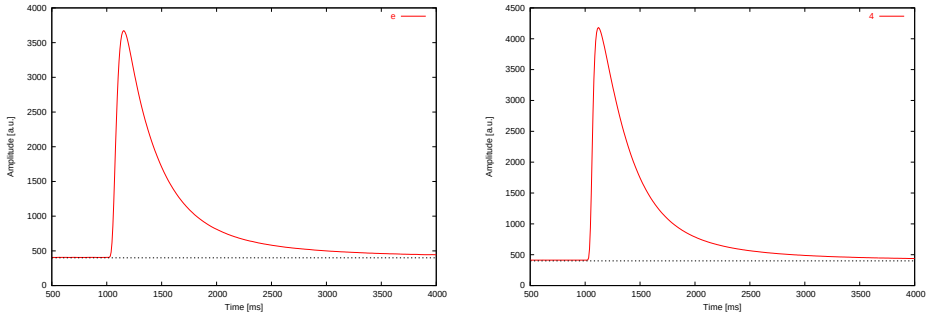


(a) plane 11, crystal E

(b) plane 11, crystal 4

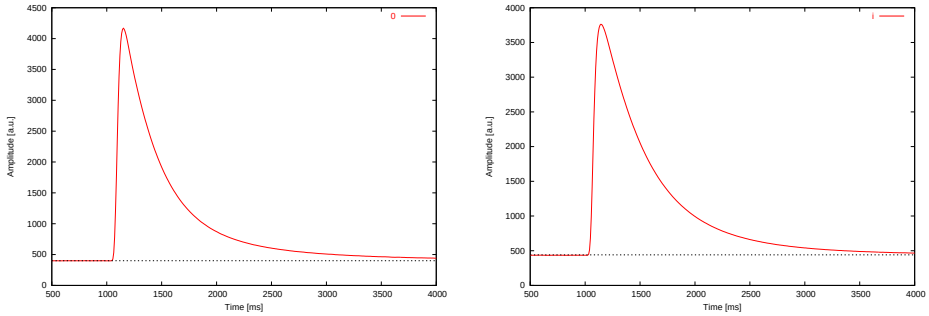


(c) plane 11, crystal 0

(d) plane 11, crystal I

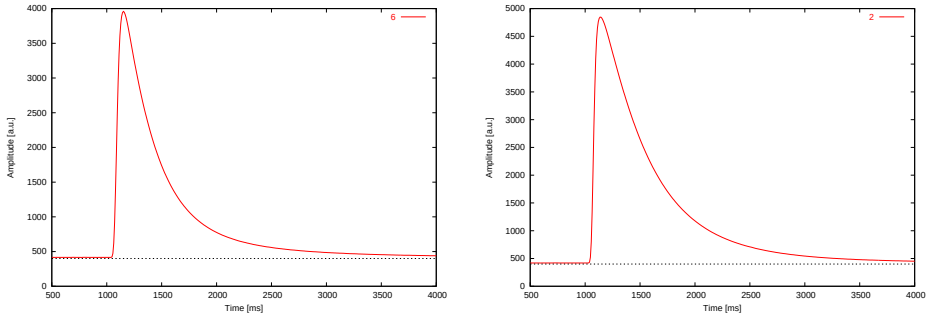


(e) plane 11, crystal 6

(f) plane 11, crystal 2

Figure 6.39 - Pulses obtained with the 3×3×6 $cm^3$ crystal detectors of Cuoricino.

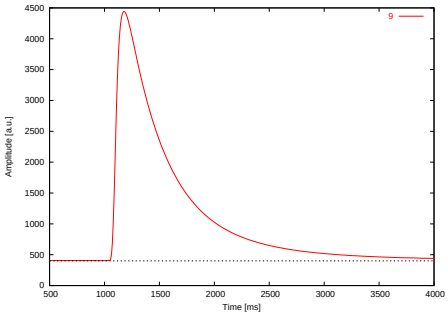


(a) plane 11, crystal 9

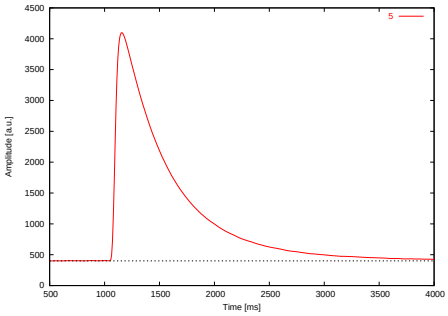


(b) plane 11, crystal 5

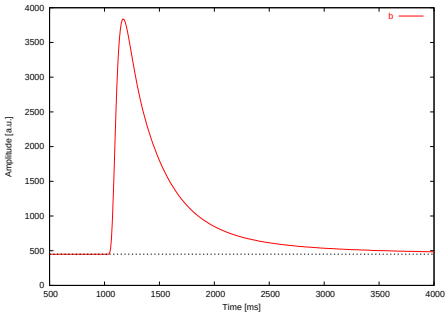


(c) plane 12, crystal B

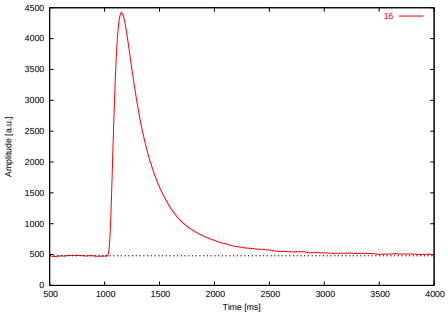


(d) plane 12, crystal 16

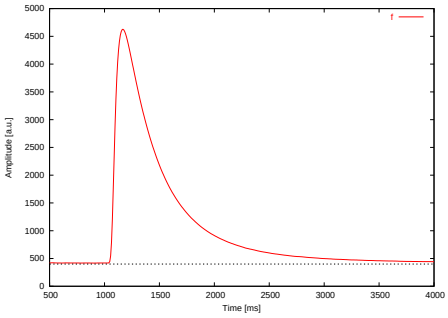


(e) plane 12, crystal F

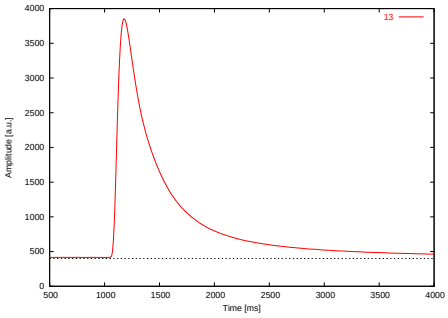


(f) plane 12, crystal 13

Figure 6.40 - Pulses obtained with the $3\times3\times6$ cm$^3$ crystal detectors of Cuoricino.

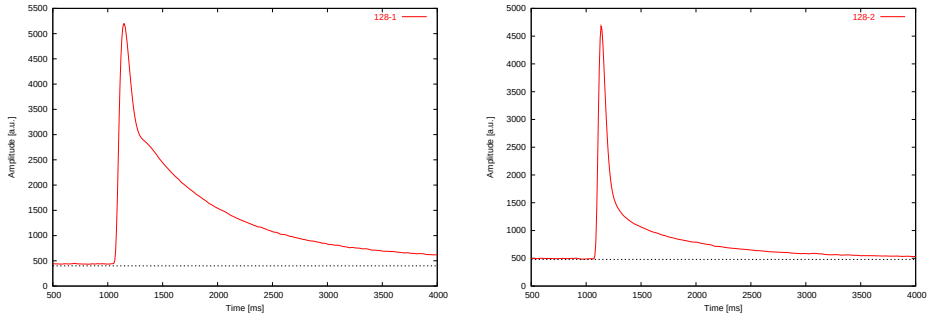


(a) plane 12, crystal 128-1

(b) plane 12, crystal 128-2

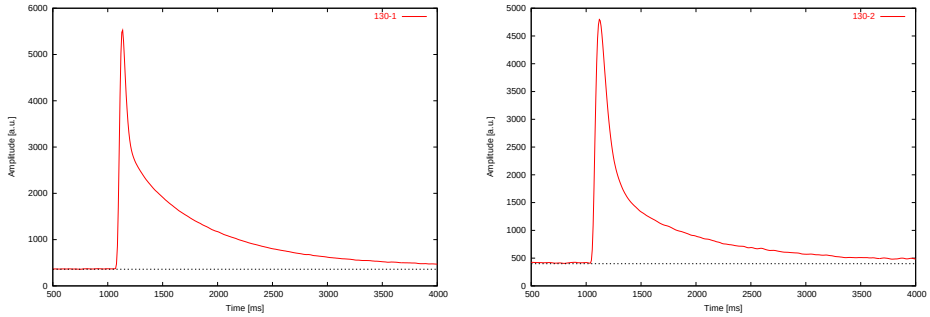


(c) plane 12, crystal 130-1

(d) plane 12, crystal 130-2

Figure 6.41 - Pulses obtained with the 3×3×6 cm$^3$ enriched crystal detectors of Cuoricino.

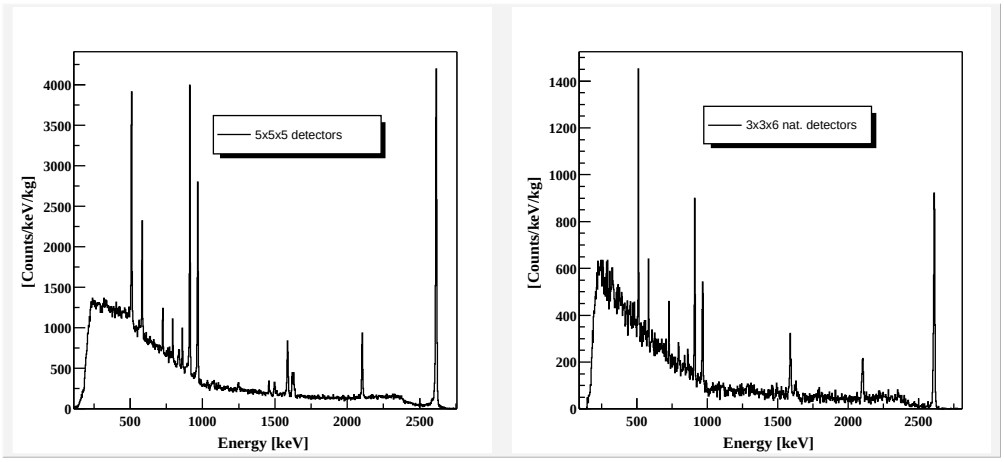


Figure 6.42 - Summed calibration spectra from all the operating 5×5×5 cm$^3$ and 3×3×6 cm$^3$ crystal detectors.

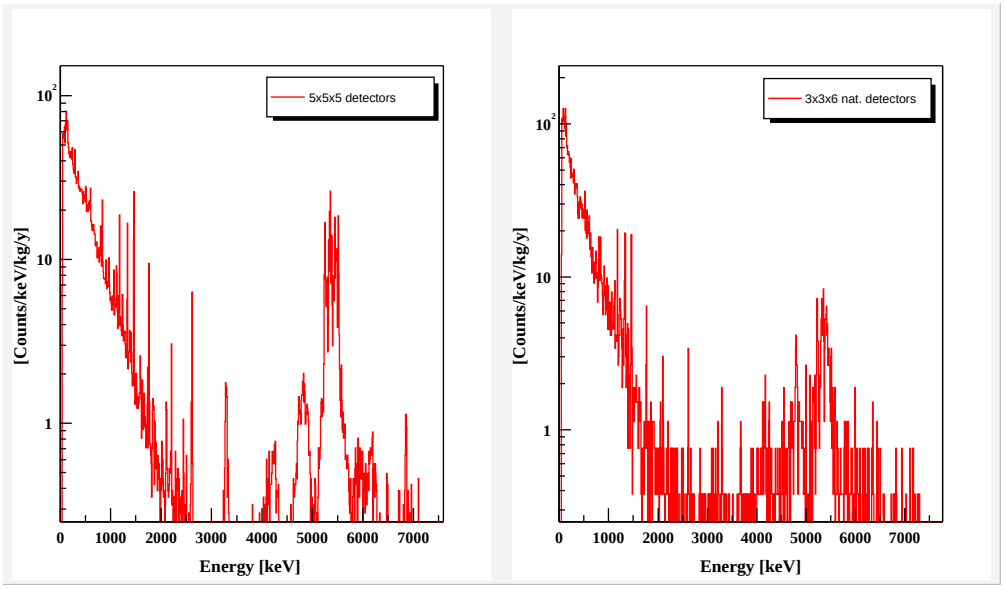


Figure 6.43 - Summed background spectra from the operating 5×5×5 and (natural abundance) 3×3×6 crystals.

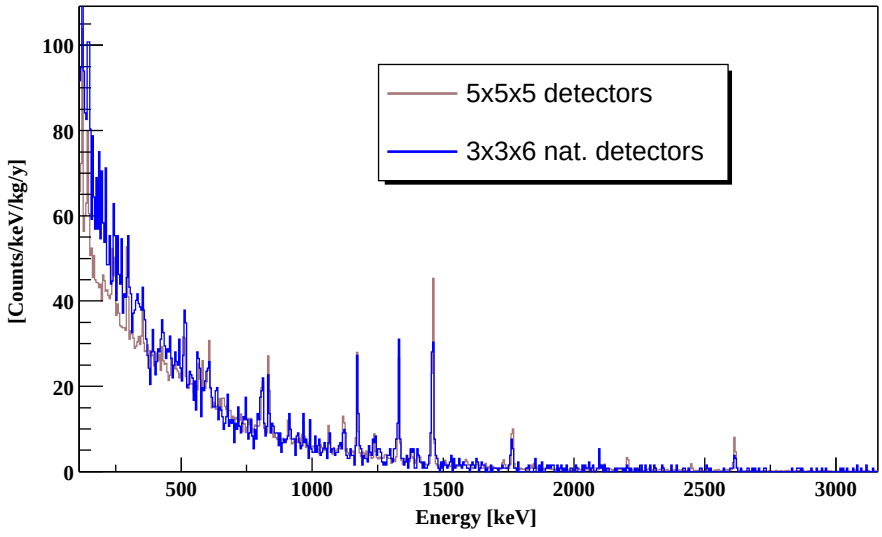


Figure 6.44 - Comparison between the background of the big and the small size crystals in the gamma region.

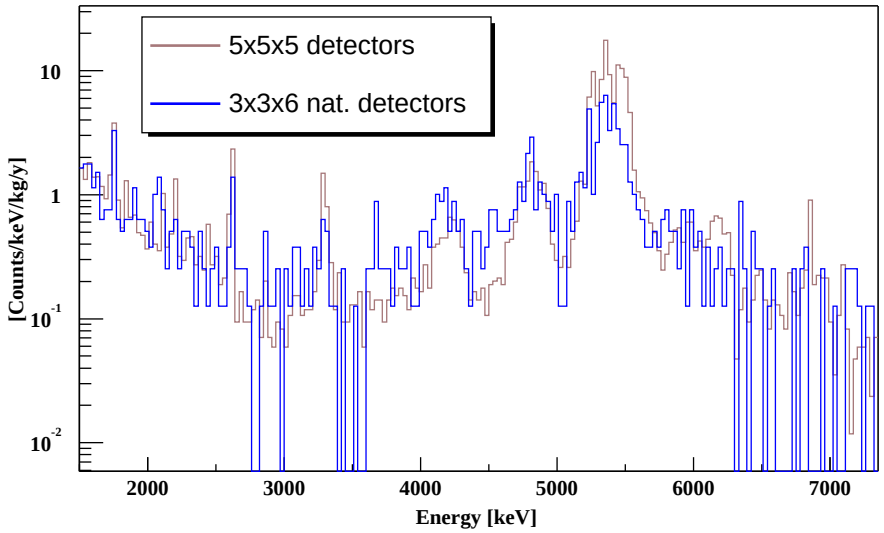


Figure 6.45 - Comparison between the background of the big and the small size crystals in the alpha region.

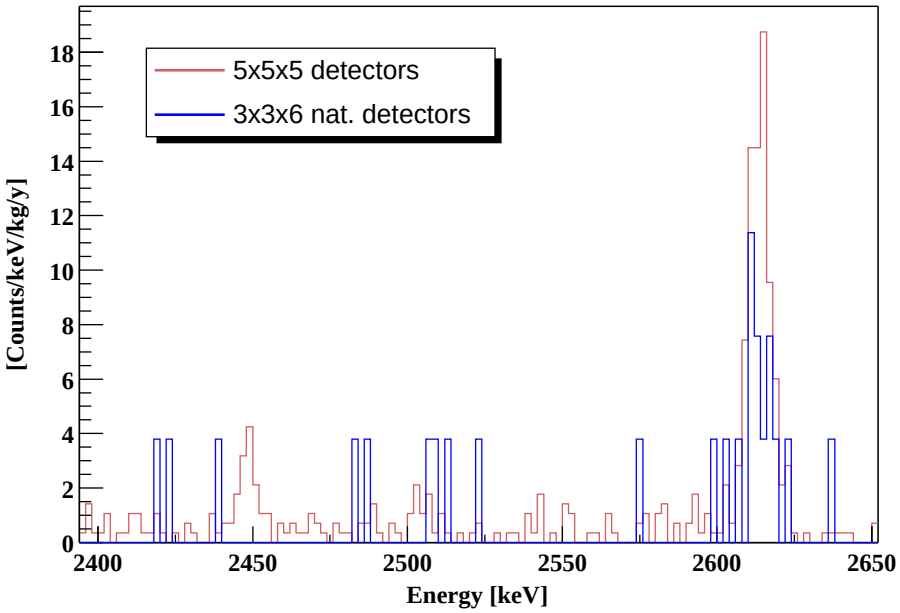


Figure 6.46 - Comparison between the background of the big and the small size crystals in the double beta decay region.

on the both kind of detectors while the $^{60}$Co lines show a higher intensity per unit mass in the small crystals. Moreover they undergo a larger reduction by the anticoincidence cuts than the other lines. The values of background levels in the different energy spectra regions are reported in tab. 6.8. It is clearly evident

| counts/keV/kg/year | 1-2 MeV | 2-3 MeV | 3-4 MeV | 4-5 MeV |
|---|---|---|---|---|
| MiDBD–II | 3.21±0.08 | 0.61±0.04 | 0.29±0.02 | 1.88±0.06 |
| 3×3×6 natural | 3.29±0.11 | 0.38±0.04 | 0.24±0.03 | 0.78±0.05 |
| 5×5×5 | 3.25±0.09 | 0.41±0.03 | 0.17±0.02 | 0.55±0.03 |

Table 6.8 - Background levels obtained in various energy regions by the Cuoricino experiment.

that an improvement was obtained in the 2-3 MeV region (a reduction of 30% in the counting rates per unit mass either of the small and of the big crystals) despite the reduced internal lead shield used in Cuoricino ($\sim$ 1.2 cm thickness of roman lead) with respect to MiDBD–II ($\sim$ 3 cm thickness of roman lead). An even better reduction was obtained in the 3-4 MeV region where the background is mainly dominated by surface contamination contributions.

To understand the reasons for this variation in the counting rates and also for the differences between small and big crystals, more statistics are needed. The study of small energy regions at the left and at the right of the $^{208}$Tl will allow us to disentangle the different background sources. In fact, the background in the region between the two gamma peaks at 2448 and 2615 keV ($^{238}$U and $^{232}$Th chains respectively) has contributions both from degraded $\alpha$'s from surface contaminations and from $^{208}$Tl $\gamma$'s from bulk ones. Indeed in the region just above the $^{208}$Tl 2615 keV line, the background is only due to surface contamination. Moreover, it should be stressed that the effect of disconnected detectors in reducing the efficiency of the anticoincidence cut (a fundamental tool to study and localize background sources) is not negligible.

However, as for the MiDBD analysis, the MonteCarlo simulation has been used to study the shape and counting rate of the Cuoricino background spectra taking into account that both the detector structure and the cryostat internal set–up were changed (the roman lead shield and the cryostat copper radiation ones).
This analysis was limited to the 5×5×5 cm$^3$ crystal detectors for which the statistics are higher. The result, in terms of percentage of the background measured in the DBD region, is summarized in tab. 6.9. It should be noticed that Cuoricino data seem to indicate a shallower depth for the crystal surface contaminations with respect to MiDBD. A better determination of the actual depth and a density profile of this contamination will be available only when Cuoricino will be fully operating and higher statistics will allow a more significant multiple event analysis. We tried to localize the $^{232}$Th responsible for the 2615 keV line by comparing all the measurements made using the same cryostat during the last 10 years. According to the low intensity of the Th chain 238 keV peak with respect to the 2615 keV one it is proven that the contamination has to be outside the internal lead shield. It is very likely located in the refrigerator thermal shields or in the OVC that contains aluminated mylar foils. In order to verify

| Contamination source | $^{208}$Tl | $0\nu$DBD region | 3-4 MeV region |
|---|---|---|---|
| $^{238}$U, $^{232}$Th from $TeO_2$ surface | - | 20±15% | 20±10% |
| $^{238}$U, $^{232}$Th from Cu surface | 15% | 50±20% | 80±10% |
| $^{232}$Th from cryostat Cu shields | 85% | 30±10% | - |

Table 6.9 - Estimate of the weight of the different sources responsible for the background measured in Cuoricino.

this hypothesis it is planned to measure, during the next stop of Cuoricino, the gamma background inside the OVC using a Ge detector.

Regarding the 4 enriched crystals a reduction of $\sim$ 20% in the background level between 1 and 3 MeV and in the alpha peaks between 4 and 6 MeV has been observed. On the other hand the counting rate corresponding to their $^{40}$K line is the same. In MiDBD–II an excess on one of the $^{130}$Te enriched crystals was observed. However, for this experiment longer measurements were required in order to improve the evaluation obtained for the $2\nu$DBD half–life, by reducing the statistical and systematic errors.

The 2 central crystals of the 9 detector modules were intended to disentangle the background contributions due to the $TeO_2$ crystals and copper mounting structure surface contaminations. Indeed the two central crystals face a copper surface that is $\sim$ 3 times smaller than the one faced by the crystals placed at the edges of the modules. This kind of analysis requires to have a good statistics in the 3-5 MeV region, together with a good detector. At the moment these requirements are not met so it has to be postponed.

Because of the poor statistics acquired with the small crystals, only the big size ones have been used to obtain limit on the $0\nu$DBD half–life .
No peak appears in the background spectrum at the position of the $^{130}$Te beta decay transition energy (see fig. 6.47).

Using the Maximum Likelihood procedure to establish the maximum number of $0\nu$DBD events compatible with the measured background, an upper limit of $5.5\times10^{23}$ years was determined (with a 90% confidence level) for the $0\nu$DBD half–life, this corresponds to an effective neutrino mass ranging from 0.38 to 2.2 eV, depending on the used nuclear model.

This early Cuoricino results already show that the experiment is competitive in the field of neutrinoless double beta decay. When Cuoricino will be fully operational, it will have a 5 year sensitivity (at 68% C.L.) equal to $\sim10^{25}$ years for the $0\nu$DBD of $^{130}$Te . This means that Cuoricino will be able to test the Majorana mass in the 100-500 meV range.

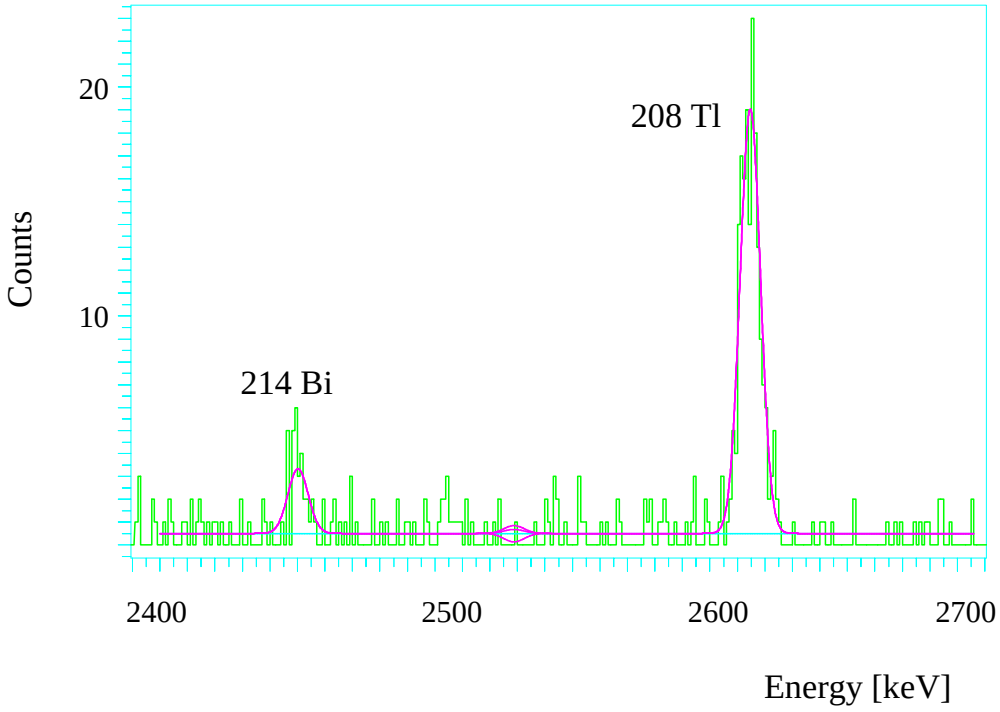


Figure 6.47 - Summed background spectrum from all the operating crystals in the region of neutrinoless double beta decay of $^{130}$Te (Q-value=2528.8 keV).

# Chapter 7

# The Cuoricino single module: thermal model

## 7.1 Introduction

In this chapter the work on the detector behavior simulation performed by the Como group will be detailed. The main reasons to perform these simulation are:

- to understand the Cuoricino detector behavior in terms of its principal thermal parameters;
- to apply the simulation work to the optimization of the single CUORE module;
- to use information achieved in the Cuoricino detector simulation to design innovative devices for the CUORE experiment.

In chap. 2 a naive thermal model of the detector was introduced. It describes the detector as a single system weakly coupled to the heat bath. A more complete thermal model will be introduced in the sec. 7.2. This model will allow the introduction of equations describing the static and dynamic detector behaviors. The static equations permit to obtain the temperatures of the various components of the detector, when it is at thermal equilibrium. The dynamic equations describe the temporal behavior of the detector when a certain quantity of energy is released in the energy absorber.
The equation systems obtained from the thermal model cannot be solved analytically, but numerical methods are needed. For this reason numerical programs have been specifically developed for both detector behavior problems. Otherwise, it is possible to analytically solve the dynamic behaviors by making some approximations. The pulses obtained analytically are in good agreement with the numerical ones.
In the first part of this chapter, a complete thermal model, the equation system that describes its static and the dynamic behavior and the approximated analytical solution of dynamic problem, will be detailed.

In the second part of the chapter the simulation results will be presented.
In order to perform the optimization of the detector parameters, a criterion to

compare different detector performances is described. The results of the optimization work are reported in sec. 7.12.
In sec. 7.13 and 7.15 the comparison between the simulated and the Cuoricino experimental results are described. The comparison of the static behavior is satisfactory whereas regarding the dynamic one, there are more problems. In order to solve these problems, new hypotheses have been made and a corresponding correction of the thermal model has been performed. The corrected thermal model is presented in sec. 7.16.
In the last section, a preliminary detector optimization made by using the corrected thermal model is presented. However it must be remarked that, although the results reported in this chapter give valuable indications both on the detector comprehension and on the bolometer optimization, a more detailed work is needed, in particular in the comparison between simulated and experimental data.

## 7.2 Complete thermal model

To achieve a more complete thermal model it is necessary to take into account the heat capacities of the various components of the detectors and the thermal conductance between them and towards the heat bath. Furthermore, electric powers are dissipated on some of these thermal systems. These powers flow in the thermal nodes and arrive at the heat bath through the thermal links. A simple thermal model is represented in fig. 7.1. It is constituted by 2 thermal systems: the energy absorber A and the sensor S having heat capacities $C_a$ and $C_s$ respectively. The energy absorber is connected to the heat bath by a conductance $G_{ab}$ and the two systems are thermally connected by the conductance $G_{as}$. The heat bath has a temperature $T_b$ that is hypothesized to be constant. The temperatures of the energy absorber and of the sensor are indicated with $T_a$ and $T_s$ respectively.

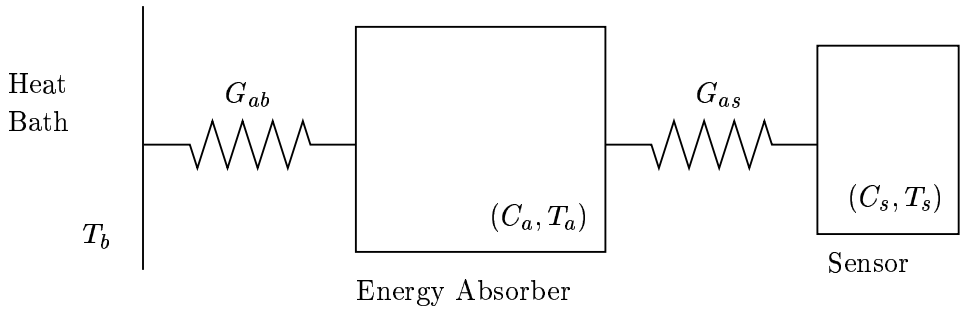


Figure 7.1 - Simple scheme of a bolometric detector composed by 2 stages.

In ideal static conditions all the temperatures are equal to the heat bath temperature, but this is true only if there aren't thermal powers. In the reality, constant thermal background powers $P_b$ act on the energy absorber and on the sensor. The background power on the crystal absorber is probably due to the micro-vibrations, while the one on the sensor is probably due to para-

sitic currents caused by electromagnetic interferences. Taking assumed values for the thermal conductances, the background power and the temperature of the thermal bath, the thermal model can determine the temperatures $T_a$ and $T_s$ and so reproduce the typical load curves of detectors at different heat bath temperatures. Furthermore the thermal model is able to reproduce the dynamic conditions and thus the temporal evolution of the temperatures of the different systems after the conversion into phonons of the energy deposited in the absorber.

The thermal model of fig. 7.1 doesn't take into account that the power dissipated in the thermistor causes a non-ohmic effect explained by the so-called "Hot Electron Model" (HEM). This model envisages a decoupling between the electron system and the lattice one. Due to the powers dissipated, the two sensor systems are characterized by different temperatures, that are indicated respectively as $T_e$ and $T_r$. So, to obtain a more complete thermal model one also has to

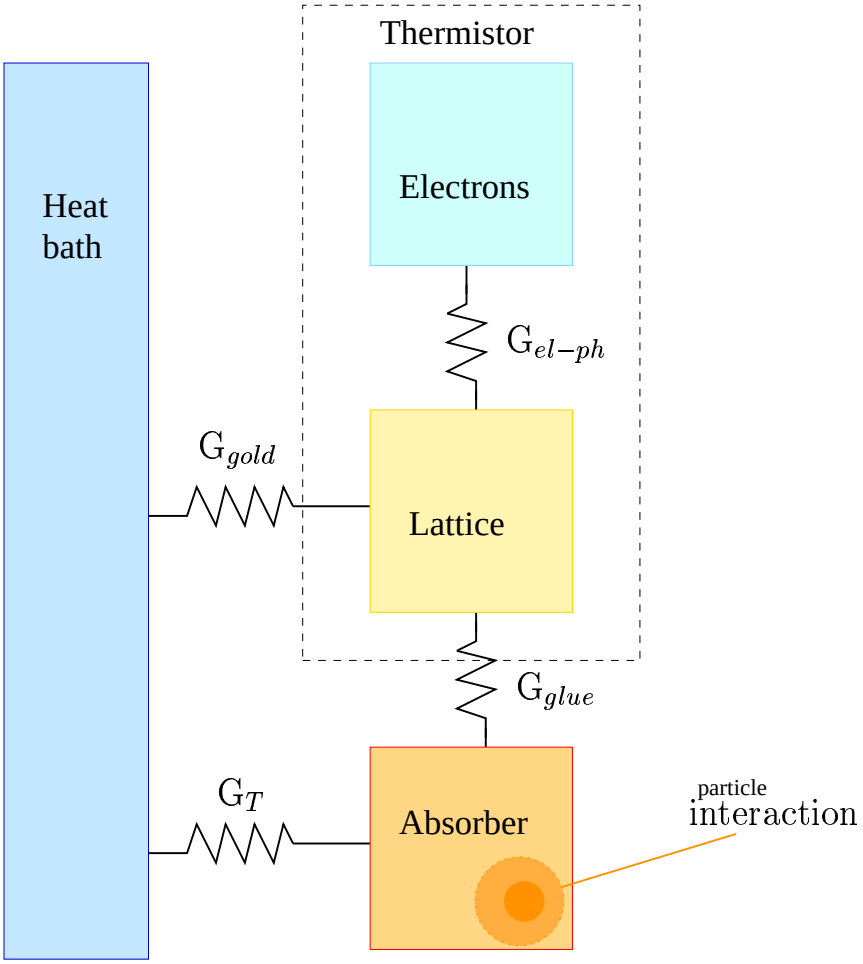


Figure 7.2 - Complete thermal model of a bolometric detector.

take into account the conductance between the electron and the lattice system,

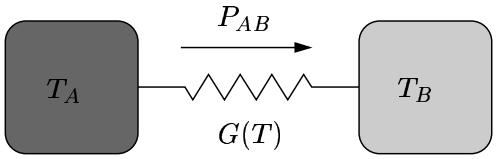


Figure 7.3 - A thermal power $P_{AB}$ flows following the laws of thermodynamics between two systems having temperatures $T_A$ and $T_B$, with $T_A > T_B$ connected by $G$.

named electron-phonon conductance $G_{el-ph}$, and of the gold wires (the electric connections of the sensor), that allow the read-out of the signals and that correspond also to an additional thermal link of the detector to the bath. The electric read-out thermal conductance is indicated by $G_{gold}$. The thermal circuit obtained is reported in fig. 7.2 where the physical nature of the conductances has been taken into account: the conductance between the sensor lattice and the absorber is due to a set of glue spots and is indicated as $G_{glue}$; the conductance of the absorber to the heat bath is due to the Teflon pieces and is indicated as $G_T$.
It can be noted that there aren't couplings between the sensor electron system and the heat bath, and that the thermal conductance $G_{gold}$ links the lattice system to the heat bath. This could appear strange, in particular considering that the thermal transmission is performed by electrons in the conduction band. However a thermal connection between the thermistor electron system and the heat bath was never experimentally observed.
The thermal equations corresponding to the thermal circuit in fig. 7.2 have also to consider the presence of the polarization network of the detector. In fact, the power dissipation raises the sensor temperature and acts back on its resistance, until an equilibrium is reached. This phenomenon makes the V-I relation deviate from linearity. This characteristic behavior of bolometers is often referred to as "electrothermal feedback". The effects of the electrothermal feedback will be explained in sec. 7.5.1.

## 7.3 Static detector behavior

To solve the static problem means to determine the equilibrium configuration for the thermal circuit reported in fig. 7.2. The detector is in thermal equilibrium when the input thermal powers at each node are equal to the output ones.
Let 2 systems, having temperatures $T_A$ and $T_B$ respectively, be coupled by a thermal conductance $G = G(T)$ as fig. 7.3 describes. From the principles of thermodynamics, the heat flows through the conductance from the higher temperature system to the lower temperature system. Then the flowing power is given by:

$$P_{AB} = \int_{T_B}^{T_A} G(T)dT \tag{7.1}$$

The Thermal Model (TM) considered here assumes naively that the detector can be described as three thermal "nodes" with finite heat capacities ($TeO_2$ crys-

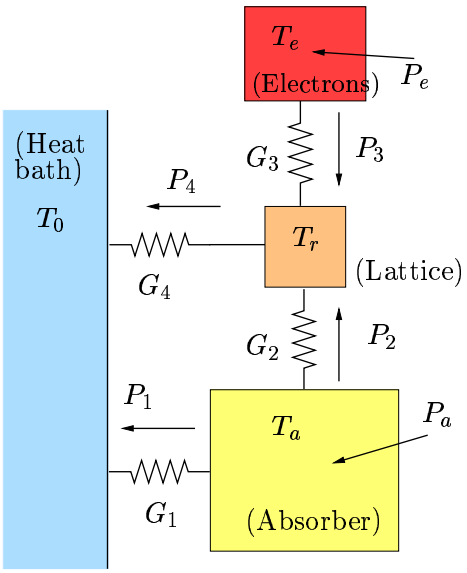


Figure 7.4 - Three system thermal model. The temperature values are unknown and also the directions of the flowing powers.

tal absorber, Ge thermistor lattice, Ge thermistor electrons), connected among them and to the heat sink by means of thermal conductances as described in the previous section. Here the problem is generalized as the system shown in fig. 7.4. The figure also indicates the various thermal powers. $P_a$ is the background thermal powers on the absorber system, while $P_e$ is the power dissipated on the electron system of thermistor, composed by the Joule power $P_J$ due to the signal read-out and by the electron background thermal power $P_{b,e}$ due mainly to electromagnetic interferences:

$$P_e = P_J + P_{b,e}. \tag{7.2}$$

Using the polarization circuit introduced in sec. 2.5, the expression of $P_J$ is

$$P_J = I^2 \cdot R(T_e) = R(T_e) \cdot \left( \frac{V_{\text{BIAS}}}{R(T_e) + R_L} \right)^2 \tag{7.3}$$

where $R_L$ is the load resistance, and the thermistor resistance depends on the electron temperature as

$$R(T_e) = R_0 \cdot \exp \left( \frac{T_0}{T_e} \right)^{1/2} \tag{7.4}$$

The equation system describing the static condition is

$$\begin{cases} P_e = P_J + P_{b,e} = P_3 \\ P_4 = P_3 + P_2 \\ P_a = P_2 + P_1 \end{cases} \tag{7.5}$$

All the conductances depend on the temperature T according to the following law:

$$G(T) = g_0 \cdot T^{\alpha}, \tag{7.6}$$

and then, using the 7.1, it is easy to obtain the power law

$$P_{AB} = \frac{g_{0,AB}}{\alpha_{AB}+1}\left[T_A^{\alpha_{AB}+1} - T_B^{\alpha_{AB}+1}\right]. \tag{7.7}$$

In this way, the equation system 7.5 can be expressed as a function of the three unknown temperatures $T_e$, $T_a$, $T_r$ and the conductance parameters $g_0$ and $\alpha$. The background powers $P_{b,e}$, $P_{b,a}$and the bath temperature $T_b$ are treated as known constants whereas the $P_J$ is calculated from the eq. 7.3. The equation system obtained is non linear, for example the equilibrium condition at the thermal electron node gives

$$R(T_e)\cdot\left(\frac{V_{\mathrm{BIAS}}}{R(T_e)+R_L}\right)^2 + P_{b,e} = \frac{g_{0,3}}{\alpha_3+1}\left[T_e^{\alpha_3+1} - T_r^{\alpha_3+1}\right] \tag{7.8}$$

where, due to the expression of $R(T_e)$, there is an exponential term depending on $T_e$. The equation system becomes

$$\begin{cases} R(T_e)\cdot\left(\dfrac{V_{\mathrm{BIAS}}}{R(T_e)+R_L}\right)^2 + P_{b,e} = \dfrac{g_{0,3}}{\alpha_3+1}\left[T_e^{\alpha_3+1} - T_r^{\alpha_3+1}\right] \\ \dfrac{g_4}{\alpha_4+1}\left[T_r^{\alpha_4+1} - T_b^{\alpha_4+1}\right] = \dfrac{g_{0,3}}{\alpha_3+1}\left[T_e^{\alpha_3+1} - T_r^{\alpha_3+1}\right] + \dfrac{g_2}{\alpha_2+1}\left[T_a^{\alpha_2+1} - T_r^{\alpha_2+1}\right] \\ P_a = \dfrac{g_2}{\alpha_2+1}\left[T_a^{\alpha_2+1} - T_r^{\alpha_2+1}\right] + \dfrac{g_1}{\alpha_1+1}\left[T_a^{\alpha_1+1} - T_b^{\alpha_1+1}\right] \end{cases} \tag{7.9}$$

It is not possible to analytically solve this system and the use of numerical calculation methods is needed.
The objective of the thermal model equations is to obtain all the three unknown temperatures, but the most interesting one is the electron temperature $T_e$ that allow to calculate, through the eq. 7.4 of the sensor resistance $R(T_e)$. In fact, $R(T_e)$ is the quantity experimentally measured.
It can be noticed that the static behavior is not determined by the heat capacities.

## 7.4 Dynamic detector behavior

In the dynamic behavior one takes into account the temporal evolution $T(t)$ of the temperatures after particle interaction.

In a monolithic model, let's imagine a bolometric detector having a total heat capacity C in thermal contact with a heat bath at a temperature $T_0$ through a conductance G. Let a constant power P be released in the detector. Let's assume that the energy E released in the crystal absorber produces a fast change of temperature equal to the ratio between E and $C_a$. Let $T(t)$ be the temperature of the absorber as a function of time and assume that $\Delta T \equiv |T(t)-T_0| \ll T_0\ \forall t$,

so that C and G can be treated as constant quantities. The previous section describes the static behavior as

$$P = \int_{T_0}^{T_s} G dt = G \cdot (T_s - T_0) \tag{7.10}$$

where $T_s$ is the temperature of the bolometer seen as a single system in thermal equilibrium with the heat sink.
Energy conservation in the time $dt$, taking into account the variation of internal energy of the crystal, gives the relationship (7.10):

$$P dt - C dT = G \cdot (T(t) - T_0) dt$$

and so

$$P - C\dot{T} = G \cdot (T(t) - T_0). \tag{7.11}$$

If, as supposed, at $t = 0$ the system is in a static condition, then

$$P - C\dot{T} = G \cdot (T(t) - T_s) + G \cdot (T_s - T_0).$$

Using the 7.10, with $\Delta T(t) = T(t) - T_s$, it is possible to derive the relationship

$$-C\dot{\Delta T} = G \cdot \Delta T \tag{7.12}$$

that describes the dynamic behavior. Remembering the initial condition

$$\Delta T(t = 0) = \frac{E}{C}, \tag{7.13}$$

it's easy to obtain the exponential solution

$$\Delta T(t) = \frac{E}{C} \cdot e^{-t/\tau} \quad \text{with} \quad \tau = \frac{C}{G}. \tag{7.14}$$

Obviously the model just treated is an extreme simplification of the general problem. However it permits to observe typical aspects of the full general case:

- the detector behavior is represented by differential equations that describe the energy conservation at each node of the thermal system, as in the static case.

- the temperature variation, due to the particle interaction, starts from the well known detector static conditions. After the thermal pulse the system recovers to the initial equilibrium conditions.

- the characteristic times of the thermal pulse are those of thermal relaxation ($\tau$=C/G for monolithic approach); they are about 1-2 seconds for large mass detectors described in this thesis.

- the thermal relaxation to the equilibrium is in general described by exponentials.

Let's consider now the more complete thermal model described in fig. 7.4. Let $T_e(t)$, $T_r(t)$ and $T_a(t)$ be the temperatures of the three thermal systems (to be determined) and $C_e$, $C_r$ and $C_a$ their heat capacities. The thermal network in dynamical conditions is described by the equation system

$$\begin{cases} -C_e\dot{T}_e = -P_J - P_{b,e} + P_3 \\ -C_r\dot{T}_r = -P_3 + P_4 - P_2 \\ -C_a\dot{T}_a = +P_2 - P_a + P_1 \end{cases} \tag{7.15}$$

Using the explicit expressions of the thermal powers flowing in the nodes,(7.15) becomes a system of three coupled differential equations:

$$\begin{cases} -C_e\dot{T}_e + P_J + P_{b,e} = \dfrac{g_3}{\alpha_3+1}\left[T_e^{\alpha_3+1} - T_r^{\alpha_3+1}\right] \\ -C_r\dot{T}_r = -\dfrac{g_3}{\alpha_3+1}\left[T_e^{\alpha_3+1} - T_r^{\alpha_3+1}\right] + \\ \qquad\qquad -\dfrac{g_2}{\alpha_2+1}\left[T_a^{\alpha_2+1} - T_r^{\alpha_2+1}\right] + \dfrac{g_4}{\alpha_4+1}\left[T_r^{\alpha_4+1} - T_b^{\alpha_4+1}\right] \\ -C_a\dot{T}_a + P_a = \dfrac{g_2}{\alpha_2+1}\left[T_a^{\alpha_2+1} - T_r^{\alpha_2+1}\right] + \dfrac{g_1}{\alpha_1+1}\left[T_a^{\alpha_1+1} - T_b^{\alpha_1+1}\right] \end{cases} \tag{7.16}$$

with initial conditions

$$\begin{cases} T_e(0) = T_e^0 \\ T_r(0) = T_r^0 \\ T_a(0) = T_a^0 + \dfrac{E}{C_a} \end{cases} \tag{7.17}$$

The superscript "0" indicates that these temperatures are referred to the static equilibrium, so that the temperatures $T_e^0$, $T_r^0$, $T_a^0$ correspond to the static temperatures of the electronic, phonon and absorber systems respectively, while the dynamical temperatures of these systems are indicated as $T_e$, $T_r$, $T_a$ respectively. It is necessary also to remark that the heat capacity depends on the temperature and that a complete model has to take that into account.
In general

$$C(T) = c \cdot T^{\beta} \tag{7.18}$$

where $c$ is a coefficient experimentally measured and $\beta$ following the Debye law for the crystal absorber and so is equal to 3, while for the thermistor system it is equal to 1. Furthermore, it is necessary to remark that the initial condition

$$\Delta T_a = \frac{E}{C_a}$$

is valid only if the heat capacity variation with temperature can be supposed negligible and then $\Delta T \ll T$. This approximation is not true for energy absorbers with very small heat capacity and for big releases of energy. The correct expression is

$$E = \int_{T_a}^{T_a+\Delta T} C(T)dT = \int_{T_a}^{T_a+\Delta T} cT^{\beta} = \frac{c}{\beta+1}\left[(T_a+\Delta T)^{\beta+1} - T_a^{\beta+1}\right] \tag{7.19}$$

that leads to an initial condition expressed by

$$\Delta T = \left[\frac{\beta+1}{c}E + T_a^{\beta+1}\right]^{1/\beta+1} - T_a \tag{7.20}$$

## 7.5 Approximated analytic solution

The equation system 7.15 can be solved only in a numerical way, however it is linearizable by making opportune approximations. The main hypothesis is that the thermal pulse generated in the crystal absorber is considered as a **small perturbation of the working point** determined by the static problem. Let's consider the integral that describes the power flowing to the heat bath $T_b$ in the dynamic conditions:

$$\int_{T_b}^{T_s} G(T)dT \tag{7.21}$$

where $T_s$ is the temperature reached by the node under study. This integral can be written as

$$\int_{T_b}^{T_s} G(T)dT = \int_{T_b}^{T_s^0+\Delta T} G(T)dT = \int_{T_b}^{T_s^0} G(T)dT + \int_{T_s^0}^{T_s^0+\Delta T} G(T)dT \tag{7.22}$$

where $T_s^0$ is the static temperature of the node determined by the static powers, while $\Delta T$ is the temperature variation during pulse evolution.
"Small" perturbation means that the heat conductances and capacities don't change within the variation range of the pulses, and so at every time the integral 7.22 can be written in the following way:

$$\int_{T_b}^{T_s^0} G(T)dT + \int_{T_s^0}^{T_s^0+\Delta T} G(T)dT \simeq \int_{T_0}^{T_s^0} G(T)dT + G(T_s)\cdot\Delta T \tag{7.23}$$

The approximation contained in eq. 7.23 allows one to express the dynamical equations in terms of heat capacities and thermal conductances evaluated at the operation point temperatures.

To see how to linearize the dynamic equations, let's rewrite the static conditions of system 7.9 in the following way

$$\begin{cases} P_e = \displaystyle\int_{T_r^0}^{T_e^0} G_3(T)dT \\ \displaystyle\int_{T_r^0}^{T_e^0} G_3(T)dT + \int_{T_r^0}^{T_a^0} G_2(T)dT = \int_{T_b}^{T_r^0} G_4(T)dT \\ P_a = \displaystyle\int_{T_b}^{T_a^0} G_1(T)dT + \int_{T_r^0}^{T_a^0} G_2(T)dT \end{cases} \tag{7.24}$$

The solution of the static condition permits one to determine the temperatures $T_r^0$, $T_e^0$ and $T_s^0$ once known the initial data $T_0$, $P_a$, $P_s$ and the conductances $G_1$, $G_2$, $G_3$ and $G_4$.

On the other hand the dynamic equation system can be written as

$$\begin{cases} -C_e\dot{T}_e + P_e = \int_{T_r}^{T_e} G_3(T)dT \\ -C_r\dot{T}_r + \int_{T_r}^{T_e} G_3(T)dT + \int_{T_r}^{T_a} G_2(T)dT = \int_{T_b}^{T_r} G_4(T)dT \\ -C_a\dot{T}_a + P_a = \int_{T_b}^{T_a} G_1(T)dT + \int_{T_r}^{T_a} G_2(T)dT \end{cases} \tag{7.25}$$

At this point the second important hypothesis can be introduced: **the heat capacity of the lattice system is considered negligible** compared with the other ones. In fact, at the working temperatures the relation between the heat capacities is $C_r \ll C_e \ll C_a$ for the Cuoricino detector. Using this approximation the system 7.25 becomes

$$\begin{cases} -C_e\dot{T}_e + P_J + P_{b,e} = \int_{T_r}^{T_r^0} G_3(T)dT + \int_{T_r^0}^{T_e^0} G_3(T)dT + \int_{T_e^0}^{T_e} G_3(T)dT \\ \int_{T_r}^{T_r^0} G_3(T)dT + \int_{T_r^0}^{T_e^0} G_3(T)dT + \int_{T_e^0}^{T_e} G_3(T)dT + \int_{T_r}^{T_r^0} G_2(T)dT + \\ \quad + \int_{T_r^0}^{T_a^0} G_2(T)dT + \int_{T_a^0}^{T_a} G_2(T)dT = \int_{T_b}^{T_r^0} G_4(T)dT + \int_{T_r^0}^{T_r} G_4(T)dT \\ -C_a\dot{T}_a + P_a = \int_{T_b}^{T_a^0} G_1(T)dT + \int_{T_a^0}^{T_a} G_1(T)dT + \\ \qquad + \int_{T_r}^{T_r^0} G_2(T)dT + \int_{T_r^0}^{T_a^0} G_2(T)dT + \int_{T_a^0}^{T_a} G_2(T)dT \end{cases} \tag{7.26}$$

Starting from the static system 7.25, the dynamical one becomes

$$\begin{cases} -C_e\dot{T}_e = \int_{T_r}^{T_r^0} G_3(T)dT + \int_{T_e^0}^{T_e} G_3(T)dT \\ \int_{T_r}^{T_r^0} G_3(T)dT + \int_{T_e^0}^{T_e} G_3(T)dT + \int_{T_r}^{T_r^0} G_2(T)dT + \int_{T_a^0}^{T_a} G_2(T)dT = \int_{T_r^0}^{T_r} G_4(T)dT \\ -C_a\dot{T}_a = \int_{T_a^0}^{T_a} G_1(T)dT + \int_{T_r}^{T_r^0} G_2(T)dT + \int_{T_a^0}^{T_a} G_2(T)dT \end{cases} \tag{7.27}$$

Using now the approximation 7.23 the system can be written as

$$\begin{cases} -C_e\dot{T}_e = -G_3(T_r^0)(T_r - T_r^0) + G_3(T_e^0)(T_e - T_e^0) \\ -C_a\dot{T}_a = G_1(T_a^0)(T_a - T_a^0) - G_2(T_r^0)(T_r - T_r^0) + G_2(T_a^0)(T_a - T_a^0) \\ -G_3(T_r^0)(T_r - T_r^0) + G_3(T_e^0)(T_e - T_e^0) - G_2(T_r^0)(T_r - T_r^0) + \\ \qquad + G_2(T_a^0)(T_a - T_a^0) = G_4(T_r^0)(T_r^0 - T_r) \end{cases} \tag{7.28}$$

From the third equation of the last system it is possible to extract the expression of $T_r$-$T_r^0$ that describes the temporal evolution of the lattice system temperature. Moreover by substituting this expression in the other two equations it is possible to reduce the complete thermal system to a problem of two thermal stages. In fact after some simple mathematical steps the dynamical problem can be written as:

$$\begin{cases} -C_a \cdot \dfrac{dT_a}{dt} = G_{aa} \cdot (T_a - T_a^0) + G_{ae} \cdot (T_e - T_e^0) \\ -C_e \cdot \dfrac{dT_e}{dt} = -G_{ea}(T_e^0) \cdot (T_a - T_a^0) + G_{ee} \cdot (T_e - T_e^0) \end{cases} \tag{7.29}$$

where $G_{aa}$, $G_{sa}$, $G_{as}$, $G_{ss}$ are defined as

$$\begin{aligned} G_{aa} &= G_1(T_a^0) + G_2(T_a^0) - \frac{G_2(T_r^0) \cdot G_2(T_a^0)}{G_2(T_r^0) + G_3(T_r^0) + G_4(T_r^0)} \\ G_{ae} &= -\frac{G_2(T_r^0) \cdot G_3(T_e^0)}{G_2(T_e^0) + G_3(T_r^0) + G_4(T_r^0)} \\ G_{ea} &= -\frac{G_2(T_a^0) \cdot G_3(T_r^0)}{G_2(T_r^0) + G_3(T_r^0) + G_4(T_r^0)} \\ G_{ee} &= G_3(T_e^0) - \frac{G_3(T_r^0) \cdot G_3(T_e^0)}{G_2(T_r^0) + G_3(T_r^0) + G_4(T_r^0)} \end{aligned} \tag{7.30}$$

The system 7.28 can be rewritten as

$$\begin{cases} \dot{x} = -\dfrac{G_{aa}}{C_a} \cdot x - \dfrac{G_{ae}}{C_a} \cdot y \\ \dot{y} = -\dfrac{G_{ea}}{C_e} \cdot x - \dfrac{G_{ae}}{C_e} \cdot y \end{cases} \tag{7.31}$$

where x(t) and y(t) are

$$\begin{aligned} x(t) &= T_a(t) - T_a^0, \qquad \dot{x}(t) = \dot{T}_a(t); \\ y(t) &= T_e(t) - T_e^0, \qquad \dot{y}(t) = \dot{T}_e(t). \end{aligned}$$

with the initial conditions

$$\begin{cases} x(0) = \dfrac{E}{C_a} \\ y(0) = 0 \end{cases} \tag{7.32}$$

Using the new substitutions

$$\begin{cases} A = -\dfrac{G_{aa}}{C_a} \\ B = -\dfrac{G_{ae}}{C_a} \\ C = -\dfrac{G_{ea}}{C_e} \\ D = -\dfrac{G_{ae}}{C_e} \end{cases} \tag{7.33}$$

the system becomes

$$\begin{cases} \dot{x} = A \cdot x + B \cdot y \\ \dot{y} = C \cdot x + D \cdot y \end{cases} \tag{7.34}$$

These equations can be solved with the usual methods and the solution is

$$\begin{cases} x(t) = \dfrac{E}{C_a} \cdot \dfrac{1}{\lambda_2 - \lambda_1} \left[ (\lambda_2 - A) e^{\lambda_1 t} + (A - \lambda_1) e^{\lambda_2 t} \right] \\ y(t) = \dfrac{E}{C_a \cdot B} \cdot \dfrac{1}{\lambda_2 - \lambda_1} \left[ (\lambda_2 - A)(\lambda_1 - A) e^{\lambda_1 t} + (A - \lambda_1)(A - \lambda_2) e^{\lambda_2 t} \right] \end{cases} \tag{7.35}$$

with

$$\begin{aligned} \lambda_1 &= \frac{(A + D) + \sqrt{(A + D)^2 + 4(BC - AD)}}{2} \\ \lambda_2 &= \frac{(A + D) - \sqrt{(A + D)^2 + 4(BC - AD)}}{2} \end{aligned} \tag{7.36}$$

Therefore, the dynamical equations are simply coupled linear equations with constant coefficients, having trivial solutions expressed by a sum of exponentials and analytically computable once the operation point is known. Substituting the expressions of A, B, C and D in the previous expressions, and remembering that the initial conditions state that

$$\begin{cases} T_a(0) = T_a^0 \\ T_e(0) = T_e^0, \end{cases} \tag{7.37}$$

the solutions can be written as

$$\Delta T(t) = T_e(t) - T_e^0 = \frac{E}{C_a \cdot B} \cdot \frac{(\lambda_2 - A)(\lambda_1 - A)}{\lambda_2 - \lambda_1} \cdot (e^{\lambda_1 t} - e^{\lambda_2 t}) \tag{7.38}$$

where

$$\lambda_{1,2} = -\frac{1}{2}\left(\frac{G_{aa}}{C_a} + \frac{G_{ss}}{C_s}\right) \pm \frac{1}{2}\sqrt{\left(\frac{G_{aa}}{C_a} + \frac{G_{ss}}{C_s}\right)^2 + 4\frac{G_{as} \cdot G_{sa}}{C_a C_s} - 4\frac{G_{aa} \cdot G_{ss}}{C_a C_s}} \tag{7.39}$$

The solution 7.38 gives the temporal temperature evolution of the electron system, that, as already underlined, is the most relevant thermal parameter.

### 7.5.1 The electrothermal feedback

We describe the power in the electron system as

$$P_e = P_{b,e} + P_J = P_{b,e} + I^2 R(T_e) \tag{7.40}$$

where the first term is a parasitic static power and the second term is due to the Joule effect. The Joule power in equation 7.40 becomes smaller during the evolution of the thermal pulse since the increase of the temperature, due to the particle interaction, produces a reduction of the thermistor resistance. The decrease of the dissipated Joule power causes a faster relaxation of the electron temperature to the static equilibrium temperature. This effect, that is important when the power in the electron system isn't dominated by the parasitic power, is named "electrothermal feedback".

The electrothermal feedback is taken into account by introducing a proper effective thermal conductance. The analytical solution is very similar to the one obtained with the numerical solution of the differential equations.
The equation 7.40 in the static case is

$$P_e^0 = P_{b,e} + I^2 R(T_e^0), \tag{7.41}$$

where $P_{b,e}$ is constant during the dynamic evolution of the system. Remembering the method used in the previous paragraph (equation 7.23), the first equation of the system 7.25 becomes

$$I^2 R(t_e) - I^2 R(T_e^0) - C_e \frac{dT_e}{dt} = G_3(T_r^0) \cdot (T_r^0 - T_r) + G_3(T_e 0) \cdot (T_e^0 - T_e) \tag{7.42}$$

Remembering the definition of logarithmic sensitivity A

$$A = \frac{dlogR}{dlogT} = \frac{T}{R} \cdot \frac{dR}{dT}, \tag{7.43}$$

it is possible to write:

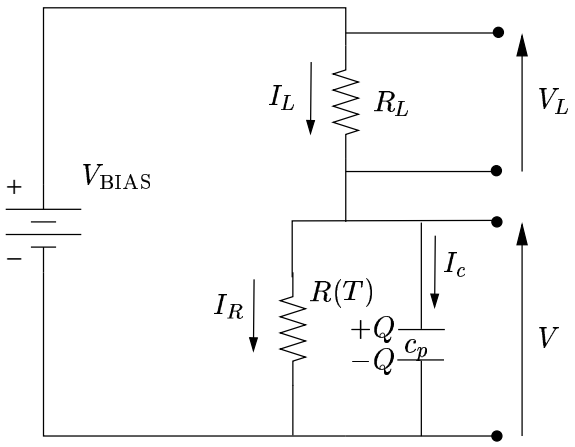


Figure 7.5 - Electrical scheme of the bias circuit for the voltage read-out of the sensor. The electric parasitic capacitance is represented by $c_p$ in parallel with the resistance $R$ of the detector.

$$R(T_e) - R(T_e^0) = \left[R(T_e^0) + \frac{dR(T)}{dT} \cdot (T_e - T_e^0)\right] - R(T_e^0) = \frac{R(T_e^0)}{T_e^0} \cdot A \cdot (T_e - T_e^0). \tag{7.44}$$

So, equation 7.42 becomes:

$$-C_e \frac{dT_e}{dt} = G_3(T_r^0)(T_r - T_r^0) + \left[G_3(T_e^0) - \frac{I^2 R(T_e^0) A(T_e^0)}{T_e^0}\right] \cdot (T_e - T_e^0). \tag{7.45}$$

In this way it is found that it is possible to take into account the effects produced by the electrothermal feedback making the following substitution

$$G_3(T_e^0) \rightarrow \left[G_3(T_e^0) - \frac{I^2 R(T_e^0) A(T_e^0)}{T_e^0}\right]. \tag{7.46}$$

in the expressions of $G_{ae}$ and $G_{ee}$. In this way the solution 7.38 maintains its structure.

## 7.6 Effects due to the parasitic capacitances in the bias circuit

The sensor signal is measured using the electric circuit in fig.2.5. Since the bolometric detectors work in a cryogenic environment, the signal is read-out by a couple of wires up to the room temperature electronic stage. Experimentally, parasitic capacitances are observed between the wires or between the wires and the ground. In both cases, this effect can be accounted for by introducing, in parallel with the thermistor, a capacitance, as described in fig. 7.5, and taking it into account in the equations of the thermal model.

Using the scheme in fig. 7.5, the laws of electric networks and Ohm's law, the following formula holds for the bias circuit:

$$V_{\mathrm{BIAS}} = R_L I_L + V = R_L(I_R + I_c) + V$$

Introducing in this equation the expression that defines the currents:

$$\begin{cases} I_R = \dfrac{V(t)}{R(t)} \\ I_c = \dfrac{dQ}{dt} = c_p \dfrac{dV}{dt} \end{cases}$$

it follows that

$$V_{\text{BIAS}} = R_L \left[ \frac{V(t)}{R(t)} + c_p \frac{dV}{dt} \right] + V(t) = \left[ 1 + \frac{R_L}{R(t)} \right] \cdot V + c_p R_L \cdot \dot{V}$$

which leads to the differential equation:

$$\dot{V} = \frac{1}{c_p R_L} \left[ V_{\text{BIAS}} - \frac{R + R_L}{R} V \right]. \tag{7.47}$$

This equation is coupled with those in system 7.15; in fact the sensor resistance is a function of the temperature $T_e$ and then of time. Moreover, bias voltage and temperature are connected by the electrothermal feedback.

Notice that a new time constant $\tau = c_p R_L$ characterizes the bias circuit. By estimating the parasitic capacitance with typical value of the load resistance (10 G$\Omega$), the value resulting of $\tau$ is a few seconds and so comparable with the evolution times of thermal pulses.

The introduction of this equation leads to the modification of expression 7.8 of the Joule power $P_J$:

$$P_J = \frac{V^2(t)}{R(T_e(t))} \tag{7.48}$$

Moreover it is necessary to state the initial condition for the differential equation (7.47), depending on the bias voltage value of the thermistor at the static conditions.

$$V(0) = V_s \tag{7.49}$$

In conclusion, the equation system that describes the dynamic behavior of the detector is:

$$\begin{cases} C_e \dot{T}_e = \dfrac{V^2}{R(T_e)} + P_{b,e} - \displaystyle\int_{T_r}^{T_e} G_3(T) dT \\ C_r \dot{T}_r = -\displaystyle\int_{T_e}^{T_r} G_3(T) dT - \int_{T_a}^{T_r} G_2(T) dT + \int_{T_b}^{T_r} G_4(T) dT \\ C_a \dot{T}_a = P_{b,a} + \displaystyle\int_{T_r}^{T_a} G_2(T) dT - \int_{T_b}^{T_a} G_1(T) dT \\ c_p R_L \dot{V} = V_{\text{BIAS}} - \frac{R+R_L}{R} V \end{cases} \tag{7.50}$$

Recall that an analytical solution of the previous system does not exist. So, to take into account the electrical parasitic capacitances it is necessary to develop dedicated numerical programs.

The parameters involved in these equations, inputs of the numerical calculation, are:

- the temperatures of heat bath: $T_b$
- the thermal capacities and conductances: $c_k$, $g_{0k}$ and $\alpha_k$
- the background power in the absorber and in the electron systems: $P_{b,a}$ and $P_{b,e}$
- the thermistor parameters: $R_0$ e $T_0$
- the bias circuit parameters: $R_L$ e $c_p$

The temperature $T_k^0$ and the voltage $V_s$ at the static equilibrium, with the value of the energy $E$ released in the absorber, define the initial condition of the thermal problem.

## 7.7 The algorithms for numerical calculation

The equation systems 7.5 and 7.50, describing the static and dynamic detector behaviors, can be solved using numerical calculation methods. For this reason, two programs have been developed based on standard algorithms of numerical calculation with a specific interface for the bolometer analysis.
The simulations have been implemented using the `C` language under the `Linux-i386` operating system..
The Burlirsch-Stoer method has been used to solve the exact ordinary differential equation system. Furthermore this technique allows us to develop more general and complicated thermal systems and to simulate some occasional features of the pulse shapes, like long tails or "kinks", that cannot be obtained with the simple thermal model.

## 7.8 Working with the thermal simulations

The second part of this chapter is devoted to the use of the simulation and its power. First of all examples of the detector simulation outputs will be obtained. This task requires a preliminary work that must be done in order to identify the detector parameters that act as inputs for the simulation programs and to introduce reasonable values for them so that the outputs could describe a Cuoricino-like detector.
Starting from these simulation results, the following part of the chapter is dedicated to the description of an important application of the detector simulation: the parameter optimization. A problem arises immediatly from this subject and must be solved: the necessity to introduce a method for detector comparison. After that, the optimization of an hypothetical Cuoricino-like detector will be performed for different constructive parameters. In the last part of the chapter, a quantitative comparison between the detector simulation results and the experimental measurements will be carried out.

## 7.9 Simulation procedure and inputs

The detector simulations are performed through a procedure involving different steps:

1. design of the system configuration;
2. simulation of the detector static load curve;
3. evaluation of the optimum working point on the load curve;
4. dynamic pulse simulation.

In order to define the thermal behavior of bolometers and therefore to execute the simulation programs, several parameters are needed:

- temperature of the thermal bath
- thermal conductance coefficients and exponents
- heat capacity coefficients and exponents
- parasitic (background) powers in electrons and crystal
- energy released in the crystal
- sensor and polarization circuit parameters
- bias voltage values

It can be noticed that some of these parameters (e.g. the heat capacities) are not necessary in the static simulation but they are relevant only in the dynamic one and vice-versa. However all parameters have been listed together because the configuration file is the same for both the static and the dynamic simulation and also because the results from the static simulation must be used for the dynamic one.

For the real experimental set-ups described in this thesis it has been already underlined that the bath temperatures are between 6 and 13 mK. Referring to the scheme of fig. 7.4 the Cuoricino-like detector conductances correspond to

$$\begin{cases} G_1 = G_{\mathrm{T}} \\ G_2 = G_{\mathrm{glue}} \\ G_3 = G_{\mathrm{el-ph}} \\ G_4 = G_{\mathrm{gold}} \end{cases}$$

and so the quantities required to completely define a bolometer in the present thermal model are the following [119]:

- thermistor characteristic curve, expressed in terms of the Variable Range Hopping parameters $R_0$, $T_0$ and $\gamma$. Specific measurements have been performed in Florence University for the sensors used in the Cuoricino experiment and the measured values are shown in tab. 7.1.

- background power acting on the crystal and on the sensor electron system. No direct experimental data are available to assign a precise valued to these parameters. A reasonable value for the power in the absorber is 6.5 pW. The power on the electrons seems to be lower and a value around 0.1 pW has been used. Dedicated measurements should be made in the near future.

- glue spot thermal conductance, expressed by the relationship (Milano Group measurement):

$$G_{\rm glue}[{\rm W/(K\cdot spot)}] = 2.6\times 10^{-4} T[{\rm K}]^3; \tag{7.51}$$

  as reported in sec. 5.3 the glue spots are used to connect the thermistor to the crystal;

- thermal conductance between the thermistor lattice and the heat sink, probably due to the interface between the thermistor and the gold pads (and so proportional to the pad area) and expressed by (Milano Group measurement):

$$G_{\rm gold}[{\rm W/(K\cdot mm^2)}] = 0.8\times 10^{-5} T[{\rm K}]^{2.4}; \tag{7.52}$$

- thermal conductance between the crystal and the heat sink, provided by the Teflon frame and expressed by (Milano Group measurement):

$$G_{\rm T}[{\rm W/K}] = 4\times 10^{-5} T[{\rm K}]^2; \tag{7.53}$$

- electron-phonon conductance (inside the thermistor itself) measured by the Milano Group in a special set up [119] as:

$$G_{\rm el-ph}[{\rm W/(K\cdot mm^3)}] = 7.8\times 10^{-2} T[{\rm K}]^{4.37}; \tag{7.54}$$

- $TeO_2$ crystal specific heat: dedicated measurements, carried out in Florence University, confirmed the good agreement of the $TeO_2$ heat capacity dependence of temperature with the Debye Law and fixed its Debye temperature to $\Theta_D = 232$ K [120].

- thermistor electron specific heat, given by

$$C_{\rm elect}[{\rm J/(K\cdot mm^3)}] = 1.1\times 10^{-9} T[{\rm K}]; \tag{7.55}$$

  It should be noted that this relationship has not been measured separately, but chosen to account for the observed pulse rise times: a direct measurement should be included in future plans.

- thermistor lattice specific heat, corresponding to the Ge specific heat, given by

$$C_{\rm latt}[{\rm J/(K\cdot mm^3)}] = 3\times 10^{-9} T[{\rm K}]^3; \tag{7.56}$$

  using germanium debye temperature.

Some of the parameters listed above are not well known. In particular, nobody has ever measured the intensity of the background power and its values should be better determined either by direct measurements or by comparing simulations and experimental data. Similar considerations can be made for the parasitic capacitances of the biasing circuit (their values are $\sim$ 20 - 500 pF). Moreover it is possible that different sets of parameters lead to the same results. For example, it's easy to find different combinations of the heat sink temperature and of the background power that give the same static absorber temperature. Many measurements were performed with the old detector designs. For example the Teflon conductance has been made with the old masks (see 3.4). New measurements should be included in future plans.
The parameters used to create the plots shown in the next section have been calculated considering a typical 3x3x6 $cm^3$ bolometer and a 5x5x5 $cm^3$ one. Their values are summarized in table 7.1.

As already said, the first step of the simulation procedure is the construction of the load curve with the static simulation program. Then a working point is chosen on this curve and the dynamic simulation program is used to predict the pulse shape for a certain energy deposition in the absorber. Usually a bolometer is operated at its *optimal working point* that is defined as that point on the load curve where the pulse amplitude is maximum. In order to calculate this optimum point, a special program was developed. This program uses simulations to create and scan the load curve and to determine the bias voltage value for which the pulse is highest. Since this program does not require any special library, it has been developed using `Octave`, a high–level programming language freely avaible for `Linux`.

| Crystal | | 3x3x6 $cm^3$ | 5x5x5 $cm^3$ |
|---|---|---|---|
| Thermistor | | 3x1.5x0.4 $mm^3$ | 3x3x1 $mm^3$ |
| $C_{TeO_2}$ | [J/K] | $9.86 \times 10^{-4} \cdot T^3$ | $2.29 \times 10^{-3} \cdot T^3$ |
| $C_{latt}$ | [J/K] | $5.4 \times 10^{-9} \cdot T^3$ | $2.7 \times 10^{-8} \cdot T^3$ |
| $C_{elect}$ | [J/K] | $2.0 \times 10^{-9} \cdot T$ | $9.9 \times 10^{-9} \cdot T$ |
| $G_{gold}$ | [W/K] | $9.6 \times 10^{-6} \cdot T^{2.4}$ | $4.8 \times 10^{-5} \cdot T^{2.4}$ |
| $G_T$ | [W/K] | $4.0 \times 10^{-5} \cdot T^2$ | $4.0 \times 10^{-5} \cdot T^2$ |
| $G_{el\text{-}ph}$ | [W/K] | $0.14 \cdot T^{4.37}$ | $0.7 \cdot T^{4.37}$ |
| $G_{glue}$ | [W/K] | $1.56 \times 10^{-3} \cdot T^3$ | $2.34 \times 10^{-3} \cdot T^3$ |
| $R_0$ | [$\Omega$] | 7.2 | 1.15 |
| $T_0$ | [K] | 3.3 | 3.35 |
| $P_{b,e}$ | [W] | $1.0 \times 10^{-13}$ | $1.0 \times 10^{-13}$ |
| $P_{b,a}$ | [W] | $6.5 \times 10^{-12}$ | $6.5 \times 10^{-12}$ |

Table 7.1 - Parameters used to simulate large and small size detectors.

## 7.10 Simulation results

### 7.10.1 Static simulation

The static simulation gives, for every bias voltage, the following data as solutions of the system (7.5):

- the equilibrium temperatures of the three system nodes: sensor electrons, thermistor lattice and absorber;
- the thermistor voltage, current, and resistance at equilibrium.

From these values it is possible to simulate the (I,V) or (P,R) load curves for the desired bolometer, as shown in fig. 7.6 and fig. 7.7.

### 7.10.2 Dynamic simulation

In fig. 7.8 a typical pulse is shown (as voltage and temperature pulses). This pulse has been obtained with a dynamic simulation of a 1 MeV energy deposition in the absorber. In fig. 7.9, the effects of the parasitic capacitance in the biasing circuit are shown. The main effect seems to be an increase of the pulse rise time. It could be possible to originate oscillating pulses from particular selection of the parasitic capacitance value, of the load resistance and of the bias voltage value. This is in fact the typical behaviour of an RLC circuits. (Bolometers have an inductive behavior in the small signal limit.)

The simplest way to test the correctness of the dynamic behavior is to simulate no energy deposition in the absorber. In this situation the system should remain in the static condition during time evolution. This is exactly what happens. Moreover, as a cross–check between the static and dynamic simulations, it is possible to simulate the temperature evolution of a thermal system starting from a generic set of temperatures that differs from that given by the solution of the static problem. In this case it can be observed, as shown in fig. 7.10, that the temperatures change during time until the system reaches an equilibrium condition. It is easy to check that the temperatures in this situation are exactly the same given by the static simulation program.

### 7.10.3 Comparison with the analytic solution

Figure 7.11 shows a comparison between a pulse obtained through the numeric simulation and another one obtained using the analytic approximations. Since the analytic calculations are not able to evaluate the presence of any parasitic capacitance, they have been supposed negligible while simulating both pulses. It can be noticed that the two curves are indistinguishable; this means that the approximations done in section 7.5 were correct.

## 7.11 A method to compare bolometer performance

The performance comparison of two or more bolometers with different thermal parameters is not an easy and trivial task to solve. The intuitive method of

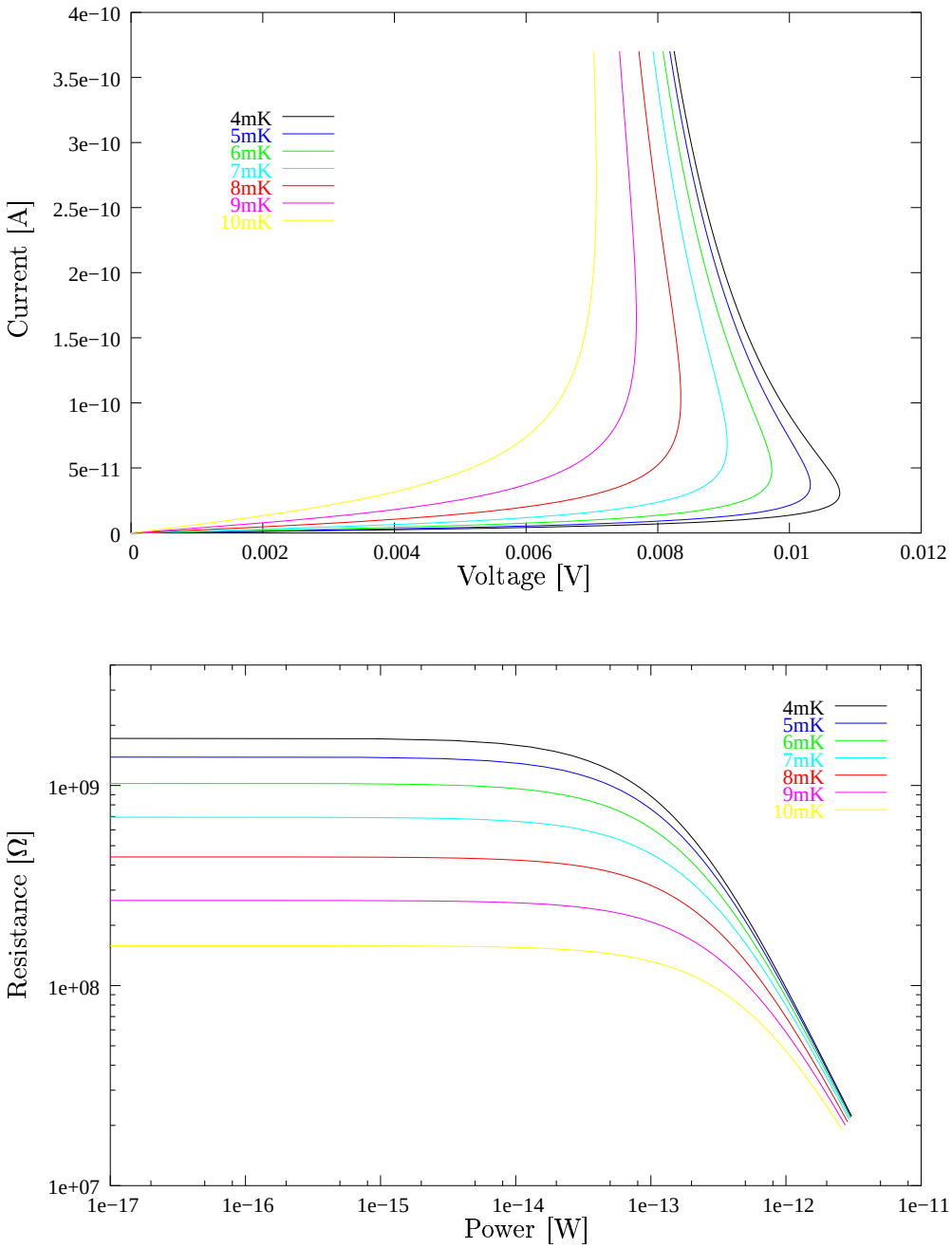


Figure 7.6 - Simulated (I,V) e (P,R) curves of a small size bolometer for different values of the heat sink temperature.

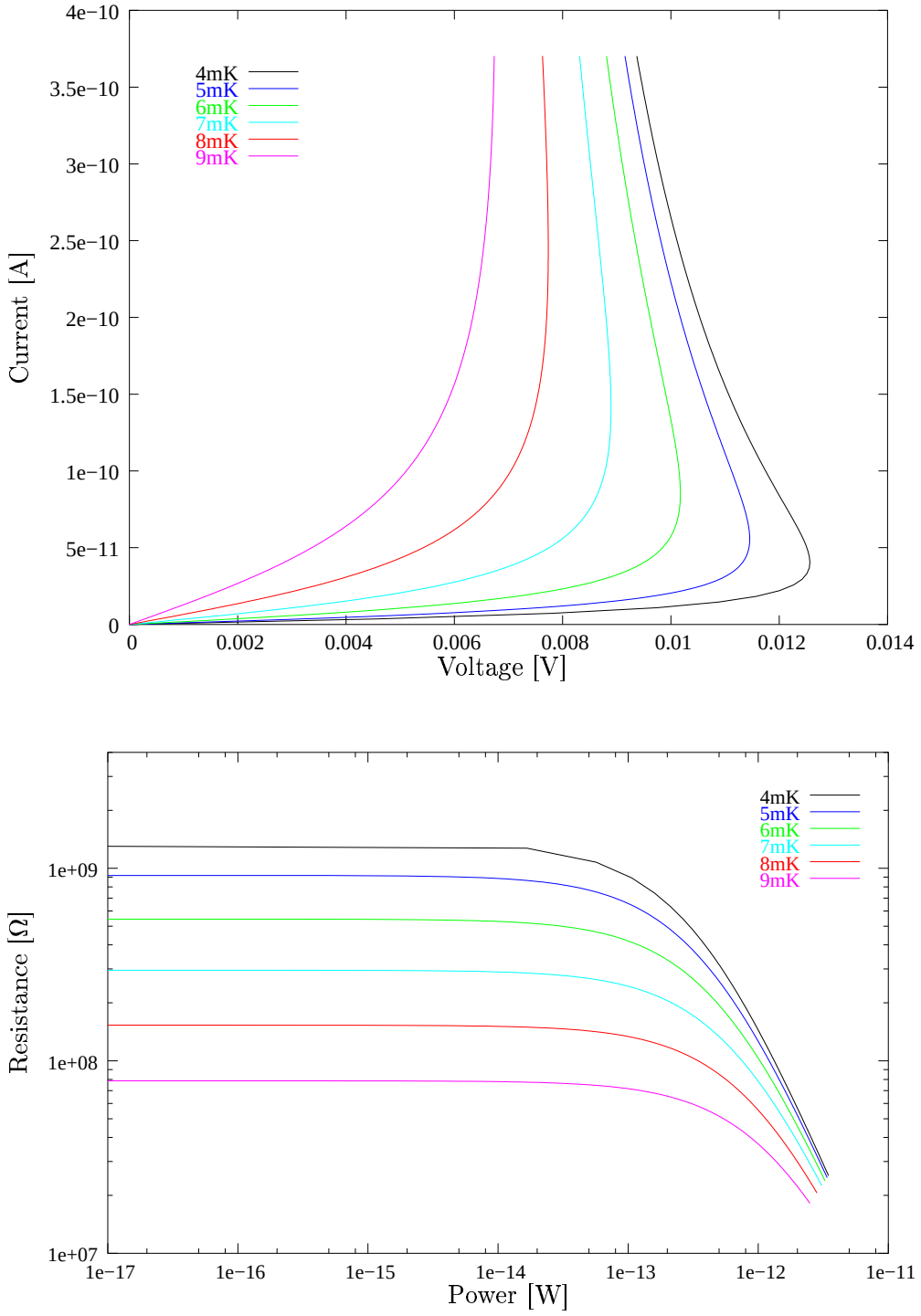


Figure 7.7 - Simulated (I,V) e (P,R) curves of a large size bolometer for different values of the heat sink temperature.

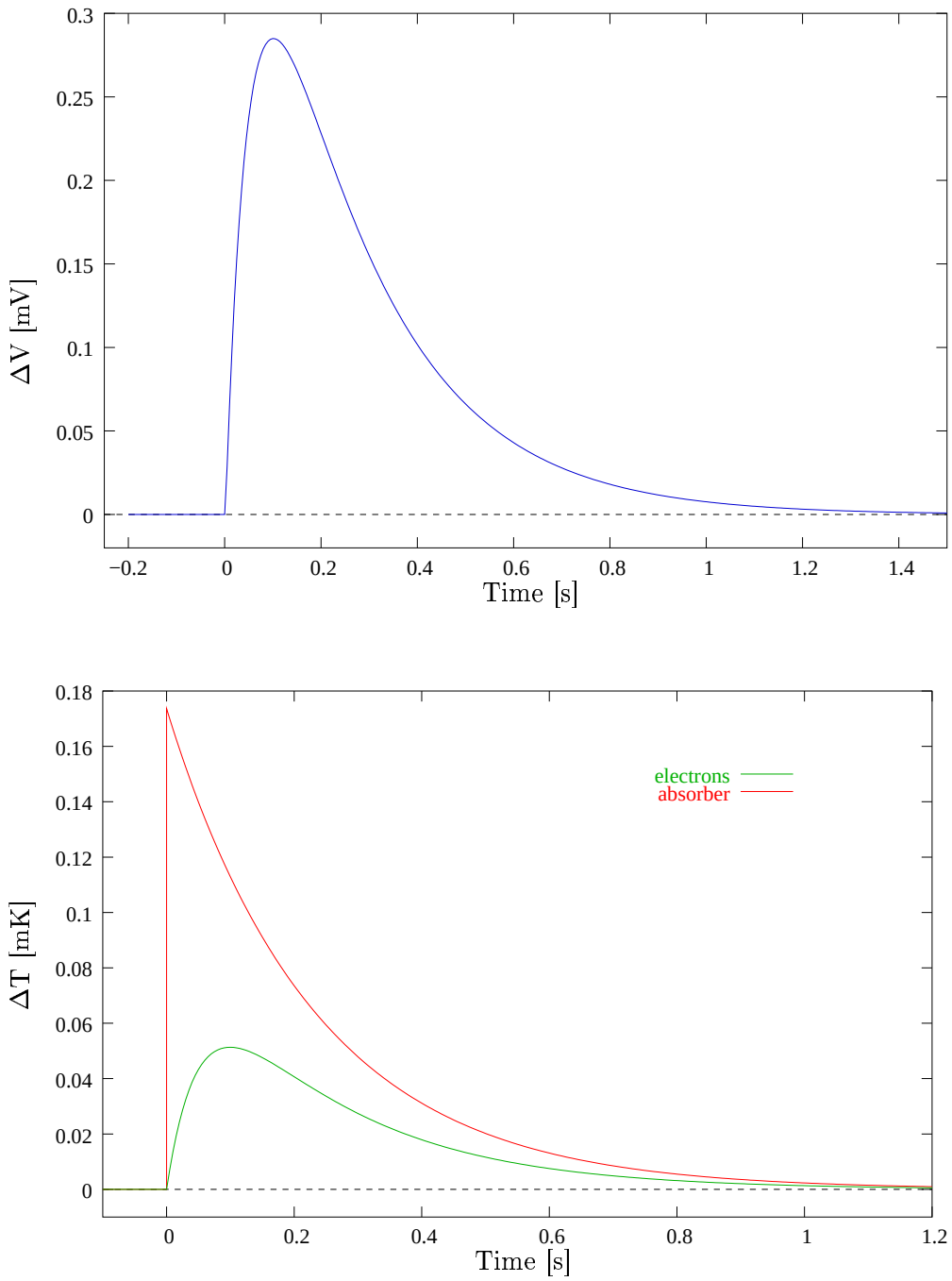


Figure 7.8 - Typical pulses produced releasing 1 MeV in a 3x3x6 $cm^3$ absorber. The pulse is expressed as voltage (upper plot) and temperature (bottom plot) change. In the temperature plot, the time evolution of the absorbing crystal temperature is shown.

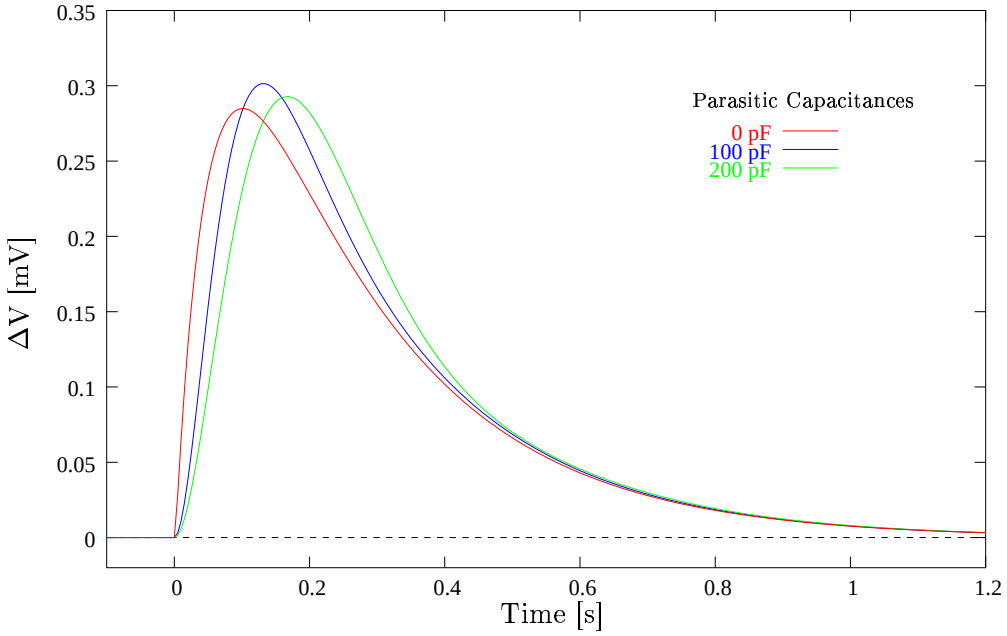


Figure 7.9 - Pulses obtained for different values of the parasitic capacitance in the bias circuit. The slight increase of the rise times can be noticed.

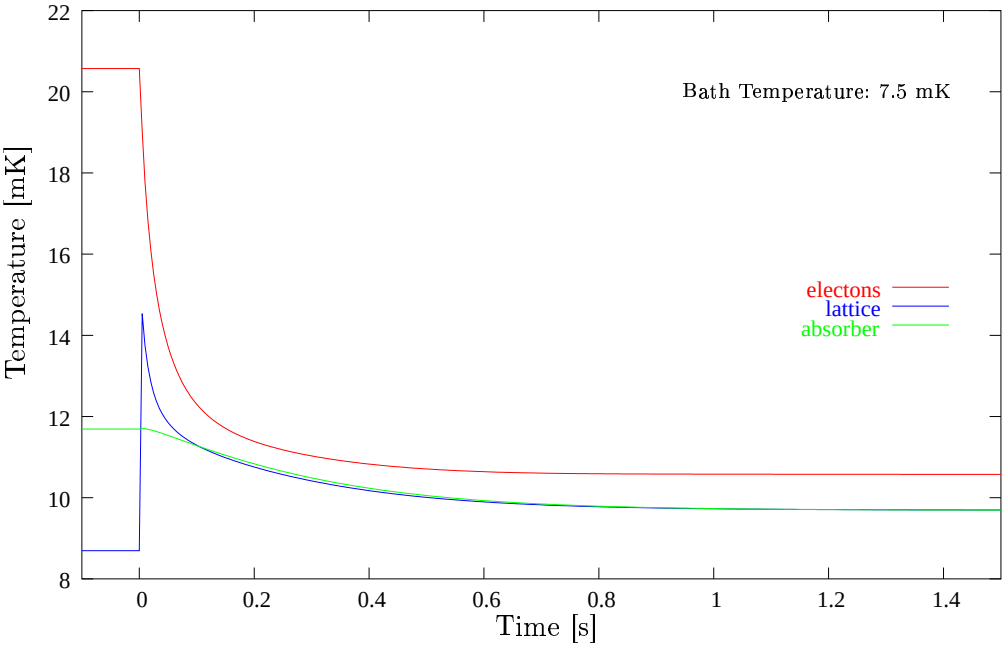


Figure 7.10 - Evolution of the thermal system starting from non equilibrium condition. It can be noted that at the asymptotical thermal equilibrium, the electron temperature is higher than the other two ones, that are almost the same. A simple reason for that exists: electrons are not directly coupled with the heat bath and a constant Joule power is dissipated in it. Moreover the presence of a constant background power in the absorber maks its temperature higher that the one of the heat bath.

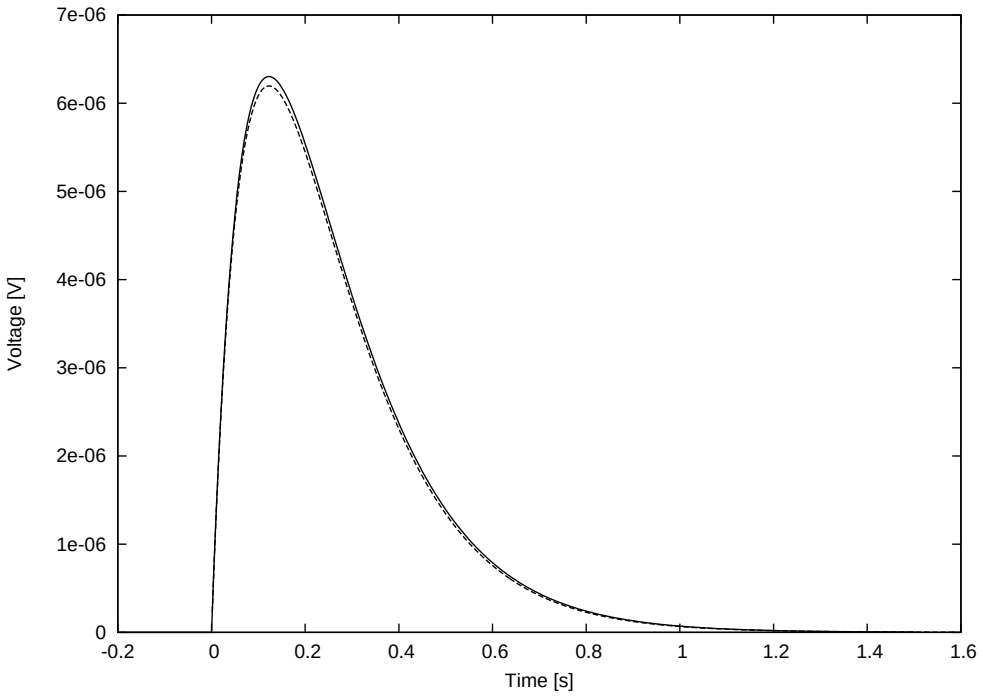


Figure 7.11 - Comparison between the pulse given by the analytical calculation (dashed line) and the numerical simulation program. The thermal parameter for both methods are the same.

comparing pulse amplitudes for the same energy released in the absorber requires some considerations. In fact, higher pulses do not necessary imply higher signal-to-noise ratio.

As already said, the thermal bath temperature is usually fixed at a value between 6 and 13 mK. As explained in sec. 2.5, the thermistor resistance is measured for every bath temperature $T_b$ at different power supplied to the electron system. In this way the Resistance-Power load curve is collected for each base temperature. Of course, this data could be arranged to produce an I-V (Current-Voltage) load curve. The load curves are useful while determining the "optimum operation point" that is given, once the temperature of the heat bath has been fixed, by the voltage bias that yields the highest pulse. Usually this step is experimentally performed by releasing a constant power in the detector heater 6.3.

The optimum points can be collected for every detector at different heat sink temperatures and so it is possible to create a new curve plotting the maximum signals amplitudes (in unit of $\mu V/\mathrm{MeV}$) versus the sensor resistance at these optimum points. In a bi-logarithmic scale this curve is a straight line at a reasonable approximation. This curve is usually named A-R curve.

Let's try now to understand why the A-R curve is useful in detector comparisons. Generally, thermistors with higher sensitivities and resistances give higher pulses, but this fact does not necessary imply better performances. In fact, higher resistances are responsible also for higher sensitivity to spurious noise (microphonics, cross talks, and slow heat pulses, which excite the very

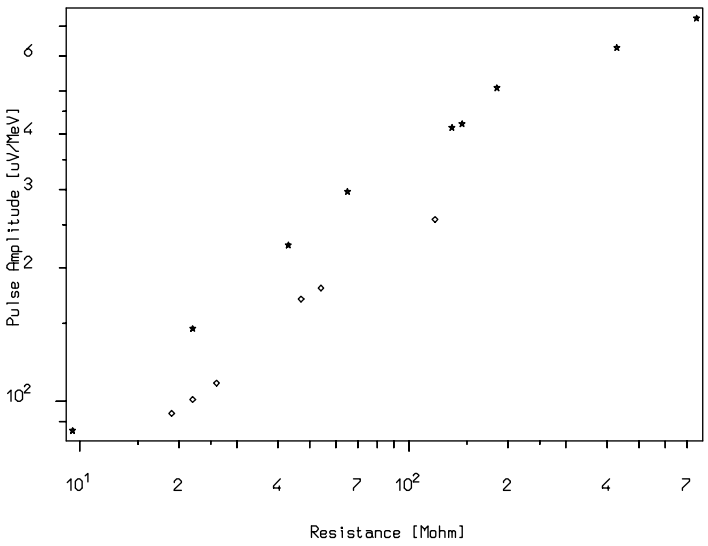


Figure 7.12 - Example of the comparison between different detectors using their A-R curves.

low frequency part of the noise spectrum, 1-5 Hz). Furthermore, lower heat sink temperatures mean higher pulses but the price for that is again higher resistance and therefore worse spurious noise. Then, since both the intrinsic and spurious noise increases as the resistance increases, a variation of the bath temperature doesn't make a big difference in detector performances: the S/N ratio of the detector is thus roughly constant along a given A-R curve.

For this reason the A-R curve completely characterizes the detector performance, and provides a meaningful way to compare two different detectors' performances: if the curve of a detector $A$ lies above the curve of a detector $B$, (as shown in 7.12), then detector $A$ is better than detector $B$. Moreover it clear that pulse amplitudes for different detectors must be compared at the *same* resistance value.

From these remarks, a new parameter, the Detector Figure of Merit (DFM), has been introduced. It's defined as the signal amplitude (in $\mu V$/MeV) at a fixed operation resistance (100 $M\Omega$).

It is interesting to compare the behavior of two bolometers at the same operation resistance not only by comparing their pulse amplitude but also using other detector parameters:

- voltage across the sensor;
- thermistor working temperature;
- pulse rise time (10% - 90%);
- pulse decay time (90% - 10%).

A bi-logarithmic plot of the optimum point resistance (used as the independent variable) versus one of these parameters makes the comparison of bolometers with different features really easy. Thus, one of the main purposes of the thermal

model that has been developed, is to foresee the detector A-R curve in order to optimize its performance.

Unfortunately, detailed A-R curves are not available for all the 790 g detectors used in the Cuoricino tests. However it has been observed that, in a log-log scale, the slopes of the A-R curves are approximately the same. With the existing complete A-R curves, the best-fitting common slope has then been determined. Its value is about 0.6. Figure 7.13 shows an example of an A-R curve for a 5x5x5 $cm^3$ detector. The superimposed straight line has the best-fitting common slope.

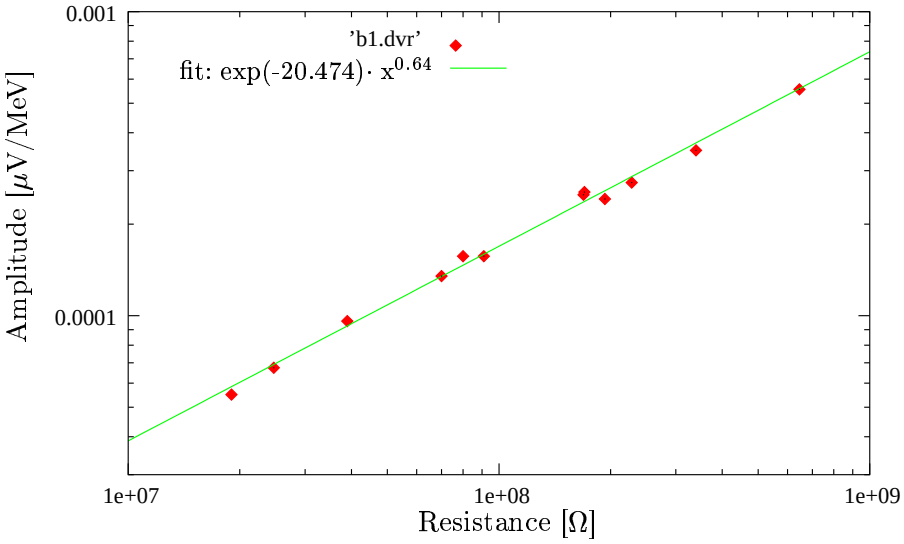


Figure 7.13 - Example of an A-R curve obtained with the "historical" detector B1. These data are collected in the Cuoricino test. It can be noticed that the A-R curve is reasonably close to a straight line in a log-log scale. The fit parameters are reported in the legend.

For those detectors that do not have a detailed A-R curve but only one point, the DFM has been extrapolated using the common slope evaluated above. The results show that, for these detectors, a not negligible DFM spread exists (fig. 7.14). However, it must be remarked that the compared detectors were built with different features.

## 7.12 Detector optimization through simulations

This section reports on the optimization work performed on the detectors parameters with the simulation help.

The guideline is to start from a typical Cuoricino large mass detector and then vary the parameters. Usually, when optimizing a specific parameter, all the others are fixed, except for those that are evidently involved. For example, changing the sensor volume implies a proper modification of the sensor lattice heat capacity, of the electron system heat capacity, of the electron–phonon conductance and, in some cases, also the sensor–heat sink conductance (because the gold pad area may vary as well).

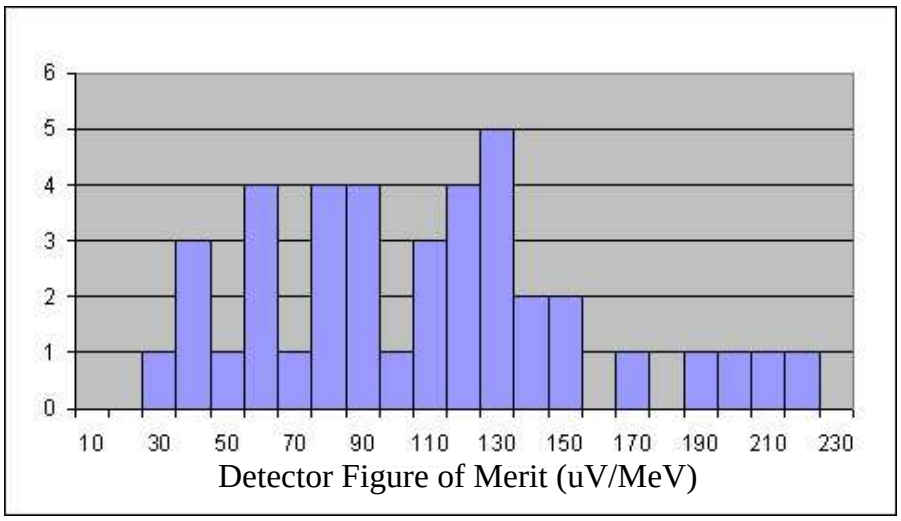


Figure 7.14 - Distribution of the DFM obtained in Cuoricino tests.

In this first approach to the optimization problem, the delicate correlations among the various parameters have not been examined. For example the consequences of the variation of the electron-phonon conductance with $T_0$ is unknown, and so the optimization of the detector acting on the $T_0$ parameter is currently difficult, especially without introducing major hypotheses.
For this reason it is preferable to work out the detector optimization only for the number of glue spots that couple the sensor to the absorber and for the thermistor volume.

### 7.12.1 Thermistor gluing

In sec. 5.3 the thermal-mechanical connection between the absorber and thermistor was described. The coupling is realized with some glue drops. Moreover it has been underlined that the quantity of heat that reaches the thermistor relies on this conductance, and, as a consequence, the pulse rise time also depends on this parameter. Since our specific measurements estimate the sensor–absorber conductance to be a function of the spot number $n$, it is convenient to find the optimum value of this conductance by changing this value.

The following procedure has been carried on for the analysis of the pulse amplitude variation as a function of the glue spots number:

1. preparation of a set of configuration files for the static and dynamic simulation programs. Those files include all the detector thermal parameters and the only difference among the various files is the value of the sensor–absorber conductance. In fact detectors with 1, 6, 9, 12, 24 and 30 glue spots have been simulated.

2. for each such file the static detector behavior is obtained and then, using the specific program the optimum working point on the load curve is found.

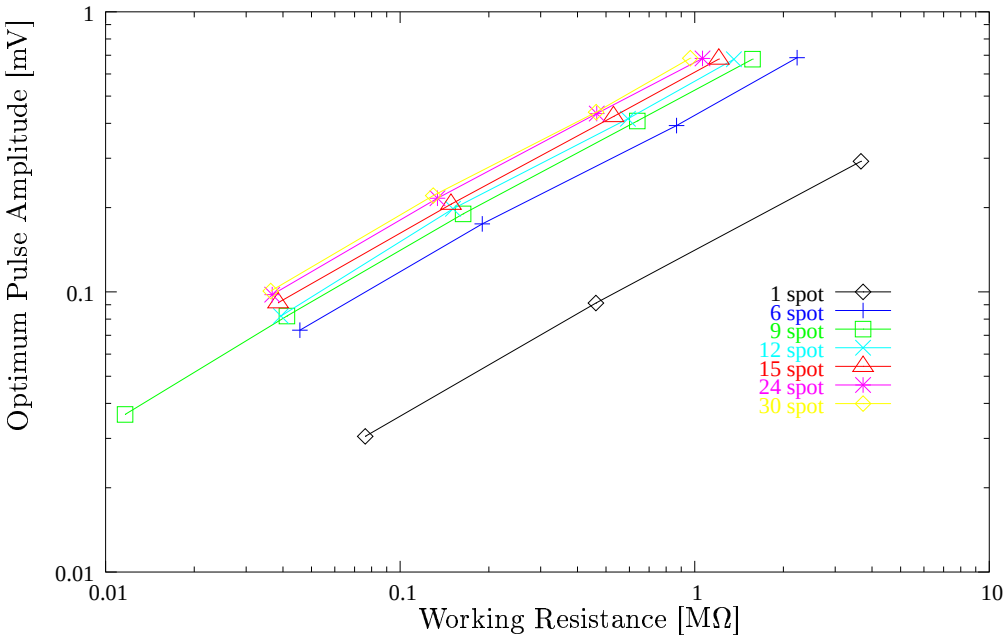


Figure 7.15 - A-R curves obtained with the simulation of different detectors characterized by different numbers of glue spots between the energy absorber and the thermistor.

This step is performed for several bath temperatures (3.5, 5.5, 7.5, 9.5 and 11.5 mK) changing the input file accordingly.

3. thanks to the results of the previous step, an A-R detector curve is collected for each glue spot number. The DFM is then extracted with a linear fit.

4. finally, the DFM values are plotted as a function of the glue spot number.

The A-R curves obtained from the third step are shown in fig. 7.15.

The plot 7.16 shows the final curve obtained performing the last step. Looking at this figure, an improvement can be observed at the beginning but then the pulse amplitude seems to achieve a constant value. This result is not unexpected: increasing the number of glue spots, the electron-phonon decoupling becomes more important with respect to the sensor-absorber one.

### 7.12.2 Thermistor volume

The same analysis presented in the previous section has been performed in order to study the relationship of the detector performance with the size of the NTD-Ge sensor. The procedure described above is exactly the same used for this optimization. The thermistor volume has been varied without changing the distance between the contacts (3 mm). As already anticipated, the variation of this parameter affects not only the other parameters directly connected to the volume (thermistor heat capacities and phonon-electron decoupling) but also those associated with the cross section of the thermistor: $R_0$ and the gold pad area.

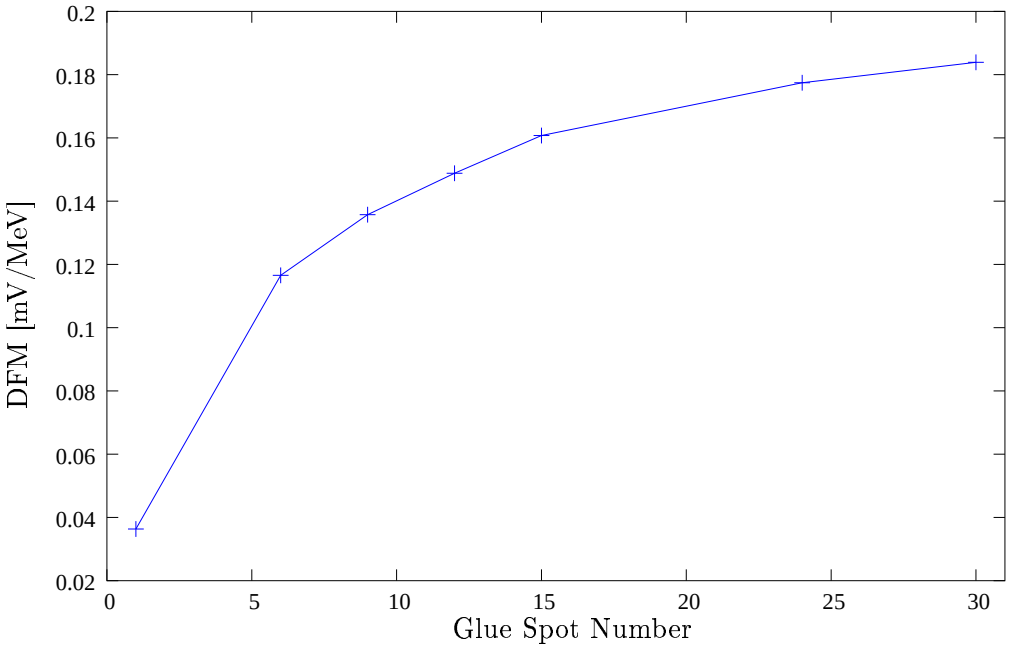


Figure 7.16 - Trend of the DFM at 100 MΩ of thermistor resistance as a function of the glue spot number that couple the sensor to the absorbing crystal.

The results are shown in fig. 7.17 showing the fixed resistance pulse amplitudes. An optimum for the volume exists: it is about 10% higher than the present volume. Even better results could be achieved if it were possible to increase the thermistor volume without increasing simultaneously its conductance to the heat bath. The existence of an optimum value is due to the fact that small volumes imply high electron-phonon decoupling, while large volumes imply both large thermistor heat capacity and large thermistor coupling to the bath.

## 7.13 Qualitative comparison of load curves

Every physics model should be compared with the experimental data in order to test its validity. For this purpose a comparison between the MiDBD and Cuoricino experimental measurements and the simulation results has been performed. The aim of this work is to verify the simulation assumptions on the detector model and the correctness of the values of the parameters. For this reason a preliminary qualitative comparison has been made between experimental and simulated load curves and between measured and simulated thermal pulses. The simulation parameters used are those reported in section 7.9. This comparison points out that the bolometer physics model has been reasonably well understood: indeed the shape of the pulses and of the load curves have been reproduced. Moreover the orders of magnitude are correct. In figure 7.18 some Cuoricino bolometer (I,V) load curves are shown. It seems that the simulation programs are able to reproduce, at least in a qualitative way, the detector static behaviour. On the other side it is not so easy to compare experimental and sim-

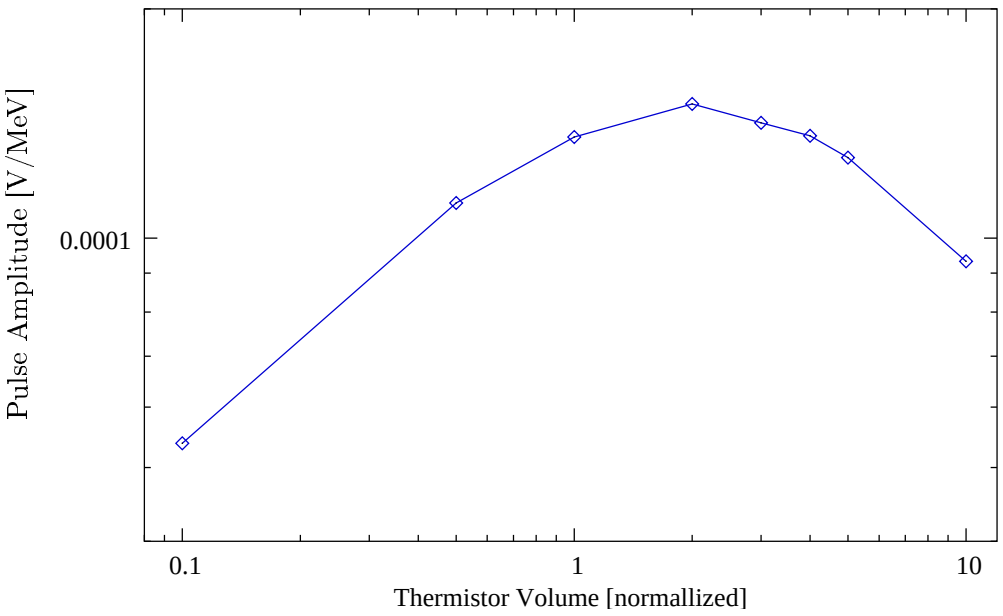


Figure 7.17 - Trend of the DFM at 100 MΩ of thermistor resistance as a function of the sensor volume (log–log scale).

ulated pulses, especially taking into account the various typology of observed events, as detailed in sec. 6.3.

## 7.14 Fit programs

Although simulations can reproduce the qualitative bolometer behaviors, they are not useful if it is not possible to make a quantitative comparison with experimental data. A special program has been implemented to carefully evaluate the thermal parameters of every bolometer. This program is able to find the best set of thermal parameters that fit the experimental data. Thanks to this analysis, the simulation precision in the detector load curve reproduction can be checked.

Furthermore, it is not possible to know the exact values of many thermal parameters because of construction differences between detectors. For example, because of its dependence on the contact area, the glue conductance can change because of the crystal polishing procedure, of the strength used to place the thermistor or of the time taken to perform the glue operation. The developed fit program could help to speed up and better tune the thermal parameters of each bolometer.

Through a minimization, the implemented fit program is able to find out the best thermal parameter set for which the simulations agree with the experimental data. The static behavior has been addressed first. A simple Montecarlo algorithm was initially used for this purpose but, in the end, it has been necessary to switch to the `Minuit` routines of the CERN library. Infact, in spite of its complexity, the use of `Minuit` allowed more efficient and clever algorithms

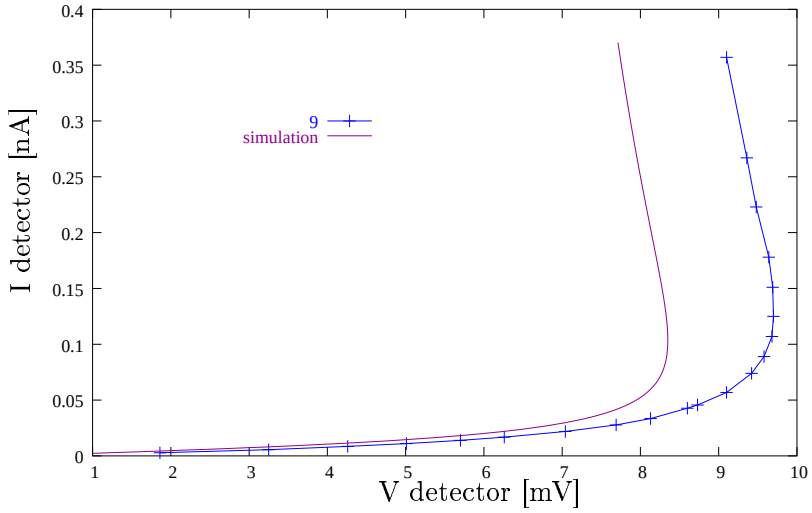


(a)

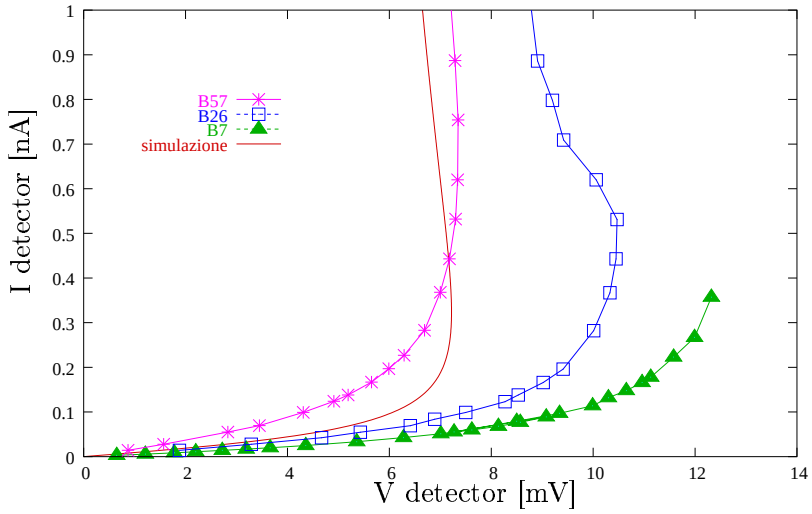


(b)

Figure 7.18 - Experimental load curve obtained with a 3x3x6 $cm^3$ bolometer (a) and several 5x5x5 $cm^3$ (b). All measurements are from the Cuoricino experiment. In both cases, a simulated load curve is superimposed. The simulation parameter are those from tab.7.1 and no optimization work has been performed.

for function minimization.

For the static part, the simplest way to fit the data uses the experimental $V_{\rm BIAS}, V_{\rm BOL}$ curves. In fact the comparison among the static simulation results and the experimental data could be easily done through the minimization of the function:

$$q = \left[\sum \left(V_{\rm BOL}(\text{sperim}) - V_{\rm BOL}(\text{simulat})\right)^2\right]^{1/2} \tag{7.57}$$

where the sum is done on every experimentally measured $V_{\rm BIAS}$ value.

The software that has been implemented to fit the detector load curves evaluate $V_{\rm BOL}$(simulat) using the numerical static simulation program and then calculate $q$ from a provided datafile. This evaluation needs to be done several (hundreds or more) times before the fit can converge. For this reason the dynamic pulses fit has been performed using the approximate analytical solution instead of the numerical one. In fact, the numerical approach is too time consuming as it requires usually about ten seconds to calculate a single pulse. On the contrary, the analytical approximation is faster and, as already observed, the differences with the numerical calculation are negligible in normal detector conditions.

## 7.15 Quantitative comparison

From simulations, it is evident that the load curves, and thus also detector static behaviors, are particularly sensitive to some parameters and not to others. For example a small variation of the electron-phonon conductance $\rm G_{el-ph}$ leads to a noticeable change of the load curve shape. On the other hand, the dependence of the load curves on the glue spot conductance $\rm G_{glue}$ is not so marked, as could be noticed in fig. 7.19. Furthermore it has already been underlined that, acting on different parameters, it is possible to obtain the same load curve. For example, different configurations of the base temperature $\rm T_b$, of the PTFE conductance $\rm G_T$, and of background powers $\rm P_{b,e}$ and $\rm P_{b,a}$ give the same load curve. In fact an increase of the power dissipated in the energy absorber can be balanced by reducing the heat bath temperature or by increasing the conductance of the crystal to the thermal bath. In this way very similar load curves can be obtained from different sets of ($\rm T_b$, $\rm P_{b,e}$, $\rm P_{b,a}$, $\rm G_T$).

The above considerations lead to the conclusion that some thermal parameters can be constrained only by the static simulations whereas for other ones it is also necessary to use the dynamic simulations. On the other hand, the dynamic behavior exhibits unequal sensitivities to the various parameters as well. For example the pulse amplitude strongly depends on the $\rm G_T$, $\rm G_{glue}$ values and on the $\rm T_b$, $\rm P_{b,e}$, $\rm P_{b,a}$ ones. Acting on the last three parameters in fact it is possible to modify the temperatures of the three thermal nodes and thus their heat capacities.

The static simulation is able to reproduce the detector load curve with great detail. For example, fig. 7.20 shows the comparison between the simulated and experimental load curves of a 3x3x6 $\rm cm^3$ detector and a 5x5x5 $\rm cm^3$ one, both measured in the Cuoricino experiment.

The starting point for the fit program is the set of thermal conductances given in section 7.9. The heat sink temperature and the parasitic powers on

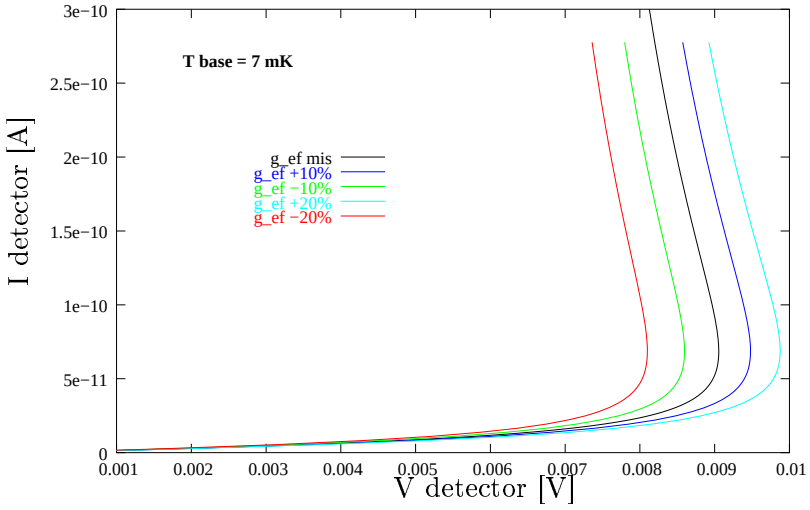


(a)

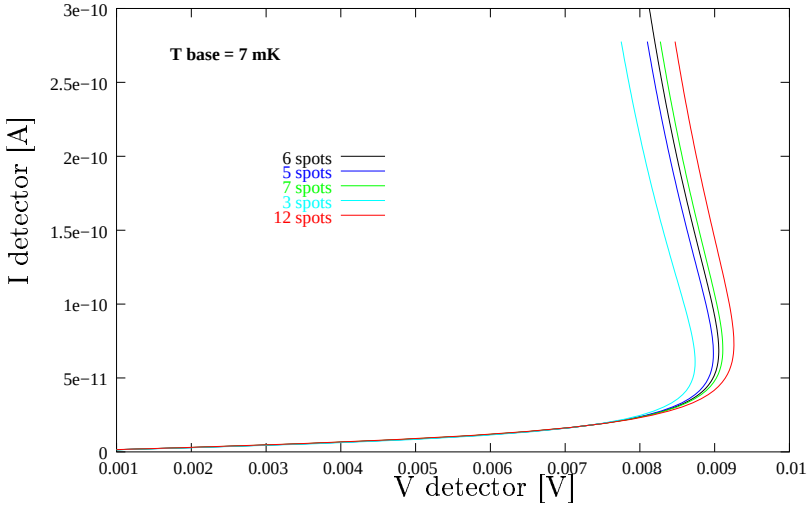


(b)

Figure 7.19 - Comparison of the load curves for different values of the electron–phonon conductance (a) and of the glue spots number (b). Note that a 20% variation of the $G_{\text{el-ph}}$ is enough to produce a substantial modification of the load curve. On the contrary, the load curve is almost independent of the $G_{\text{glue}}$ value. The other parameters used here have been extracted from tab. 7.1.

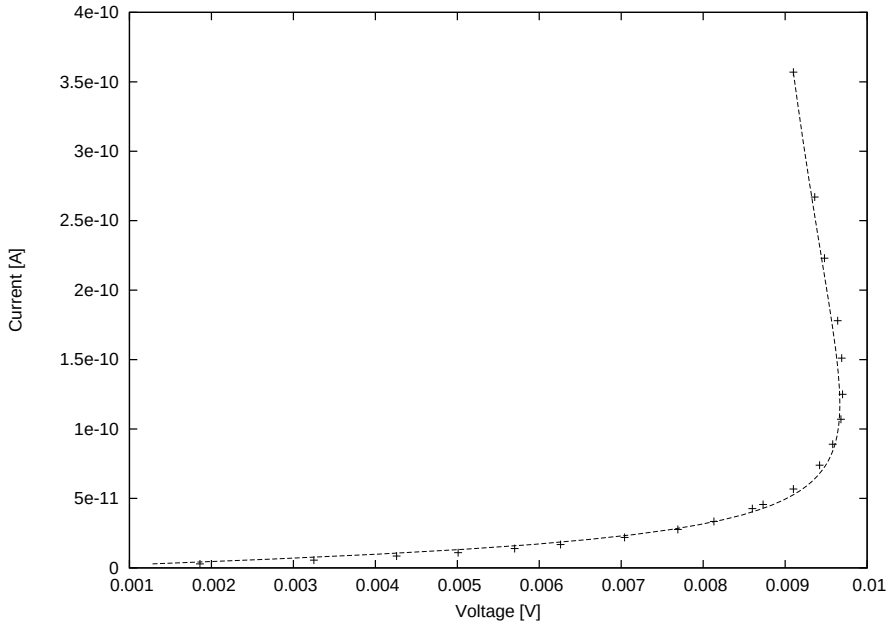


(a)

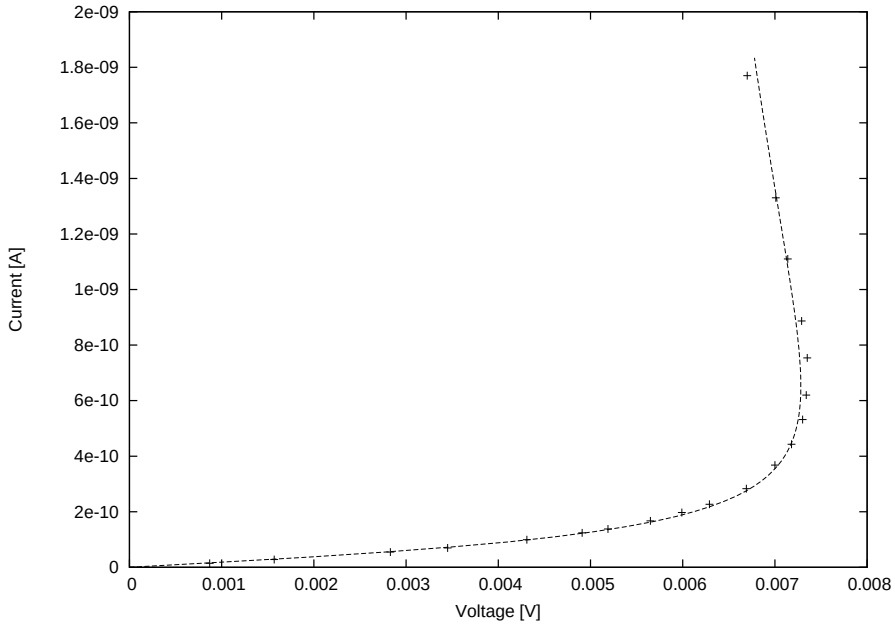


(b)

Figure 7.20 - Comparison between the experimental (points) and the simulated (continuous line) load curve of a 3x3x6 $cm^3$ bolometer (a) and a 5x5x5 $cm^3$ one (b). The upper load curve corresponds to detector 9 while the bottom one corresponds to detector B57, both measured in the Cuoricino experiment.

the absorber and on the thermistor electron system have been chosen as free fit parameters. The coefficients appearing in the temperature power law for the thermal conductances were also free to vary, but they did not change substantially with respect to the initial point. In addition, the ratio between $G_{el-ph}$ for the 3x3x6 detector and that for the 5x5x5 one is about 1/5. This was expected given the different sensor size used in the two cases (3x1.5x0.4 $mm^3$ in the first case and 3x3x1 $mm^3$ in the second one). Correctly, the bath temperature is almost the same in both cases. There are differences between glue spots and PTFE conductances, but they seem to lie within the range given by the intrinsic irreproducibility of the mounting procedure. The exponents of the potential due to conductance laws have been fixed since they derive from physical laws that are intrinsic properties of materials. Tab. 7.15 reports the value obtained by using the fit program from which the comparison of fig. 7.20 is derived.

| Parameter | 3x3x6 $cm^3$ absorber | 5x5x5 $cm^3$ absorber | ratio (normalized when required) |
|---|---|---|---|
| $T_{base}$ [mK] | 8.459 | 8.35 | 1.013 |
| $G_T$ [W/K] | $3.939 \times 10^{-5}$ | $6.28 \times 10^{-6}$ | 6.272 |
| $G_{glue}$ [W/K] | $3 \times 10^{-3}$ | $4.97 \times 10^{-3}$ | 0.905 |
| $G_{el-ph}$ [W/K] | 0.1690 | 0.8003 | 1.056 |
| $G_w$ [W/K] | $9.714 \times 10^{-5}$ | $1.508 \times 10^{-4}$ | 3.221 |
| $P_{el}$ [W] | $8.9 \times 10^{-14}$ | $2.7 \times 10^{-12}$ | 0.033 |
| $P_{abs}$ [W] | $9.1 \times 10^{-12}$ | $1.5 \times 10^{-12}$ | 6.067 |

Table 7.2 - Parameters obtained in the static behavior simulation of the 3x3x3 and 5x5x5 $cm^3$ crystal detectors.

An attempt was then made to reproduce the dynamic behavior of the detectors fitting the experimental pulses with the ones obtained by the analytic simulation. Dynamic pulses are more difficult to reproduce but a good agreement was expected at least with the standard pulses. Unfortunately the use of fitting routines shows that pulses are not well reproduced. The weakest point of the dynamic model is the description of the process that permits the conversion of the particle energy into phonons. The set of parameters that has been used as a starting point for the fit comes from a satisfactory static fit (see table 7.15) and from the measured heat capacities of the thermistor electron system and of the absorber system. Those heat capacities have been let free to vary. The results are not satisfactory: the ratio between the simulated pulse amplitude and the experimental one is about 1/3 and the ratio between the decay times is about 1/5. The results are reported in fig. 7.21 However, from the previous considerations, it is clear that, because of the weak dependence of the static behavior from some parameters, it is possible that other sets of static parameters could give better dynamic results without affecting the load curve. For this reason the possibility to elaborate a procedure for a simultaneous fit of the static and

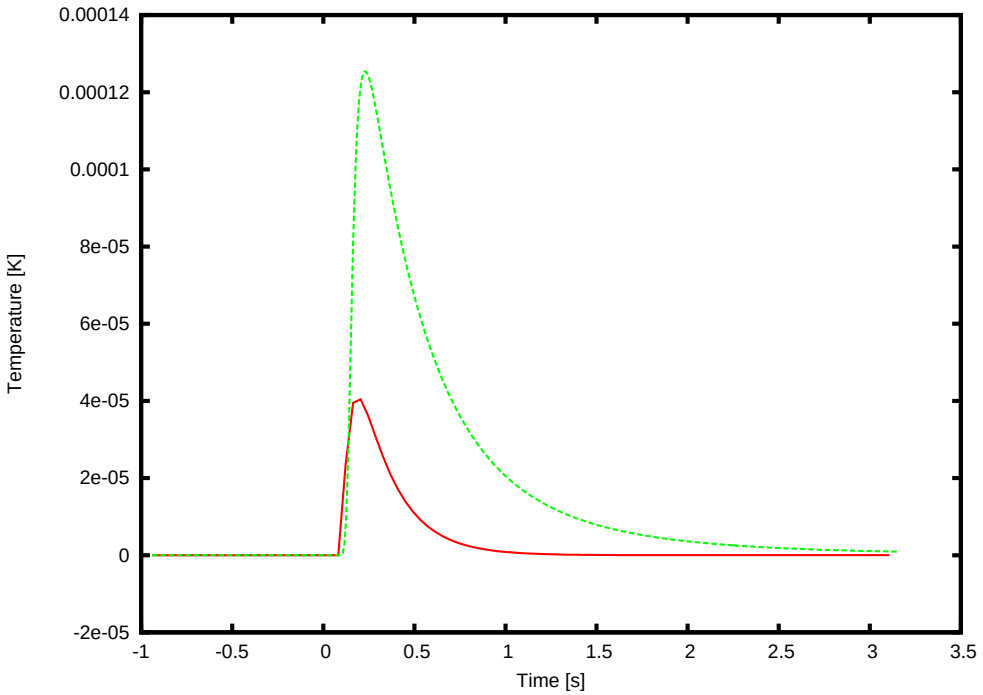


Figure 7.21 - Comparison between the simulated and the experimental thermal pulse obtained in the Cuoricino experiment.

dynamic behaviors has been taken into consideration for future improvement.

Let's stress again that the dynamical behavior of the detectors is not completely reproducible and one is still far from having a satisfactory explanation. In the Cuoricino experiment about 70% of the 5x5x5 $cm^3$ crystal detectors show pulse shapes with two decay times where the second decay "constant" is longer than the one obtained in previous Cuoricino tests. This problem is not present in 3x3x6 $cm^3$ crystal bolometers. This may be explained as a consequence of the surface polish. Indeed, the 3x3x6 $cm^3$ crystals have been grown on an axis different from the 5x5x5 $cm^3$ ones and this causes a different roughness of the crystal surfaces after the polish. Unfortunately it is not possible to simulate this pulse shape with tails using the simple thermal model presented in section 7.2, but work is going on on this problem and it might be possible to reproduce them by introducing more complicated thermal networks, which presents an additional, weakly coupled, thermal system. This new stage could be due to a system of impurities and/or defects at the detector surface. The next section will introduce a correction of the thermal model that attempts to understand the difference between the simulated and the experimental Cuoricino pulses from a different point of view.

At the end of this section, it is useful to remark that the numerical method used for dynamic behavior allows the simulation of some pulse features that cannot be obtained with the analytical approximated solution. For example the introduction of the parasitic capacitances described in sec. 7.6 had allowed sim-

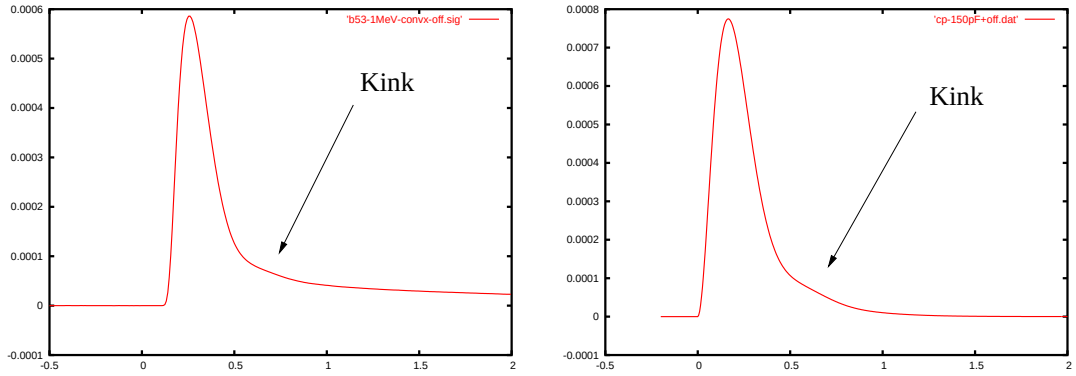


Figure 7.22 - (Left) Pulse obtained with a Cuoricino detector. A kink in decay part the pulse is indicated. (Right) Simulated pulse shape obtained introducing parasitic capacitance of 150 pF in the thermal model. A similar kink appears.

ulation of the Cuoricino pulses that have a slow-rise time or indications of oscillations in the decay part of the pulses. An example of these experimental pulses obtained with a 5x5x5 $cm^3$ crystal detector is shown in fig. 7.22 (left), while the simulated pulse obtained with the introduction of a parasitic capacitance equal to 150 pF is shown in fig. 7.22 (right).

## 7.16 Possible role of the athermal phonons

In chap. 2, the mechanisms of conversion of the particle energy to thermal phonons were described. It has been remarked that an important step of this process with regard to the conversion of "high energy" athermal phonons in thermal phonons is due to the interaction of the former with the crystal surfaces and the lattice impurities.
These phenomena are important for the establishment of a new thermal equilibrium characterized by a temperature $T + \Delta T$, where T corresponds to the thermal equilibrium before the particle interaction. It is possible to speak in terms of temperatures because the system was at equilibrium before particle interaction and because a new equilibrium condition is achieved when particle energy is converted into thermal phonons.
As the processes than permits the new phonon distribution to be obtained are faster that the development of the thermal pulse it is possible to make a hypothesis of instantaneous thermalization and so to introduce in the thermal model the conditions 7.32.

There is however the possibility that athermal phonons hitting the sensor-absorber interface could be transmitted to the sensor where their energy is quickly thermalized by the interactions of phonons with the conduction electrons of the thermistor. Up to now this possibility has been ignored by the thermal model, but it could be relevant to explain unusual pulse shapes obtained with the Cuoricino detectors.

Let's suppose that a fraction $\eta$ of energy is transmitted to the sensor in form of athermal phonons having energy of the order of $\varepsilon \simeq k\Theta_D \simeq 20$ meV. On the other hand, the energy $(1-\eta)$E is thermalized in the energy absorber causing an increase of temperature of

$$\Delta T_{\text{ass}} = \frac{E}{C_{\text{ass}}} \tag{7.58}$$

The initial phonon number is equal to

$$N_0 = \frac{\eta}{\varepsilon} = \frac{\eta}{k\Theta_D} \tag{7.59}$$

The probability that an athermal phonon is absorbed by the sensor is

$$p = \alpha \cdot \frac{\sigma}{S} \tag{7.60}$$

where $\sigma$ is the glue spots surface ($\sim$ 1 mm$^2$), S is the surface of the crystal absorber ($\sim$ 25 cm$^2$) and $\alpha$ is the transmission coefficient of the high energy phonons from the crystal to the sensor. This coefficient does not take into account more subtle effects, for example that the glue spots could act as a filter for phonons selecting the phonon energy. Furthermore, this mechanism could depend on the type of glue used. If the crystal absorber is a cube of side L it is possible to assume, as a first approximation, that the mean free path of a phonon between two consecutive surface scatterings is of the order of L and the mean time between them is

$$< t > \simeq \frac{L}{v_s} \tag{7.61}$$

where $v_s$ is the phonon propagation velocity that is equal to the sound velocity in the crystal. It is possible to express the probability for unit time that an athermal phonon be thermalized in the sensor as

$$P = \frac{1}{6} \cdot p \cdot \frac{1}{< t >} \tag{7.62}$$

In the time $dt$, the variation of the phonon number is

$$dN(t) = -N(t) \cdot P \cdot dt \tag{7.63}$$

and so

$$N(t) = N_0 \cdot e^{-t/\tau} \quad \text{with} \quad \tau = \frac{1}{P} \tag{7.64}$$

The increase of temperature dT due to the phonon transmitted in the sensor is

$$\begin{aligned} dT &= dt \cdot N(t) \cdot P \cdot \frac{k\Theta_D}{C_{\text{el}}} = \\ &= dt \cdot \frac{e^{-t/\tau}}{\tau} \cdot \eta \frac{E}{C_{\text{el}}} = dt \cdot \frac{e^{-t/\tau}}{\tau} \cdot \Delta T_{\text{el}} \end{aligned} \tag{7.65}$$

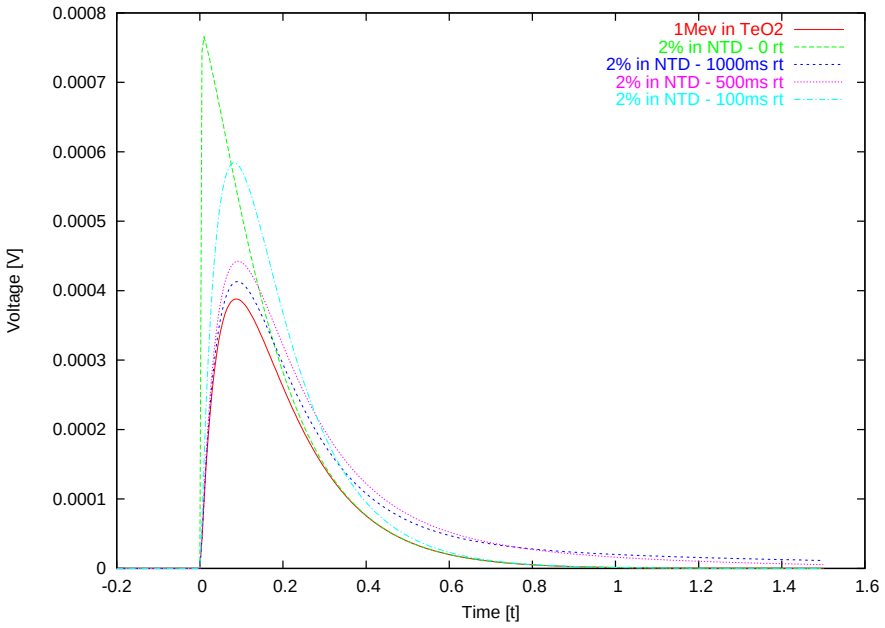


Figure 7.23 - Simulated pulses obtained releasing a total energy of 1 MeV, and different values of $\tau$. The smaller pulse corresponds to the simulation obtained with only thermal phonon component.

This means that the release of the energy of the athermal phonons in the sensor is characterized by a time constant $\tau$. For a $TeO_2$ crystal with L = 5 cm, $v_s \simeq 10^3$ m/s, $S/\sigma \sim 10^4$, it can be is estimated

$$\tau \simeq 750\text{ms} \tag{7.66}$$

that is comparable with the characteristic times of the Milano group bolometers.

Then, it holds that

$$dE = dt \cdot \frac{e^{-t/\tau}}{\tau} \cdot \eta E \tag{7.67}$$

and the following formula expresses the energetic balance for the sensor electrons:

$$C_{\text{el}} \frac{dT_e}{dt} = -\int_{T_e}^{T_r} G(T)dT + \frac{\eta E}{\tau} e^{-t/\tau} + \frac{V^2}{R(T_e)} + P_{b,e} \tag{7.68}$$

Two new parameters have been added in the thermal simulation: the fraction of energy not thermalized in the absorber $\eta$ and the time constant $\tau$ that characterizes the transmission of this energy to the sensor in form of athermal phonons.

The simulation results obtained using this correction are shown in fig. 7.23, 7.24 and 7.25. The consequences are an increase of the pulse amplitude and the presence of an additional time constant in the decay phase of the pulse.

This correction has been implemented in the numerical simulation but it is also possible to use the same procedure used in sec. 7.5 to achieve an analytical approximate solution. Making the calculations the solution can be expressed as

$$T(t) - T_0 = \eta \cdot \frac{E}{C_{el}} \cdot \frac{\tau_{th}}{\tau_{th} - \tau} \left( e^{-t/\tau_{th}} - e^{-t/\tau} \right) \tag{7.69}$$

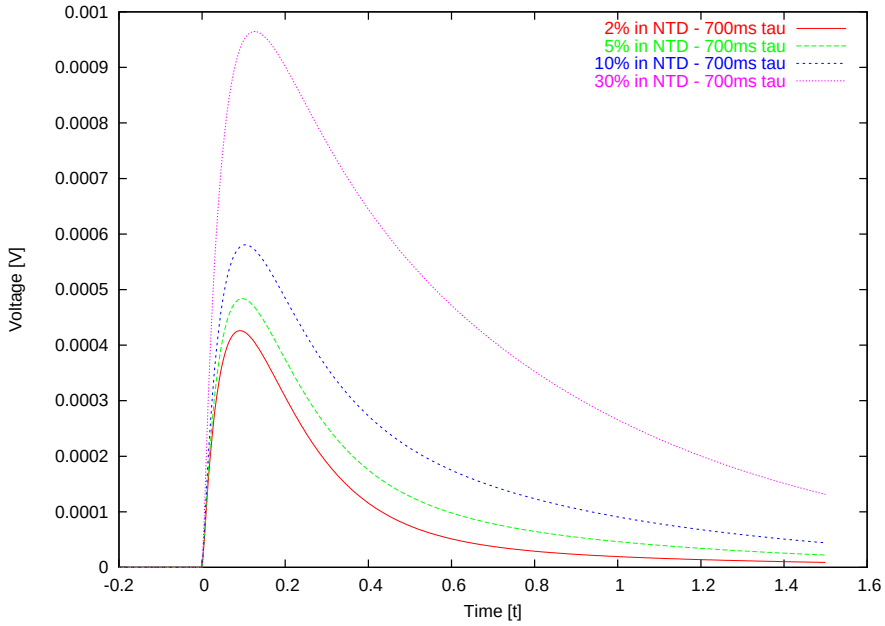


Figure 7.24 - Simulated pulses obtained releasing a total energy of 1 MeV, and different values of the fraction of energy $\eta$ absorbed by the sensor as athermal phonons.

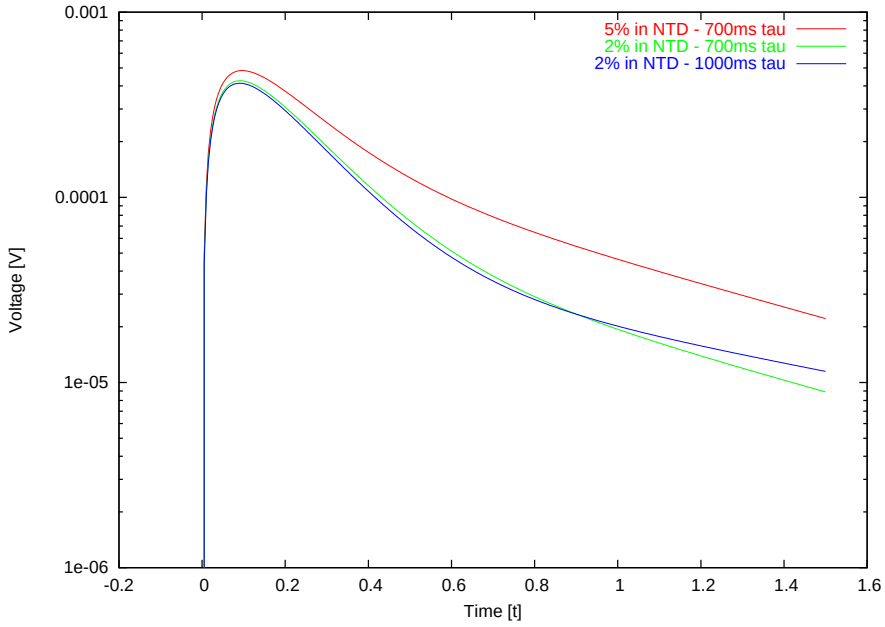


Figure 7.25 - Semilogaritmic plot of pulses with a fraction of energy thermalized in sensor as athermal phonons. It can be seen that there are two decay time constants.

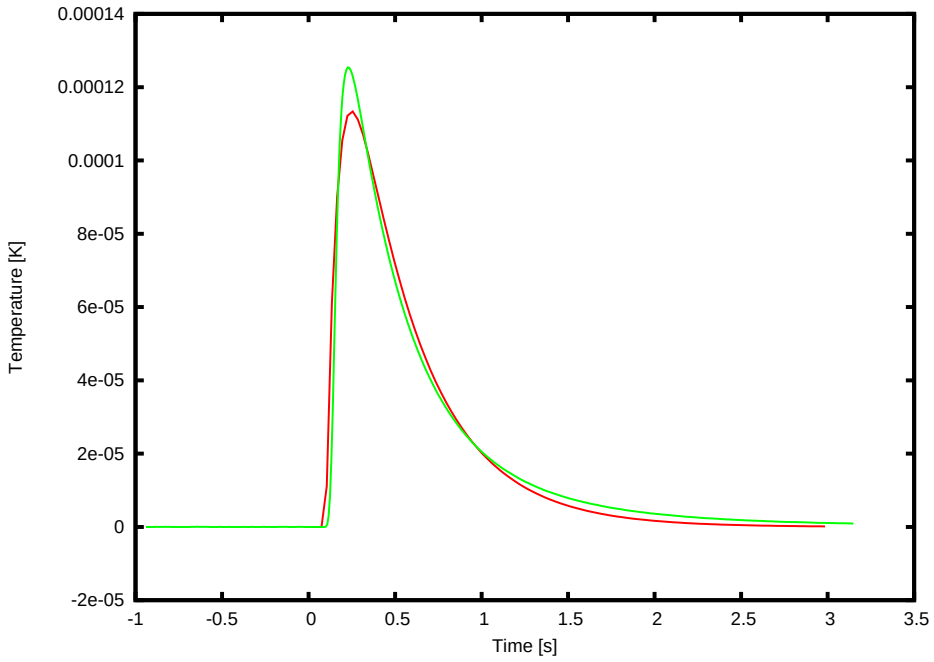


Figure 7.26 - Comparison between an experimental pulse (green line) of a Cuoricino detector and one obtained with simulation procedure (red line) considering the existence of a balistic phonon component.

The possibility of an analytical approximate solution is important because it allows its use in the fit procedure of the experimental pulse. Fig. 7.26 is shows the comparison between pulse produced by dynamic simulation considering the existence of athermal phonons and the experimental one obtained with a Cuoricino detector. The values of conductance used are those obtained by fitting the load curve while the heat capacity of the electron system, $\eta$ and $\tau$ are the only free parameters of the fit procedure. The values obtained for the new parameters are

$$\eta = 28\% \qquad \tau = 0.41 \text{ [s]} \tag{7.70}$$

It must be stressed that a more detailed work on the comparison between the simulated and the Cuoricino experimental pulses is needed in order to accumulate good statistics for the parameters describing the athermal component of the signal.

# Chapter 8

# The Cuoricino single module: innovations towards the CUORE project

## 8.1 The CUORE Project

As explained in chapter 1, the recent results on neutrino flavor oscillations are spurring the scientific community to devote more efforts toward the development of more sensitive experiments searching for $0\nu$DBD .
In this context, a new project named CUORE (Cryogenic Underground Observatory for Rare Events) has been proposed. The CUORE Project is the natural evolution of the Cuoricino experiment.

### 8.1.1 The CUORE detector

The CUORE detector will consist of an array of 25 towers. Each tower will contain 40 $TeO_2$ crystal bolometers for a total of 1000 low temperature detectors. The basic idea is that these bolometers will have a Cuoricino-like structure, described in the previous chapters of this thesis. In this way, the Cuoricino detector may be thought as a test of a single tower of the CUORE detector.
A single CUORE detector will consist, therefore, of a 5x5x5 $cm^3$ single crystal of $TeO_2$ that will act both as a detector and as a source. The crystals will be produced by the Shanghai Institute for Ceramics (SICCAS).
NTD-Ge thermistors will be used as sensors for the detectors sensors. They will be developed and produced at the Lawrence Berkeley National Laboratory (LBNL) and UC Berkeley Department of Material Science, as those already utilized in the MiDBD and Cuoricino experiments.
The coupling between sensor and energy absorber will be realized using glue spots as detailed in sec. 5.3. The thermal and mechanical coupling of detector to the copper frame will be realized by using PTFE (Polytetrafluoroethylene or Teflon) stand-offs, as described in sec. 5.4. The detectors will be supported by copper frames forming the 25 tower configuration shown in fig. 8.1. As described in chap. 6, the excellent performance of the 5x5x5 $cm^3$ crystals to be used in CUORE has already been already proved by Cuoricino, which utilizes a larger tower than those of CUORE, both in length and number of floors. The bolometers will operate at $\sim$ 10 mK. It was decided to arrange the detectors

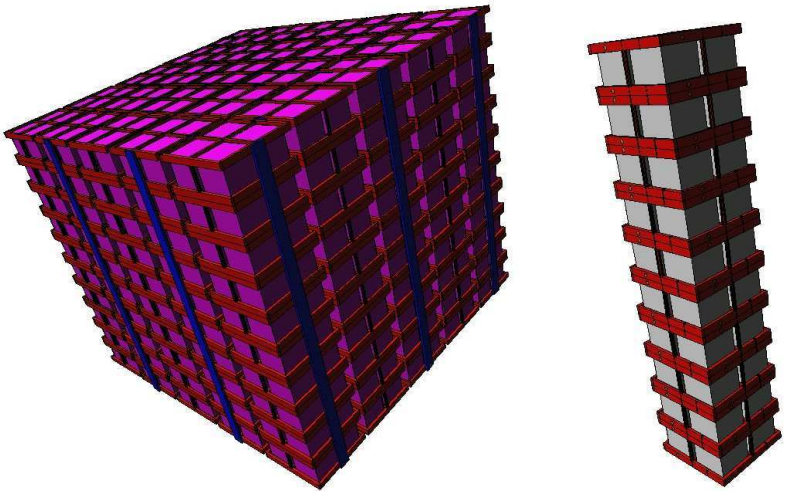

Figure 8.1 - Drawing of the CUORE detector (left). ilt will be composed by 25 Cuoricino-like tower (right) that will work at 10 mK. Each tower will contain 40 $TeO_2$ bolometers.

in a cubic shape to make use of the full experimental volume available in the dilution refrigerator as shown in fig. 8.1.
Therefore the CUORE detector will be the final version of a three step development comprising: MiDBD, Cuoricino, and finally CUORE. The progress made so far, plus the fact that CUORE requires no isotopic enrichment, puts CUORE ahead of other options of the next generation $0\nu$DBD experiments.

### 8.1.2 The CUORE potential

The main scientific objective of the CUORE detector is the search for the neutrinoless double-beta decay of the $^{130}$Te contained in (natural) $TeO_2$ crystals.

As explained in chap. 1, to estimate the potentiality of the $0\nu$DBD experiment using the direct counting technique, the sensitivity to the $0\nu$DBD half life is used. Let's recall that this quantity is expressed as:

$$T_{1/2}^{0\nu} \simeq ln2 \times \frac{N \cdot t}{S} \tag{8.1}$$

where N is the number of emitter nuclei used as a source, and S is the number of observed decay counts recorded during the time t. When no evidence of decays is found, this expression represents the limit on the decay half-life; in this case S is the background fluctuation in the energy region studied. The *neutrinoless sensitivity (1 $\sigma$)* has be introduced as:

$$F_D = 4.17 \times 10^{26} \left(\frac{f}{A}\right) \sqrt{\frac{M \cdot t}{B \cdot \Gamma}} \cdot \epsilon_\Gamma \qquad years \tag{8.2}$$

where $f$ is the isotopic abundance and $A$ the mass number, B is the background rate (in c/(keV kg y)), M the mass of $\beta\beta$ emitter (in kg), $\epsilon_\Gamma$ the detector efficiency in the energy interval $\Gamma$ around the energy transition of the searched decay, and t the measurement running time measurement in years.

To estimate the sensitivity of the CUORE experiment, it is necessary to introduce the experiment parameter values in the expression 8.2. Let's start with the values introduced in the previous section. Then, hypotheses on the possible background rate and on the possible energy resolution obtainable in the CUORE $0\nu$DBD energy region must be made.

In the $0\nu$DBD region, the Cuoricino background rate improved by a factor 1.5 with respect to what that was measured in MiDBD-II. The measured background level in Cuoricino is $0.20 \pm 0.03$ counts/keV/kg/y.
On the other hand, MiDBD and Cuoricino have shed light on how the background contamination dominating the two regions of interest is mostly the intrinsic background, due to bulk and surface contaminations of the constructing materials. With the presently achieved quality of low contamination materials, considering the worst possible condition for bulk contaminations (i.e. all the contamination equal to the present 90%,C.L. measured upper limits), and assuming to have solved the surface background problems (i.e. to have reduced it by a factor $\sim 50$) the corresponding contribution to the CUORE background will be $\sim 0.004$ counts/(keV $\cdot$ kg $\cdot$ y) at the $0\nu$DBD transition energy, and $\sim 0.025$ counts/(keV $\cdot$ kg $\cdot$ d) near threshold. Even at using these conservative values therefore, bulk contaminations will not represent a problem for the CUORE sensitivity. A larger background contribution is however expected, however, when extrapolating to CUORE the surface contributions measured in Cuoricino. The goal of the CUORE technical R&D will be the reduction of background rate to the level of 0.001 counts/(keV $\cdot$ kg $\cdot$ y) at the $0\nu$DBD transition energy, and to $\sim 0.01$ counts/(keV $\cdot$ kg $\cdot$ d) at the threshold.

As far as the energy resolution obtained in the double beta decay region, values of 3-4 keV at 2615 keV were achieved in some of the test measurements mentioned in chap. 5. On the other hand, a 7-9 keV average value has been measured in the Cuoricino calibration spectra. A possible energy resolution interval of 5-10 keV (taking into account possible improvements in the foreseen CUORE R&D) is therefore assumed for CUORE.

Using the eq. 8.2 and the above considerations, the following scenarios are foreseen:

$$\begin{cases} \text{natural crystals} \\ \text{B} = 0.01 \text{ c/(keV}\cdot \text{ kg}\cdot \text{ y)} \\ \Gamma = 5\text{keV} \end{cases} \quad \Rightarrow \quad F_D^{0\nu} = 9.4 \times 10^{25}\sqrt{t}$$

$$\begin{cases} \text{natural crystals} \\ \text{B} = 0.01 \text{ c/(keV}\cdot \text{ kg}\cdot \text{ y)} \\ \Gamma = 10\text{keV} \end{cases} \quad \Rightarrow \quad F_D^{0\nu} = 6.5 \times 10^{25}\sqrt{t}$$

$$\begin{cases} \text{natural crystals} \\ \text{B} = 0.001 \text{ c/(keV}\cdot \text{ kg}\cdot \text{ y)} \\ \Gamma = 5\text{keV} \end{cases} \Rightarrow \quad F_D^{0\nu} = 2.96 \times 10^{26}\sqrt{t}$$

$$\begin{cases} \text{natural crystals} \\ \text{B} = 0.001 \text{ c/(keV}\cdot \text{ kg}\cdot \text{ y)} \\ \Gamma = 10\text{keV} \end{cases} \Rightarrow \quad F_D^{0\nu} = 2.1 \times 10^{26}\sqrt{t}$$

$$\begin{cases} \text{enriched crystals} \\ \text{B} = 0.001 \text{ c/(keV}\cdot \text{ kg}\cdot \text{ y)} \\ \Gamma = 10\text{keV} \end{cases} \Rightarrow \quad F_D^{0\nu} = 8.32 \times 10^{26}\sqrt{t}$$

It is clear from the above cases that the R&D efforts have to be devoted to obtain reproducible single detector performance, and to improve the signal-to-noise ratio, and but, above all, to achieve a dramatic reduction of the background level.

## 8.2 Innovative proposals

In sec. 8.1 a very conservative design of the CUORE detector was presented. However, the CUORE collaboration has proposed a number of innovative modifications to the base structure, in order to improve the detector performance and the background count rate, namely:

- to introduce a series of "pulse tubes" in the CUORE cryogenic set-up;
- to increase the $TeO_2$ crystal size;
- to use crystal absorbers containing other type of isotope candidates at the $0\nu$DBD ;
- to design new types of sensor-absorber couplings;
- to study new types of temperature sensors to be used instead of the NTD-Ge thermistors;
- to develop new surface sensitive $TeO_2$ elements.

In addition, modifications of to the crystal-module structure coupling, and a study of the thermistor parameter optimization are suggested. In the following sections the outline of the main proposals will be reported. It must be stressed that all this R&D activity can be carried out without any interruption of the presently running Cuoricino experiment, using the hall C in Gran Sasso, the Insubria cryogenics laboratory, and the other collaboration laboratories.

## 8.3 Innovations in the cryogenic set-up

It was already remarked, in sec. 3.7 and sec. 4.4, that experiments using cryogenic set-ups are affected by thermal instability problems.
This problem is mainly due to the variation of the cryogenic liquids in the refrigerator, in particular of $^4$He, in the refrigerator. To reduce this problem a stabilization technique was developed, as detailed in sec. 3.7. Nevertheless, too rapid changes of cryogenic liquid conditions cause fast modification of the cooling power, and then of the detector thermal working point, leading to a decreased efficiency of the stabilization technique. It has been observed that a constant (or very slowing varying, of the order of 1% a day) level of liquid helium in the main bath of the cryostat helps in achieving a steady response of the detectors.

To reduce the above problem, an alternative cryogenic configuration will be studied at the R&D level. This configuration could allow us to keep the 4 K stage temperature constant for the whole duration of the experiment. This solution is based on a new commercial device provided by the modern cryogenic technology: a Pulse Tube (PT) cooler. The PT is a novel type of mechanical cooling system exhibiting an extremely low vibration performance level, not reached by conventional coolers. PT coolers consist of a compressor, a rotary valve, and a cold head. Their advantages are:

- low maintenance, due to the absence of moving displacers and cold seals;
- low noise, due to the lack of moving parts in the cold head, which assures a very quiet system;
- low cost, due to its simplicity, which allows the PT to be manufactured at less cost than common cryo-refrigeration systems.

Commercial two stage PT's provide two cold points, typically at 80 K and 4 K, with cooling power of the order of 1 W at 4 K. In this framework, a liquid-helium-free medium-power dilution refrigerator was installed in September 2003 at the Insubria University (Como). This refrigerator does not use cryogenic liquids at all: a PT cools the 80 K and the 4 K shields, while the $^3$He-$^4$He mixture is condensed by a Joule-Thompson expansion after thermalization at the 4 K stage. In fig. 8.2 a picture of the PT installed in the Insubria Laboratory is shown.
This refrigerator will be a valuable test-bench for this new technique, in terms of reliability and noise level. In the event of convincing performance of this the system, a refrigerator for CUORE equipped with an array of PT's will be designed with the goal to stop or to reduce the main bath boil-off or, as an extreme solution, to get rid of cryogenic fluids completely. This solution could help to solve the stability problem at the root.

## 8.4 Innovations in the energy absorber

As anticipated in sec. 8.2, there are two main possible innovations concerning the detector energy absorber.


Figure 8.2 - Pulse Tube of the cryogenic liquid-free dilution refrigerator installed in the University of Insubria Laboratory.

- Part of the CUORE Project R&D will be devoted to study the possibility of increasing the crystal size. In particular the idea of the CUORE collaboration is to test $6\times6\times6$ cm$^3$ $TeO_2$ absorbers. This modification could lead to a worse detector performance, as a bigger crystal absorber introduces higher heat capacities and causes lower pulse amplitudes. However, at present, the energy resolution at 2.6 MeV is higher by a significant factor (typically a factor $\sim$5) than that expected from the detector noise. So it is possible that the energy resolution at the $0\nu$DBD region won't deteriorate. On the other hand, some advantages could be achieved by using a larger mass bolometer, also even if the total $^{130}$Te mass involved in the CUORE experiment remains constant. The most important advantage consists in the decrease of the surface-to-weight ratio. This ratio is important: if the quantity of $TeO_2$ crystal surfaces decreases, than, at least in principle, also the background level due to surface contaminations could decrease. This strategy was already used while when moving from the MiDBD to the Cuoricino experiment. In this case the improvement of the surface-to-weight ratio corresponds to a factor of 1.728.
  It must be underlined that this could translate into a real improvement of the background counting rate only if the surface contaminations dominate the background measurements. The other advantages are mainly of practical and economical nature: if the total mass is kept constant, less electronic channels will be necessary, resulting in shorter and easier assembly operations.
  Two possible configurations are taken into consideration to arrange these crystals:

  - the CUORE detector could be composed of 16 towers arranged in a $4\times4$ matrix. Each tower will be composed of 9 modules containing 4 large size crystals each.
  - the elementary modules of the CUORE experiment will be constituted by a single detector. Each tower will be composed of 9 single crystal modules and the tower will be arranged in a $8\times8$ matrix.

  In both solutions, 576 instead of 1000 crystal detectors would be used. A final decision on the crystal size should be taken not later than 18 months after CUORE starts: this should leave sufficient time for the production of the crystals. That implies much R&D work on $6\times6\times6$ $TeO_2$ crystals in the first year will be necessary.

- An R&D work was proposed to study the feasibility to of using crystals composed of other $\beta\beta$ candidates. The most appealing candidate nuclei, from the thermal and nuclear point of view, are listed in tab. 8.1. Probably the best candidate for $0\nu$DBD is $^{150}$Nd, thanks to its high transition probability, due both to favorable nuclear matrix elements, and to the high transition energy (3.37 MeV). Unfortunately, this candidate has a low natural isotopic abundance, of $\sim$5.6%, and no dielectric diamagnetic compound of Nd exists. If the first problem could be solved studying the use of new techniques for isotopic enrichment, the second one is of

| Compound | Isotopic abundance (%) | Transition energy (keV) |
|---|---|---|
| $^{48}CaF_2$ | 0.0187 | 4272 |
| $^{76}Ge$ | 7.44 | 2038.7 |
| $^{100}MoPbO_4$ | 9.63 | 3034 |
| $^{116}CdWO_4$ | 7.49 | 2804 |
| $^{130}TeO_2$ | 34 | 2528 |
| $^{150}NdF_2$ | 4.64 | 3368 |

Table 8.1 - Most favorable $\beta\beta$ candidate nuclei.

more difficult solution. In fact, crystals containing Nd present a magnetic ordering that imply implies inevitably high specific heat at low temperatures. However the thermal models used to try to explain the large-mass phonon-mediated bolometer behavior, are not completely convincing. In particular, there are indications that a non-thermal component of the signal, due to "high" energy phonons, may be important, and it is possible that the specific heat could be a scarcely relevant parameter.
Following these considerations it was decided to test $NdF_3$ crystals (a paramagnetic material with huge Schottky peaks in the heat capacity at about 70 mK), and of $NdGaO_3$ crystals (which present a more promising anti-ferromagnetic ordering below $\sim$1 K). If these tests give good results, the possibility to replace part of the $TeO_2$ crystal absorbers with elements containing $^{150}$Nd will be considered. This would allow the CUORE experiment to achieve an outstanding sensitivity in the $0\nu$DBD field.

## 8.5 Innovations in the sensor-absorber coupling

As pointed out in chap. 5.3, in the Cuoricino R&D, work has been performed in order to study innovative sensor-absorber couplings. The aim of this work is to achieve a safer mechanical connection of these two components and, above all, a more reproducible thermal conductance between them. In fact, as underlined in sec. 7.10, the pulse amplitude and shape of the pulses are very sensitive to variations of this coupling conductance. The decision of the CUORE collaboration is to continue the tests on the special NTD-Ge thermistors with "pedestals" and "legs", studying different geometry. The idea is to make the gluing operation less critical. In fact using this new thermistors, the glue spots used up to now will be replaced by a glue layer and the thermal conductance between sensor and absorber will be tuned by adjusting the pedestal area in contact with the crystal surface or by varying the leg number of legs.

Moreover, the CUORE collaboration intends to test eutectic coupling between NTD-Ge thermistors and energy absorbing crystal, in a thin film laboratory. The most promising couplings will be realized in small scale prototype detectors, and compared with the standard 9-araldyte-spot coupling.

In the MiDBB and Cuoricino experiments, the Araldit rapid, epoxy glue by Ciba Geigy (now Novartis) epoxy glue was used. It has been decided to test other types of glues. The main reason for this decision is to achieve an improvement of the sensor-absorber coupling, in order to obtain better detector performance. In particular, it would be beneficial if a glue with a thermal contraction coefficient close to the coefficient of the detector components ($TeO_2$ and Ge crystals) could be found. Furthermore, as reported in sec. 7.16, indications of the existence of athermal components of pulses were found. These components determine the pulse shape properties; it will be interesting to observe the effect of different glues on it. In fact, it is possible that the glue acts as a filter on the pulse components, so that phonons with different energy have different probability to be transmitted to the sensor system.
It has to be remarked that the new selected glues have to be tested from the point of view of radioactivity, in order to avoid the introduction of contamination sources.

## 8.6 Innovations in the detector sensor

Two possibilities are taken into consideration:

- to improve the sensor performance making an optimization of the NTD-Ge thermistor properties,

- to study new sensor types, based on other temperature dependent physical material properties of the materialsthat depend on temperature.

The $T_0$ sensor parameter used in previous experiments has never been optimized. In the MiDBD experiment the value of $T_0$ was $\sim$ 3.3 K while in the Cuoricino experiment it was $\sim$ 3.0 K. Actually, MiDBD and Cuoricino thermistors belong to the same series (31). We cannot exclude that the discrepancy between the two values be is due to a systematic error in the calibration procedure, determined by the much lower resistance (at the same temperature) for the Cuoricino case (explained by the different thermistor geometry). A dedicated and detailed study on the consequences of $T_0$ variations on the detector performance has been proposed. However, it is probable that a reduction of the $T_0$ value could permit an improvement on the signal-to-noise ratio results. In fact, lower $T_0$ values allow working at lower temperatures and, therefore, to achieve higher signals, thanks to the reduction of the detector heat capacities, without increasing the sensor resistance and the consequent sensitivity to spurious noise. Furthermore, it is well known that lower $T_0$ thermistors have better electron-phonon coupling, favoring therefore a more efficient heat transmission to the thermistor electrons, with consequent higher pulse amplitudes. For this R&D activity, several thermistors species with $T_0$'s ranging from 2 through to 3 K will be produced by the Berkeley group, and test detectors will be realized in order to select the best doping level.

### 8.6.1 Capacitive sensors

Up to now, the temperature sensor used in bolometers has been dissipative, with an increase of temperature (a few mK/pW in Cuoricino-like bolometers) caused by the bias current, and a Johnson noise contribution to be added to the intrinsic thermodynamic fluctuation of the internal energy of the crystal absorber. The study of non dissipative sensors, and, in particular, of capacitive ones, has been proposed. The use of a capacitive sensor aims at achieving a better signal-to-noise ratio thanks to:

- the elimination of the intrinsic Johnson noise;
- increase of the signal amplitude, thanks to the reduction of the working temperature, due to elimination of the bias power.

At least in principle, capacitive bolometers could give better resolution and threshold. These latter qualities could be advantageous for the "secondary" goals of CUORE such as the detection of the dark matter and of the solar axions[121]. DERBY (DEvelopment of Reactive BolometrY) is a Research and Development project aiming to develop capacitive sensors. In this direction, preliminary measurements of the temperature dependence of the capacitance and the time constant of commercial SMD (Surface Mount Device) capacitors have been performed in at Florence University. The results show that it is rather easy to get samples with the adequate temperature sensitivity, whereas the question is still open as to whether these devices, intrinsically slow, can have a sufficiently fast time response.

The first goal is to find materials with an adequate temperature dependence of the relative dielectric constant $\varepsilon_r$, even at the lowest temperatures (10-20 mK). This property can be found among amorphous solids, in particular glasses. As regards the low-temperature physical properties, there is a general agreement[122, 123] (with significant exceptions[124]) that only the quantum tunneling between two minima controls the physical behavior at such temperatures. This "two level model", in the case of a material like the pure amorphous $SiO_2$, leads to a characteristic temperature $T_0$ for which the dielectric constant $\varepsilon_r(T)$ shows a minimum. Around this minimum $\varepsilon_r$ varies as $\ln(T/T_0)$ for $T > T_0$, and as $\ln(T_0/T)$ for $T < T_0$. Besides Moreover, $T_0 \propto f^{\frac{1}{3}}$, where $f$ is the frequency of the field used to measure $\varepsilon_r$. For the same material, an almost linear dependence on $T$ is found for the specific heat [125] at very low temperature ($T \ll 1$K).

In a conventional readout, the capacitor C is biased by a DC voltage $V_b$ through a load resistor $R$: a voltage change $V_c$ represents the electrical signal. Since in this case the excitation frequency is zero ($T_0 = 0$), $C(T)$ can be represented by:

$$C(T) = a \cdot \ln T + b \tag{8.3}$$

where $a$ fixes the sensitivity of the method and may be obtained from graphs reported in the literature for glasses[126, 127, 128]. Observed sensitivities correspond to values of $K = 1/C \cdot (dC/dT)$ of about 5 x$10^{-2} K^{-1}$ at the temperatures of interest. The current flowing in the capacitor can be written as:

$$i_c = C(t=0)\frac{dV_c}{dt} + V_c(t=0)\frac{dC}{dt} \tag{8.4}$$

Note that $V_c(t=0)$ represents a "multiplier" that is limited only by the dielectric strength of the material. If $E$ is the energy released to the absorber, the maximum variation in temperature $\Delta T = \frac{E}{C_T}$, with $C_T$ total thermal capacity of the detector. In a naive thermal model of the bolometer, which assumes instantaneous thermalization of the deposited energy, fast response of the temperature sensor, and relaxation controlled by the physical coupling of the bolometer to the heat bath. It can be shown that the voltage signal $V_c(t)$ is given by:

$$V_c(t) \;=\; V_b \cdot K \cdot \Delta T \cdot \frac{1}{\tau_T - \tau_e} \cdot \left(\tau_T \exp\left(-t/\tau_e\right) - \tau_e \exp\left(-t/\tau_T\right)\right) \tag{8.5}$$

where $\tau_T = C_T/G$, $\tau_e = RC$, and $G$ is the thermal conductance of the detector towards the heat bath.

The signal appears like that shown in fig. 8.3. There is a maximum at $t = 0$. The fall time is controlled by the read-out time constant $\tau_e$.

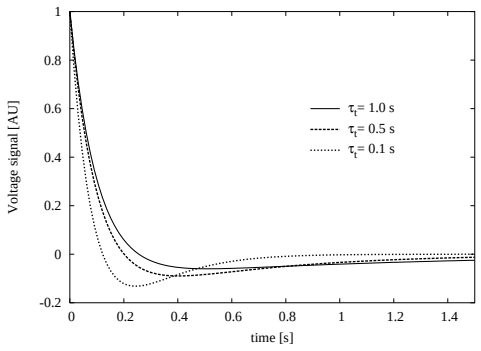


Figure 8.3 - Signal shape of voltage for $\tau_e$ = 0.1 s and different values of $\tau_T$.

The base line is recovered, after an undershoot, with the thermal time constant $\tau_T$. In the above analysis, the finite response time $\tau_R$ of the capacitive sensor has been optimistically neglected. $\tau_R$ is , defined as the characteristic time required by the dielectric constant to change as a consequence of an instantaneous temperature variation. $\tau_R \ll \tau_T, \tau_e$ have been assumed. This assumption is critical, since amorphous solids show an intrinsically slow behavior. An important part of the future experimental work will deal with the minimization of the response time. It is unlikely that capacitive bolometers based on glass sensors could ever be used in high rate applications, while their intrinsic time limitations could be negligible in rare event searches.

The maximum signal $\Delta V_c$ for a $\Delta T/T$ fractional temperature change is given by:

$$\Delta V_c \;=\; V_b \cdot A_c \cdot \frac{\Delta T}{T} \quad \text{with} \quad A_c \;=\; \frac{d\log C}{d\log T} \;=\; K_c \cdot T \tag{8.6}$$

to be compared with the following expression for resistors:

$$\Delta V_R \;=\; V_b \cdot A_R \cdot \frac{\Delta T}{T} \quad \text{with} \quad A_R \;=\; \frac{d\log R}{d\log T} \;=\; K_R \cdot T \tag{8.7}$$

In the case of massive resistive bolometers, such as in the CUORE case, $A_R \approx 8$, $V_b \approx$ 5mV and $V_b \cdot A_R \approx$ 4x10$^{-2}$ V; in the capacitive case $K \approx 0.05$, and $A_C \approx$ 5x10$^{-4}$ at 10 mK. However $V_b$ could be in principle as high as 100 V if the dielectric strength of the material is sufficiently high. With $V_b$=20 V, a quite low value, a 50 $\mu$V/Mev signal is expected from a capacitive sensor in a CUORE-like bolometer, to be compared with 200 $\mu$V/Mev from a resistive sensor. This reduction in the signal may be, however, largely compensated by lower contributions to the noise, i.e.:

- intrinsic noise from the load resistor $R$;
- preamplifier noise;
- microphonic noise.

Detailed calculations of the S/N ratio for a capacitive bolometer in a CUORE-like detector show that an energy resolution $\sim$ 5 times better than the present one ( $\approx$ 1 keV *rms*) can be achieved, assuming $\tau_e = 1$ s, a value quite compatible with the intrinsic slowness of large mass bolometers and, hopefully, of the capacitive sensors [129, 130, 131]. Other approaches to the signal read-out could be used leading to higher S/N ratios:

(1) a SQUID could be employed to realize a read-out system of the type used for resonant gravitational antennas;

(2) the sensor could be a component of a resonant circuit, like a piezoelectric crystal: the variation of capacitance could be detected as a frequency modulation of the sinusoidal signal.

In this case, several sensors working at different frequencies could share a single pair of wires, with a great simplification in the wiring of a multidetector experiment.

### Preliminary experimental results

A few types of commercial SMD capacitors were tested in a dilution refrigerator. The measurements on two Ceramic Y5V SMD ceramic capacitors are (1) B1 25V DC, 0.1$\mu$F at 300K, 1.6x0.8x0.8 mm$^3$; (2) B2 50V DC, 47 nF at 300K, 1.6x0.8x0.8 mm$^3$.
Measurements were carried out at 1 kHz by means of an Andeen-Hagerling capacitance bridge. Fig.8.5 shows that there is a small overheating in data of Fig.8.4 for temperature below the minimum, with a contact resistance $R_k \approx$ 3 10$^2$ T$^{-3}$ [K/W], which is quite reasonable for the SMD contact surface. The shift below the minimum is attributed to an overheating effect and not to a field effect because the latter should move data to the left when the field decreases [132].

The relaxation time constant for capacitor B2 is was also measured. It was mounted on top of a Neutron Transmutation Doped (NTD) Ge thermistor used as a fast heater ($\tau_{Ge} \approx 2\ 10^{-4}$ s at 25 mK). The capacitor acted as a thermometer. The time response of the system was measured by injecting a constant Joule power through the NTD thermistor and by suddenly releasing this power. The relaxation time constant was $\sim$ 5 s, as the example of thermal discharge of

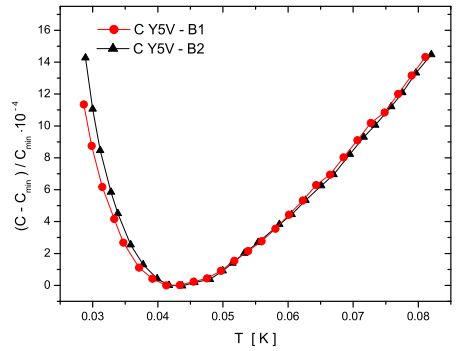


Figure 8.4 - $(C - C_{min})/C_{min}$ for capacitors B1 and B2.

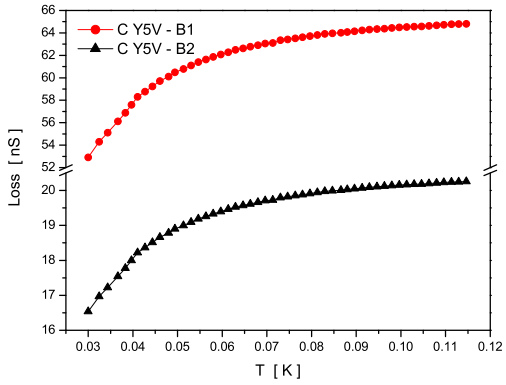


Figure 8.5 - Losses of B1 and B2.

Fig.8.6 shows. It is unlikely that this characteristic time is due to the thermal recovery time of the system $C/G$, which is expected to be much faster, but it should be attributed to the intrinsic response time $\tau_R$ of the capacitive sensor. Data so far obtained so far suggest that additional measurements should be made on components with higher working voltage, lower capacitance and at lower frequencies in order to get even lower losses. In fact, in the case of capacitor B2, the loss gives a power of about 4 pW, for using the applied measuring voltage (0.015 V rms).

In the future, integrated capacitors developed for this project by ITC-irst (Trento, Italy), a company which produces microelectronic devices for Research and Development purposes, will be tested. These integrated capacitors consist of an amorphous $SiO_2$ layer grown on a silicon substrate. Two planar electrodes are realized below the amorphous layer (through high silicon doping) and above it (through a metal film). Samples have been produced with different layer thicknesses (ranging from 0.1 to 1 $\mu$m) and different layer areas (ranging from 2×2 mm$^2$ to 10×10 mm$^2$). B and P impurities were also introduced in some samples in order to test their effect on the temperature dependence of the dielectric constant. The dielectric strength of these devices should be very high, of the order of 1 V/nm, allowing the application of a high static potential, of

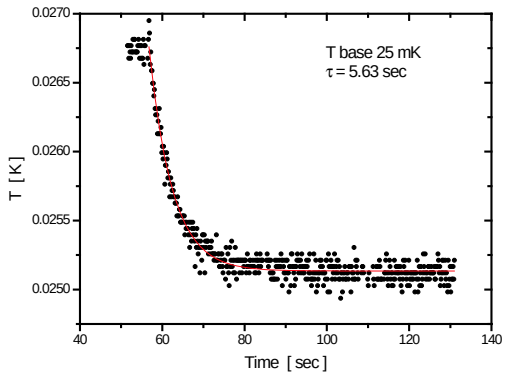


Figure 8.6 - Example of thermal discharge at 25 mK.

the order of tens or hundreds of volts. In addition, it is hoped that the complete elimination of the spurious materials (contacts, substrate) inevitably present in commercial samples and the reduced size of the devices could lead to faster time responses.

Also in the case of this R&D activity particular care must be taken in order to avoid the use of non radiopure materials that could lead to a worsening in the background counting rate.

## 8.7 Development of surface sensitive $TeO_2$ elements

One of the main tasks of the research and development program for CUORE is certainly the study of a method for background control and rejection, especially for the background that comes from surface contaminations of the material of the cryostat and detector holder. In fact, it looks like that this background component is the most difficult to control and that could compromise the experiment results.

Furthermore, Monte Carlo simulations, compared with experimental data, show that the dominant background originates in passive elements which surround the detectors (in particular, the copper supports for the crystals). This background is to be ascribed to surface contaminations in Th and U, which emit energy-degraded alpha and beta particles able to deposit their energy at the detector surfaces, (see 6.4) populating the spectral region between 2 and 4 MeV.

The presently designed CUORE configuration would not allow a substantial improvement of this background, expected to be of the order of 0.1 c/(keV kg y). On the contrary, in order to reach limits on the neutrino Majorana mass of the order reported in sec. 1.7 (required to test the whole inverted-mass-hierarchy region), it is mandatory to dramatically reduce this background and this constraint could be very hard to achieve with the present surface contaminations.

The surface background events reduction for CUORE can be achieved in three ways:

- dramatically improving the quality of the copper surface treatment;

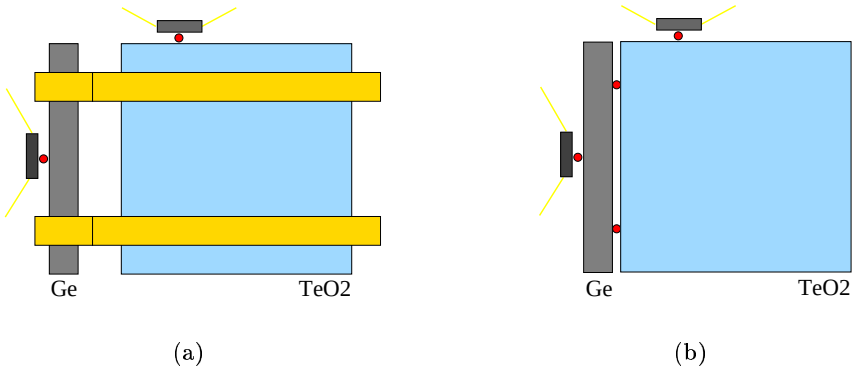


Figure 8.7 - Model for a bolometer with only one active surface shield. In (a) an external structure holds the shield while in (b) the shield is glued directly on the $TeO_2$ crystal.

- realizing single Cuoricino and CUORE elements with a radically innovative structure, in which the copper surface facing the detectors is reduced by a factor at least 100-1000;
- realizing "clever" bolometers able to distinguish an event originated at the surface from one originated in the crystal bulk.

All these three points are currently part of the R&D program for CUORE but here only the third point is discussed.

The fundamental idea behind the possibility that a bolometer could discriminate surface events is quite simple: it consists in the active shielding of the crystal absorber with thin, large-area, ultrapure Ge-foils (figure 8.7(a)). On each of these shields a small NTD thermistor for temperature reading is attached. Using common anticoincidence techniques, it's possible to detect and discard those events that, come from outside the crystal bulk and release their energy in a Ge-shield. The main problem of this configuration consist in the difficulty of realizing a holder structure that avoids the thermal coupling between the central $TeO_2$ bolometer and the Ge-shields and, at the same time, keeps the single module dimensions small enough.

A simpler and perhaps more efficient and powerful way to solve this problem could be to thermally couple the Ge shields with the $TeO_2$ crystal (figure 8.7(b)). In this way the auxiliary Ge bolometers completely surround the crystal, since they are glued to it exactly in the exact same way as the NTD thermistor on $TeO_2$. Such a configuration is simply a composite bolometer, realized with a main $TeO_2$ bolometer and six (one for each face) auxiliary Ge bolometers that act as active shields. Each of these bolometers will have its own thermistor with its signal channels (this means 7 channels for a single detector).

It's straightforward to understand that the origin of the events could be easily determined comparing the amplitude of the pulses from the different detector elements.

If an $\alpha$ particle comes from outside the bolometer, it interacts with a Ge shields releasing all its energy there. As a consequence, the temperature will

rise and there will be a signal on both the Ge thermistor and the $TeO_2$ one. Because of the small heat capacity of the Ge shields, its thermistor signal will be higher than those on the $TeO_2$ thermistor and moreover the Ge-sensor pulse could reach the saturation value in very little time. On the other side, an event inside the $TeO_2$ crystal will lead to similar and "classical" pulses on both the thermistors.

Furthermore, the pulse shape (e.g. the rise and decay times) will likely be different, depending on the place of the initial energy release. However, this intuitive behavior must be verified by simulations and experimental measurements.

This feature gives a very simple method for event discrimination: events produced in the energy absorber bulk produce two "classical" pulses whereas events coming from outside, for example produced on the copper surface, will give a fast high and maybe saturated pulse on the Ge sensor and a "classical" pulse on the $TeO_2$ sensor.

One of the complications of this kind of detectors is the presence of several electronic channels, needed for signal acquisition from each detector. In a large experiment, such as CUORE, this issue grows dramatically. Luckily, it should be possible, using the Ge shields in the saturation range as indicators of surface events, to operate in parallel or in series all the six auxiliary surface bolometers. In this way, the total number of channels would just be doubled.

### 8.7.1 Modelization of a generic thermal network with $n$ nodes

Since there is no experimental setup (e.g. a dilution refrigerator), at the moment, usable for testing the composite bolometer described above, the first step has been to try to simulate its behavior from the knowledge and the properties of the single $TeO_2$ crystal bolometers.
The following considerations have been obtained without taking into account athermal components of pulses. In fact, the understand of the causes and effects of the athermal components are too poor, and moreover it is not yet clear yet how to apply this information to the Ge bolometers shielding the $TeO_2$ detector.

The thermal model initially introduced in chapt. 7 has been referred to a specific thermal network with only three nodes. That approach was a practical simplification. In fact, it is clear that such a model will work perfectly after some generalizations, even for a system with any number of nodes. Moreover, the systems of equations 7.5 and 7.50 that describe the static and dynamic behavior of the thermal network, have been deduced from a very general consideration (e.g. the conservation of energy at each node) and so they could be easily extended for $n$ number of nodes.

Let's consider a generic thermal network with $n$ nodes (0,1,2,...,$n$). In order to simplify the notation, let's pretend that the node $n = 0$ is the heat sink at temperature $T_0$. The generic node $k$ could be connected to the node $i$ with a conductance

$$G_{ki}(T) = g_{ki}T^{\alpha_{ki}} \tag{8.8}$$

where, clearly, $G_{ki} = G_{ik}$ e $G_{kk} = 0$. If $\pi_k$ is the parasitic power at the $k$ node then the equation that rules the power balance at this node in static conditions

is given by:

$$\pi_k - \sum_{i=0}^{N} P_{ki} = 0 \tag{8.9}$$

where

$$P_{ki} = \frac{g_{0,ki}}{\alpha_{ki}+1}\left[T_k^{\alpha_{ki}+1} - T_i^{\alpha_{ki}+1}\right] \tag{8.10}$$

For those nodes that are the electrical component of a thermistor, it is necessary to add, on the left-hand side of equation 8.9, the term due to the dissipated Joule power:

$$\pi'_k(\text{Joule}) = R_k\left[\frac{V_{\text{BIAS},k}}{R_k + R_{L,k}}\right]^2 \tag{8.11}$$

where $R_k(T_k)$ is the sensor resistance given by 7.4 and $R_{L,k}$ is the load resistance of the bias circuit for that specific thermistor.

The system of $n$ equations, given by 8.9 for each node, describes the static behavior of a general thermal network.

In the same way, it's easy to write the conservation of energy in the dynamic situation can be written

$$C_k(T_k)\cdot\dot{T}_k = \pi_k - \sum_{i=0}^{N} P_{ki} \tag{8.12}$$

In this case, we have also to take into account the equations that are needed to describe the bias circuits for the thermistors nodes:

$$\dot{V}_j = \frac{1}{c_{p,j}\cdot R_{L,j}}\left[V_{\text{BIAS},j} - \frac{R_j(T_j)+R_{L,j}}{R_j(T_j)}V_j\right] \tag{8.13}$$

For a thermal network with $n$ nodes and assuming that $m$ of them are thermistors, the equations 8.12 and 8.13 lead to a system of $n+m$ equations that gives the time behavior of the temperature at each node and of the voltage at the thermistor ends. The starting conditions are derived in a natural way.

As already pointed out in the previous chapter, the algorithms for numerical computing keep their validity also for a network with $n$ nodes and they have been already developed in such a general way.

### 8.7.2 Thermal parameters of the simulated composite bolometer

Initially the preferred option has been to study the behavior of these new detectors by making the hypothesis that a Ge bolometer shields only a one side of the $TeO_2$ main bolometer. In fig. 8.8 the thermal model representing this composite detector is shown.

The two bolometers of the simulated composed detector are realized in the following way:

- a usual Cuoricino-like bolometer with a 5x5x5 $cm^3$ size $TeO_2$ crystal. The energy absorber is coupled with a 3x3x1 $mm^3$ Ge-NTD sensor using 9 glue spots;

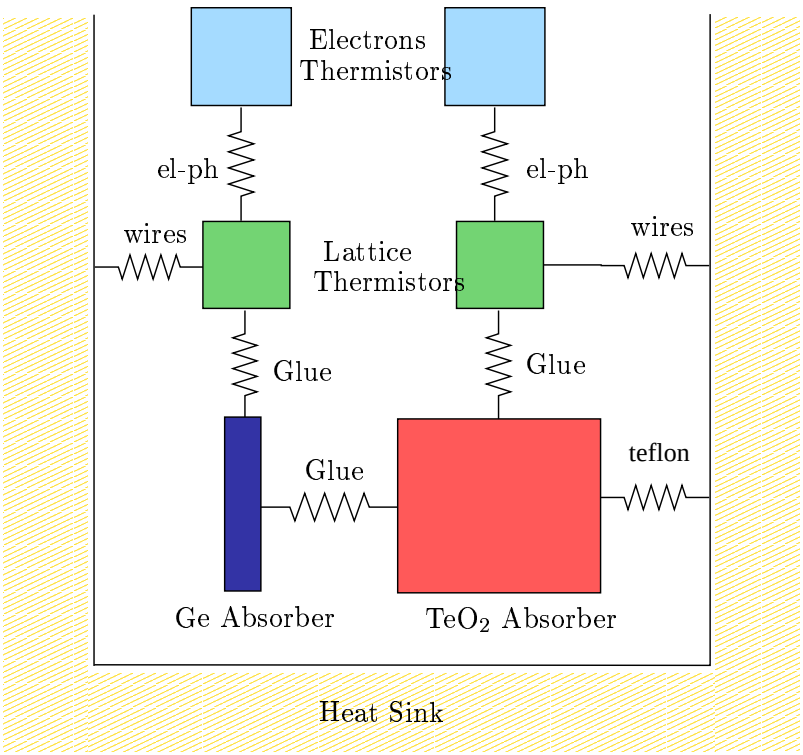


Figure 8.8 - Thermal network representing a bolometer composite composed by a Cuoricino-like $TeO_2$ main detector and a Ge bolometer.

- a 50x50x0.3 $mm^3$ size Ge crystal used as energy absorber coupled with 3x1.5x0.4 $mm^3$ using 6 glue spots;

The two bolometers are coupled by means of 3 glue spots. Only the background power on the $TeO_2$ absorber has beenis introduced and its value is 6.5 pW.

The initial step consists in the determination of the composite bolometer optimal working point. Since the two thermistors could be biased independently, the following procedure has been performed in order to understand if the optimization of the working point of a bolometer could influence the optimal working point of the other one.

1. the $TeO_2$ bolometer optimal working point is searched for without polarizing the Ge bolometer. The optimal working point of $TeO_2$ bolometer corresponds to $V_{BIAS,1} \simeq 0.85$ V, as fig. 8.9(a) shows.

2. the same operation described in the previous step has been performed inverting the thermistor order. The result is shown in fig. 8.9(b). The optimal working point for the Ge bolometer, and using 54 G$\Omega$ as load resitance, corresponds to $V_{BIAS,2} \simeq 0.18$ V.

3. the optimal working point of the $TeO_2$ bolometer is searched for again but this time with the Ge bolometer in its optimal working point. It has been

found that the $TeO_2$ optimal operation point does not change as shown in fig. 8.9(c).

The pulses generated by depositing 2.5 MeV on the $TeO_2$ crystal (corresponding to a $0\nu$DBD event), were simulated. They are collected by the Ge bolometer sensor and by the $TeO_2$ bolometer sensor working at their optimal operation points. Fig. 8.10 shows them. It is possible to observe that both pulses have "classical" shapes.

The pulses developed after the deposition of 2.5 MeV on the Ge shield have been simulated in the same conditions of the previous simulation. Fig. 8.10 shows the results. It is possible to see that the thermal pulse detected by the main bolometer has a "classical" shape whereas the one collected by the Ge detector is saturated. This is the signature that allows one to recognize events coming from outside and to reject them. It must be remarked that $0\nu$DBD events are bulk events. In fact the range of electrons in the $TeO_2$ crystal is very short (the efficiency of the $TeO_2$ bolometer is $\epsilon = 0.86$). Without active Ge shield the simulated event could be confused as a $0\nu$DBD event or originate a background count in the $0\nu$DBD energy region. The active Ge shield with a coincidence analysis will allow us to recognize the origin of the event (active shields or TeO2 crystal) by means of the comparison among pulses coming from the different elements.

The comparison between the pulses on the two sensors could be carried out by means of a *scatter plot*, i.e. plotting the Ge-bolometer pulse amplitudes versus the corresponding main bolometer pulse amplitudes. Two clearly separated curves distinguish the events generated in the shield from the events generated in the main crystal, as it is shown in fig. 8.12. Events corresponding to the bulk interactions form a straight line in the scatter plot, whereas the ones that occurred in the Ge shield correspond to a saturated curve. This scatter plot was obtained by releasing all the energy in one of the absorbers.

On the other hand it is possible that a particle interacts with the Ge shield releasing only part of its energy and then impacts impacting with the $TeO_2$ absorber depositing all of the remaining energy. It is likely that in this condition the event be is located in the scatter plot region between the two curves. This possibility hasn't been thoroughly analyzed yet.

The CUORE collaboration proposes to study these innovative detectors. Small composite bolometers were constructed and will soon be soon tested at the University of Insubria by means of a calibrated radioactive source, in order to experimentally verify the reported simulation results.

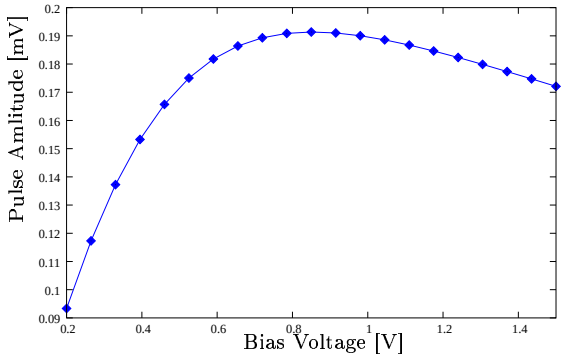


(a)

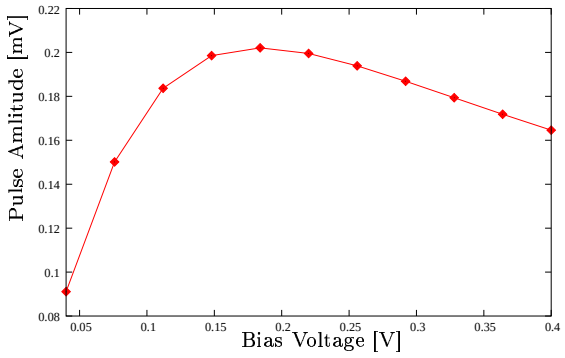


(b)

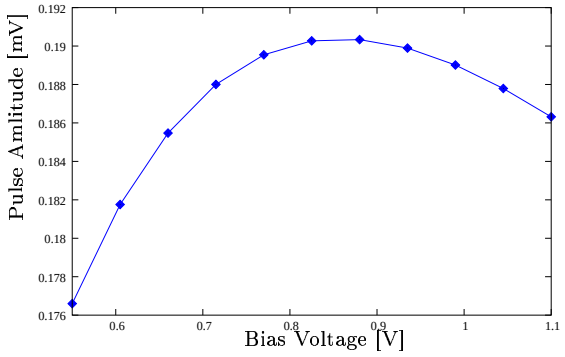


(c)

Figure 8.9 - Searching for the optimal working point of a composite bolometer. Figure (a) corresponds to the first point of the procedure described above, while (b) corresponds to the optimal working point for the Ge bolometer. In figure (c) it is verified that the polarization on a bolometer does not influence the optimal working point of the other one.

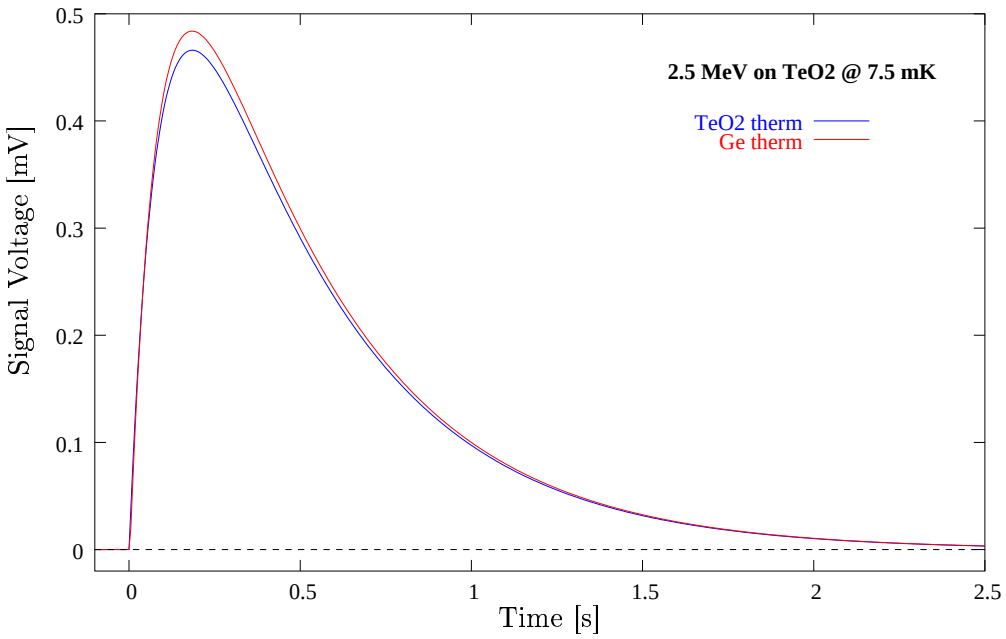


Figure 8.10 - Signals collected by the two thermistors releasing 2.5 MeV in the $TeO_2$ energy absorber.

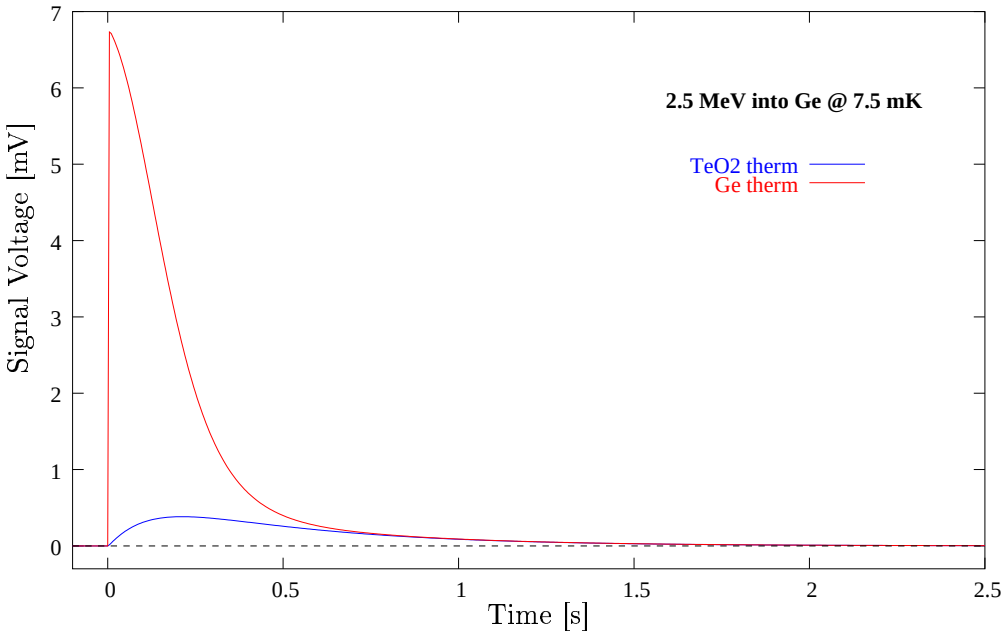


Figure 8.11 - SegnalsSignals collected by the two thermistors releasing 2.5 MeV in the Ge energy absorber.

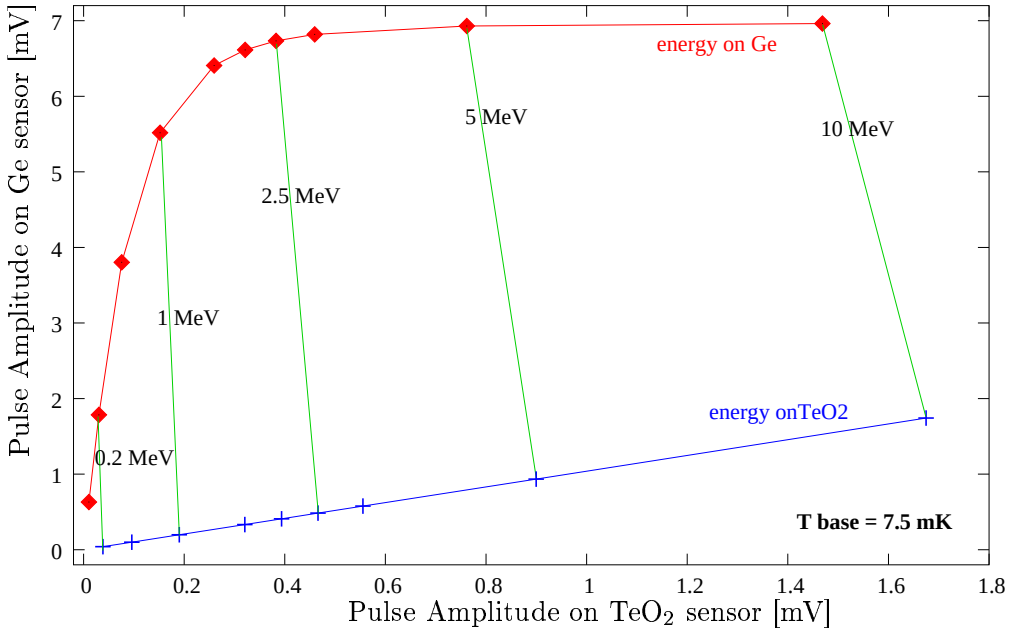


Figure 8.12 - Scatter plot obtained simulating energy depositions in $TeO_2$ and Ge crystals.

# Bibliography


[1] B. Kayser, (2001), hep-ph/0104147.

[2] C. Giunti and M. Laveder, (2003), hep-ph/0310238.

[3] C. Giunti and C. W. Kim, Found. Phys. Lett. **14**, 213 (2001), hep-ph/0011074.

[4] S. M. Bilenky, C. Giunti, and W. Grimus, Prog. Part. Nucl. Phys. **43**, 1 (1999), hep-ph/9812360.

[5] B. Kayser, J. Phys. **G29**, 1463 (2003), hep-ph/0306073.

[6] J. N. Bahcall, M. H. Pinsonneault, and S. Basu, Astrophys. J. **555**, 990 (2001), astro-ph/0010346.

[7] B. T. Cleveland *et al.*, Astrophys. J. **496**, 505 (1998).

[8] R. Davis, Phys. Rev. Lett. **12**, 303 (1964).

[9] J. Davis, Raymond, D. S. Harmer, and K. C. Hoffman, Phys. Rev. Lett. **20**, 1205 (1968).

[10] SAGE, J. N. Abdurashitov *et al.*, J. Exp. Theor. Phys. **95**, 181 (2002), astro-ph/0204245.

[11] D. N. Abdurashitov *et al.*, Phys. Lett. **B328**, 234 (1994).

[12] GALLEX, P. Anselmann *et al.*, Phys. Lett. **B285**, 376 (1992).

[13] GALLEX, W. Hampel *et al.*, Phys. Lett. **B447**, 127 (1999).

[14] GNO, M. Altmann *et al.*, Phys. Lett. **B490**, 16 (2000), hep-ex/0006034.

[15] KAMIOKANDE-II, K. S. Hirata *et al.*, Phys. Rev. Lett. **63**, 16 (1989).

[16] Kamiokande, Y. Fukuda *et al.*, Phys. Rev. Lett. **77**, 1683 (1996).

[17] Super-Kamiokande, M. B. Smy *et al.*, (2003), hep-ex/0309011.

[18] Super-Kamiokande, Y. Gando *et al.*, Phys. Rev. Lett. **90**, 171302 (2003), hep-ex/0212067.

[19] Super-Kamiokande, Y. Fukuda *et al.*, Phys. Rev. Lett. **82**, 2430 (1999), hep-ex/9812011.

[20] B. Ananthanarayan and R. K. Singh, Curr. Sci. **83**, 553 (2002), physics/0208096.

[21] SNO, Q. R. Ahmad *et al.*, Phys. Rev. Lett. **87**, 071301 (2001), nucl-ex/0106015.

[22] SNO, Q. R. Ahmad *et al.*, Phys. Rev. Lett. **89**, 011301 (2002), nucl-ex/0204008.

[23] SNO, Q. R. Ahmad *et al.*, Phys. Rev. Lett. **89**, 011302 (2002), nucl-ex/0204009.

[24] SNO, S. N. Ahmed *et al.*, (2003), nucl-ex/0309004.

[25] Super-Kamiokande, Y. Fukuda *et al.*, Phys. Rev. Lett. **82**, 2644 (1999), hep-ex/9812014.

[26] Super-Kamiokande, Y. Fukuda *et al.*, Phys. Lett. **B433**, 9 (1998), hep-ex/9803006.

[27] Super-Kamiokande, Y. Fukuda *et al.*, Phys. Rev. Lett. **81**, 1562 (1998), hep-ex/9807003.

[28] MACRO, M. Ambrosio *et al.*, Phys. Lett. **B434**, 451 (1998), hep-ex/9807005.

[29] ICARUS, F. Arneodo *et al.*, (2001), hep-ex/0103008.

[30] LSND, C. Athanassopoulos *et al.*, Phys. Rev. Lett. **77**, 3082 (1996), nucl-ex/9605003.

[31] E. D. Church, K. Eitel, G. B. Mills, and M. Steidl, Phys. Rev. **D66**, 013001 (2002), hep-ex/0203023.

[32] LSND, A. Aguilar *et al.*, Phys. Rev. **D64**, 112007 (2001), hep-ex/0104049.

[33] M. Apollonio *et al.*, Eur. Phys. J. **C27**, 331 (2003), hep-ex/0301017.

[34] CHOOZ, M. Apollonio *et al.*, Phys. Lett. **B466**, 415 (1999), hep-ex/9907037.

[35] F. Boehm *et al.*, Phys. Rev. **D62**, 072002 (2000), hep-ex/0003022.

[36] KamLAND, K. Eguchi *et al.*, Phys. Rev. Lett. **90**, 021802 (2003), hep-ex/0212021.

[37] KamLAND, K. Eguchi *et al.*, (2003), hep-ex/0310047.

[38] K2K, M. H. Ahn *et al.*, Phys. Rev. Lett. **90**, 041801 (2003), hep-ex/0212007.

[39] K2K, S. H. Ahn *et al.*, Phys. Lett. **B511**, 178 (2001), hep-ex/0103001.

[40] G. L. Fogli, E. Lisi, A. Marrone, A. Palazzo, and D. Montanino, Nucl. Phys. Proc. Suppl. **118**, 177 (2003).

[41] E. Fermi, Z. Phys. **88**, 161 (1934).

[42] F. Perrin, Comptes Rendues **197**, 1625 (1933).

[43] S. C. Curran *et al.*, Nature **162**, 302 (1948).

[44] B. Pontecorvo, Phys. Rev. **983**, 75 (1949).

[45] J. Bonn *et al.*, Phys. Atom. Nucl. **63**, 969 (2000).

[46] V. M. Lobashev, Phys. Atom. Nucl. **63**, 962 (2000).

[47] M. Galeazzi, F. Fontanelli, F. Gatti, and S. Vitale, Phys. Rev. Lett. **86**, 1978 (2001).

[48] A. Nucciotti *et al.*, AIP Conf. Proc. **605**, 453 (2002).

[49] H. Paes and T. J. Weiler, Phys. Rev. **D63**, 113015 (2001), hep-ph/0101091.

[50] M. Lindner, (2002), hep-ph/0209083.

[51] A. D. Dolgov, Surveys High Energ. Phys. **17**, 91 (2002), hep-ph/0208222.

[52] K. Kainulainen and K. A. Olive, (2002), hep-ph/0206163.

[53] G. G. Raffelt, New Astron. Rev. **46**, 699 (2002), astro-ph/0207220.

[54] C. L. Bennett *et al.*, Astrophys. J. Suppl. **148**, 1 (2003), astro-ph/0302207.

[55] W. M. Alberico and S. M. Bilenky, (2003), hep-ph/0306239.

[56] S. R. Elliott and P. Vogel, Ann. Rev. Nucl. Part. Sci. **52**, 115 (2002), hep-ph/0202264.

[57] A. Faessler and F. Simkovic, J. Phys. **G24**, 2139 (1998), hep-ph/9901215.

[58] M. Goeppert-Mayer, Physics Rev. Lett. **59**, 512 (1987).

[59] M. K. Moe, Nucl. Phys. Proc. Suppl. **38**, 36 (1995).

[60] F. Boehm *et al.*, Phys. Rev. **D64**, 112001 (2001), hep-ex/0107009.

[61] S. Pascoli and S. T. Petcov, (2003), hep-ph/0308034.

[62] S. Pascoli and S. T. Petcov, Phys. Lett. **B544**, 239 (2002), hep-ph/0205022.

[63] J. Suhonen and O. Civitarese, Phys. Rept. **300**, 123 (1998).

[64] A. Staudt *et al.*, Phys. Rev. C **46**, 871 (1992).

[65] G. Pantis *et al.*, Phys. Rev. C **53**, 695 (1996).

[66] P. Vogel *et al.*, Phs. Rev. Lett. **57**, 3148 (1986).

[67] O. Civitarese *et al.*, Phys. Lett. B **194**, 11 (1987).

[68] T. Tomoda, Rep. Prog. Phys. **54**, 53 (1991).

[69] C. Barbero *et al.*, Nucl. Phys. A **650**, 485 (1999).

[70] F. Simkovic, Phys. Rev. C **60**, 055502 (1999).

[71] J. Suhonen *et al.*, Nucl. Phys. A **543**, 645 (1992).

[72] K. Muto *et al.*, Z. Phys. A **334**, 187 (1989).

[73] S. Stoica *et al.*, Phys. Rev. C **63**, 064304 (2001).

[74] A. Faessler *et al.*, J. Phys. G **24**, 2139 (1998).

[75] J. Engel *et al.*, Phys. Lett. **B 225**, 5 (1989).

[76] M. Aunola *et al.*, Nucl. Phys. A **643**, 207 (1998).

[77] V. A. Rodin *et al.*, nucl-th/0305005.

[78] W. Haxton *et al.*, Prog. Part. Nucl. Phys. **12**, 409 (1984).

[79] E. Caurier *et al.*, Phys. Rev. Lett. **77**, 1954 (1996).

[80] J. Hirsh *et al.*, Nucl. Phys. A **589**, 445 (1995).

[81] O. Cremonesi, Nucl. Phys. Proc. Suppl. **118**, 287 (2003), hep-ex/0210007.

[82] H. V. Klapdor-Kleingrothaus *et al.*, Eur. Phys. J. **A12**, 147 (2001), hep-ph/0103062.

[83] C03-06-23.1, A. M. Bakalyarov, A. Y. Balysh, S. T. Belyaev, V. I. Lebedev, and S. V. Zhukov, (2003), hep-ex/0309016.

[84] H. V. Klapdor-Kleingrothaus, A. Dietz, H. L. Harney, and I. V. Krivosheina, Mod. Phys. Lett. **A16**, 2409 (2001), hep-ph/0201231.

[85] C. E. Aalseth *et al.*, Mod. Phys. Lett. **A17**, 1475 (2002), hep-ex/0202018.

[86] H. V. Klapdor-Kleingrothaus, (2002), hep-ph/0205228.

[87] H. L. Harney, (2001), hep-ph/0205293.

[88] NEMO, X. Sarazin and D. Lalanne, (2000), hep-ex/0006031.

[89] S. Simon, Nature **135**, 763 (1935).

[90] D. H. Andrews *et al.*, Phys. Rev. **76**, 154 (1949).

[91] E. Fiorini and T. O. Niinikoski, Nucl. Instr. Meth. **A224**, 83 (1984).

[92] A. Giulini, AIP Conference Proceedings **605** (2001).

[93] C. Brofferio *et al.*, Nucl. Phys. Proc. Suppl. **48**, 238 (1996).

[94] A. Alessandrello *et al.*, Phys. Lett. **B433**, 156 (1998).

[95] A. Alessandrello *et al.*, Phys. Lett. **B486**, 13 (2000).

[96] C. Arnaboldi *et al.*, Phys. Lett. **B557**, 167 (2003), hep-ex/0211071.

[97] CUORE, C. Arnaboldi *et al.*, Astropart. Phys. **20**, 91 (2003), hep-ex/0302021.

[98] CUORE, C. Arnaboldi *et al.*, (2002), hep-ex/0212053.

[99] A. Alessandrello *et al.*, Physics Review Letters **513A**, 82 (1999).

[100] R. Bernabei *et al.*, Physics Letters B **424**, 185 (1998).

[101] Y. B. Levinson, Phonon propagation with frequency down-conversion, in *Nonequilibrium Phonons in Nonmettalic Crystals*, edited by W. Eisenmenger and A. Kaplyanskii, chap. 3, pp. 91–143, Elsevier Science Publisher B.V., Amsterdam, 1986.

[102] B. Taylor, H. Maris, and C. Elbrum, Phys. Rev. Lett. **49**, 416 (1969).

[103] K. Irwin *et al.*, Rev. Sci. Instr. **66**, 5322 (1995).

[104] C. Cozzini *et al.*, LTD9 conference proceedings **605**, 481 (2001).

[105] N. Mott and J. Davis, Phil.Mag. **B42**, 845 (1980).

[106] S. Moseley, J. Mather, and D. McCammon, J. Appl. Phys. **56**, 1257 (1984).

[107] A. Alessandrello *et al.*, Nucl. Instrum. Meth. **B17**, 411 (1986).

[108] A. Alessandrello, D. V. Camin, E. Fiorini, A. Giuliani, and G. Pessina, Nucl. Instrum. Meth. **A264**, 93 (1988).

[109] A. Alessandrello *et al.*, Prepared for 3rd International Workshop on Low Temperature Detectors for Neutrinos and Dark Matter, L'Aquila, Italy, 20-23 Sep 1989.

[110] A. Alessandrello *et al.*, Prepared for 3rd International Workshop on Low Temperature Detectors for Neutrinos and Dark Matter, L'Aquila, Italy, 20-23 Sep 1989.

[111] R. Firestone, John Wiley and Sons (1996).

[112] G. R. Dyck *et al.*, Phys. Lett. **B245**, 343 (1990).

[113] A. Guiliani *et al.*, Nucl. Instrum. Meth. **A263**, 233 (1988).

[114] E. E. Haller *et al.*, Proc. Fourth Int. Conf. on Neutron Transmutation Doping of Semiconductor Materials , 21 (1984).

[115] A. Alessandrello *et al.*, Nucl. Instr. and Meth. A **454**, 412 (1998).

[116] P. Belli *et al.*, Nuovo Cimento **A101**, 953 (1989).

[117] G. Zdesenko *et al.*, Phys. Lett. B **546**, 206 (2002).

[118] F. Piquemal, Nucl. Phys. B **77**, 352 (1999).

[119] A. Alessandrello *et al.*, Czechoslovak J. Phys. **46-S5**, 2893 (1996).

[120] M. Barucci *et al.*, J. Low Temp. Phys. **123**, 303 (2001).

[121] A. Giuliani, Physica B **280**, 501 (2000).

[122] W. Phillips, Rep.Prog.Phys **50**, 1657 (1987).

[123] C. Yu and A. Leggett, Comments Cond.Mat.Phys **4**, 231 (1988).

[124] J. Lopes *et al.*, Phys Rev.B **61**, 273 (1999).

[125] P. Strelow and M. Meissner, Physica B **273**, 263 (1999).

[126] P. Strehlov, J.Non-Cryst.Solids **121**, 463 (1990).

[127] P. Strehlov, Physica B **25**, 165 (1990).

[128] P. Strehlov, Cryogenics **34**, 421 (1994).

[129] A. Fascilla and G. Pessina, Nucl.Instr.Meth.A **469**, 116 (2001).

[130] A. Arnaboldi *et al.*, IEEE Trans.Nucl.Sci. **47**, 1851 (2000).

[131] A. Arnaboldi *et al.*, IEEE Trans.Nucl.Sci. **49**, 1808 (2002).

[132] S. Reijntjis *et al.*, Rev.Sci.Instrum. **57**, 1413 (1986).